ENHANCING SIGNAL TO NOISE RATIO FOR ELECTROSTATIC TRANSDUCERS

SYAMSUL BAHRIN ABDUL HAMID

Submitted in August 2013

in fulfilment for the degree of

Doctor of Philosophy

Centre for Ultrasonic Research

Department of Electronic and Electrical Engineering

University of Strathclyde

204 George Street, Glasgow, G1 1XW

Declaration of Authenticity

This thesis is the result of the author's original research. It has been composed by the author and has not been previously submitted for examination which has lead to the award of a degree.

Copyright Notice

Signed: 

Date: 23-SEP-2014

Acknowledgement

First of all, I would like to thank God All Mighty who has made it possible for me to complete this Thesis. Without His help and inspiration, I do not think that I could complete this journey as expected.

Secondly, thanks to my patience wife Zuraidah who has always supported me in my time of need and giving me the strength to endure and move on in such a grave and difficult time. To my mom Umi Kelesom and my dad Abdul Hamid, thank you for your continuous support in my struggle to complete my PhD. I would also like to thank my two lovely little girls Nur Aleesya Sofea and Nur Adeena Sofea, for their continuing effort in getting my attention; thus making me more efficient and focus towards the work ahead.

Special thanks to Dr Richard O'Leary and Prof. Gordon Hayward who have helped me to understand the sensitivity and noise concept and its main derivatives from start to finish. My personal thanks to Dr Nishal Ramandas and Dr Simon Whiteley who have started and help me within the start of my journey. Thanks to all the members of the Centre for Ultrasonic Engineering especially Dr John Mackersie, Mr Tommy McCunnie and Mr Duncan Lindsay in helping me to complete the manufacturing process for all the electrostatic transducers.

Lastly, thanks to all those who have helped me either directly or indirectly towards the completion of my PhD.

Abstract

This Thesis describes the design, manufacture and evaluation of a **Fl**uidically **A**mplified **U**ltrasonic **T**ransducer (FLAUT) for an air-coupled application. The transducer utilises a pipe as an amplification mechanism to increase the output pressure; and as a dissipation mechanism to reduce inherent noise within the transducer. The new transducer design introduces the concept of matched thin plate, cavity and pipe, of which the individual geometry enhances one another. Design methodologies, which consist of analytical modelling and Finite Element (FE) Modelling, have been implemented. The analytical modelling identifies the required geometry for the FLAUT based on the desired operating resonant frequency; while FE then verifies the vibrational characteristics of the design. Through the application of FE modelling and practical analysis, FLAUT devices have been designed, developed and compared with experiment.

The sensitivity analysis is utilised to realise a design and manufacturing tolerance requirements. The devices were manufactured in the operating range of 25 kHz to 85 kHz. Air-coupled pulse-echo insertion loss was found to be 61.3 dB, an improvement of 9.1 dB over the conventional cavity only design. Results from the proof of concept prototype indicate that the output of the FLAUT is maximised when the pipe radius is designed to be as large as practically possible while maintaining the matched resonant frequencies. This correlates well with theory both in term of sensitivity and noise. Furthermore, the pressure output of a FLAUT array is maximised by arranging the cell spacing to be as close as practically possible. Thus, the cells were spaced at multiples of 2.25 to the cavity radius – to reduce the risk of cell damage. An analytical method to simulate, and a technique to measure the inherent noise using a specially designed hybrid isolation vessel has been developed. From the measurement, the FLAUT noise is found to be 5.8 W, an improvement of 2.7 dB compared to the conventional cavity only design.

Table of Contents

Acknowledgement ii

Abstract iii

List of Figures x

List of Tables xx

List of Symbols xxi

List of Acronyms xxii

1. Introduction 1

    1.1 Background 1

    1.2 Aims and Contribution of the Thesis 2

        1.2.1 Aims of the Thesis 2

        1.2.2 Contribution of the Thesis to the Field of Air-Coupled Electrostatic Transducer 2

    1.3 Publication to Date Arising From the Thesis 3

        1.3.1 Publications 3

    1.4 Overview of the Thesis 4

2. Theoretical Background and a Review of Transducer Technology and Applications 7

    2.1 Introduction 7

    2.2 Generation and Detection of Ultrasound 8

    2.3 Tailoring Ultrasonic Transducer to Its Applications 11

        2.3.1 Propagating Ultrasound Signal 13

            2.3.1.1 Longitudinal Waves 14

            2.3.1.2 Transverse Waves 14

            2.3.1.3 Rayleigh and Lamb Waves 15

        2.3.2 Review of Different Applications in Relations to Coupling Media 17

            2.3.2.1 Solid 19

            2.3.2.2 Liquid 19

2.3.2.3 Gas (Mainly Air) 20
2.3.3 Analysis of Reflection and Transmission Losses at Normal Incidence 25
2.4 Review of Electrostatic Transducers 31
2.4.1 Rigid Backplate Design 32
2.4.1.1 Roughened Backplate 33
2.4.1.2 Regularly Patterned Backplate 34
2.4.2 Capacitive Micro-Machined Ultrasonic Transducer Design 36
2.5 Current Electrostatic Transducer and Its Limitation 39
2.5.1 Bias Voltage 39
2.5.2 Membrane Configuration 40
2.5.3 Air Gap Configuration 41
2.5.4 Key Design Consideration 42
2.6 Proposed Design to Enhanced Electrostatic Transducer 43
2.7 Conclusion 46
3. Modelling and Simulation Review and Analysis 48
3.1 Introduction 48
3.1.1 Modelling of Thin Plate 50
3.1.2 Modelling of Cavity 53
3.1.3 Modelling of Pipes 53
3.1.4 Expected Results from Analytical Modelling 56
3.2 Alternate Analytical Modelling Approaches 64
3.3 Modelling Using Finite Element Analysis 65
3.4 Review and Simulation of Different Diaphragm Vibrational Modes 71
3.4.1 Modelling and Simulation of a Diaphragm Vibrational Modes 74
3.5 Review of Cavity / Pipe Design for Single Cell Transducer 77
3.5.1 Analytical Analysis for Developing Single Cell Transducer 78
3.5.2 Finite Element Analysis Techniques for Geometric Analysis 82
3.5.3 Finite Element Analysis Techniques for Excited Model Analysis 88

3.5.3.1 Modelling using Comsol 89
3.5.3.2 Modelling using PZFlex 90
3.5.3.3 Comparison between Analytical Model, Comsol and PZFlex 92
3.6 Conclusion 93
4. Manufacturing Review, Prototyping and Analysis of Fluidic Amplified Electrostatic Transducer (FLAUT) using Surface Displacement 94
4.1 Introduction 94
4.2 Manufacturing Review for FLAUT Manufacture 94
4.2.1 Review on Different Manufacturing Techniques 95
4.2.2 Challenges in Manufacturing FLAUT Backplate 95
4.2.2.1 MSL 96
4.2.2.2 EDM 98
4.2.2.3 Drilling and Milling 100
4.2.2.4 Laser Cutting and Engraving 101
4.2.2.5 Photolithography 103
4.2.3 Final Determination of Manufacturing Techniques Implemented 104
4.3 Manufacturing, Assembly and Prototyping of Transducers 105
4.4 Review of Different Measuring Techniques 109
4.4.1 Laser Interferometer 110
4.4.2 Impulse Response 117
4.4.3 Directivity and Frequency response 120
4.5 Measuring and Verification of Prototypes 122
4.6 Effect of Resonant Frequency Due to Pipe Radius 128
4.6.1 Introduction 128
4.6.2 Identification of Suitable Pipe Radius 130
4.6.3 Summary 135
4.7 Effect to Resonant Frequency due to Machine Resolution 136
4.7.1 Introduction 136

4.7.2 Manufacturing Sensitivity Analysis 137
4.7.2.1 Thin Plate 139
4.7.2.2 Cavity 140
4.7.2.3 Pipe 142
4.8 Conclusion 143
5. Modelling and Measuring FLAUT Noise 145
5.1 Introduction 145
5.2 Modelling of Noise in a FLAUT 146
5.2.1 Transducer Noise 148
5.2.2 Modelling of Transducer SNR 148
5.2.2.1 Main Dissipation Mechanism 150
5.2.2.2 Other Dissipation Mechanism 153
5.2.3 Analytical Noise Model Evaluation 154
5.2.3.1 Transducer 154
5.2.3.2 Environmental Considerations 156
5.3 Development of Noise Isolation Vessel 157
5.3.1 Review on Different Measuring Techniques 158
5.3.2 Proposal for Hybrid Acoustic Isolation Vessel (HAIV) 160
5.3.2.1 Development of Isolation Vessel 161
5.3.2.2 Transducer Calibration 168
5.3.2.3 Leak Test for Isolation Vessel 168
5.3.2.4 Through-Transmission for Isolation Vessel 170
5.4 Measurement and Validation of Noise for FLAUT 172
5.4.1 Comparison of Noise Modelling and Measurements 174
5.5 Conclusion 178
6. Development of High Frequency FLAUT 180
6.1 Introduction 180
6.2 Modelling and Simulation of FLAUT in High Frequency 181

6.2.1 Modelling a FLAUT with a Single Cell Backplate Design 181
6.2.1.1 Analytical Model to Determine Geometry 181
6.2.1.2 Simulation and Geometric Analysis using FEA for 84.8 kHz Device 184
6.2.2 Backplate Array Design 193
6.2.2.1 Optimising Array Separation 194
6.2.3 Beam Profile Simulation 198
6.2.4 Simulation of a FLAUT Noise 199
6.3 Manufacturing and Assembly 201
6.3.1 Manufacturing Tolerance Review 201
6.3.2 Choice of Manufacture 203
6.3.3 Manufacturing Sensitivity Analysis 204
6.3.4 Prototyping and Assembly 206
6.4 Characterisation of FLAUT Prototype and Modelling Validation 208
6.4.1 Measurement of a FLAUT Sensitivity 208
6.4.1.1 Measurement of Single Unit Cell 209
6.4.1.2 Measurement of Array 210
6.4.1.3 Beam Profile Measurement 215
6.4.2 Measurement of a FLAUT Noise 216
6.4.3 Comparison between Measured FLAUT and Measured Conventional Electrostatic Transducer with Cavity Only Design 217
6.5 Conclusion 226
7. Conclusion and Recommendation for Further Work 228
7.1 Conclusion 228
7.1.1 General Overview 228
7.1.2 Main Finding of this Thesis 228
7.2 Suggestions for Further Work 230
7.2.1 Analytical Modelling 230
7.2.2 Finite Element Modelling 231

7.2.3 Backplate Manufacturing Process Improvement (Analysis and Fabrication) 232

7.2.3.1 Utilising Higher Repeatability Tolerance for Manufacture of the FLAUT 233

7.2.3.2 Utilising Deep Reactive Ion Etching (DRIE) as a Manufacturing Process 233

7.2.3.3 Utilising Ultra Violet (UV) based-LIGA as a Manufacturing Process 234

7.2.3.4 Utilising Generalised Application Technique in MEMS/NEMS (Nano Electro-mechanical System) Area which utilises Small Cavities and Pipes as a Manufacturing Process Consideration 236

7.2.4 Assembly Process 237

8. References 240

9. Appendixes 257

9.1 U.S. Navy Workshop on Acoustic Transduction Materials and Devices 2011 257

List of Figures

Figure 2.1: Schematic Diagram of a Piezoelectric Transducer 10

Figure 2.2: Schematic Diagram of an Electrostatic Transducer 10

Figure 2.3: Schematic Diagram of Pulse-Echo Technique 11

Figure 2.4: Schematic Diagram of Through-Transmission Technique 12

Figure 2.5: Schematic Diagram of Pitch-Catch Technique Typically Utilised with Rayleigh and Lamb Waves 13

Figure 2.6: Schematic Diagram of Particle Motion in Longitudinal Wave 14

Figure 2.7: Schematic Diagram of Particle Motion in Shear Wave 15

Figure 2.8: Schematic Diagram of Particle Motion in Surface or Rayleigh Wave 15

Figure 2.9: Schematic Diagram of Thin Plate Wave (Lamb). Symmetric Mode (Top) Anti-Symmetric Mode (Bottom). 16

Figure 2.10: Applicability of Different Air-coupled Transduction Technologies as a Function of Frequency - Shaded: Piezoelectric Unshaded: Electrostatic 22

Figure 2.11: Schematic Diagram of Wave Propagation between Two Planar Medium 25

Figure 2.12: Schematic Diagram of a Boundary Condition for a Pulse-Echo System in Water with Polymer Transducer as the Transmitter/Receiver 27

Figure 2.13: Schematic Diagram of a Electrostatic Transducer with Roughened Backplate 34

Figure 2.14: Schematic Diagram of V-Groove Backplate [66] 35

Figure 2.15: Schematic Diagram of a Cavity Backplate 36

Figure 2.16: Schematic Diagram for a CMUT Design with Silicon Nitrate Membrane and Silicone Substrate Backplate [74] 37

Figure 2.17: Schematic Diagram of CMUT in Conventional-Mode [68] 38

Figure 2.18: Schematic Diagram of CMUT in Collapse-Mode [68] 38

Figure 2.19: Schematic Diagram of Typical Condenser Microphone with Acoustic Relief Slot and Free Edges Slit [25, 85] 44

Figure 2.20: Schematic Diagram of FLAUT with DC biased and AC Excitation Connected 45

Figure 3.1: Flow Diagram of a General Modelling Technique Utilised for Design and Development of Electrostatic Transducer 49

Figure 3.2: Visual Representation of the Limit that Separates the Thick Plate, Thin Plate and the Membrane Theory 50

Figure 3.3: Cross Section Diagram of a Circular Diaphragm 51

Figure 3.4: Schematic Diagram of First Four Normal Mode of Vibration (Harmonics) in Terms of Pressure for an Open Cylinder [96] 54

Figure 3.5: Schematic Diagram of First Four Normal Mode of Vibration (Harmonics) in Term of Pressure for a Closed Cylinder [97] 54

Figure 3.6: Plot of Parameter Sweep with 50 μm Thickness Kapton for: a. Thin Plate Radius as Function of Frequency and b. Cavity Depth as a Function of Frequency . 58

Figure 3.7: Plot of Parameter Sweep with 8 μm Thickness Kapton for: a. Thin Plate Radius as a Function of Frequency and b. Cavity Depth as a Function of Frequency 60

Figure 3.8: Plot of Parameter Sweep Utilising Helmholtz Resonator Formula: a. Thin Plate Radius as a Function of Frequency and b. Cavity Depth as a Function of Frequency 62

Figure 3.9: Plot of Parameter Sweep Utilising Helmholtz Resonator Formula: a. Pipe Radius as a Function of Frequency and b. Pipe Length as a Function of Frequency 62

Figure 3.10: Plot of Different in Resonant Frequency between Mass-Spring Formulation and Helmholtz Formulation in FLAUT for Different Cavity Radius to Pipe Radius Ratio 63

Figure 3.11: Schematic Diagram of Symmetrical Boundary Condition: Cube (Top) and Cylinder (Bottom) 67

Figure 3.12: Plot of Simulated Frequency Response of Diaphragm Displacement for a FLAUT 70

Figure 3.13: Plot of Simulated Mode Shape Magnitude and Phase Diagram for a FLAUT Operating at 25 kHz 71

Figure 3.14: Plot of Several Modes of Vibration of a Circular Diaphragm [110] 73

Figure 3.15: Plot of Frequency Response for a Single Membrane Displacement Fixed at Its Edges 74

Figure 3.16: Plot of Diaphragm Vibrational Mode at Fundamental Frequency 75

Figure 3.17: Plot of Diaphragm Vibrational Mode Gradual Change from a) Vibrational Mode (0,1) at 80 kHz to b) Vibrational Mode (1,1)+ at 82.5 kHz to c) Vibrational Mode (1,1) at 88 kHz 77

Figure 3.18: Schematic Diagram of FLAUT with Single Cavity and Pipe Designed Backplate 78

Figure 3.19: Plot of Thin Plate Diameter as a Function of Resonant Frequency for a Range of Thin Plate Thickness 79

Figure 3.20: Plot of Cavity Depth as a Function of Frequency for a Range of Thin Plate Thickness 79

Figure 3.21: Plot of Pipe Length as a Function of Frequency for a Range of Cavity Diameter to Pipe Diameter Ratio 81

Figure 3.22: Plot of Thin Plate's Velocity at the Centre of the Thin Plate as a Function of Frequency 83

Figure 3.23: Plot of Mode Shape for Thin Plate at Resonant Frequency of 34.5 kHz 83

Figure 3.24: Plot of Pressure at Cavity-Thin Plate Interface as a Function of Frequency 84

Figure 3.25: Plot of Pressure Trend in Cavity 85

Figure 3.26: Plot of Pressure at Pipe-Air Interface as a Function of Frequency 86

Figure 3.27: Plot of Pressure Output in Pipe at 34 kHz 86

Figure 3.28: Plot of Pressure at the Centre of the Pipe Geometry as a Function of Pipe Axial Length at Resonant Frequency of 34 kHz 86

Figure 3.29: Plot of Pressure Output for a Matched Cavity and Pipe as a Function of Frequency 87

Figure 3.30: Plot of Pressure Output in Pipe and Cavity at 33 kHz 88

Figure 3.31: Plot of Pressure at the Centre of the Cavity/Pipe Geometry as a Function of Pipe Axial Length at Resonant Frequency of 33 kHz 88

Figure 3.32: Plot of FLAUT Simulated Frequency Response with Designed Resonant Frequency of 34.5 kHz Utilising Comsol Multiphysics 90

Figure 3.33: Plot of Mode Shape for FLAUT at Resonance Frequency of 34.5 kHz 90

Figure 3.34: Plot of FLAUT Simulated Frequency Response with Designed Resonant Frequency of 34.5 kHz Utilising PZFlex 91

Figure 3.35: Plot of Mode Shape for FLAUT at 33.2 kHz 92

Figure 3.36: Plot of Simulated Excited Model Analysis Measured at the Centre of the Thin Plate-Air Interface as a Function of Frequency for Three Different Modelling Techniques (Comsol, PZFlex and Analytical (Red Dash Line)..... 93

Figure 4.1: Schematic Diagram of Basic Principle MSL..... 97

Figure 4.2: Schematic Diagram of Wire EDM 98

Figure 4.3: Schematic Diagram of Ram EDM..... 99

Figure 4.4: Schematic Diagram of Small Hole EDM 99

Figure 4.5: Flow Diagram of a Photolithography Process Utilising Positive and Negative Photo Resins. 104

Figure 4.6: Picture of Kapton Film Bonded on a Metallic Ring 106

Figure 4.7: Schematic Diagram of Thermal Evaporation Process. Left: Preparation Stage Right: Evaporation Stage 107

Figure 4.8: Picture of Backplate Produced using MSL Technique on a Final Assembly (Without Membrane on Top) 108

Figure 4.9: Picture of Full FLAUT Transducer Assembly 109

Figure 4.10: Schematic Diagram of Setup for Scanning Laser Interferometer Measurement [88] 111

Figure 4.11: Plot of 3D View of Thin Plate Surface Deformation 112

Figure 4.12: Plot of a 2D Plan View of Thin Plate Surface Displacement: Magnitude (Left) and Phase (Right) 113

Figure 4.13: Plot of Cross Section View of Thin Plate Surface Velocity 113

Figure 4.14: Plot of Periodic Chirp Excitation in Voltage as a Function of Frequency 114

Figure 4.15: Plot of FLAUT Thin Plate Average Displacement as a Function of Frequency 114

Figure 4.16: Plot of a 2D Plan View of Thin Plate Surface Velocity for the 30 mm Diameter Electrostatic Transducer Backplate: Magnitude (Left) and Phase (Right) 115

Figure 4.17: Plot of Cross Section View of Thin Plate Surface Velocity for 30 mm Diameter Electrostatic Transducer Backplate 116

Figure 4.18: Plot of Thin Plate Surface Deformation Outside the Cavity Periphery for Different Phases 117

Figure 4.19: Schematic Diagram of Setup for Pulse-Echo Measurement [57] 118

Figure 4.20: Plot of Time Domain for Signal Receive through the Pulse-Echo Method 119

Figure 4.21: Plot of Frequency Spectrum through FFT Transformation 119

Figure 4.22: Plot of Surface Deformation Profile for FLAUT at Frequency of 220 kHz 119

Figure 4.23: Schematic Diagram of Setup for Directivity and Frequency Response Measurement [55] 121

Figure 4.24: Plot of Simulated Beam Profile (Left) and Measured Directivity Profile Response (Right) and for 25 kHz Transducer Design as a Function of Normalised Pressure Amplitudes 122

Figure 4.25: Plot of Frequency Response for Measured 34.5 kHz Cavity/Pipe Design 124

Figure 4.26: Plot of Vibrational Mode for 34.5 kHz Transducer Design, which Shows Left: Magnitude and Right: Phase of the Vibrational Mode..... 124

Figure 4.27: Plot of Comparison between Measured Using Laser Interferometer and Simulation Using Comsol and PZFlex as a Function of Frequency for 34.5 kHz FLAUT Device 125

Figure 4.28: Plot of Simulated Frequency Domain Response for 34.5 kHz FLAUT Device Incorporating Supporting Cavity Periphery..... 127

Figure 4.29: Plot of Simulation for Thin Plate Cavity and Supporting Influence; Magnitude (Top), Phase (Bottom) 128

Figure 4.30: Plot of Pipe Length as a Function of Frequency for a Given Pipe Radius with Ratio of 2.5, 1.5 and 1.07..... 131

Figure 4.31: Plot of Pipe Length as a Function of Pipe Radius at Resonant Frequency of 29.44 kHz..... 132

Figure 4.32: Plot of Simulation of Geometrical Pressure Output at Pipe-Air Interface Using Comsol as a Function of Frequency for Three Different Pipe Radii Identified in Table 4.3 132

Figure 4.33: Plot of Simulation of FLAUT Normalised Amplitude as a Function of Resonant Frequency for Three Different Pipe Radii..... 134

Figure 4.34: Plot of Comparison between Simulated and Measured Results for 700 μm pipe radius..... 134

Figure 4.35: Plot of Frequency Response using Laser Interferometer Measurement for 700 μm, 500 μm and 300 μm Pipe Radius Dimensions..... 135

Figure 4.36: Plot of Propagation Error with respect to Resonant Frequency of Thin Plate..... 140

Figure 4.37: Plot of Propagation Error with respect to Resonant Frequency of Cavity 141

Figure 4.38: Plot of Propagation Error with respect to Resonant Frequency of Pipe 143

Figure 5.1: Schematic Diagram of Simple Pressure Sensor and the Mass/Spring/Damper System. Schematic Diagram (Right), Free Body Diagram (Left) 149

Figure 5.2: Plot of Transducer Resistance for 34.5 kHz FLAUT versus Different Frequency 155

Figure 5.3: Plot of Noise Frequency Spectrum for the 34.5 kHz FLAUT Design with a Pipe Radius of 300 μm 155

Figure 5.4: Noise Frequency Spectrum for the 34.5 kHz FLAUT design with a pipe radius of 450 μm 156

Figure 5.5: Picture of Noise Measuring Equipment by Ngo [145] (Left) and Olson [147] (Right) 159

Figure 5.6: Picture of Experimental Arrangement by Tarnow [138] 159

Figure 5.7: Schematic Diagram of Hybrid-Acoustic Isolation Vessel 160

Figure 5.8: Plot of Mean Free Path of Air as a Function of Pressure at 20^{o}C 162

Figure 5.9: Visual Representation of the Isolation Vessel Assembled in a Five-Media Model 164

Figure 5.10: Plot of Theoretical Transmission Coefficient as a Function of Isolation Pressure at 40 kHz and 80 kHz Resonant Frequencies 164

Figure 5.11: Picture of Overall View of Hybrid Acoustic Isolation Vessel System 165

Figure 5.12: Picture of the Connection between the Inner Vessel and the Outer Vessel 166

Figure 5.13: Picture of Inner Vessel 167

Figure 5.14: Plot of Measured Inner Vessel Pressure Level as a Function of Time for the Duration of 60 minutes 169

Figure 5.15: Plot of Measured Outer Vessel Pressure Level as a Function of Time for the Duration of 60 minutes 169

Figure 5.16: Plot of Measured Inner Vessel Pressure Level as a Function of Time after the Vacuum Pump removed for the Duration of 5 minutes 170

Figure 5.17: Plot of Measured Outer Vessel Pressure Level as a Function of Time after the Vacuum Pump Removed for the Duration of 5 Minutes 170

Figure 5.18: Schematic Diagram of Through-Transmission Assembly for HVAIC 171

Figure 5.19: Plot of Measured Transmission Coefficient as a Function of Isolation Pressure at 40 kHz Frequency 171

Figure 5.20: Schematic Diagram of Setup Arrangement for Measurement of FLAUT 174

Figure 5.21: Plot of Noise Measured at Different Configuration for Operating Frequency of 34.5 kHz for 300 μm Pipe Radius 175

Figure 5.22: Plot of Segmented View between 30 kHz and 40 kHz for Noise Measured at Different Configuration for Operating Frequency of 34.5 kHz for 300 μm Pipe Radius 175

Figure 5.23: Plot of Comparison between Simulation and Measured for Transducer Noise at Operating Frequency of 34.5 kHz for 300 μm Pipe Radius 176

Figure 5.24: Plot of Noise Measured at Different Configuration for Operating Frequency of 34.5 kHz for 450 μm pipe radius 176

Figure 5.25: Plot of Segmented View between 30 kHz and 40 kHz for Noise Measured at Different Configuration for Operating Frequency of 34.5 kHz for 450 μm Pipe Radius 177

Figure 5.26: Plot of Comparison between Simulation and Measurement for 34.5 kHz FLAUT transducer with pipe radius of 450 μm..... 177

Figure 5.27: Comparison of Measured Transducer Noise for Different Pipe Size the 300 μm and the 450 μm Pipe Diameter 178

Figure 6.1: Plot of Cavity Diameter as a Function of Resonant Frequency for an 8 μm Thin Plate Thickness..... 182

Figure 6.2: Plot of Cavity Depth as a Function of Frequency for an 8 μm Thin Plate Thickness 182

Figure 6.3: Plot of Pipe Length as a Function of Frequency for a Range of Cavity Diameter to Pipe Diameter Ratio 184

Figure 6.4: Plot of Velocity on the Surface of the Thin Plate at the Centre as a 185

Figure 6.5: Plot of Mode Shape for Thin Plate at Resonant Frequency of 84.8 kHz 185

Figure 6.6: Plot of Pressure at Cavity-Thin Plate Interface as a Function of Frequency..... 186

Figure 6.7: Plot of Pressure Trend in Cavity 186

Figure 6.8: Plot of Pressure at Pipe-Air Interface as a Function of Frequency 187

Figure 6.9: Plot of Pressure Output in Pipe Geometry for Design Frequency of 84.8 kHz 188

Figure 6.10: Plot of Pressure at the Centre of the Pipe Geometry as a Function of Pipe Axial Length at Design Resonant Frequency of 84.8 kHz 188

Figure 6.11: Plot of Pressure Output for a Matched Cavity and Pipe as a Function of Frequency..... 189

Figure 6.12: Plot of Pressure Output in Cavity and Pipe Geometry at 82.4 kHz 189

Figure 6.13: Plot of Pressure at the Centre of the Cavity/Pipe Geometry as a Function of Pipe Axial Length at Resonant Frequency of 84.8 kHz 190

Figure 6.14: Plot of Simulated Frequency Response for Coupled FLAUT at Designed at 84.8 kHz Utilising Comsol Multiphysics 191

Figure 6.15: Plot of Mode Shape for FLAUT: Magnitude (Top) Phase (Bottom) at Resonant Frequency of 83.5 kHz (Comsol) 192

Figure 6.16: Plot of Simulated Frequency Response for Coupled FLAUT at Designed at 84.8 kHz Utilising PZFlex 192

Figure 6.17: Plot of Mode Shape for FLAUT at 83.5 kHz (PZFlex) 193

Figure 6.18: Schematic Diagram of Circular Cell with Different Fill Factor a) Hexagonal b) Orthogonal/Rectangular c) Circular 195

Figure 6.19: Schematic Diagram of Hexagonal Packing Tolerances (All Dimensions are in mm) 197

Figure 6.20: Schematic Diagram of a FLAUT Array Incorporating Hexagonal Packing and Separation of $d = 2.25a$ or 0.63 mm. 198

Figure 6.21: Plot of Transducer Resistance as a Function of Frequency for a FLAUT Designed to Operate at 84.8 kHz for Frequency Range of 60 kHz to 120 kHz 199

Figure 6.22: Plot of Transducer Resistance as a Function of Frequency for a FLAUT Designed to Operate at 84.8 kHz for Full Frequency Range Until 120 kHz 199

Figure 6.23: Plot of Simulated Noise as a Function of Frequency Spectrum for FLAUT Designed at 84.8 kHz 200

Figure 6.24: Plot of Simulated Noise as a Function of Frequency Spectrum for Conventional Electrostatic Transducer Designed at 84.8 kHz 200

Figure 6.25: Plot of Thin Plate Resonant Frequency Error as a Function of Frequency for Different Manufacturing Tolerance of 1 μm, 5 μm, 10 μm and 20 μm 202

Figure 6.26: Plot of Cavity Geometry Resonant Frequency Error as a Function of Frequency for Different Manufacturing Tolerance of 1 μm, 5 μm, 10 μm and 20 μm 202

Figure 6.27: Plot of Pipe Geometry Resonant Frequency Error as a Function of Frequency for Different Manufacturing Tolerance of 1 μm, 5 μm, 10 μm and 20 μm 202

Figure 6.28: Resonant Frequency Error as a Function of Frequency for Three Different FLAUT Geometry Configuration 205

Figure 6.29: Picture of Single Cell FLAUT on an Ebalta Backplate (Top) and Array of FLAUT Cells on an Ebalta Backplate (Bottom) 207

Figure 6.30: Picture of a Fully Assembled FLAUT 208

Figure 6.31: Plot of Comparison between Simulation and Measured Results for a Single Cell FLAUT Designed at 84.8 kHz 209

Figure 6.32: Plot of Measured Mode Shape 84.8 kHz transducer design. Left: Magnitude Right: Phase 210

Figure 6.33: Plot of Normalised Average Surface Velocity in the Active Area of the FLAUT as a Function of Frequency Measured Using Laser Interferometer 210

Figure 6.34: Plot of Surface Deformation Profile for FLAUT with Cavity Pipe Design. Left: Magnitude Right: Phase 211

Figure 6.35: Plot of Focused Surface Deformation Profile for FLAUT with Cavity Pipe Design from Figure 6.34 212

Figure 6.36: Plot of Cross Section View of Thin Plate Surface Velocity for Two Cavity at the Edge of the Backplate 213

Figure 6.37: Plot of a FLAUT Surface Velocity Profile for Frequency until 150 kHz 214

Figure 6.38: Plot of Surface Velocity Profile for FLAUT at 150 kHz 214

Figure 6.39: Plot of Pressure Output Frequency Response for FLAUT transducer 215

Figure 6.40: Plot of Simulated Beam Profile (Left) and Measured (Right) for FLAUT Operating at 84.8 kHz as a Function of Normalised Pressure Amplitude 216

Figure 6.41: Plot of Comparison between Simulation and Measurement for FLAUT Noise at Operating Frequency of 84.8 kHz..... 217

Figure 6.42: Plot of Comparison between FLAUT (Cavity/Pipe) and Conventional Electrostatic (Cavity Only) for Surface Velocity Profile of a Single Cell Design... 217

Figure 6.43: Plot of Comparison between FLAUT (Cavity/Pipe) and Conventional Electrostatic (Cavity Only) for Surface Velocity Profile of an Array Design 218

Figure 6.44: Plot of Comparison between FLAUT (Cavity/Pipe) and Conventional Electrostatic (Cavity Only) for Pressure Output of an Array Design Measured Using Frequency Response Technique..... 218

Figure 6.45: Plot of Mode Shape for Cavity Only Design Single Cell..... 219

Figure 6.46: Picture of an Offset Concentric Cavity and Pipe..... 220

Figure 6.47: Plot of Surface Deformation Profile for Conventional Electrostatic Transducer with Cavity Only Design..... 221

Figure 6.48: Plot of Comparison of Pressure Output Beam Profile in dB (ref: 20μPa) Between FLAUT and Conventional Electrostatic Transducer..... 222

Figure 6.49: Plot of Comparison between Simulation and Measured for Conventional Electrostatic Transducer Noise at Operating Frequency of 84.8 kHz..... 223

Figure 6.50: Plot of Comparison of Detected Pressure Input Voltage in mV for FLAUT and Conventional Electrostatic Transducer Front Face 224

Figure 7.1: Process Flow of a Typical MEMS Production Process..... 234

Figure 7.2: Schematic Diagram of a Two-Layer SU-8 Structure Fabrication Process to Fabricate a FLAUT: (a) Spin-Coating of Omnicoat™, (b) First Lithography, (c) Second Lithography, (d) Development (e) Released SU-8 Structure and (f) Metallisation..... 235

List of Tables

Table 2.1: Table of Acoustic Impedance for Different Media [49] 27

Table 2.2: Table of Intensity Transmission Coefficient for Three Different types of Materials with Respect to Water and Air Load..... 28

Table 3.1: Table of FLAUT Design Dimensions and the Expected Resonance Frequency..... 59

Table 3.2: Table of FLAUT Design Dimensions Utilising Helmholtz Model for Resonant Frequency of 25 kHz..... 63

Table 3.3: Table of FEA Analysis Types and Its Purpose..... 68

Table 3.4: Table of Modelling Parameters for Diaphragm Simulation Using Comsol 74

Table 3.5: Table of FLAUT Design Dimensions and the Expected Resonance Frequency..... 81

Table 3.6: Material Properties for FEA Simulation..... 82

Table 4.1: Polytec PSV300 Scanner Laser Vibrometry Specification..... 110

Table 4.2: Table of Thin Plate and Cavity Combination with Resonant Frequency of 29.44 kHz..... 130

Table 4.3: Table of FLAUT Design Dimensions and the Expected Resonance Frequency for Pipe Radius Changes..... 131

Table 5.1: Table for Properties of the Inner and Outer Vessel..... 163

Table 5.2: Table of Noise Measurement and Expected Output..... 173

Table 5.3: Table of Noise Measurement Configuration..... 173

Table 6.1: Table of Suggested Design for Cavity Geometry..... 183

Table 6.2: Table of Geometric Design Configuration for a FLAUT Device Operating at 84.8 kHz..... 184

List of Symbols

This list comprises most of the main symbols used throughout this Thesis.

Symbol	Definition	Unit
f_n	Resonant frequency	Hz
v	Poisson ratio	
E	Young's modulus	Pa
D	Flexural rigidity	$Pa \cdot m^3$
r_m	Membrane radius	m
d_m	Membrane thickness	m
ρ_m	Membrane density	$kg \cdot m^{-3}$
γ	Adiabatic constant	
P	Pressure	Pa
d_a	Cavity depth	m
c	Speed of sound	$m \cdot s^{-1}$
r_p	Pipe radius	m
l_e	Pipe effective length	m
l_a	Pipe actual length	m
λ	Wavelength	m
n	Pipe mode of operation	
τ	Tension	$N \cdot m^{-1}$
k	Stiffness constant	
E_s	Noise voltage	$V/\sqrt{Hz}$
T	Transducer temperature	K
r	Resistance	Ω
k_b	Boltzmann's constant	$J \cdot k^{-1}$
ω	Angular resonant frequency	$rad \cdot s^{-1}$
μ	Fluid viscosity	$kg \cdot m^{-1}s^{-1}$

List of Acronyms

This list comprises most of the main acronyms used throughout this Thesis.

B&K	Brüel & Kjær
CMUT	Capacitive Micromachined Ultrasonic Transducers
CNC	Computer Numerical Control
EDM	Electrical Discharge Machining
FE	Finite Element
FEA	Finite Element Analysis
FFT	Fast Fourier Transform
FLAUT	Fluidically Amplified Ultrasonic Transducer
MEMS	Micro-Electro-Mechanical System
MSL	Micro-Stereo Lithography
MUT	Micromachined Ultrasonic Transducer
NDE	Non Destructive Evaluation
NDT	Non Destructive Testing
NEMS	Nano-Electro-Mechanical System
RMS	Root Mean Square
SA	Sensitivity Analysis
SNR	Signal to Noise Ratio

1. Introduction

1.1 Background

Although ultrasound has a wide range of different applications, the need for non-contact applications poses a great challenge for most ultrasonic transducer designers. In the aerospace industry for instance, the conventional liquid or gel-coupled methods of inspection require complicated arrangement as more fibre composites are used in aircraft manufacture. Certain components such as honeycomb components and sandwich parts or parts with a foam core should not have any contact with water or any liquid coupling medium [1]. Thus, there is a desire within many industries to increase output sensitivity in a non-contact imaging environment. Due to high attenuation and transducer-load medium impedance mismatch in air, the output sensitivity of air-coupled (non-contact) applications is much lower compared to operation in water. Therefore, it is the aim of this thesis to be able to enhance the Signal to Noise Ratio (SNR) within the context of non-contact applications.

Commonly, the term transducer is used to illustrate a type of sensor or detector, which converts one form of energy into another. In the case of ultrasound, there are two main modes of operation; transmit-receive using two transducers: pitch-catch or through-transmission and transmit-receive using the same transducer: pulse-echo. In both modes, a transducer is used to transmit the ultrasonic signals through a medium of interest (water, air, grease, metal etc). The resultant backscattered energy is detected and converted back to an electrical signal. As the signal received is usually weak, specialised reception electronics coupled with additional signal processing are required to improve and interpret the signal further before the final results are displayed to the end user. The main limitation of any form of ultrasonic system is commonly due to the transducer front-end. A design that has higher transmission and detection sensitivity over the desired frequency range is needed. Historically, the main focus of transducer improvement has been in sonar and biomedical sectors with improvements being transferred to industrial applications such as Non Destructive Evaluation (NDE).

As bandwidth and sensitivity are mutually exclusive, an optimised trade off between a wide bandwidth and high sensitivity electrostatic devices is needed. The main advantage of an electrostatic transducer is that it generally exhibits good mechanical matching to fluid loads without matching layers, and over a hundred percent bandwidth when operating in water load.

1.2 Aims and Contribution of the Thesis

1.2.1 Aims of the Thesis

- Implementation of a suite of experimental and theoretical analysis tools (analytical and finite element modelling) to rapidly assess electrostatic transducer designs.
- Analysis of noise sources on wideband and efficient transducers.
- Implementation of novel fluidic amplified ultrasonic transducers.

1.2.2 Contribution of the Thesis to the Field of Air-Coupled Electrostatic Transducer

- Implement design guidelines of the FLAUT transducer through identification of individual geometry frequency resonant, which is analysed using both analytical method and finite element method.
- Development, implementation and analysis of different design parameters to enhance and optimise the performance of a FLAUT through the use of finite element methodology and verified using experiment.
- Analysis of different manufacturing methods to fabricate a FLAUT backplate using the error propagation technique in order to identify the maximum allowable design and manufacturing tolerances. This enables the designer to identify and match the suitable design objective to manufacture, making the process more effective and efficient.

- Implementation of a noise measurement system to measure the intrinsic noise for the FLAUT device and to identify the suitable design parameters to enhance the FLAUT performances.
- Demonstration of enhanced operation of the FLAUT when compared with a conventional device with improvement of 2.7 dB (ref: 1 μPa/V) for the transmit voltage response and 3.2 dB (ref: 1 V/μPa) for the open circuit voltage response.
- Demonstration of reduction in insertion loss for FLAUT when compared to conventional device with 9.1 dB two-way insertion loss reductions presented.
- Demonstration of thermal noise reduction for 120 kHz bandwidth in FLAUT when compared to the conventional device with measured improvement of 2.7 dB.
- Illustration of higher overall pressure output in dB for the FLAUT beam profile when compared with the conventional device.

1.3 Publication to Date Arising From the Thesis

1.3.1 Publications

R. L. O'Leary, S. B. Abdul Hamid, A. J. Walker and A. J. Mulholland, "Improving the Sensitivity of Air-Coupled Ultrasound Transducer through Fluidic Amplification", U.S. Navy Workshop on Acoustic Transduction Materials and Devices, The Pennsylvania State University, PA, USA, May 2011.

1.4 Overview of the Thesis

Chapter 2: Theoretical Background and a Review of Transducer Technology and Applications

This Chapter introduces different ultrasound applications and describes the two main transduction mechanisms for ultrasound: piezoelectric and electrostatic. The requirements to tailor the different ultrasonic transducers are then detailed, which includes how the transducers are setup and ultrasound signal propagation. Subsequently, the review of current ultrasonic applications are presented, citing the applicability to solid, liquid and air coupled operations. Issues surrounding the use of air as a coupling media are reviewed quantitatively and qualitatively. The benefit and challenges in air-coupled operation are discussed along with a review of current air-coupled sensor technology. Finally, design requirements for an air-coupled ultrasonic transducer device incorporating a fluidic amplification are discussed.

Chapter 3: Modelling and Simulation Review and Analysis

This Chapter illustrates the design process and methodology associated with the analysis and simulation of an ultrasonic transducer. There are two sections that concern modelling method: the analytical and the finite element method. The analytical method is utilised to determine the geometry of the device; while Finite Element (FE) concerns the overall operation of the device. Different diaphragm vibrational modes are discussed in detail, with specific examples shown to illustrate the different state of vibration and its relationship to the FLAUT. Finally, a detailed proof of concept design review for a FLAUT, which operates at 34.5 kHz is presented; utilising the concept and technique discussed in the earlier section of the Chapter.

Chapter 4: Manufacturing Review, Prototyping and Analysis of Fluidic Amplified Electrostatic Transducer (FLAUT) using Surface Displacement

This Chapter reviews different manufacturing techniques – conventional drilling, Micro-Stereo Lithography (MSL), Electrical Discharge Machining (EDM), Computer Numerical Control (CNC) drilling, laser cutting and photolithography. A

choice of manufacture is then finalised. Next, techniques to manufacture and assemble the FLAUT transducers are discussed. Reviews of three different measuring techniques – laser interferometer, impulse response, directivity and frequency response are detailed. Finally, the FLAUT is measured and a prototype is validated. In addition, topics that relate the effect of different pipe radius and the effect of equipment and machine resolution are discussed as a conclusion to the Chapter.

Chapter 5: Modelling and Measuring FLAUT Noise

A review of the associated noise sources and damping mechanism active within a typical electrostatic transducer device are presented. Noise modelling is performed by identifying three different dissipation mechanisms namely the squeeze film damping resistance, the radiation resistance and the mechanical resistance due to the pipe. The total thermal noise is then expressed as a parallel combination of each individual noise resistance. A technique to develop and validate the FLAUT noise measurement system is then described. Three main approaches to noise measurement are discussed. From the discussion, a hybrid approach of a temperature controlled two-layered vessel has been considered. Suitable vessel geometry is then identified, analytically simulated and validated for its purpose. Once the validation process has been performed, the noise measurements are then performed in the isolation vessel by utilising a specific configuration that relates to a specific combination of noise sources. The noise modelling and measurement are then corroborated. As a conclusion, key design criteria are discussed and finding noted.

Chapter 6: Development of High Frequency FLAUT

Model, build and test of a single unit cell and an array cell of FLAUT device operating at 84.8 kHz are presented. Analytical and FEA simulations of sensitivity and noise are performed for the proposed transducer design. In addition, the use of an array is introduced with different possible configurations detailed and suitable array design proposed. The use of sensitivity analysis to identify a suitable mode of manufacture is illustrated, with critical control dimensions presented. Next, the characterisation of FLAUT is performed for both single unit cell and the array

design, which indicates that the FLAUT array is moving generally in phase and within the expected frequency range. Finally, a comparative study between the FLAUT and the conventional electrostatic transducer are discussed throughout the end of the chapter, with important noticeable improvement in term of transmit voltage response, open circuit voltage response and two-way insertion loss fully characterised and documented.

Chapter 7: Conclusion and recommendation for further work

In this final Chapter, the output of the FLAUT design and development methodology has been reviewed with respect to the original guidelines. Comments have been made on the overall effectiveness of the method. The effectiveness and the overall efficiency of the new transducer design are concluded. Finally, suggestions are made for future work on improving the design method and manufacturing methodology to further improve the efficiency of the FLAUT transducers.

2. Theoretical Background and a Review of Transducer Technology and Applications

2.1 Introduction

Ultrasound is applied in many different fields. The application of ultrasound is quite diverse due to the range and ease of implementation that could be utilised to different industrial scenarios such as [2]:

- Sensing
- Imaging
- Positioning
- Cleaning
- Sono-chemistry
- Welding
- Machining

In all of the applications above, a specific transducer design and configuration should be implemented in order to tailor the transducer to the task at hand. Different ultrasound applications require different operating frequency, ultrasound power and field characteristics. In an ultrasonic cleaning, the ultrasonic transducer is used to produce high acoustic pressure, which induces cavitation within the medium of interest. This process removes contaminants such as dirt, dust, oil etc to clean items such as jewellery, dental equipment, coins etc. The frequency range for these transducers is typically between 20 kHz to 90 kHz [3, 4].

In the electronic industry for example, a fine wire bonding technique utilising the ultrasonic welding technique is commonly applied - to interconnect electrical conductors, contacts and terminals [5]. Ultrasonic welding which generally operates at a frequency of 20 kHz to 40 kHz and low amplitude mechanical vibration, to join simple and complex parts together is also of great interest in the plastic industry [6]. In contrast to ultrasonic welding, by having an abrasive slurry flowing between the

vibrating tip of an ultrasonic transducer and the workpiece, hard and brittle materials such as ceramics, glass, sapphire and even diamond could be removed with high precision through microchipping [7, 8] - an ultrasonic machining process. Based on a review by Thoea *et al*, ultrasonic machining with an operating frequency larger than 20 kHz and large vibrating tool amplitude of 5 $\mu m_{p\text{-}p}$ to 50 $\mu m_{p\text{-}p}$ is suitable to machine ceramic coated turbines blades used in the aerospace industry - due to the little or no surface/sub-surface damaged [8].

Lastly, in non-destructive testing [9], transducers typically operating between 2 MHz to 10 MHz are commonly used to image the internal structure of engineered components - examples include identifying and sizing defective regions, such as cracks or delaminations, or ensuing critical dimensions such as wall thickness are maintained. In certain specialist applications of non-destructive testing, such as concrete, wood or cement, a lower operating frequency between 50 kHz to 500 kHz is usually utilised to inspect such objects [10].

In performing any non-destructive tests, maximising the energy transfer from the transducer into the load medium and into the test object is essential to ensure that the amplitude of the reflected waves is high enough to be detected by the receive transducer. In addition, depending on the positional accuracy required, a focusing type transducer may be used to enable material flaw detection or thickness identification to be performed at a specific area of interest [11, 12].

2.2 Generation and Detection of Ultrasound

There are a wide range of methods that can be employed for the generation and detection of ultrasound. In most cases, the generation of ultrasound signals could be categorised based on their mechanism, which are mechanical, piezoelectric and electrostatic. In the early days, ultrasound was generated by exciting a flow of gas or fluid. Galton's whistle and Hartmann generator [13] are two of the early devices used to generate the ultrasound signal. One of the main discoveries in the 19th century

which has shown to be crucial for the future development of ultrasound technology is the discovery of the piezoelectric effects by J. and P. Curie brothers in 1880 [14]. Although the electrostatic effect has been found almost at the same time [15] and was utilised for acoustic generation and detection in the form of speakers and microphones, respectively, it is still not a very popular device to generate ultrasound signal for imaging purposes during those early implementation. This is mainly due to the high electric fields that needs to be maintained to achieve an acceptable efficiencies at higher frequencies [16]. However, advancement in IC fabrication introduced in 1993 by Haller and Khuri-Yakub [17] have enabled the development of submicron gaps between electrodes thus allowing the possibility of high electric fields to be achieved. In addition, the expectation of a wider bandwidth and the potential for integration with electronic circuits are other advantages associated with the electrostatic transducer especially the Capacitive Micromachined Ultrasonic Transducers (CMUT) [17, 18]. This has led to the first proof of concept experiment for an imaging application which utilises a 64 element 1-D CMUT array in 1998 as demonstrated by Jin *et al* [19]. In addition, 2 years later Oralkan *et al* [20] has successfully demonstrated for the first time a pulse-echo imaging using a 16 element 1-D CMUT array.

Nowadays, the most common transducers used to generate ultrasound are piezoelectric and electrostatic devices. A piezoelectric device consists of a layer of piezoelectric material such as quartz crystal or certain engineered ceramic materials, with thin metal electrodes applied as shown in Figure 2.1. The piezoelectric effect is defined as the accumulation of surface charge on the component as a result of external mechanical stimulus. Conversely, for the inverse piezoelectric effect, internal generation of mechanical strain in the material results when an electrical field is applied. Thus, the former and the latter could be used for ultrasound detection and generation of ultrasound, respectively [21].

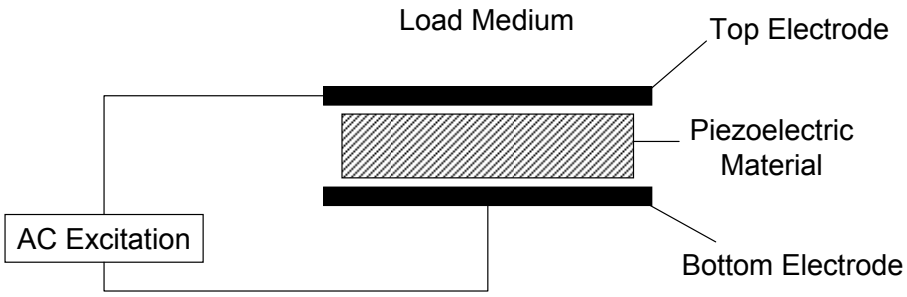

Figure 2.1: Schematic Diagram of a Piezoelectric Transducer

An electrostatic device comprises of a single sided metallised dielectric film stretched over an electrically conductive backplate as shown in Figure 2.2 [21]. The dielectric film or membrane and the backplate form the free and the fixed plates of the device, respectively. Typically, a DC or bias voltage between 40 V to 500 V is connected to the fixed backplate, while a ground is connected to the membrane. The bias voltage will enable a static deflection of the membrane towards the bottom electrode. In order to excite the membrane, an excitation frequency of the AC voltage with amplitude much smaller than the bias voltage is used to excite the membrane. This causes the free membrane to move up and down generating a pressure wave in the load. Conversely, in receive mode, the compression and rarefaction of an incident pressure wave will cause the free plate to vibrate causing the surface charge to vary with the same manner as the incident pressure wave.

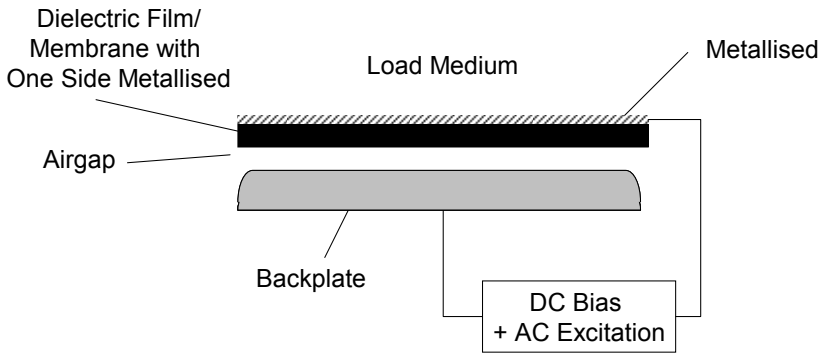

Figure 2.2: Schematic Diagram of an Electrostatic Transducer

There are many design constructional and operational parameters that effect the operation of the electrostatic transducer. Among them are applied bias voltage [22], membrane thickness and the dimension, quantity and distribution of the air gap [23-25]. To solve this issues, micromachining techniques [16] have been utilise in the fabrication of the electrostatic devices. This will be discussed in detail in the later section of this Chapter.

2.3 Tailoring Ultrasonic Transducer to Its Applications

In order for the transducer to be utilised effectively and efficiently, a specific design of transducer can be tailored to the specific requirements of the application. In any ultrasonic applications, there are three main ways that the transducers are utilised and setup: pulse-echo, through-transmission and pitch-catch. In a pulse-echo configuration as shown in Figure 2.3, one transducer will be used for both transmission and detection of the ultrasound. The ultrasound waves will travel from the transmitter to the test object interface, to the back of the test object, and travel back to the same transmitter to be detected. From the different time-of-flight between the transmitter and the receiver, the distance between the transducer and the test object can be calculated. Furthermore, any changes in the receive amplitude signal could be use to locate and measure defects within the test object.

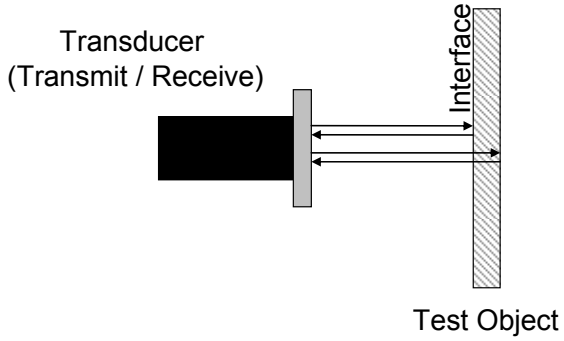

Figure 2.3: Schematic Diagram of Pulse-Echo Technique

In a through-transmission experiment as shown in Figure 2.4, a pair of matched transducers are used; one for transmission and one for detection. The ultrasound waves will travel from the transmitter to the receiver on the opposite end of the test object. As in pulse-echo technique, any changes in the received ultrasonic sound waves can be use to locate and measure defects within the test object.

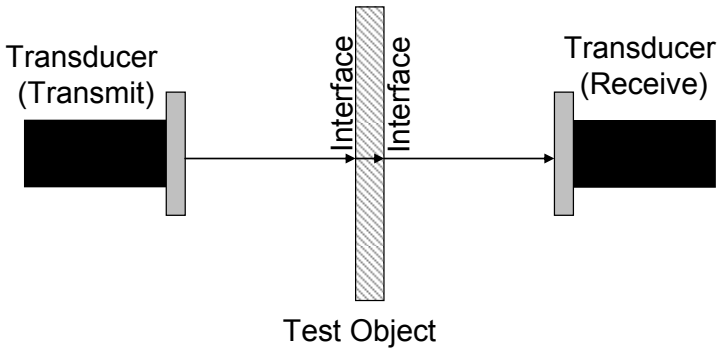

Figure 2.4: Schematic Diagram of Through-Transmission Technique

In pitch-catch as shown in Figure 2.5, two transducers as in through-transmission will be used. However, rather than having the receiver at the opposite side of the test object, the receiver will be arranged on the same surface as the transmitter. Thus, this arrangement will include a change of direction due to the reflection at the interface and at the back of the object as in a pulse-echo technique. This technique is typically used in Lamb wave inspection of plate like structures due to the required incident angle for these particular waves to be generated.

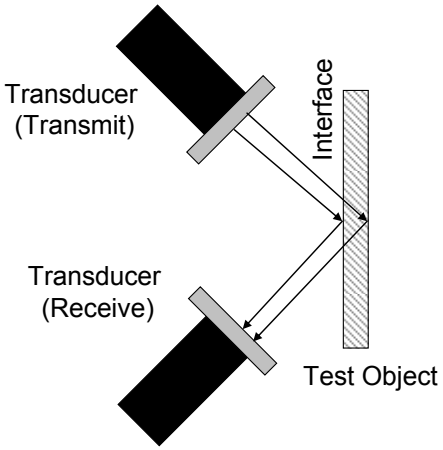

Figure 2.5: Schematic Diagram of Pitch-Catch Technique Typically Utilised with Rayleigh and Lamb Waves

However, the transmission and reception above does not fully consider the coupling media and wave propagation. Since wave propagation and coupling are interrelated, the different types of wave propagation will be discussed, along with a review of different applications in relation to the coupling media.

2.3.1 Propagating Ultrasound Signal

The excitation source and the medium of interest govern the type of wave propagation. In fluids, sound propagates primarily as longitudinal pressure waves where the particle motion is parallel to the direction of wave propagation [26]. In solid materials, additional modes of wave propagation can be supported; the transverse mode is the simplest of these additional modes. Furthermore, solids are capable of supporting more complex types of wave propagation, some of which are geometry dependent. A good example of the complex types of waves that is geometry dependent is the Rayleigh wave – which travels along the surface of a thick solid object.

2.3.1.1 Longitudinal Waves

In a longitudinal wave, the particle displacement is parallel to the direction of wave propagation. The particles oscillate back and forth about their equilibrium position, and only moves in the direction of wave propagation. Thus, the wave motion is a series of compressions and rarefactions as illustrated in Figure 2.6. This type of wave is supported in both fluid and solid media.

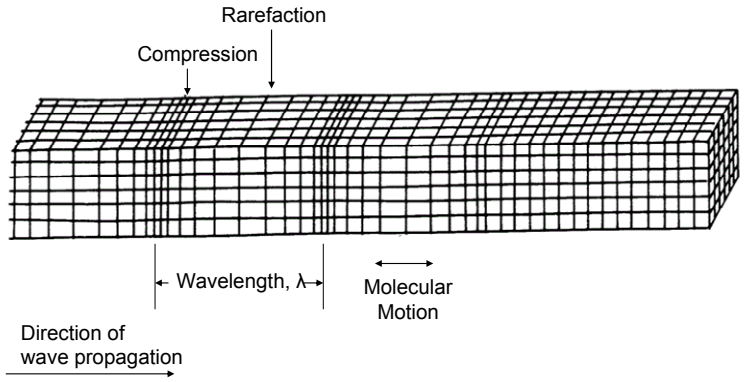

Figure 2.6: Schematic Diagram of Particle Motion in Longitudinal Wave

2.3.1.2 Transverse Waves

On the contrary, a transverse wave is when the particle oscillates at a transverse or right angle to the direction of the wave propagation as shown in Figure 2.7. Transverse waves requires a solid medium for propagation, thus are not supported in fluids. However, sound waves may be converted from one form to another by mode conversion. One such example is the generation of transverse waves in a test object, where a longitudinal wave front is incident upon the surface of the specimen at an appropriate angle as in the pitch-catch setup shown in Figure 2.5 [12]. The angle of the incident transverse mode propagation is a function of the wave velocities in the specimen and the coupling medium, defined by the Snell's Law [27]. However, to ensure that only a single beam is present, the beam angle is controlled to be within the first and second critical angle. These two critical angles are defined as incident

angles which make the angle of refraction for the longitudinal and shear wave to be at 90 degrees respectively [27].

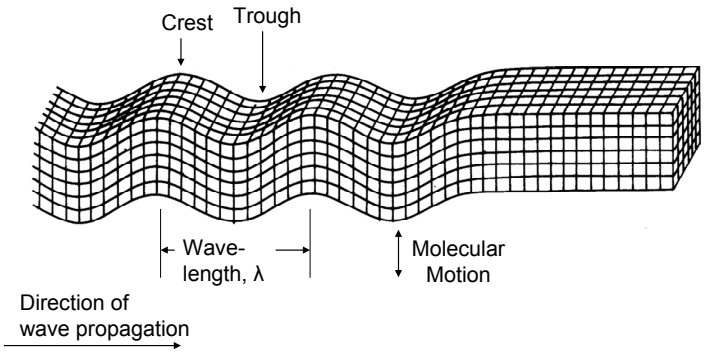

Figure 2.7: Schematic Diagram of Particle Motion in Shear Wave

2.3.1.3 Rayleigh and Lamb Waves

In addition to the bulk longitudinal and transverse waves, there are also other types of waves that are supported by solids such as Rayleigh and Lamb waves. Rayleigh waves or surface waves travel along the surface of a thick solid material penetrating with a significant displacement at a depth of approximately one wavelength [26, 28]. The waves include both longitudinal and transverse motion which decrease exponentially from the surface of the material up to a maximum of approximately two wavelengths [28]. In an isotropic solid, the propagating Rayleigh wave results in elliptic particle motion in planes normal to the surface and parallel to the direction of propagation. Figure 2.8 details a schematic of the particle motion in Rayleigh wave where the major axis of ellipse is aligned with the vertical axis.

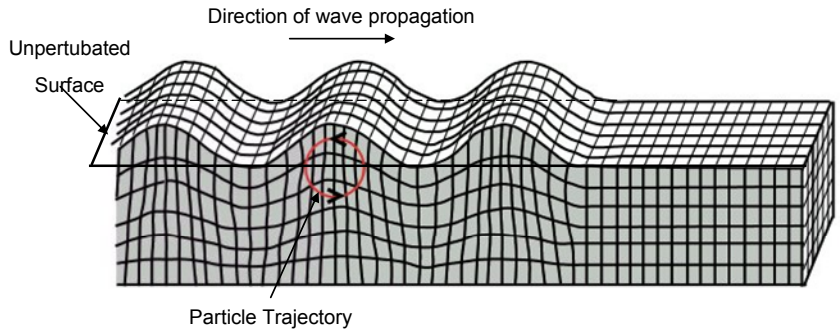

Figure 2.8: Schematic Diagram of Particle Motion in Surface or Rayleigh Wave

On the other hand, Lamb waves are similar to the surface waves except they can only be generated in solid materials, which are a few wavelengths thick. Lamb waves propagate parallel to the surface throughout the thickness of the material. In addition to the elastic properties of the materials and operating frequency, Lamb waves are also influenced by thickness of the material. In some cases, Lamb waves can be propagated over long distances, and as a result are employed in a variety of long-range non-destructive evaluation in plates, wires and tubes [26]. Although, there are many different modes of particle vibration for the Lamb wave, the two fundamental modes are the symmetric (stress) and asymmetric (bending) waves modes as shown in Figure 2.9 [28]. From the Figure 2.9, it could be observed that there are three distinct particle displacement vibration modes within the thin plate during lamb wave propagation. For the symmetric modes, it could be observed that the particle in the middle of the plate vibrate purely in longitudinal, while in anti-symmetric is in transversal. The rest of the particle vibrates elliptically as illustrated.

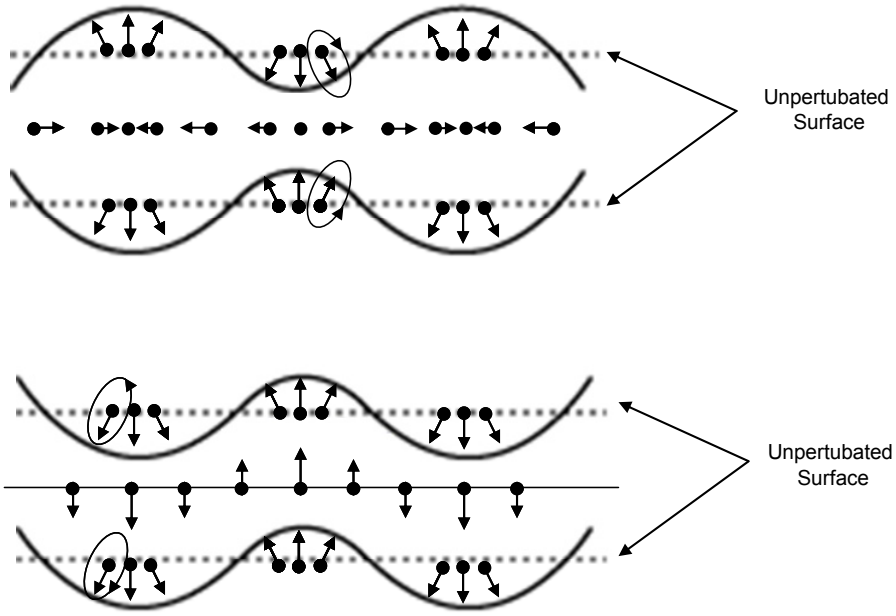

Figure 2.9: Schematic Diagram of Thin Plate Wave (Lamb). Symmetric Mode (Top) Anti-Symmetric Mode (Bottom).

2.3.2 Review of Different Applications in Relations to Coupling Media

Since each application has their own sets of requirements; in order to tailor the transducers to the application, few considerations need to be made. One of the considerations is the choice of coupling media. In most cases, liquid has been utilised as a coupling media. Solid has also been utilised but to a limited sense [29].

However, the choice of a coupling media in a specific application will be dependent on a few criteria such as the nature of the sample, the anticipated defects and the requirement for scanning of the sample during the inspection. For example, inspecting the thickness of a thick aircraft composite material will require a different transducer operating frequency ranges and gauge sizes when compared to a thinner material [11]. For common and standard composites materials with thickness range of 1.25 mm to 20 mm - would generally require the use of a standard gauge and standard selected transducers. However, for non standard composites that are thicker than 20 mm, a modified setup is usually required – the use of a specialised gauge incorporating high penetration option and a lower frequency transducer is needed for such an arrangement [11].

While, to detect defects in polymer materials, glycerine is usually a suitable couplant due to the near matched acoustic impedance [30]. In addition, a larger and non-moveable sample would require different treatment compared to a smaller and moveable sample. A specialist arrangement needs to be made to inspect a large non-moveable sample such as using a water jet or squirter [29, 31], while for a smaller and moveable sample an immersion tank may suits. For example, in the inspection of welds in metallic components, a gel based couplant is commonly used. The gel couplant is spread across a large surface area for the transducer to scan along the weld.

Different treatment is also required for different material constituent, wood [32] would require different setup and arrangement compared to a concrete [29] or a metal [33]. Thus, a specific transducer and setup arrangement are required to match

the sample and inspection requirement. In addition, as there are no universal couplant that could be used for all materials and conditions, a specific type of couplant is generally required for a specific purpose, condition and material. This is a problem, especially in industry that uses composite such as aerospace since a special formulation for the specific composite structure may need to be made. According to Larson [33], there are various criteria that need to be considered for an ultrasonic coupling selection, among them are:

- **The coupling should not be corrosive:** corrosion damage may cause various issues such as damaged plating or even major damage to the sample/test object.
- **Suitable acoustic impedance:** very high acoustic impedance couplant have been found to improved results in concrete testing and corroded metal surface.
- **Temperature range:** the choice of couplant utilised in a test inspection will depend on the test environmental temperature and the temperature of the sample to be tested - most couplant have a minimum and a maximum operating range.
- **Viscosity:** enhanced coupling on curved surfaces could be achieved through higher viscosity couplants. In addition, the choice of couplant also needs to consider the viscosity stability, for example - does not thin when it is in contact with salts.
- **Surface Wetting:** couplants needs to bind well with the sample to enable a good acoustic interface between the transducer and the test sample.
- **Couplant Removal:** the choice of couplant removal such as wiping, water or solvent cleaning, complete removal or leave at site will determine the choice of couplant to be used.
- **Non Toxic:** especially important when the inspection and test is performed at high temperatures, as the couplant may evaporate and evolve volatile components that may be hazardous to health.

As described above, the choice of couplant is important in ensuring that the results obtained from the imaging and inspection is potentially of use to the user. However, in this thesis the approach is to cover the different coupling in general, with some specific example to cover various coupling applications and setup arrangements. This is mainly to illustrate the important influence the sample has with regards to the final

choice of coupling medium and the required transduction system arrangement. In order to demonstrate the difference, the coupling media application have been generalised into three main types of coupling - solid, liquid and gas mainly air; with the relevant and required setup described.

2.3.2.1 Solid

The use of solid coupling such as those expressed by Roye and Schieke [29], require a roller and a relatively soft tyre as the coupling medium to move through the area of interest. The inclusion of fixed rollers within the inspection system reduces the overall system flexibility. Bourne *et al* [34] has also demonstrated the use of hydrophilic polymers as the solid coupling medium on a wheel probe which can be operated both in 'wet and dry' condition. However, as in any solid coupling, it still lacks the movement flexibility when compared to either liquid or air. In addition, due to the inherent surface roughness between two solid surfaces (i.e. rollers and sample), there will be trapped air within the two layers. This trapped air will cause a high acoustic impedance mismatch, which effectively reduces the transmission coefficient. (The concept of acoustic impedance and transmission coefficient will be introduced in the next section). Furthermore, the use of roller requires that a certain pressure is applied to the sample; which is not always suitable especially for sample which are fragile and delicate [35].

2.3.2.2 Liquid

Historically, petroleum based oil and grease has been extensively used as a coupling media especially for ferrous metals [33, 34]. Nowadays, oil or grease liked chemical (paste) is seldom used due to environmental concern, fire hazard and operator health concerns; except for applications which requires an electrical isolation [36] or applications with very high operating temperature [30]. Petroleum based couplants were originally chosen due to their superior corrosion inhibition which are able to protect the surfaces of the specimen under inspection; even if the surfaces are not

cleaned afterwards. Nowadays, glycerine, water or water based-gel couplants, which incorporate corrosion inhibitors agents, are common [37]. All these intermediate layer of material is important to enable a good acoustic impedance match and to compensate for imperfect contact between two surfaces.

In non-destructive testing (NDT), pulse-echo technique is typically employed to detect defects within a material. Since, the size and location of defects within a structure are typically unknown; it is not feasible to affix a transducer to a single location. Thus, it is essential that the transducer is utilised to scan across the entire surface of the component under test. To solve this issue, a squirter and a transducer probe is installed to a movable robot or motor to perform the inspection [31]. This increases the transmission coefficient of the probe and the inspection speed [29] at the cost of increasing the complexity of the inspection system.

2.3.2.3 Gas (Mainly Air)

In many applications, it is desirable to undertake the ultrasonic imaging of engineered components in the absence of liquid coupling media, examples includes:

- Inspection of fibre reinforced polymer composites [1] and other highly attenuative materials such as foam sandwich structures and honeycomb within the aerospace industry [38], of which the use of couplant may cause damage during or after inspection.
- Inspection of wood [32] or paper based products, of which contact with water may cause immediate damage to the product. Alternatively, the sample could also be damaged when heated or dried after the use of couplant [35].
- Detection of defects such as delamination. As delaminations are easily filled with couplant such as water due to capillary action, the possibility of detection in liquid is less likely [35].
- Inspection of electronics printed circuit board of which the use of couplant may cause damage to the electronics and the board [35].

This has resulted in gas mainly air being used as the coupling medium of choice for a variety of applications. However, air-coupled ultrasonic inspection is encumbered with some inherent difficulties including poor impedance matching between the sample and the transducer(s), and high attenuation of ultrasonic signal in air. These limitations have been overcome mainly through optimised transduction system design. Various transduction systems have been employed in air-coupled inspection; some of the key transduction system types and their frequency ranges are shown in Figure 2.10 [37]. From the Figure 2.10, it could be observed that there are two type of transduction system utilised - piezoelectric which includes the piezoelectric bender or twister mode, the piezoelectric thickness mode and the piezoelectric composites; and electrostatic which includes the condenser microphone, solid dielectric microphone and capacitive micro-machined devices.

For piezoelectric transducer designs, the use of a planar or focussed transducers [37], either line focus (using cylindrical lens) or point focus (using spherical lens) [39], or a combination of both planar and focussed transducers have been utilised to inspect thick homogenous material in air-coupled environment. The focussed transducers exhibit some benefits due to their better signal-to-noise ratio, increased sensitivity to small flaw and beam correction for contoured surfaces [39]. In all the piezoelectric device implementations, a thin matching layer, typically polymer based, is used to improve the transmission and reception efficiencies.

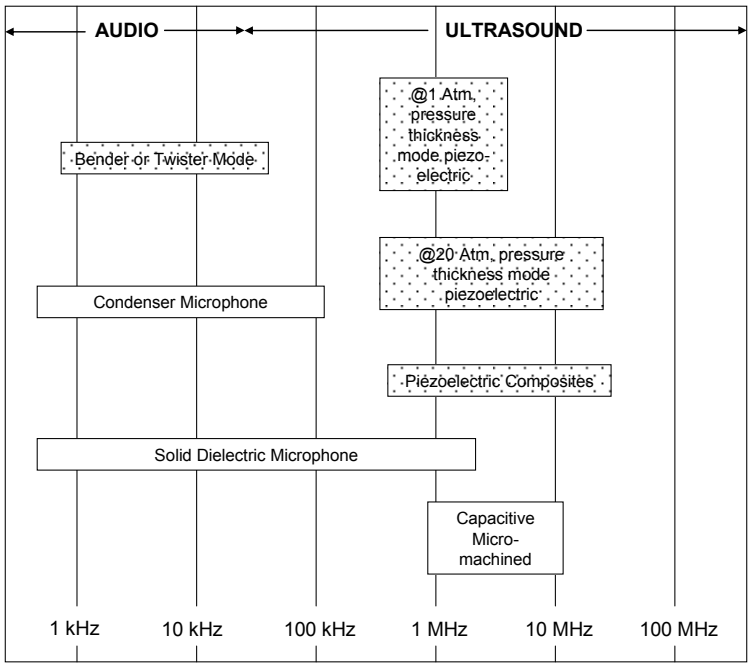

Figure 2.10: Applicability of Different Air-coupled Transduction Technologies as a Function of Frequency - Shaded: Piezoelectric Unshaded: Electrostatic

While, for electrostatic transducer design, condenser microphone has been used to generate and receive ultrasonic signal in air for frequencies below 100 kHz; with restoring force provided by the tension in the high-strength steel membrane. On the other hand, solid-dielectric microphones can operate at frequencies well above 100 kHz, with restoring force due to the presence of air pocket between the backplate and the membrane. Capacitive micro-machined devices, which use a much thinner membrane when compared to solid-dielectric microphones, utilises the residual stress in the membrane to provide the restoring force - giving the capacitive micro-machine a higher sensitivity when compared to the solid-dielectric microphone with an even higher operating frequency range.

As describe earlier, the use of fibre reinforced polymer composites [1] and other highly attenuative hygroscopic materials [38] have made the use of air as a coupling medium within an inspection environment to become increasingly important [34]. In

addition, transducer probes that are able to move along the fuselage and wings of an aircraft in a production line without complicated water jet arrangements will be an ideal situation. The need for a higher sensitivity and better bandwidth to enable a good material inspection and imaging within the domain of air-coupled transducer is thus needed [28, 40].

Taking the different applications and implementation aside; nowadays, proximity and distance sensing, process control and flow measurements form a few of the common uses of an air-coupled ultrasound [37, 41], typically found in the manufacturing and process plant. In a water treatment plant, ultrasound transducers are placed on strategic locations either on top or at the side of the tank, to identify the level of water. In most cases, either a pulse-echo or a through-transmission technique is utilised to measure the level of water within the tank. In industrial applications such as those in the manufacturing plant, ultrasonic sensors are installed through out the production lines to perform such tasks like counting and measuring goods dimensions on a conveyor, determining status of a container whether it is full or empty, identifying defect of a product and locating tilted object etc [42].

Other than the air-coupled applications above, Fortunko *et al* [43] have demonstrated the feasibility of a gas-coupled acoustic microscope, operating in a pulse-echo, c-scan mode, using nitrogen or argon gas at pressures in excess of 30 atmospheres. In addition, Shuttleworth *et al* [44] has demonstrated in the laboratory that gas-coupled ultrasound can accurately measure thickness in high pressure gas pipelines. This increases the possibility of using a gas-coupled system to carry out an in-line inspections of natural-gas pipelines as noted by Grandia and Fortunko [37].

The main benefits of air-coupled ultrasound is the non-contact nature and removing the requirement for a solid or liquid coupling medium between the transducer and specimen [32, 45]. In addition, being a non contact operation, air-coupled ultrasound could be considered as minimally invasive method of ultrasound inspection because the coupling medium in this case air is part of the natural environment [37].

Moreover, the setup of air-coupled ultrasound applications will be simpler since the complicated arrangement of a continuous couplant feed can be eliminated. Furthermore, as there is no couplant other than air required in performing the ultrasound inspections or diagnostics; the risk of inspected object or material becoming contaminated or damaged by the couplant is eliminated. This is especially true for industry such as textiles, wood, metal fabrications, certain electronic assemblies, and aerospace contemporary applications.

Blomme *et al* [46], expressed that although, liquid coupled technique may be sufficient for static measurements, it is impractical for on-line monitoring and testing. Furthermore, by employing air as the coupling medium, the necessity to clean the test object before and after measurements is also reduced. As previously noted, in a liquid couplant environment, cleaning of the surface is generally needed once the inspection is completed. However, cleaning is not an ideal solution as the dried couplant residue may require a complex process to remove thus increasing the risk of damage to the inspected material [30].

In addition to the issues above, Bourne *et al* [34] states that the use of couplant other than air is an inconvenient and places many limitations to the test and inspection that could be performed. The loss of couplant from the transducer front face for example can affect the device SNR to vary intermittently, making interpretation difficult. As with the benefits obtained from the use of air as the coupling medium in ultrasonic applications such as level and range sensing; the same industry would be benefited when full imaging capabilities of air-coupled transducers are fully developed.

Although, in most of the application above, air as a coupling medium is desirable; the problem with low transmission coefficient caused by impedance mismatch to air, has made liquid to be the current couplant of choice. In order to illustrate the severity of losses due to the use of air as a coupling medium, an analytical model which are able to demonstrate the level of losses will be presented next.

2.3.3 Analysis of Reflection and Transmission Losses at Normal Incidence

Previously, different detection techniques such as through-transmission, pulse-echo and pitch-catch have been introduced. In addition, a specific coupling medium is generally needed to match each inspection criteria, nature of the sample and to reduce losses due to transmission and detection of ultrasonic signals. From the discussion above, it has been shown that although air as a coupling medium is desirable; the loss associated with air as a couplant have made liquid as a coupling of choice. The main rationale behind this choice, as well as issues with air as a coupling medium will be explain next from a mathematical point of view.

First, consider a simple ultrasonic scanning system, with a transducer located at a distance, *d* from a test object as shown in Figure 2.11. Assuming the output of the transducer is at a single frequency and planar, then the sound transmitted will be incident to the plane boundary of the test object. Hence, as illustrated, part of the sound striking the boundary will generate a reflected wave, while the remainder of the sound wave will be transmitted to the test object.

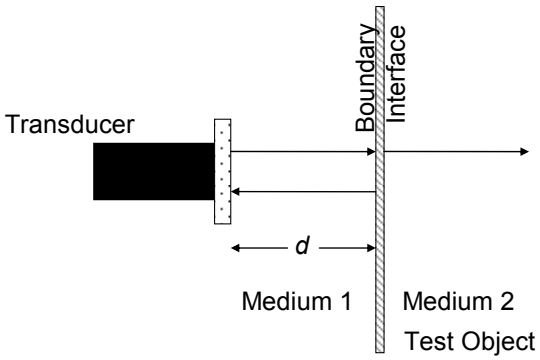

Figure 2.11: Schematic Diagram of Wave Propagation between Two Planar Medium

Following the analysis by Kinsler *et al* [47] in the example above, the medium of propagation (medium 1) and the medium into which the sound is being transmitted (medium 2) has *specific acoustic impedance, Z* and is defined as:

$$Z = \frac{p}{v}$$ **Equation 2.1**

where: p is the acoustic sound pressure and v is the particle velocity in the medium.

For a plane wave propagating though an isotropic lossless medium, the equation above could be re-arranged as follows:

$$z = \rho c$$ **Equation 2.2**

where: ρ is the density of the material and c is speed of sound in the material.

The above equation is then referred to as *characteristic acoustic impedance* of a material, z.

Given the above formula, the characteristic acoustic impedance of air at 20^{o}C is:

$z_{air} = \rho_{air}\, c_{air}$

$= 1.20 \text{ kg}\cdot\text{m}^{-3} \text{ x } 343 \text{ m}\cdot\text{s}^{-1}$

$= 413$ Rayl [$1 \text{ kg}\cdot\text{m}^{-2}\,\text{s}^{-1} = 1$ Rayleigh or Rayl].

Now, if we consider the above case of which the sound wave is on the planar boundary and the boundary is assumed to be lossless. Then, the entire incident pressure wave is converted to either reflected or transmitted pressure waves. Considering the impedance of the two media then the intensity transmission coefficient α_t for an interface between the two media with acoustic impedance of Z_1 and Z_2 may be identified from the following well known equation [48]:

$$\alpha_t = \frac{4Z_1Z_2}{(Z_1 + Z_2)^2}$$ **Equation 2.3**

From Equation 2.3, it could be deduced that as the acoustic impedance of the second medium, Z_2, approaches that of the first, Z_1, the amount of sound transmitted at the boundary will approach 100%.

In a practical example, as shown in Figure 2.12, the ultrasound is being propagated between the polymer transducer to the test object in water.

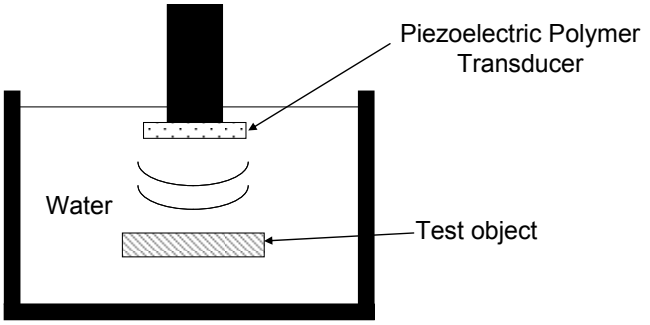

Figure 2.12: Schematic Diagram of a Boundary Condition for a Pulse-Echo System in Water with Polymer Transducer as the Transmitter/Receiver

The specific acoustic impedance of the media is shown in Table 2.1 and assuming that the materials are in direct contact; utilising the Equation 2.3, the intensity transmission coefficient for the acoustic signal into the test object could be calculated.

Table 2.1: Table of Acoustic Impedance for Different Media [49]

Media	Acoustic Impedance, *Z*
Piezoelectric with Polymer Transducer	2 MRayls
Water	1.5 MRayls

In the setup above, a fully matched Piezoelectric Polymer Transducer (Kapton and PZT-5H form the 1-3 air composite of Piezoelectric Polymer Transducer) [49] would enable 98% of the ultrasound acoustic signal to be transmitted through water ensuring enough energy to be reflected by the test object for further exploitation.

However, this is not the case when the same transducer is utilised to transmit through air to the test object. In this new setup, only around less than 0.1% of the ultrasound signal is being transmitted to the test object. This contributes to more than -60 dB losses per trip. If a round trip of **transducer – air - test object – air – transducer** is considered, then the total loss could easily amounted to -150 dB or more [46]. Further refinement in the transducer designs are generally required to enable a good intensity transmission coefficient into air. An intensity transmission coefficient for three different types of transducer technology along with the expected signal loss in decibels (dB) shown in bracket for two different coupling media could be seen in Table 2.2. From Table 2.2, it could be observed that there is single trip intensity transmission coefficient loss, which ranges from -62 dB to -70 dB when the coupling medium is changed from water to air for the three different types of transducer technologies.

Table 2.2: Table of Intensity Transmission Coefficient for Three Different types of Materials with Respect to Water and Air Load

Material	Water 1.5 MRayls	Air 413 Rayls
Piezoelectric Carbon Fiber, 23 MRayls [50]	23% (-13 dB)	<0.01% (-83 dB)
Piezoelectric Composite, 16 MRayls [51]	31% (-10 dB)	0.01% (-80 dB)
Piezoelectric with Polymer Transducer, 2 MRayls [49]	98% (-0.2 dB)	0.08% (-62 dB)

Loss in dB (=20 Log α_T).

Thus, from the exercise above it is apparent that the replacement of water as a coupling medium to air leads to considerable reduction in system sensitivity of around -130 dB round trip. Despite the low transmission coefficient in air-coupled operations, the benefit achieved through the use of air as a coupling medium has made it an attractive choice. In spite of all the potential benefits that could be harnessed when air is utilised as a coupling medium, increasing the efficiency of the transducer output is still the greatest challenge that needs to be tackled.

In addition, issues due to attenuation in air-coupled operation need to also be considered. Air being a viscous media will consume a certain amount of thermal energy when sound propagates through it. Thus, as the energy of sound propagates through a medium, a certain amount of loss is expected due to this thermal energy consumption. This measure of loss is defined as attenuation [47]. A standard ISO 9613-1 (1993) attenuation, α table with 10% uncertainty level, given in dB/km is available for a standard air temperature and pressure of 20^{o}C and 101.325 kPa respectively [52].

For operating frequency of 40 kHz, with a relative humidity of 60% would have the tabled attenuation coefficient, α of 1300 dB/km [52]. As such assuming the detection is performed at 100 mm distance, the loss due to attenuation in air is at 0.13 dB. This may be small due to the low frequency operation. However, assuming that the operating frequency is increased to 1 MHz given the same condition previously, then the attenuation coefficient, α is 164 dB/m [53], giving the loss due to attenuation in air at about 16 dB for a 100 mm distance.

With this, the effect of high attenuation needs to be considered for air-coupled inspection operation, especially those in the high frequency region. This consideration is important as it involves two main issues – energy and resolution capability loss. First, the amount of acoustic energy loss due to attenuation will effectively reduced the amount of acoustic energy transmitted to the test object. With the test object also has its own acoustic impedance, which reflects and transmits the acoustic energy according to the acoustic matching condition, the effect of attenuation is now much more important to be considered especially at high frequency. Next, although the imaging resolution could be improved at high frequency due to low wavelength, this capability could not be fully utilised. As the frequency increases, the loss due to attenuation in air increases, which creates an impasse between improvement needed in imaging resolution and improvement needed in the amount of ultrasound energy required for transmission and thus available during reception.

Another issue that needs to be considered is the issues of diffraction – in which the sound waves change in direction around a small obstacle and spread beyond the small opening [54]. Thus, in this case identifying the optimum operating frequency of the device is important. In an imaging application, in order for a defect to be detected the wavelength needs to be smaller than the expected defect. In general, what this implies is the operating frequency needs to be high, thus smaller wavelength for an effective small defect/object to be detected during an imaging process. Although, this solves the issue of imaging a small object, there is the previous issue that needs to be considered – the loss of ultrasonic signal in air due to attenuation. As the operating resonant frequency increases, the wavelength reduces which improves the imaging resolution. However, with the increase in resonant frequency, the loss due to attenuation in air increases proportionally. The previous example has illustrated that a loss of about 16 dB could be expected when the operating frequency is increased from 40 kHz to 1 MHz, given the same operating environment conditions, beam shape and directivity.

Thus, in air since most of the energy into the test object is either reflected due to the impedance mismatch or lost due to high attenuation in air, increasing the transducer output is the main option to ensure that more energy could be reflected back from the test object hence being utilised for imaging and sensing purposes. Thus, in order to design a feasible air-coupled scanning system, these losses must be overcome through better design of transducer by enhancing the Signal to Noise Ratio (SNR) of the transducer.

Grandia and Fortunko [37] suggested that the transducer output could be increased and made more efficient in three general ways:

- **Matching the acoustic impedance:** A good mechanical match without the use of matching layers has been demonstrated by Ergun *et al* [24] with the use of electrostatic types of transducers. This is mainly due to the air-pocket/membrane system having much lower acoustic impedance compared to piezoelectric transducers [18, 41, 55, 56].

- **Increasing the sound pressure output of the transmitter**: This could compensate for the high reflection losses to the test object. Increasing the bias voltage or the surface displacement with some form of velocity amplifier could improve the sound pressure output. Gan *et al* [57] suggested that the use of a swept-frequency signal (chirp) rather than an impulse allows for a high power, broad bandwidth signal to be used for wideband device applications. For a resonant device, a tone burst signal or continuous wave would suit.
- **Increasing the device SNR:** By introducing a low noise preamplifier and by reduction of thermal noise associated with electrostatic transducer; coupled with the increase in the sound pressure output, the overall SNR could be improved. This is especially important when the transducer is used in receive mode.

Conclusively, two main challenges in tailoring a transducer to air-coupled applications are matching the acoustic impedance of air to the transducer and improving the output pressure signal. The use of electrostatic transducer will help to reduce the issue of impedance mismatch, but further action is still needed to improve the output pressure from the electrostatic transducers which will be discuss next.

2.4 Review of Electrostatic Transducers

Although electrostatic transducers and piezoelectric transducers are of the same age in term of their discovery, the dominance of piezoelectric and its variants are obvious. Oralkan *et al* [58] based on the statement made by Paul Langevin in 1915 has commented that the need for high electric field strength on the order of a million volts per centimetre (10^6 V/cm) has historically hampered further development of the electrostatic transducer. However, recent advances in micro-fabrication and the increasing need for an improved bandwidth and sensitivity, for ultrasonic transducer operating in air has prompted industry to invest further in this field. There is a wide applications base for electrostatic transducers [58], detection of metal condition [59] and applications which requires high power and penetration depth [60] have been spurred since the 90s due to two main characteristics of the device which are:

- Inherently wide bandwidth as compared to typical piezoelectric devices [23, 26, 27].
- Having a good acoustic matching to air due to the membrane's low acoustic impedance [24, 61].

Historically, most of the electrostatic transducer designs were mainly based on a thin dielectric film and a rigid backplate. This kind of transducer is generally known as solid-dielectric microphone or capacitive transducer. There are two types of backplates, the roughened backplate and the regularly patterned backplate. However, as described by Oralkan *et al* [58], recent advancement in micro-fabrications have made it possible to build a CMUT, which offer various advantages such as ease of fabrication for large arrays with individual connections, improve bandwidth and integration with electronics.

2.4.1 Rigid Backplate Design

These backplates are typically manufactured using various techniques such as drilling, sandblasting, sanding, polishing, photolithography, micro-stereo lithography and other suitable manufacturing processes. If only the active elements of the electrostatic transducer are considered, i.e. the membrane and the backplate, then the backplate designs will become critical to the transducer design consideration. In term of backplate designs, there are two main designs that could be incorporated: roughened or regularly patterned.

Depending on the backplate, a roughened backplate would depend on the tension of the membrane, while for regularly patterned backplate the effect of tension could be considered negligible as demonstrated and measured by Hietanen *et al* [62]. Rafiq and Wykes [56] also indicate that the resonant frequency of a grooved backplate is governed by the thickness of the membrane and the groove geometry, if the repeatability of the device could be maintained. However, as expressed by Schindel *et al* [18], the performance and reliability of an electrostatic transducer could be

maximised when the membrane pre-tension is minimised for the regularly patterned backplate. In this respect, for a typical grooved backplate, tension is generally not significant as has been discussed, thus was not considered.

Previously, an overview of the different challenges experienced by the transducer designer and manufacturer in developing and fabricating the roughened and the regularly patterned backplate has been introduced. A detailed discussion regarding the two backplates will be presented next.

2.4.1.1 Roughened Backplate

A roughened backplate could be defined as random patterns within the surface of the transducer as show in Figure 2.13. This random pattern could be manufactured either through sandblasting, sanding or polishing techniques [63, 64]. In addition, the behaviour is generally more unpredictable due to the variation in the air thickness layer across the surface of the membrane. Pizarro *et al* [22] argued that as the surface roughness decreased; the equivalent air layer thickness will also be reduced, thus increasing the resonant frequency of the device. Since the resonant frequency of the device, is determined by the air layer and the tension of the membrane; this unpredictability is expected [56]. In addition, it has been found that the resonant frequency of the backplate varies across the surface of a single transducer [56]. This creates a difficultly in the modelling of the transducer behaviour due to the random nature of the surface backplate. Furthermore as commented by Rafiq and Wykes [56], the detailed of the surface finish also varies from one backplate to the other even when the same manufacturing process is used.

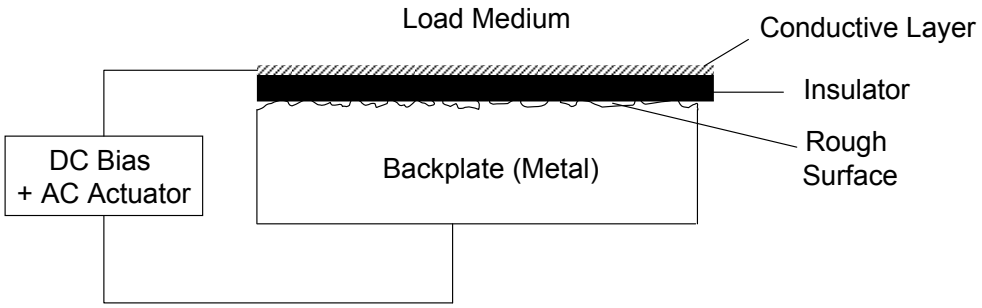

Figure 2.13: Schematic Diagram of a Electrostatic Transducer with Roughened Backplate

2.4.1.2 Regularly Patterned Backplate

In term of sensitivity, Rafiq and Wykes [56] reviewed that the regularly patterned backplate generally tends to have a higher sensitivity when compared to the roughened backplate. Other than the random design, all the other designs are considered as regularly patterned design. The two common patterns that have been utilised for regularly patterned backplates are the v-grooves and cavity designs.

A simplified schematic diagram of a backplate comprised of an array of V-shaped grooves is given in Figure 2.14. There are three main dimensions that need to be considered in the V-groove design which are the groove angle, the groove depth and the groove width. Hietanen *et al* [61] demonstrated that in order to maximise the sensitivity of the device a thin membrane and shallow grooves are required. In this study, using an 8 μm Kapton membrane, the output amplitude could be improved by about 7 dB when compared to a slightly thicker Kapton membrane of 13 μm. In addition, having a groove depth of 0.1 mm has significantly higher output amplitude of about 30 dB when compared to a 0.5 mm groove depth. Furthermore, Rafiq and Wykes [56] established that by adding a convex surface at the top of the backplate, thus ensuring that the membrane is in contact with the top of the grooves would improve the performance of the transducer. However, due to manufacturing challenges, Hietanen *et al* argued that a sharp spine on top of the ridges may occur

which reduces the capacitance of the device by about 125 pF; for a design which has a groove depth of 0.1 mm and ridge angle of 75^{o} [65], thus need to be avoided.

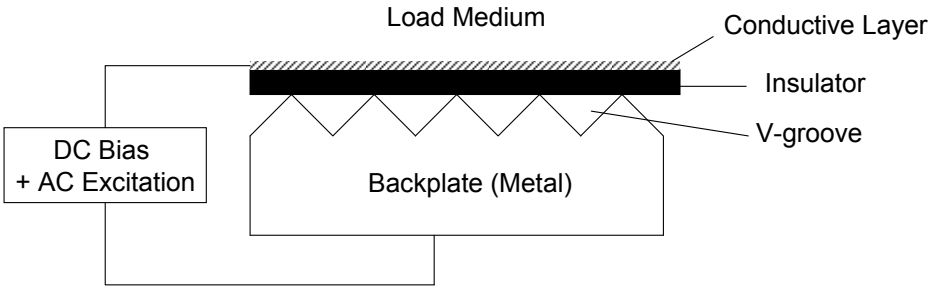

Figure 2.14: Schematic Diagram of V-Groove Backplate [66]

In a cavity design, the surface of the backplate is fabricated in such a way to form an array of hollow indentation on the surface of the backplate. Depending on the fabrication method, this array of hollow indentation could be in the form of cylinder, cube, semi-sphere etc. Assuming that a conventional slot drill is utilised to form an array of hollow indentations, the backplate will have an array of hollow cylindrical shapes imprinted on the surface backplate as shown in Figure 2.15. These hollow cylinders form a cavity of trapped air that could be forced to vibrate during the operations of the electrostatic transducers. One of the main challenges in utilising this backplate design is to identify the suitable dimensions and designs that could improve the transducer sensitivity, bandwidth and frequency range. As in V-groove backplate designs, Hietanen *et al* [61] concluded that the sensitivity of the transducer could be increased by using a light and thin membrane. However, thin membrane is easily damaged, making it unsuitable for harsh industrial applications. On the other hand, a shallow cavity increases the air stream resistance and squeeze film damping [23], thus reducing the device sensitivity at high frequency. A trade-off for an improvement in the device sensitivity is needed to ensure that electrostatic transducers are generally suitable for most industrial applications.

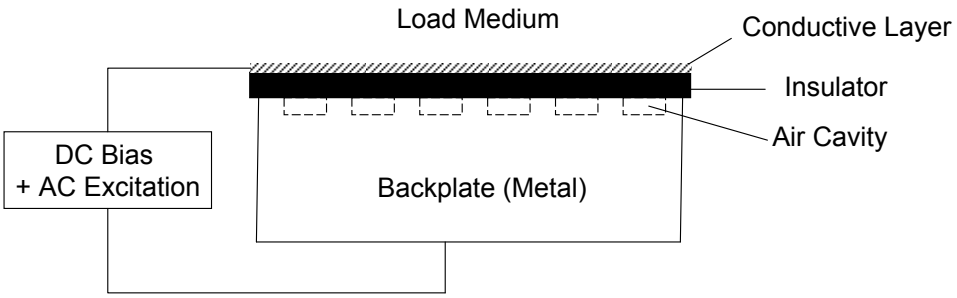

Figure 2.15: Schematic Diagram of a Cavity Backplate

However, the improvement afforded by the optimised design criteria that have been discussed earlier may be negated if the device could not be manufactured to the desired requirements. Careful control and consideration of manufacture is needed. Schindel *et al* [18] expressed the importance of producing a uniform and well defined pit geometry in a micromachined backplate through the micromachining processes. Furthermore, according to Schroder *et al* micromachining processes allow the backplate to be manufactured with a higher accuracy and repeatability; which then allows a much better control for the accuracy of the electrical and acoustic property of the transducer. In addition, McSweeney and Wright [67], demonstrate the importance of having a uniform layer of electrodes applied and the need to ensure that the variation between the pit to pit geometry to be minimised to improve the overall device characteristics.

2.4.2 Capacitive Micro-Machined Ultrasonic Transducer Design

As in the simple electrostatic transducer design, CMUT have two main active components, which are the membrane and the fixed backplate. There are various materials that could be utilised to fabricate the membrane and the fixed backplate among them are silicon nitrate and silicon substrate respectively. A typical structure of CMUT will include the upper and lower electrodes, membrane, cavity and insulation layer. The insulation layer ensures that the bottom electrode is electrically isolated from the top electrode. Typically a DC or bias voltage between 40 V to 160

V [68, 69] is connected to fixed backplate, while a ground is connected to the CMUT membrane as shown in Figure 2.16. However, for specific applications such as those utilising the pre-charged CMUT or in a wide pressure range operations, the bias voltage has been shown to operate at 200V [70] or 250V [71] respectively. The bias voltage will enable a static deflection of the membrane towards the bottom electrode. In order to excite the membrane, an excitation frequency of the AC voltage with amplitude much smaller than the bias voltage is used to excite the membrane. This causes the free membrane to move up and down generating a pressure wave. Conversely, in receive mode, the compression and rarefaction of an incident pressure wave will cause the free plate to vibrate causing the surface charge to vary with the same cycle as the incident pressure wave. In both cases, the bias voltage is applied between the two layers in order to charge the capacitor while improving and linearising the response of the device [72]. In addition, the bias voltage also changes the level of plate deflection towards the CMUT bottom electrode, thus changing the volume of the air gap in a CMUT cavity [73]. The effect of the bias voltage could be clearly seen especially when a CMUT is made to operate in a collapse-mode [68].

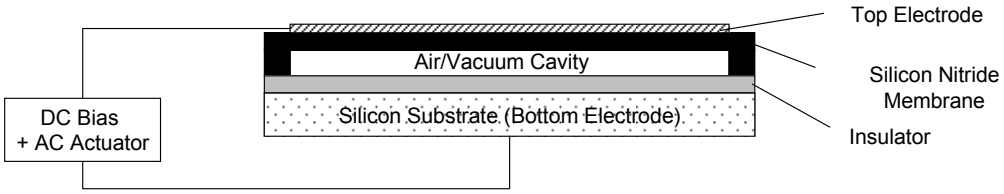

Figure 2.16: Schematic Diagram for a CMUT Design with Silicon Nitrate Membrane and Silicone Substrate Backplate [74]

Many parameters need to be considered when designing the CMUT and electrostatic transducers. Some of the key considerations are:

- **Operating Condition and Driving Signal Used [59]:** either it is resonant (narrowband) or non-resonant (broadband). In resonant or narrowband operation as in typical CMUT [67], the correct frequency range needs to be selected to maximise the transmission; and a prior knowledge of the sample resonance is required. On the other hand, in a non-resonant or broadband operation as in

typical electrostatic transducer with backplates [63], the sample itself will act as a narrowband filter thus identifying its own resonant frequency.

- **Membrane Condition:** either it is in conventional or collapse-mode. The conventional-mode as shown in Figure 2.17 operates in a piston mode as the centre of the membrane is left free to vibrate. On the other hand, in collapse-mode as shown in Figure 2.18 works on some basis of a ring shape transducer, where the transducer is biased to a point just before the membrane collapse voltage. Thus, the transducer could be considered to operate at a higher order modes, since the centre of the membrane vibration could be considered low compared to its circumferential vibrations. (The full concept of mode shape will be fully introduced in the later Chapter).

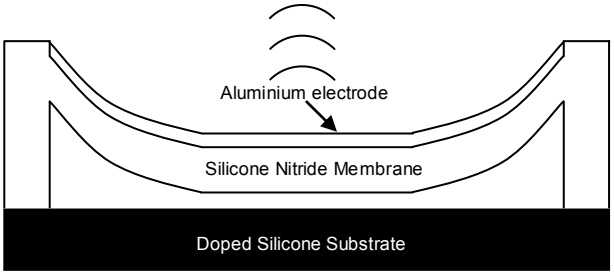

Figure 2.17: Schematic Diagram of CMUT in Conventional-Mode [68]

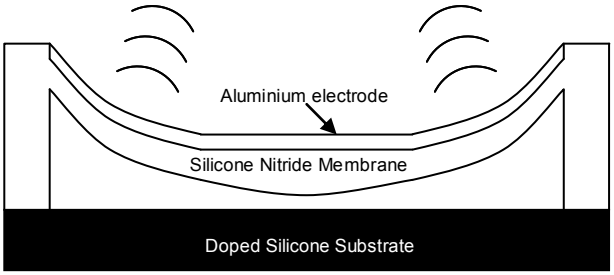

Figure 2.18: Schematic Diagram of CMUT in Collapse-Mode [68]

- **Membrane design and geometry:** membrane thickness, the gap behind the membrane [22, 25, 75] , the membrane material [76, 77].
- **Backplate design and geometry:** the fill factor [78], the type and material of backplate [22].
- **Load medium:** different load media such as air, gas, solid, water and etc [77].

2.5 Current Electrostatic Transducer and Its Limitation

One of the main limitations in utilising electrostatic transducer in a fully air-coupled industrial application currently is the inherently low output sensitivity. There are many ways to improve sensitivity, some of which have been discussed earlier. Nevertheless, improving sensitivity alone, would not improve the overall performance of the device. Other considerations need to be made for an enhanced device includes widening the bandwidth, reducing the noise and improving overall reliability of the system. As in most systems, it is usually very unlikely that a system could be improved in all functions. As such, a compromise is usually necessary.

In most cases, there are three main components that need to be optimised in order to improve the sensitivity and bandwidth of the electrostatic transducer which are the bias voltage, membrane configuration and air gap.

2.5.1 Bias Voltage

The increase in bias voltage will increase the static defection of the membrane, which in turn increases the sensitivity. However, there is a limit to this increase. Upon certain level, a collapse of the membrane would occur. This is when the membrane touches the surface of the backplate. In normal operation, the bias voltage will be maximised to just before a membrane collapse or before a voltage breakdown occurs. In addition, Oralkan *et al* [68] demonstrated that a collapse-mode CMUTs are capable of more efficient operation when compared to conventional CMUTs due to the different nature of the output pressure. Furthermore, according to Park *et al* [79] because the membrane is biased more than a pull-in voltage, the electric field strength in the cavity is much higher in the collapse-mode CMUTs compared to the conventional CMUTS, giving the collapse-mode to operate in a better efficient during a transmit and receive operations. However, in conventional CMUTs, the device operates with a piston like motion, compared to in a collapse-mode, the device operates in a higher order mode, which could be approximated to mode (0,2),

and thus are not considered for use in this Thesis. (A detail discussion on the different membrane's modes of vibration will be discussed in the subsequent Chapter 3).

In addition to the above results, Pizarro *et al* [22] have demonstrated through modelling and experiment that by increasing the bias voltage, the displacement between the cavities is reduced. This could be a positive or a negative effect to the transducer operations, since increasing the bias voltage reduces the effect of the inter-cavity or smooth area surface displacement, which is desirable for a resonant operation but may not be in a non-resonant operation.

Finally, Schindel *et al* [18], have shown through experiment that the bandwidth could be improved by increasing the bias voltage. In this experiment, it was shown that the bandwidth could be doubled when the bias voltage is increased from 100 V to 400 V. In addition, Schindel *et al* [18] also observed that the increase in bandwidth due to the increase in bias voltage occurs for both transmission or reception.

2.5.2 Membrane Configuration

Rafiq and Wykes [56] concluded that by using a thin membrane, the sensitivity of the device could be improved. This is mainly because thin membranes are more flexible and have a better contact with the backplate surface giving a more uniform structure. This in turn improves the overall mechanical response to pressure. However, thin membranes could be easily damaged [74] and reduce the performance of the transducer [24]. In addition to using a thin membrane, some authors have suggested different novel approaches to improve sensitivity by improving membrane design and choosing suitable membrane materials and design. Fuldner *et al* [80] has demonstrated that sensitivity could be improved by about –17 dB as compared to a normal condenser microphone when a combination of spring type and corrugated membrane are being utilised. While, Hsu *et al* [81] has shown through experiments

that low stress polysilicon membrane are able to achieve a sensitivity of -34 dB (ref. to 1 V/Pa).

2.5.3 Air Gap Configuration

Reducing the air gap between the membrane and the surface of the backplate would in general improve the sensitivity of the device. From the measurement performed by Hietanen *et al* [61], the sensitivity of the device is shown to increase by 40 dB when the ridge angle is decreased from 135^{o} to 75^{o} and the groove depth is reduced from 0.5 mm to 0.1 mm for a V-groove backplate. However, if reducing the air gap depth and surface area adjacent to the membrane alone could improve the sensitivity significantly, then a roughened backplate would then have the highest sensitivity since the air gap is very small.

Nonetheless, as reviewed by Scheeper *et al* [23] and Ergun *et al* [24], thin air gap will increase the air streaming resistance and the squeeze film damping, which in turn reduces the overall device sensitivity at high frequency. This effect could be eliminated by the use of vacuum sealed cavity as demonstrated by Hansen *et al* [25]. In addition, assuming that the vacuum seal is in good condition, then issues with contamination is not important. However, if the seal is broken or if it is a device which uses air cavity, then the effect of contamination such as dust or water vapour will be more pronounced, especially for devices which operates using a small air gap. The dust and water vapour could be trapped between the air layers. This causes the device to reduce in sensitivity or cease functioning. In a regular grooved pattern, reducing the air gap means to reduce the cavity depth. However, reducing the cavity depth also effect the cavity resonant frequency and bandwidth. Tan and Miao [82] have shown through experiments that reducing the cavity depth will reduce the device's bandwidth and increases the cavity resonant of the device. In addition, as noted by Ergun *et al* [24], reducing the air gap, reduces the collapse voltage of the device. This in turn reduces the amount of bias voltage available to be used to improve the sensitivity. However, as concluded in the design and experiment by Tan

and Miao [82], the bandwidth could be improved by increasing the cavity radius. Although, according to the experiment, sensitivity would not be affected, increasing the cavity radius in general reduces the resonant frequency of the device.

One of the limiting factors between bandwidth and sensitivity is that it is mutually exclusive in some domain. A good example for this contradictory effect is when reducing the air gap between the membrane and the backplate surfaces is used as a technique to improve sensitivity. Although sensitivity will be improved by reducing air gap, this improvement will be negated by a reduction in bandwidth as demonstrated in the experiments performed by Tan and Miao [82]. However, by choosing the proper size of individual cell radius and its placement within an array, Senlik *et al* [83], have shown analytically that bandwidth could be optimised by increasing its radiation resistance; albeit the resonant frequency of the device still needs to be considered. (The concept on array and optimisation of array will be introduced later in Chapter 6).

2.5.4 Key Design Consideration

In summary, for an electrostatic transducer to work efficiently in the ultrasonic range, the membrane needs to be very thin and the cavity depth needs to be very shallow. Hutchins *et al* [75] suggested that the cavity radius needs to be at least twice the thickness of the membrane and the cavity depth, for the response to be a piston like and independent of the radius. However, cavity radius influences the membrane resonant frequency, the smaller the cavity radius the higher the membrane resonant frequency. Thus, if a highly sensitive high frequency transducer is needed, the cavity depth needs to be as shallow as possible, the cavity radius needs to be as small as possible and the membrane needs to be as thin as possible, which gives a challenge in the overall sensitivity itself. Increasing and optimising the overall active area is important to ensure a good sensitivity is sustained with the reduced single unit cell size.

The basic principle of all the devices to date have been the same, which is to improve the cavity manufacturing technique by producing a more uniformly shaped cavity and to improve the cavity design by modifying the cavity morphology. In this Thesis, further modification of the cavity design to enhance the device output, through the use of a concentric cavity and pipe is proposed. This will be the focus of the next discussion.

2.6 Proposed Design to Enhanced Electrostatic Transducer

Various ways have been discussed on how to improve the device sensitivity, as well as other considerations that needs to be made when developing and designing an electrostatic transducer.

Since it is impractical to improve all factors that are needed for an efficient electrostatic transducer, a compromise in term of sensitivity and bandwidth is generally needed. The improvements in sensitivity that have been discussed much earlier are mostly based on either CMUT or a membrane with roughened backplate or a membrane with regularly patterned backplate, typically cylindrical shallow cavities.

Nonetheless, the strategies that have been utilised to improve the sensitivity for the three main devices above have their own drawbacks. By reducing the air gap layer, the bandwidth suffers; while by using a very thin membrane the durability and the robustness of the transducer reduces. In addition, increasing the bias voltage does have its limit, whereby upon certain limit the sensitivity reduces due to the coupling effect of the groove or cavity and its surrounding non patterned surfaces [84].

Typically as shown in Figure 2.2, the circumference of the transducer is clamped. This would increase the squeeze film damping and squeeze film resistance during operation, due to the trapped air between the membrane and the backplate. Adding an acoustic relief as in the condenser microphone [82] or ensuring there is a free edges

at the circumference of the transducer assembly [24, 25] would enable air to flow in and out of the transducer assembly which reduces the effect of squeeze film damping and squeeze film resistance. A typical condenser microphone consist of a membrane suspended over a single cavity, with the backplate having an array of acoustic relief and a peripheral slit as shown in Figure 2.19 [25, 82, 85].

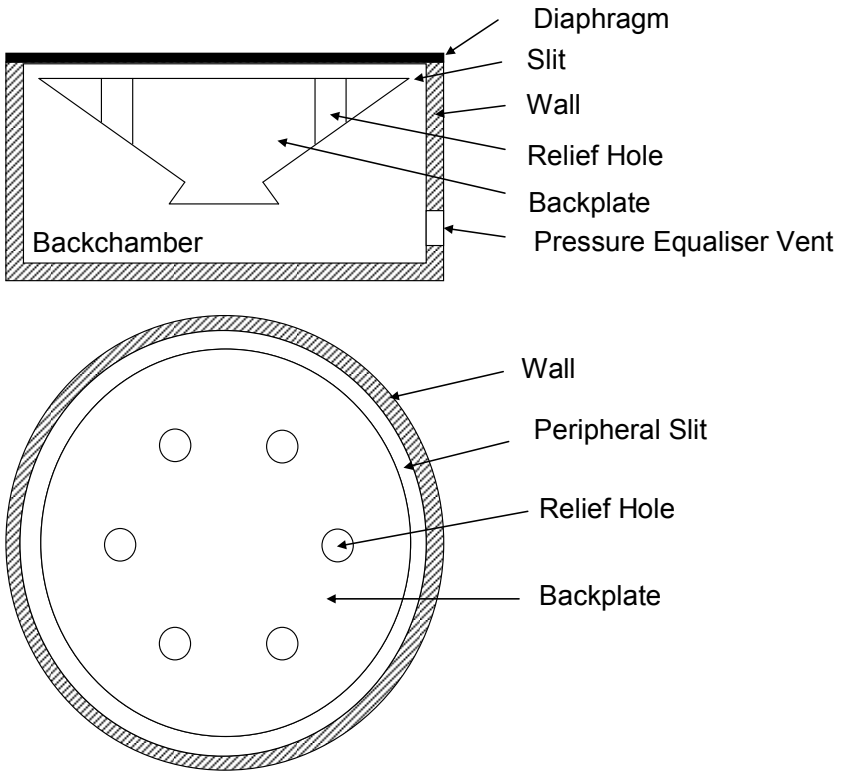

Figure 2.19: Schematic Diagram of Typical Condenser Microphone with Acoustic Relief Slot and Free Edges Slit [25, 85]

The idea of adding an acoustic relief discussed previously within a condenser microphone will compliment perfectly to the concept that will be introduced next. An approach to improve sensitivity in electrostatic devices was recently proposed by Campbell [78]. The concept, termed **FL**uidically **A**mplified **U**ltrasonic **T**ransducer or **FLAUT**, is based on employing the resonance of pipes and cavities; synonymous to those found in musical instruments. The theory states that the resonant frequency of the device is governed by a few key dimensions: pipe radius and length, cavity radius and depth, and the membrane thickness [78].

However, the main different between the typical condenser microphone previously described, and the FLAUT is in the design and construction of the acoustic relief. In a condenser microphone, there is only a single cavity with an array of acoustic relief channels. In addition, within the circumference of the condenser microphone backplate there is a peripheral slit to reduce the effect of squeeze film damping. A pressure equalisation vent is also included in the backchamber to prevent the collapse of the membrane against the backplate due to the fluctuation of the atmospheric pressure.

In this new FLAUT design, the backplate features an array of combined concentric cavity and pipes as shown Figure 2.20. Thus, contrary to the condenser microphone with a single cavity and a mass "pipes", the FLAUT cavity has an individual pipe for each cavity. Furthermore, a specific consideration of the pipe geometry in relation to the cavity and thin plate resonant frequency is also made in a FLAUT design consideration but not in the current condenser microphone design consideration. (Further discussion regarding this concept will be given in the next Chapter).

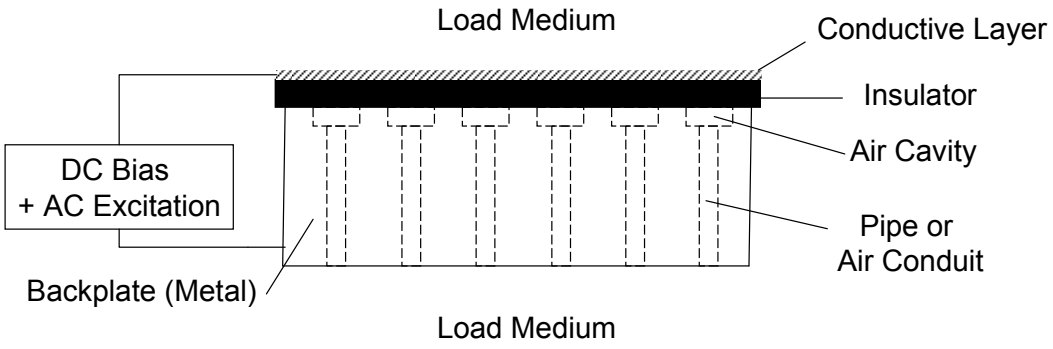

Figure 2.20: Schematic Diagram of FLAUT with DC biased and AC Excitation Connected

Comparatively, as discussed earlier the traditional electrostatic devices utilise a groove or cavity resonance operation. In conventional electrostatic transducer devices, the vibrating membrane on top of the cavity as shown in Figure 2.15 is the only face that is being coupled to the load medium. However, in this new concept, the membrane that is already excited by the AC voltage will excite the fluid filled

pipes thus amplifying the overall signal. In this case, there are two faces of the transducer that are being coupled to the load medium: the membrane and the opening of the pipes. Since, the pipes are filled with fluid, a perfect acoustic matching to the fluid load results. In addition, due to the pipe face being directly coupled to the load medium, there is no need for a pressure equalisation vent to prevent FLAUT diaphragm from collapsing.

However, since this is a new concept, the availability of the references based on this concept is extremely scarce. One of the important aspects in designing a FLAUT is the matching of cavity resonance and the pipe resonance, which will be discussed in great detail in the next Chapter. It is also important to note that, with the inclusion of the pipe in the electrostatic transducer design, further improvements both in terms of sensitivity and bandwidth is expected.

Although in terms of air gap, sensitivity and bandwidth are mutually exclusive; with the inclusion of a pipe, the effect of air gap to bandwidth could be mitigated as the squeeze film effect and the air gap resistance is reduced [25, 82]. However, as shown by the experimental results performed by Tan and Miao [82], in order for the squeeze film effect and the air gap resistance to be reduced, the size of the vent hole in this case the pipe radius needs to be as large as possible and at the centre of the cavity.

2.7 Conclusion

In the beginning of this Chapter, the different generation and detection techniques for ultrasound have been discussed, along with specific tailoring requirement for the ultrasound application detailed. The influence of different coupling media i.e. solid, liquid and gas (mainly air) have been explored which indicate that although the use of air as a coupling medium is highly desirable, issues such as low transmission coefficient have made liquid to be the current couplant of choice. Furthermore, the two main factors which influence sensitivity and bandwidth for air-coupled

applications have been identified - the impedance mismatch between the transducer and sample, and high attenuation in air.

Generally, sensitivity and bandwidth are mutually exclusive, however the use of an electrostatic transducer with its inherently wide bandwidth and good acoustic matching to air have promised an improved sensitivity and bandwidth suited for air-coupled applications. Subsequently, from the literature review, it could be summarised that there are two major types of electrostatic transducers: the CMUT and the membrane with rigid backplate. In the review, it is also found that there are a few key factors that determine the sensitivity and bandwidth of an electrostatic device which are membrane material and thickness, cavity radius and cavity depth.

Finally, a concept incorporating concentric pipe and cavity is put forward which has shown that it is possible to improve sensitivity, while still maintaining acceptable level of bandwidth. The use of a cavity and pipe system promises an increase in sensitivity but at a cost of producing a resonant device. However, albeit being a resonant device, the effect of bandwidth reduction is expected to lessen due to the reduction in squeeze film damping and air gap resistance. In the next Chapter, a review of different modelling techniques utilised and the interaction of each factor will be revealed. The use of ratios in the design of a FLAUT would also be introduced as part of the optimisation sequences as well as a technique to enhance the overall electrostatic transducer performance.

3. Modelling and Simulation Review and Analysis

3.1 Introduction

Theoretical modelling and simulations have become an integral part of modern designs and planning. All major fields of science and engineering, finance, transportation and defence rely on some form of theoretical modelling to provide simulations of design scenarios in order to enhance understanding and optimise the resultant design. With the advancement in computing technology, and the pressure to reduce the overall of cost of design and prototyping, the use of theoretical modelling and simulation software within the engineering domain has become commonplace. A wide range of different analysis tools are typically utilised to improve productivity and efficiency.

In the field of ultrasound a wide range of modelling and simulation tools are employed in the design of the transducer front-end [17, 22, 66] and electrical interface [86] or understanding wave propagation in the load medium [75, 87, 88]. These can be computationally efficient analytical models analysing one component in a system [17, 89] or complex 3D analyses encompassing the entire system and its environment [90, 91].

This Chapter will describe the relative merits of the different modelling tools employed in the design of the FLAUT device. This will be followed by introducing the concept of the diaphragm vibrational modes. Finally, as a proof of concept study, FLAUT devices operating in the frequency range of 20 kHz to 40 kHz are proposed. Two modelling and simulation methods are utilised to identify the resonant frequency, FLAUT geometry and design sensitivity analysis. The flow of the modelling, simulation and validation process that covers both the sensitivity and noise is shown in Figure 3.1. The whole modelling, simulation and verification process of the FLAUT is iterative. In this thesis, only the final iteration of the process is shown.

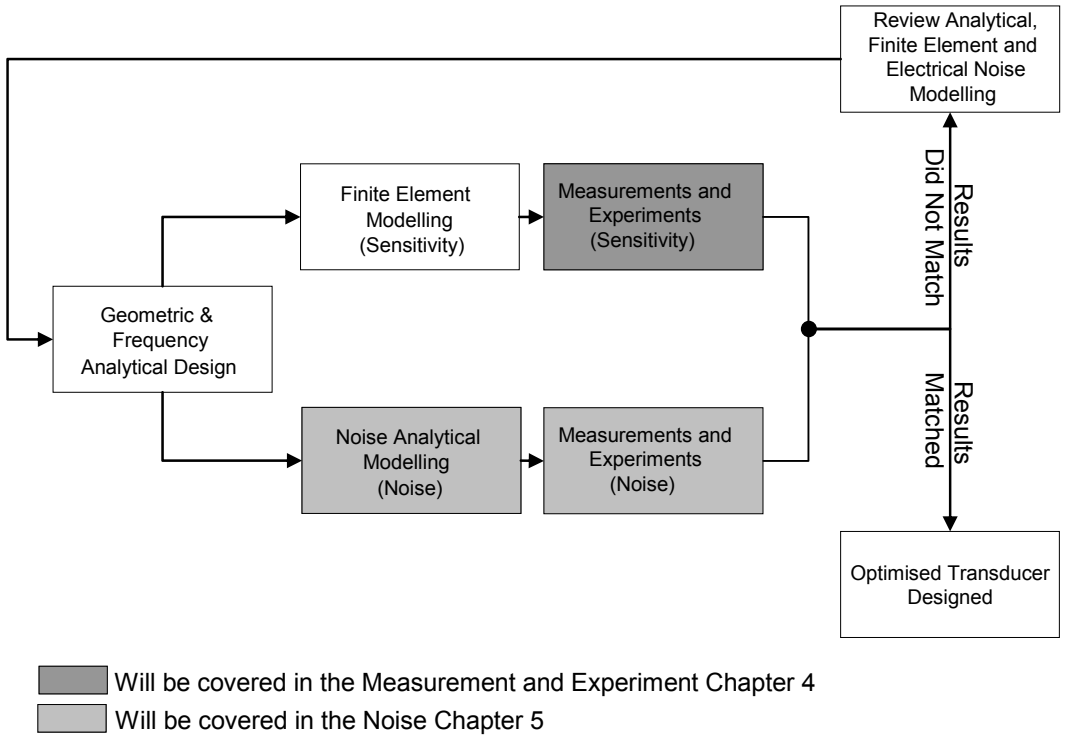

Figure 3.1: Flow Diagram of a General Modelling Technique Utilised for Design and Development of Electrostatic Transducer

In the previous Chapter, a brief schematic diagram of FLAUT that comprises of three components: the pipe, the cavity and the thin plate suspended above the cavity has been shown in Figure 2.20. In order to consider a FLAUT transducer design, these components need to be considered holistically since some matching of the resonant frequencies will be required. As such, a simple, computationally efficient analytical model for the thin plate, cavity and pipe has been employed in order that a rapid parametric sweep may be performed to provide device microstructure prior to considering the constructional parameters. Since the cavity and pipe are resonant, with the dimensions governing the resonant frequency, this will form the basis of the analytical model for a given device operational frequency

The implementation of any analytical model commences with the underlying physical behaviour of the system under analysis. In this case, analysis of the thin

plate, cavity and pipe are required, in order to represent the system in the model. Each component will now be considered in turn.

3.1.1 Modelling of Thin Plate

In order to consider the modelling of the thin plate some consideration of the physical representation of the thin plate is required. Moreover, it is important that a differentiation between a membrane and a plate is made. Previous authors in the field use the terms membrane and plate interchangeably. This is mainly due to the fact that it is of the same concept being adopted at a different situations and conditions.

Kinsler *et al* [47], makes a differentiation between membranes and plates based upon the different restoring force that acts upon them. The membrane's restoring force is entirely due to the tension applied to the membrane, while the plate's restoring force is entirely due to the stiffness of the diaphragm.

According to Ventsel and Krauthammer [92] the theoretical definition of a thick plate, a thin plate or a membrane is mainly defined by the ratio between the diameter ($2r_m$) and the thickness (d_m) of the diaphragm. In general, thick plate is when the ratio is less than 10, thin plate is when the ratio is between 10 and 80, and membrane is when the ratio is above 80 as illustrated in Figure 3.2.

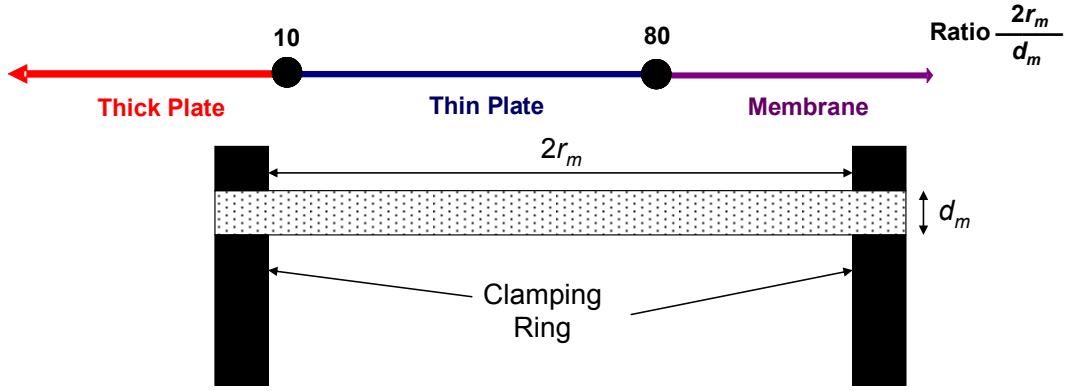

Figure 3.2: Visual Representation of the Limit that Separates the Thick Plate, Thin Plate and the Membrane Theory

This is a good way of describing why the membrane, thin plate and thick plate are of the same physical concept but exhibit different behaviour. This could be clearly seen from Equation 3.1 that described the flexural rigidity of the diaphragm and the illustration in Figure 3.3, which shows the cross section of the diaphragm structure.

$$D = \frac{Ed_m^3}{12(1-v^2)} \qquad \textbf{Equation 3.1}$$

where E is the Young's modulus, v is the Poisson's ratio, d_m is the diaphragm thickness.

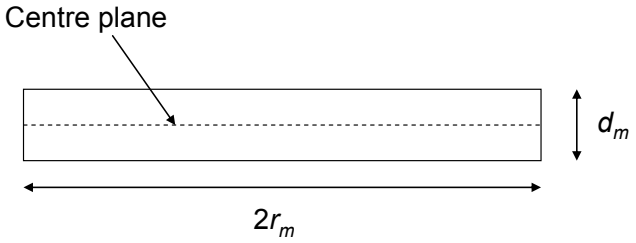

Figure 3.3: Cross Section Diagram of a Circular Diaphragm

As observed in Figure 3.3, it could be deduced that as the diaphragm thickness, d_m reduces to a negligible value with respect to the centre plane; the flexural rigidity of the diaphragm becomes zero as denoted by Equation 3.1. This concept visually depicts the structural transitional changes from a thin plate to a membrane. On the contrary, as the diaphragm thickness, d_m increases such that the ratio between $2r_m$ and d_m reduces to less than 10, then the diaphragm structure would be considered a thick plate [92]. However, it is not practical to assume that at that cut off ratio the behaviour suddenly change from one to the next. Thus, this ratio works more as an acceptable guideline to indicate which suitable theory is to be utilised, rather than an absolute principle.

All the work that is performed in this Thesis is based on the assumption that the diaphragms utilised are of a thin plate, thus no tension term is considered within the equation. This is based on work expressed by Kinsler *et al* [47] and Rafiq and Wykes [56] that the resonant frequency of a capacitive ultrasonic transducer with grooved backplate can be shown to depend only on the thickness of the diaphragm and the

geometry of the backplate groove. In addition, Hietanen *et al* [62] demonstrates that the effect of tension to the resonant frequency could be considered negligible for an electrostatic transducer.

Thus, modelling of FLAUT is developed by assuming that a thin plate suspended over a cavity can be approximated by a simple mass-spring system. Assuming piston resonator surrounded by an infinite baffle [47], the resonant frequency of such a mass-spring system can be calculated from Equation 3.2.

$$f_n = \frac{1}{2\pi}\sqrt{\frac{k}{m}} \qquad \textbf{Equation 3.2}$$

where k is the total stiffness of the system and m is the supported mass.

In this case, the resonant frequency for a circular thin plate fixed at the edges can be written [93],

$$f_n = \frac{K_n}{2\pi}\sqrt{\frac{Dg}{wr_m^{\,4}}} \qquad \textbf{Equation 3.3}$$

where K_n is a constant and take the numerical value 10.22 for circular thin plate fixed at the edges operating in the fundamental mode, D is the flexural rigidity of the thin plate and is defined by Equation 3.1 - with d_m representing the thin plate thickness, r_m is the radius of the thin plate, g is the gravitational acceleration = 9.81 ms^{-2}, w is the force or load due to the mass of the thin plate per unit area, which is given by $w = mg/A = \rho_m d_m g$, where ρ_m is the density of the thin plate. Substituting this equation into Equation 3.3 gives Equation 3.4, which is the resonant frequency of the thin plate:

$$f_n = \frac{1}{2\pi}\sqrt{\frac{K_n^2 D}{\rho_m d_m r_m^4}} \qquad \textbf{Equation 3.4}$$

3.1.2 Modelling of Cavity

Assuming air follows adiabatic compression laws, it can be shown that the first law of thermodynamics can be used to show the stiffness of the air gap, and can be described [94] as in Equation 3.5,

$$k_a = \frac{\gamma P A}{d_a} \qquad \textbf{Equation 3.5}$$

where the adiabatic constant of air, γ = 1.4, P = 101.325 kPa is the atmospheric pressure and d_a is the thickness of the cavity. Substituting Equation 3.5 into Equation 3.2, gives the resonant frequency due to the air cavity as in Equation 3.6.

$$f_n = \frac{1}{2\pi}\sqrt{\frac{\gamma P}{\rho_m d_m d_a}} \qquad \textbf{Equation 3.6}$$

From Equation 3.3 and Equation 3.6, it could be summarised that the two main resonant frequencies of the FLAUT could be determined, which are the thin plate resonant frequency and the cavity resonant frequency respectively. These two resonant frequencies, along with the pipe resonant frequency will play a pivotal role in the preliminary design requirement of the FLAUT.

3.1.3 Modelling of Pipes

In order for a FLAUT to have a matched thin plate, cavity and pipe design, a model to determine the pipe resonant frequency needs to be developed. This step, along with the previous step will enable thin plate, cavity and pipe resonant frequencies to be matched as the first step in the FLAUT design process; after which the initial design would then be analysed in more detail using Finite Element (FE) modelling to visualise the vibrational mode of the thin plate.

Extensive work has been presented on the physics behind resonant frequencies of pipes [95]. In general, the resonant frequency of a pipe is related to the length of the pipe, the shape of its cross section, i.e. circular, square, elliptical etc., and whether it has closed or open ends.

For a rigid cylindrical pipe, the term open cylinder usually refers to when both of the pipe end are left open as shown in Figure 3.4; while the term closed cylinder usually refers to when one of the pipe end is closed with a rigid surface while the other is open, as shown in Figure 3.5.

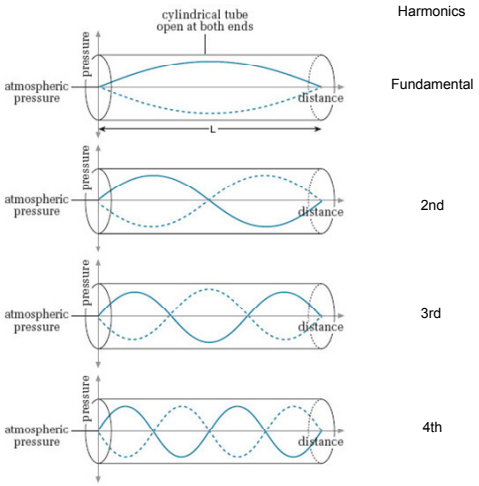

Figure 3.4: Schematic Diagram of First Four Normal Mode of Vibration (Harmonics) in Terms of Pressure for an Open Cylinder [96]

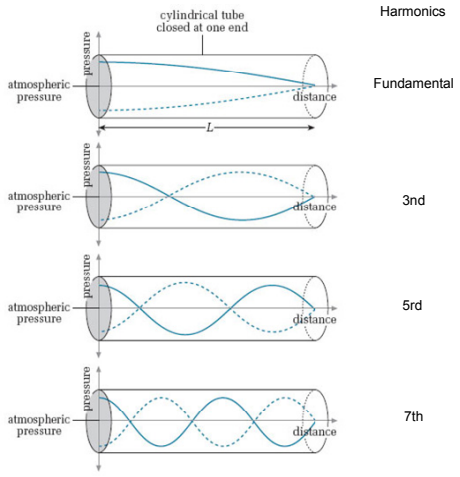

Figure 3.5: Schematic Diagram of First Four Normal Mode of Vibration (Harmonics) in Term of Pressure for a Closed Cylinder [97]

In a pipe that is open at both faces, the resonant modes occur when there is a pressure node positioned at each end of the pipe, as shown in Figure 3.4. As such, the open pipe is a half-wavelength resonator and supports both the even and odd harmonics of the fundamental mode. In this scenario, the wavelength of an acoustic wave propagating along the pipe is determined by Equation 3.7.

$$\lambda_n = \frac{2L_e}{n} \qquad \textbf{Equation 3.7}$$

where λ is the wavelength, n is the mode of operation and L_e is the effective length of the pipe. Since, the velocity of sound could be represented by the product of wavelength and frequency, the resonant frequency of the open cylindrical pipe can then be determined from Equation 3.8.

$$\frac{c}{f_n} = \frac{2L_e}{n}$$

$$f_n = \frac{nc}{2L_e} \qquad \textbf{Equation 3.8}$$

where c is the velocity of sound in the medium, n = 1, 2, 3, 4, … because open cylindrical pipe supports both odd and even harmonics and L_e is the length of the standing wave. In practice, L_e is slightly longer than the physical length of the pipe. The extension is known as the pipe end-correction. Extensive experimental work [98] and theoretical work [47] has been performed to identify this end correction.

Kinsler *et al* [47], Anderson *et al* [98] and Campbell *et al* [99] proposed the following relationship to account for the end correction based on the Equation 3.9 below:

$$L_e = L_a + 0.6r_p \qquad \textbf{Equation 3.9}$$

where L_a is the length of the pipe and r_p is the radius of the pipe.

Substituting Equation 3.9 into Equation 3.8 gives Equation 3.10.

$$f_n = \frac{nc}{2(L_a + 0.6r_p)} \qquad \textbf{Equation 3.10}$$

In the situation where the pipe is closed at one end, the resonant modes occur when there is a node at the open end of the pipe and an anti-node at the closed end of the pipe, as shown in Figure 3.5. As such, the closed pipe is a quarter-wavelength resonator, which will only support the odd harmonics of the fundamental mode. In this case, the wavelength of a mode supported by the pipe can be written Equation 3.11.

$$\lambda_n = \frac{4L_e}{n} \qquad \textbf{Equation 3.11}$$

Following the same analysis as shown previously, the resonant frequency of a closed cylindrical pipe is half of the open cylindrical pipe as shown in Equation 3.12.

$$f_n = \frac{nc}{4L_e} \qquad \textbf{Equation 3.12}$$

However, since closed cylindrical pipe requires that a pressure node at the open end and a pressure anti-node at the closed end, only odd harmonics will support this criterion. Therefore, for a closed cylindrical pipe, n = 1, 3, 5, … The end correction could be included in the final resonant frequency equation by substituting Equation 3.9 into Equation 3.12 which gives Equation 3.13.

$$f_n = \frac{nc}{4(L_a + 0.6r_p)} \qquad \textbf{Equation 3.13}$$

3.1.4 Expected Results from Analytical Modelling

The main output from the analytical modelling is to determine the fundamental frequency of individual thin plate, cavity and pipe resonances. These three resonant frequencies are important, as they will determine the total resultant output of the

FLAUT design. Since, FLAUT is based on a fluidic amplification concept, it is important that the resonant frequency of the thin plate, cavity and pipe are matched to maximise the potential benefit of the fluidic amplification. Although it is possible to operate in a higher order mode, due to the irregular pressure output and the unpredictability of the wave propagation, fundamental or piston modes are usually preferred. (The concept behind different vibrational modes will be discussed later in the Chapter).

As has been mentioned previously, FLAUT consist of three different components: the thin plate, the cavity and the pipe. These three components need to complement each other output for them to improve the overall net output. The ideal scenario being a perfectly matched thin plate, cavity and pipe resonant frequency of which all the individual component will be displacing in phase. In order for this to take place, a matching geometry between the three individual components is required.

In order to exemplify the process consider the following design scenario for a FLAUT transducer with a resonant frequency of between 5 kHz and 100 kHz, using 50 μm thickness Kapton [100]. The analytical model embodied in Equation 3.4 and Equation 3.6 is employed to perform a parameter sweep, Figure 3.6 details the results. From Figure 3.6, the suitable resonant frequency and its matching thin plate radius and cavity depth could be identified. In the example above, assuming that a 25 kHz transducer is to be constructed, then the suggested dimensions is 1151 μm for the thin plate radius and 81 μm for the cavity depth. Since thin plate radius is the cavity radius assuming that the edges of the cavity are clamped, all the required dimensions to develop a cavity only design have been identified.

However, since the configuration is designed based on individual geometrical components of thin plate, cavity and pipe, no specific transition definition could be identified to differentiate a shallow cavity to pipe (deep cavity) or from pipe to cavity (short pipe). This is due to fact that the equation of cavity and pipe are bounded by their respective relationship that relates to the operating resonant frequency as have been shown previously. (Further discussion on the different geometrical design of

cavity and pipe and their relationship to the resonant frequency will be discussed in Section 3.5.1, Section 4.6.2 and Section 6.2.1).

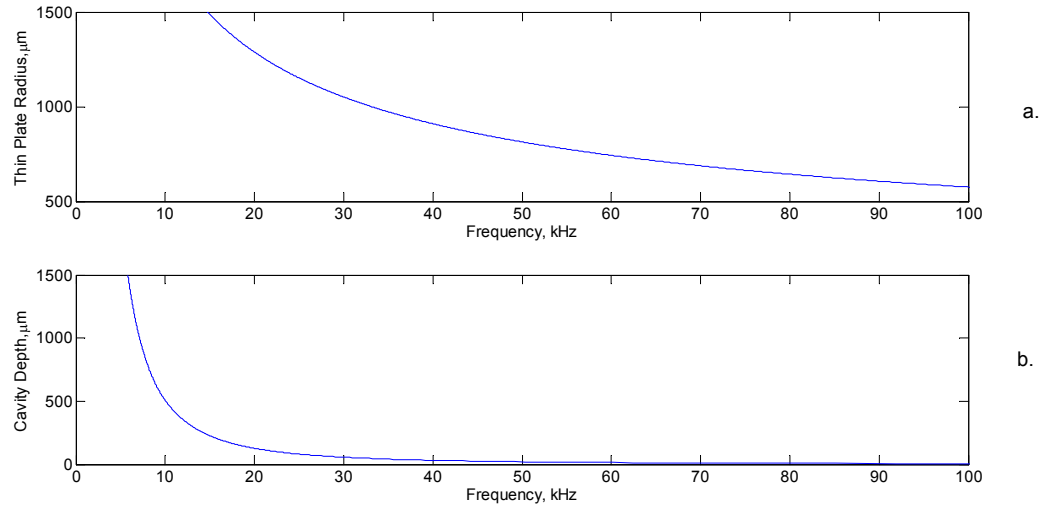

Figure 3.6: Plot of Parameter Sweep with 50 μm Thickness Kapton for: a. Thin Plate Radius as Function of Frequency and b. Cavity Depth as a Function of Frequency

Next is to identify the matching pipe dimensions. As have been mention in Chapter 2, the pipe radius needs to be as large as practically possible to reduce the squeeze film effect and the air gap resistance. In this case, assuming that a 10% reduction from the cavity radius of 1151 μm is selected, then the pipe radius will be 1036 μm. At 10% level, the edge-to-edge distance between the radius of the cavity and the radius of the pipe is 115 μm. This distance should be practical enough to ensure that there is a distinct difference in geometry between the cavity and the pipe when the parts are manufactured later. Rearranging Equation 3.10 will give Equation 3.14.

$$L_a = \frac{nc}{2f_n} - 0.6r_p \qquad \textbf{Equation 3.14}$$

where n is the number of harmonics for the pipe, which is 1 for fundamental frequency, c is the speed of sound in air at 20°C which is 343 ms^{-1}, f_n is the fundamental frequency which is 25 kHz and r_p is the radius of the pipe which is at 1036 μm.

Substituting the above value results in L_a = 6278 μm. With this, all the required dimensions for a pipe only and a matching thin plate, cavity and pipe design have been identified.

Although from the design stand point, the resonant frequency of all the FLAUT components: thin plate, cavity and pipe are now matched at 2 decimal places accuracy as shown in Table 3.1; it is important that the tolerances are still maintained during prototyping and manufacturing. Changes in any of the dimensions will change the individual component resonant frequency; thus reducing the effectiveness of the FLAUT amplification.

Table 3.1: Table of FLAUT Design Dimensions and the Expected Resonance Frequency

Design Parameters	Plate Resonance, kHz	Cavity Resonance, kHz	Pipe Resonance, kHz
Membrane thickness = 50 μm Plate radius = 1151 μm Cavity depth = 81 μm Pipe Radius = 1036 μm Pipe Length = 6278 μm	25.00	25.00	25.00

The output above only illustrates the main concept in designing the FLAUT, further analysis and design choices are required. A consideration towards a manufacturing process would also need to be included. As such, with the design parameter above, assuming that the resolution afforded by manufacturing is only at 10 μm, then the resonant of the individual geometry is at 25.03 kHz, 25.15 kHz and 25.00 kHz for thin plate, cavity and pipe resonant frequency respectively. With the 0.6% difference in resonant frequency of the three components, the FLAUT device should still operate within the expected given tolerance. (Further manufacturing tolerance and consideration will be given in the coming Chapters).

In another example, assuming that the goal of the design process is to improve the sensitivity, the thin plate thickness should be reduced to 8 μm. Then, using the same iterative method as above, it is found that 8 μm thicknesses thin plate may not feasible to build since the thin plate radius is smaller when compared to the cavity depth, as shown in Figure 3.7. A detailed analysis on the FLAUT transducer design will be given later.

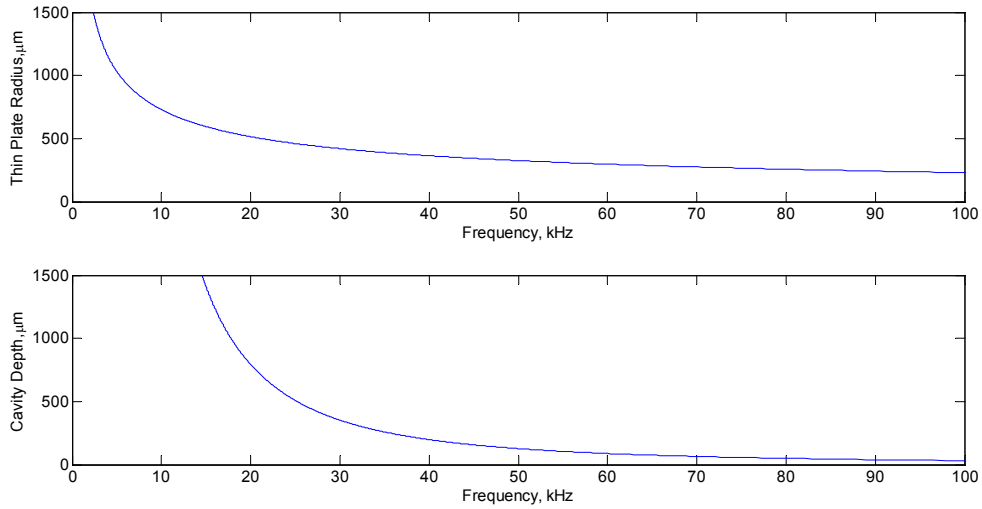

Figure 3.7: Plot of Parameter Sweep with 8 μm Thickness Kapton for: a. Thin Plate Radius as a Function of Frequency and b. Cavity Depth as a Function of Frequency

In addition to analysing the FLAUT geometry by matching the thin plate, cavity and pipe design, the FLAUT cavity and pipe could also be considered as a Helmholtz resonator, which consists of a rigid-walled cavity volume of V, with pipe area of S and pipe length of L. In the case of FLAUT, the resonant frequency of the Helmholtz resonator depends on the speed of sound, and the dimensions of the cavity and pipe with the following equations [62]:

$$f_n = \frac{c}{2\pi}\sqrt{\frac{S}{L_a V}} \qquad \textbf{Equation 3.15}$$

where c is the speed of sound in air = 343 ms^{-1}, S is the pipe cross sectional area, L_a is the length of pipe and V is the cavity volume.

Rearranging Equation 3.15, and substituting FLAUT geometry variables, would result in:

$$f_n = \frac{c}{2\pi}\sqrt{\frac{r_p^2}{L_a r_m^2 d_a}} \qquad \textbf{Equation 3.16}$$

where c is the speed of sound in air at 20°C which is 343 ms^{-1}, r_m is the radius of the cavity which equivalent to the radius of thin plate assuming that the thin plate is fixed at the edge of the cavity radius which is 1151 μm, d_a is the cavity depth which is 81μm, r_p is the pipe radius which is 1036 μm and L_a is the pipe length which is 6278 μm.

Substituting the above values results in FLAUT Helmholtz resonant frequency, f_n for the above geometry design to be equal to 69.3 kHz. This is far from the expected resonant frequency obtained through modelling using the mass-spring system and the measurements performed at around 25 kHz, an error of about 44.3 kHz is observed in comparison when Helmholtz model is utilised.

To evaluate the viability of the modelling further, a comparison plot utilising the analytical formula identified for FLAUT using the mass-spring model and Helmholtz model are shown in Figure 3.8 and Figure 3.9, for the different dimensional geometry of FLAUT. Both of the models (mass-spring and Helmholtz) assume that the pipe radius is reduced by 10% compared to the cavity radius. From Figure 3.8 and Figure 3.9, it could be observed that for a given mass-spring model in geometry as shown in Table 3.1 previously, the equivalent resonant frequency is at 69.3 kHz as discussed earlier. However, assuming that the same resonant frequency of 25 kHz is required for the Helmholtz model, then the geometry of the FLAUT needs to be adjusted as shown in Table 3.2.

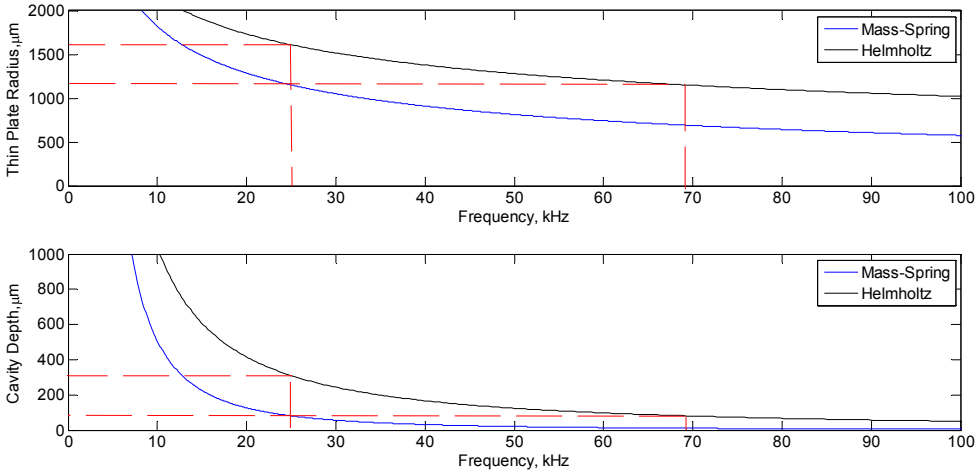

Figure 3.8: Plot of Parameter Sweep Utilising Helmholtz Resonator Formula: a. Thin Plate Radius as a Function of Frequency and b. Cavity Depth as a Function of Frequency

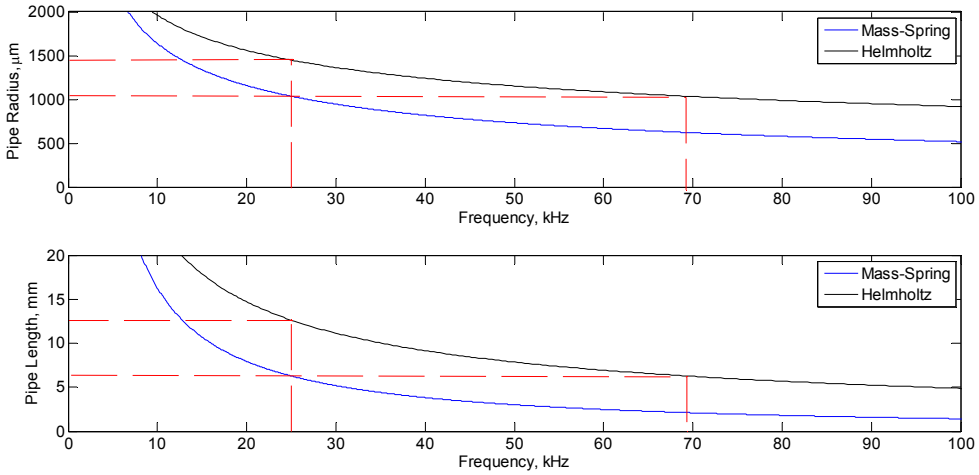

Figure 3.9: Plot of Parameter Sweep Utilising Helmholtz Resonator Formula: a. Pipe Radius as a Function of Frequency and b. Pipe Length as a Function of Frequency

Table 3.2: Table of FLAUT Design Dimensions Utilising Helmholtz Model for Resonant Frequency of 25 kHz

Design Parameters
Membrane thickness = 50 μm
Plate radius = 1609 μm
Cavity depth = 309 μm
Pipe Radius = 1448 μm
Pipe Length = 12610 μm

Furthermore, from the plots in Figure 3.8 and Figure 3.9, it could be observed that as the frequency increases, the divergence between the mass-spring model and the Helmholtz models increases. To investigate the level of divergence, a plot of Helmholtz resonant frequency as a function of mass-spring resonant frequency for different pipe radius to cavity radius ratio has been performed and is shown in Figure 3.10. Comparing the two plots in Figure 3.8 and Figure 3.9, it could be observed that as the frequency increases for the mass-spring model, the Helmholtz resonance frequency increases in a power function.

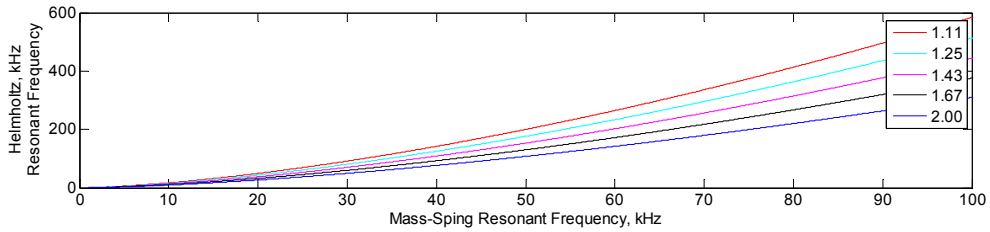

Figure 3.10: Plot of Different in Resonant Frequency between Mass-Spring Formulation and Helmholtz Formulation in FLAUT for Different Cavity Radius to Pipe Radius Ratio

However, as will be shown in the measurements later throughout the thesis, there is no direct relationship that could be applied to specify the cavity radius to pipe radius ratio, except to have them to be as large as practically possible. As illustrated in Figure 3.10, a similar trend across the different cavity radius to pipe radius ratio is observed for the Helmholtz model as a function of mass-spring model. This may be

due to the characteristics of the FLAUT, of which each component is a resonant component. As such, every component requires a specific geometry that has already been pre-determined by the operating resonant frequency. Even in the case of a pipe, the ratio of pipe diameter to pipe length has been appropriately determined by the resonant frequency.

3.2 Alternate Analytical Modelling Approaches

Before we proceed into the next chapter, it is important to note that there are also other techniques that could be utilised to perform the above analysis such as the Mason's Equivalent circuit. This technique has been utilised to analyse and model different types of electrostatic transducer devices such as silicon microphones [23], electrostatic transducers with v-grooves backplate [66], electrostatic transducer with cavity backplate [17] and CMUT [36, 83]. In this technique, the mechanical equivalent of the electrostatic transducer is converted to electrical equivalent circuit of inductance, L, capacitance, C and resistance, R to enable the analysis to be performed in the electrical domain.

In addition to Mason's equivalent circuit, Walker *et al* [101] also proposed an analytical model that could be utilised to analyse the electrostatic transducer incorporating the pipe microstructure. In the proposal by Walker *et al* [101], the 3-dimensional CMUT model by Caronti *et al* [102] has been adapted to model the effect of pipe within the single cavity microstructure. A good agreement in term of output pressure is observed, despite the model assumption that the membrane is behaving in a in a piston-like manner.

3.3 Modelling Using Finite Element Analysis

Finite Element Analysis (FEA) was first developed by R. Courant in 1943 to obtain approximate solutions to vibration systems problems. Due to the expense of the required computational hardware, initial implementations of FEA were limited to a select number of industries. Contemporary FEA is possible using desktop or cloud computing and as such it has become an integral part of engineering design.

The analytical model is fast and efficient in creating an initial design for a given thin plate, cavity and pipe combination. However, it still lacks the ability to identify any frequency shifts that may occur when the three different components are combined. As such, FEA offers the ability to model fully, virtually any geometry with its related influences. It is the intention of this Chapter to study a specific process, of which a FLAUT is designed and developed by means of analytical model, compared with FEA and finally in the next Chapter verified by experimental measurement in the form of surface displacement profiles. Although within a particular design, there will be both piston or fundamental mode and other higher order modes; the particular focus of this thesis will be in the fundamental mode only.

One of the main construct in FEA is to replicate physical processes from a real world into a virtual world. This could be performed in either a simplified or an elaborated fashion; which depends on the complexity and computational cost allowed to translate the real world into the FEA models. FEA could only represent the real world, if the conversion processes have been performed effectively. Thus, FEA requires that certain verification processes are performed to validate the effectiveness of the model. In general, if a simplified model such as a 1D/2D model is able to be validated with sufficient accuracy, then a more elaborate model is typically not required. However, if such a simplified model is unable to achieve such a requirement then a more elaborate model that may consist of full 3D FEA model may be needed.

Basically, FEA requires that the virtual model to be divided into a collection of sufficiently small (finite) elements for an analysis to be performed. Once the model has been discretised, each element will have its own sets of equations governing the behaviour of the element. This is to ensure that the charge, displacement, pressure, stress, strain etc are continuous across the element boundaries and that all the boundary conditions are satisfied.

A sufficiently small element size with respect to the model is needed for the model to accurately represent the real world. As the number of elements within a model increases, the overall solution accuracy of the model representing the real world will increase. Within the ultrasonic community, a minimum of 15 elements per wavelength is typically recommended as the starting point for Finite Element (FE) modelling.

In maintaining FEA as a viable analysis tool that incorporates accuracy and speed of analysis, it is important that appropriate analysis is performed, and the models are defined with the correct assumptions, which include:

- Identifying the appropriate boundary condition.
- Utilising the appropriate material properties.
- Identifying the limitation of the model.

In FEA an input variable such as force is usually inserted at the boundary of the model. This external input variable or external degree of freedom (DOF) constraint is placed on the model to simulate the conditions outside of the model, and is known as a boundary condition. For FLAUT, these can take the form of a pressure to simulate the fluid boundary or a voltage boundary condition to simulate the electrodes that gives the electrostatic effect and displacement to simulate the thin plate movement.

Although, it is possible to build a full model of the real world in FEA, it is normally not practical especially when computational requirement and solution time are considered. However, since most real world problems will have some form of identical boundary condition in symmetry, the total building block of the model

could be reduced. A cube for instance, could be modelled with one-eighth symmetry, while a cylinder could be modelled with an axial symmetry as shown in Figure 3.11. The planes of which the boundary conditions are symmetry to the other are known as the symmetrical boundary, and are shown in light grey in Figure 3.11 (Top). In this instance, the one-eighth smaller white cube within the larger dark grey cube is known as the unit cell, which is a multiple of the complete model. In contrast, in the 2D axial symmetrical model, the symmetry has been applied using a polar coordinate system as shown in Figure 3.11 (Bottom).

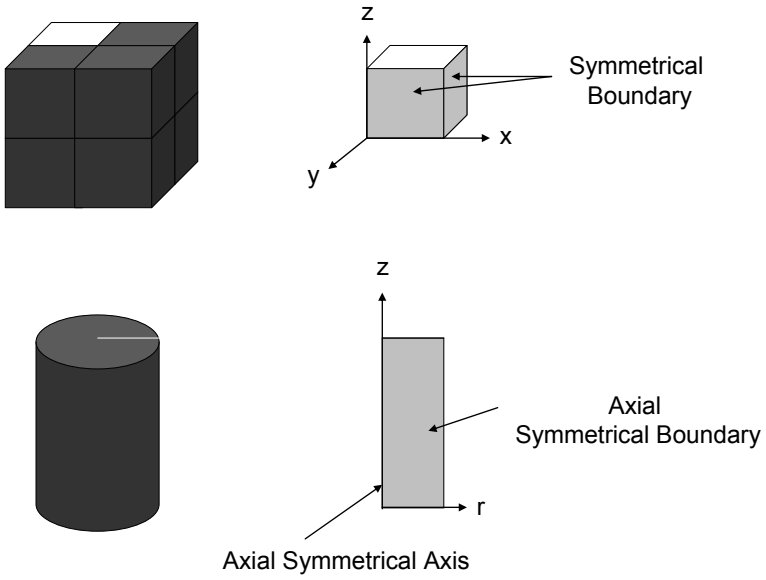

Figure 3.11: Schematic Diagram of Symmetrical Boundary Condition: Cube (Top) and Cylinder (Bottom)

There are drawbacks in symmetrical boundaries. As the model geometry and structure is reduced in size and its complexity, certain aspects of its behaviour will be lost. However, due to the nature of the FLAUT geometry, the use of axi-symmetrical boundary condition during the FLAUT FEA modelling is opted. Axi-symmetrical boundary condition is able to reduce the complexity of the FLAUT model thus reducing the computational time, while at the same time still retaining the required fundamental mode behaviour - critical for FLAUT simulation.

Once the choice of symmetrical boundary is determined, various types of analysis could be performed using FEA. The summary of the analysis that could be performed is shown in Table 3.3. In the context of FLAUT two types of analysis will be performed which are the static analysis to model a biased thin plate and the harmonic analysis to determine the resonant frequency.

Table 3.3: Table of FEA Analysis Types and Its Purpose

Analysis Type	Purpose
Static	To calculate the steady state behaviour of a system when a constant load is applied. In modelling FLAUT, this analysis is useful to determine the level of displacement due to an applied bias voltage.
Modal	To determine the resonant frequencies and its mode shape within the elastic structure. In modelling FLAUT, this analysis is useful to determine the fundamental resonant frequency and to visualise the mode shape within the model.
Harmonic	To determine the frequency response of the structure in steady state. In harmonic analysis, a sinusoidal load of known amplitude and frequency is applied to the structure. Components such as pressure, displacement, voltage, charge can be solved in an iterative approach by sweeping the sinusoidal load across a range of frequencies. In modelling FLAUT, this analysis is used to determine the frequency response of the FLAUT and to extract the mode shape at the frequency of interest.
Transient	To determine the dynamic response of a structure subject to a time dependent load, in much the same way that harmonic analysis is in a frequency dependent load. In modelling FLAUT, this analysis is used to determine the dynamic response of a FLAUT. An impulse load or excitation is usually applied to the structure.

Next, the output from FEA could be processed either internally by using the FEA post-processing software or externally by performing a data export. This data could then be manipulated by other software such as Matlab, Excel etc. For an ultrasonic

transducer model, there are two main types of information that are extracted during the post processing which are:

- The frequency response and dynamic response for different key variables such as surface displacement and acoustic pressure output.
- The mode shape of the model with its magnitude and phase.

Previously, the basic concept of FEA has been introduced in brief. However, there are various software packages that could be utilised to perform the FEA simulation. Several authors have utilised different software packages to simulate the electrostatic transducer using software such as Ansys [103, 104], PZFlex [74, 99], LS-Dyna [105] and Comsol Multiphysics [106, 107]. In the case of FLAUT, Comsol Multiphysics was chosen due to the requirement of interacting different physics such as electrical, mechanical, acoustics and fluid dynamics within the electrostatic FEA modelling domain. Moreover, Comsol Multiphysics is much more flexible generally in the finite elements interaction between different physical modelling phenomenon. PZFlex is also chosen as a comparable software package mainly due to the fact that PZFlex is a well know software package and was originally designed for piezoelectric devices and wave propagation simulations [108]. Although, the inclusion of an electrostatic module within PZFlex is reasonably new, the experience PZFlex has in acoustics would render the software package to be a valuable asset as a comparison. In addition, a comparison between PZFlex - a time domain solver and Comsol Multiphysics - a frequency domain solver could also be made with the strengths and weaknesses of each discussed.

3.3.1.1.1 Dynamic Frequency Response and Mode Shapes

Although there are many parameters that could be extracted from the FEA during post processing, only a few key characteristics pertaining to the design of the FLAUT will be of interest. These include the change in surface displacement and acoustic pressure output with respect to frequency and time. These characteristics are useful due to the fact that they could be compared with some form of measurement

technique that will be shown in the next Chapter. The frequency response modelled in Comsol Multiphysics Ver. 3.5a based on the geometrical design configuration identified in Table 3.1 is illustrated in Figure 3.12.

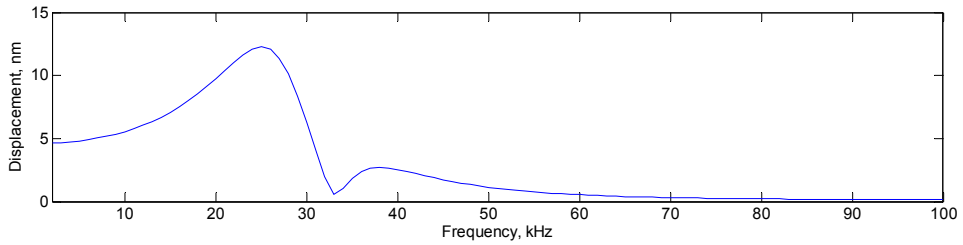

Figure 3.12: Plot of Simulated Frequency Response of Diaphragm Displacement for a FLAUT

One of the weaknesses of frequency response and dynamic response plot above is the inability of the plot to illustrate the shape of the diaphragm displacement. As shown in Figure 3.12 there are two peaks corresponding to the resonant frequencies of the modelled device. However, the behaviour of the diaphragm displacement at these two peaks is unknown. From further investigation into the diaphragm displacement mode shape, it has been identified that the 25 kHz peak is behaving in a fundamental mode as shown in Figure 3.13. In Figure 3.13, the axi-symmetry boundary conditions is utilised to reduce computational expense. From the magnitude and phase plot, it could be observed that the deformed diaphragm is displacing in the z-direction for the whole diaphragm surface. This illustrates that the current vibration mode is the fundamental mode. In addition, the phase information indicates that this particular mode of the membrane is piston like - exhibiting uniform phase. In Figure 3.13, the diaphragm radius could be determined by the x-axis, while the diaphragm thickness could be determined by the z-axis. The level of deflection for the diaphragm could be determined from the colour map correlating the location of the deflection and the colour map value.

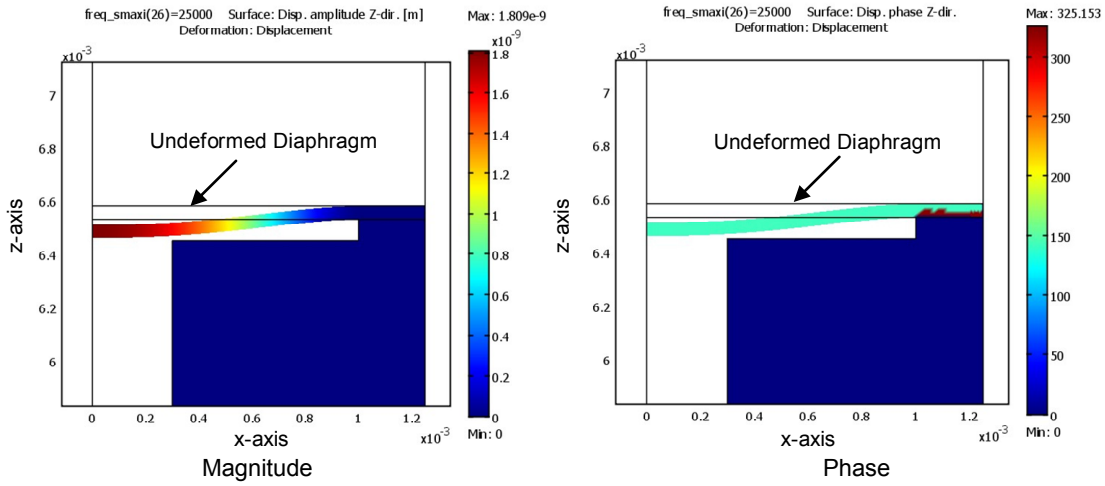

Figure 3.13: Plot of Simulated Mode Shape Magnitude and Phase Diagram for a FLAUT Operating at 25 kHz

In this Thesis, only the fundamental mode is considered in all the modelling and simulations. This is mainly because the fundamental mode produces the highest level of vibrational output when compared to the rest of the higher order modes. Furthermore, the fundamental mode is also easier to model both in term of vibrational analysis and acoustic field [88] as will be shown in section 3.5.1 and section 6.2.3 respectively. However, it is still necessary to understand the other higher modes of vibration. Thus, in the next section the different modes of vibration will be discussed along with a FEA simulation to illustrate the magnitude and phase characteristics for different vibrational modes in a diaphragm.

3.4 Review and Simulation of Different Diaphragm Vibrational Modes

In many applications of ultrasound, it is highly desirable for the transducer to exhibit planar piston type vibration with a uniform phase response across the surface. The surface deformation of the front-face of a transducer, in particular the magnitude and phase characteristics of the surface deformation, at a particular frequency will govern

the beam characteristics of the device. In the FLAUT, the thin plate interfaces with the load medium and as such, it is the thin plate that should exhibit this type of vibrational behaviour, which is critical.

From Timoshenko [109], the circular diaphragm modes of vibration will correspond to either a single type of vibration (nodal circle or nodal line); or a combination of the two types of vibrations. A nodal circle is a vibration at which the displacement is zero during vibration at the perimeter of the circle, while a nodal line is a vibration at which the displacement is zero during vibration at the cross section of the diaphragm as illustrated in Figure 3.14. For example, the mode (0,1) generally known as fundamental mode does not have any nodal lines (0,) and only has 1 nodal circle (,1). In addition, Figure 3.14 also illustrates that there could either be nodal circle modes (0, 1…2…3…n) only or nodal line modes (1…2…3…n, 1) only or a combination of both nodal circle and nodal lines for a particular vibrational mode.

In order to understand the difference observed in Figure 3.14, a sample of different modes of vibration is explained. For example in mode (0,1) also known as fundamental or piston mode, the diaphragm only moves in up and down in which the nodal circle line is at the circumference of the diaphragm. Alternatively, in mode (0,2) a higher order mode, the nodal circle lines are at two location which are at the circumference of the diaphragm as well as inside the diaphragm. Due to this, the mode (0,2) has a Mexican hat shape with high displacement in the centre, while no displacement at the nodal circle lines. Appropriately, in mode (1,1), there is only 1 nodal circle in the circumference of the diaphragm with 1 nodal line across the diaphragm. In this case the displacement of the diaphragm behaves in such a way that 180^{o} phase shift occurs between each half of the membrane. Lastly, mode (1,2) is a combination of mode (1,1) and mode (0,2). This could be observed from the deformation of mode (1,2) in Figure 3.14, whereby there is 1 nodal line across the diaphragm and 2 nodal circles (inner and outer circles). In this case rather than the Mexican hat having a single pointed dome shape, one-half of the inner circular diaphragm has been shifted into 180^{o} out of phase to the other half. In addition, one-

half of the outer circular diaphragm has been shifted into 180^{o} out of phase to the inner circular diaphragm.

As observed in Figure 3.14, other than the mode (0,1) or fundamental mode of vibration, the diaphragm behaves in complex vibrational modes. This complex mode causes a complex surface deformation of the diaphragm, thus giving irregular pressure output and unpredictable wave propagation due to various node and anti-node vibrations within the same plane. Thus, it is highly desirable to have the transducer to operate in a fundamental mode because the mode (0,1) has the highest maximum output due to uniform phase response across the membrane. The fundamental mode is also highly predictable in term of acoustic field generated when compared to the rest of the higher order modes of vibrations.

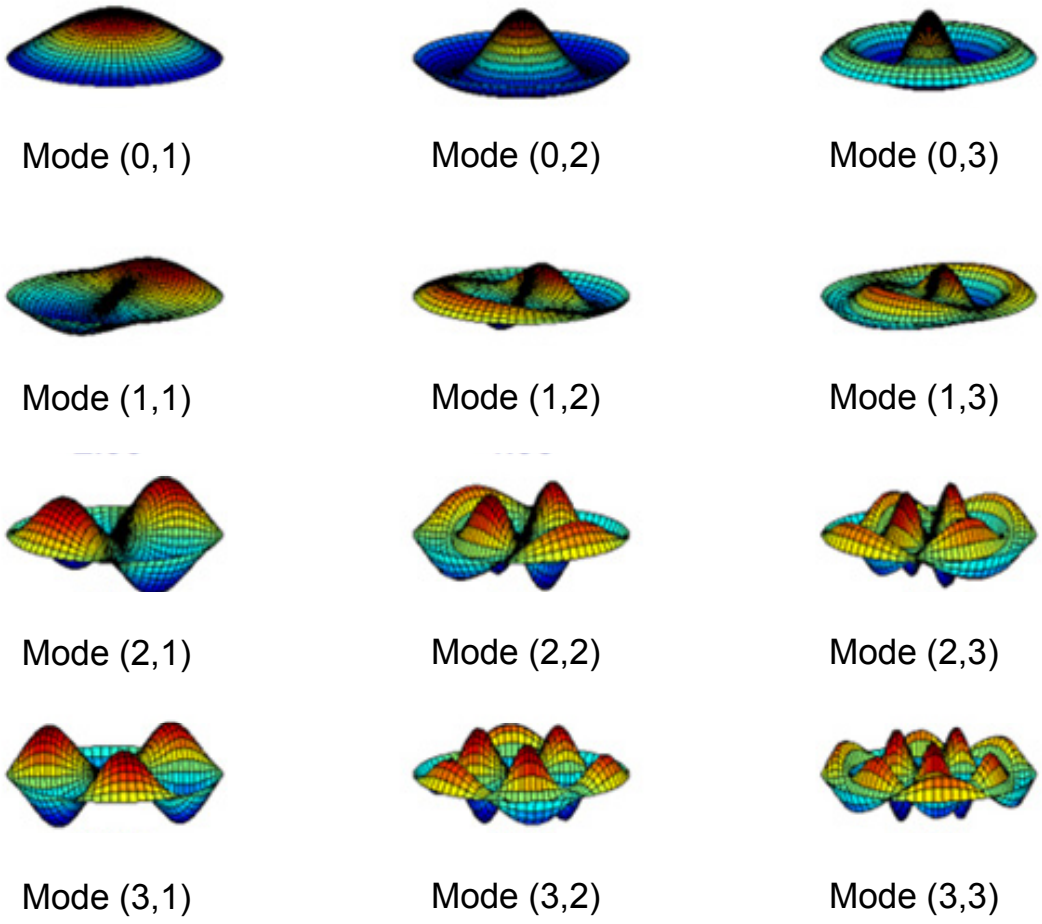

Figure 3.14: Plot of Several Modes of Vibration of a Circular Diaphragm [110]

3.4.1 Modelling and Simulation of a Diaphragm Vibrational Modes

In order to illustrate the different vibrational modes of an assumed fully clamped diaphragm, the Comsol finite element package has been employed to simulate the different mode shapes. Kapton was employed as the membrane, the parameters of the diaphragm are detailed in Table 3.4 and the simulated membrane displacement as a function of frequency is shown in Figure 3.15.

Table 3.4: Table of Modelling Parameters for Diaphragm Simulation Using Comsol

Details	Values
Diaphragm Diameter	1000 µm
Diaphragm Thickness	8 µm
Input Force/Area	1 Nm^{-2}
Young's Modulus [100]	2.5 x 10^9 Pa
Poisson's Ratio [100]	0.34
Density [100]	1420 kgm^{-3}

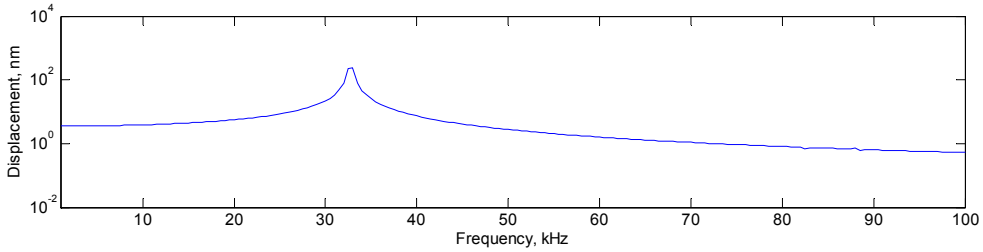

Figure 3.15: Plot of Frequency Response for a Single Membrane Displacement Fixed at Its Edges

It is clear from Figure 3.15, that the diaphragm configuration in the model has a dominant mode at 32.5 kHz and other modes at around 82.5 kHz and 88 kHz. In order to identify what are the modes of vibration, a plot of the vibrational mode at frequency of 32.5 kHz could be seen in Figure 3.16, with the left plot showing the displacement normal to the membrane surface, while the right shows the mode shape

of the membrane in orthogonal view. The scale for the left plot has been normalised in a way to compare the displacement of the whole frequency spectrum from 1 kHz to 100 kHz, while the scale for the right plot has been normalised to a single plot to enable the shape mode to be plotted. It could be observed that the mode shape of the diaphragm is first order or fundamental mode (0,1) as depicted by Figure 3.14.

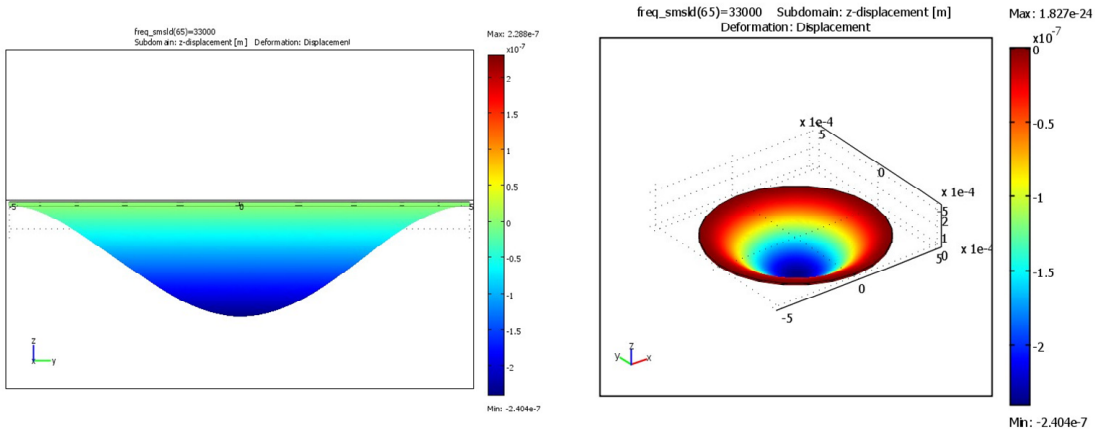

33 kHz – Mode (0,1)

Figure 3.16: Plot of Diaphragm Vibrational Mode at Fundamental Frequency

In order to evaluate the changes and effects attributed by the higher order modes in a circular diaphragm, it is important to understand that the change in the vibrational mode from mode (0,1) to the next mode (1,1) is not an abrupt change, but rather a gradual change in the diaphragm vibration mode as shown in Figure 3.17. Even after the fundamental frequency, the vibrational mode (0,1) could still be observed until 80 kHz but to a very low degree of amplitude as shown by the left side of the Figure 3.17 (a). This mode (0,1) will gradually change into the shape of mode (1,1) as the frequency increases. As the frequency increases to 82.5 kHz as shown in Figure 3.17 (b), the vibrational mode (1,1) could be clearly observed. However, it is important to note here that from 82.5 kHz onwards a scale of 10,000 has been utilised for the right side of Figure 3.17 (b) and Figure 3.17 (c) to enable a mode shape visualisation due to the low amplitude of displacement at these high range of frequencies. It is interesting to notice that the nodal line mode also incorporates a complementary of mode (1,1) which is rotated by 180^{o}, as depicted at a frequency of

88 kHz as shown in Figure 3.17 (c). In general cases, this will be signed as mode (1,1)+ and mode (1,1)- respectively, to indicate the different orientation. As an important note, comparing all the modes of vibration, it could be clearly illustrated that the mode (0,1) or fundamental mode vibration has the highest amplitude when compared with the rest of the higher order modes. This re-iterates why the focus of the thesis is on the fundamental mode of vibration only.

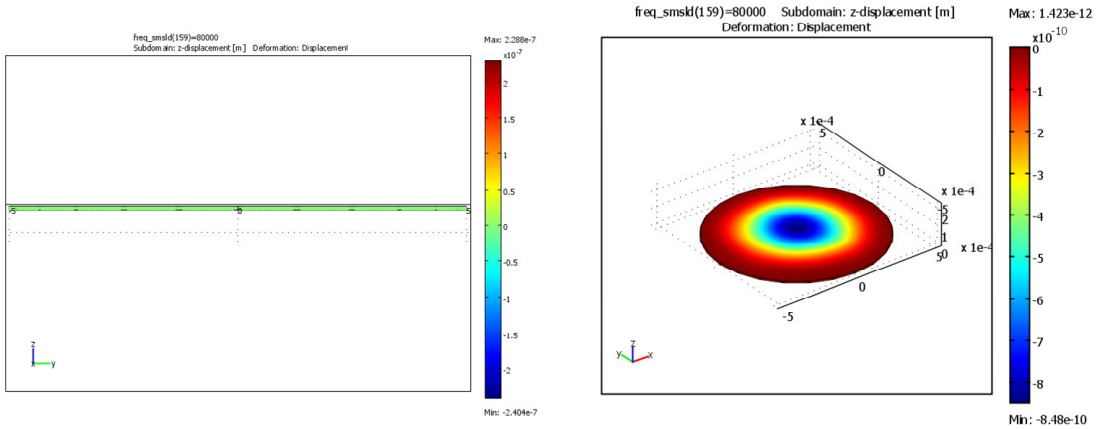

a) 80 kHz

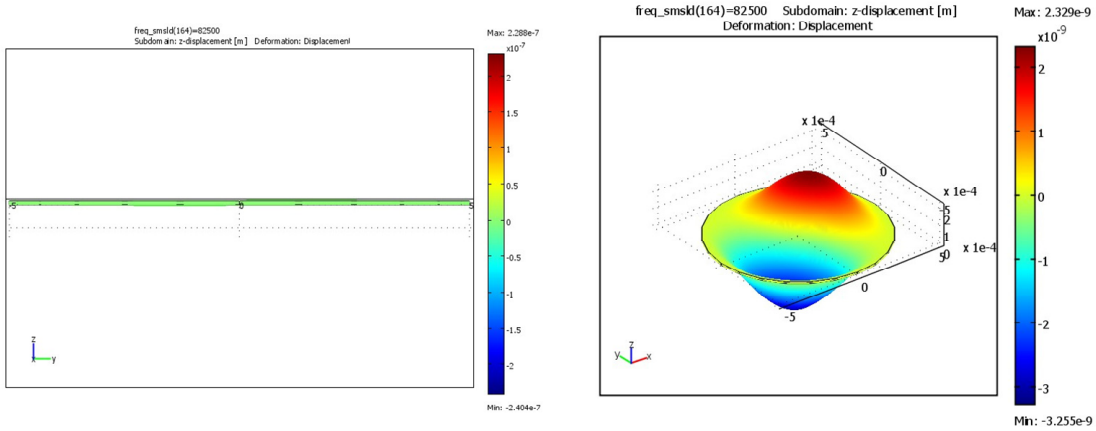

b) 82.5 kHz – Mode (1,1)+

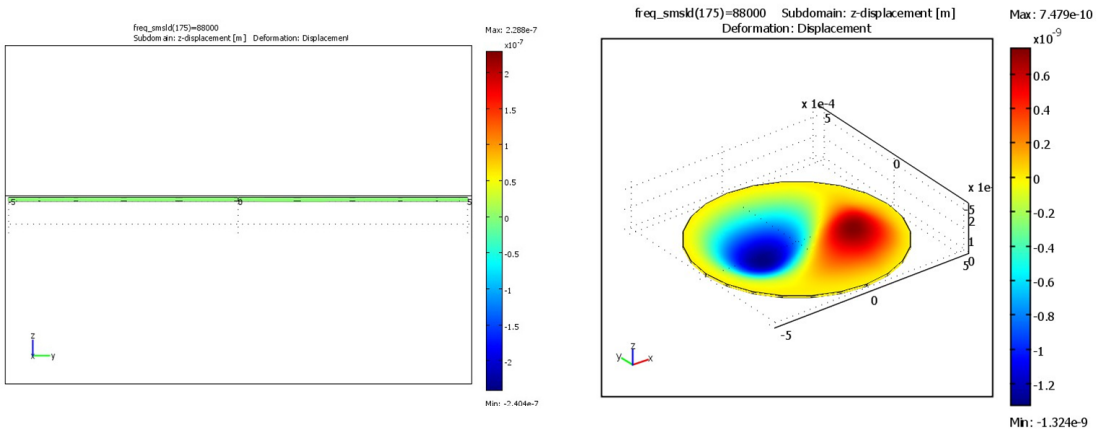

c) 88 kHz – Mode (1,1)-

Figure 3.17: Plot of Diaphragm Vibrational Mode Gradual Change from a) Vibrational Mode (0,1) at 80 kHz to b) Vibrational Mode (1,1)+ at 82.5 kHz to c) Vibrational Mode (1,1) at 88 kHz

3.5 Review of Cavity / Pipe Design for Single Cell Transducer

One of the main contributions of this thesis is the development of a method to enable a FLAUT to be designed in a systematic approach. As such, it is important that the processes towards which the FLAUT is designed and later in the next Chapter verified are presented in detail. As this is a proof of concept study, the process of the design and simulation of a FLAUT will be described in order to exemplify the methodology. In this first instance, a device with a target resonance in the range 20 kHz to 40 kHz will be described. Whilst it could be argued that 20 to 40 kHz is slightly marginal to be considered within the ultrasonic range, the need to prove the viability of the FLAUT concept out-weights the need for a higher operating frequency in the current context.

In order to design a FLAUT transducer, there are four factors that need to be considered: the target frequency range, the thin plate material, the thin plate thickness and the backplate microstructure required to provide the fluidic amplification. A FLAUT schematic is shown in Figure 3.18. Although, it is also the

intention of the author to investigate the influence of neighbouring cavity or cavity/pipe within an array, the investigation is reserved for Chapter 6, once the influence and effect of a single cavity and cavity/pipe system are fully characterised.

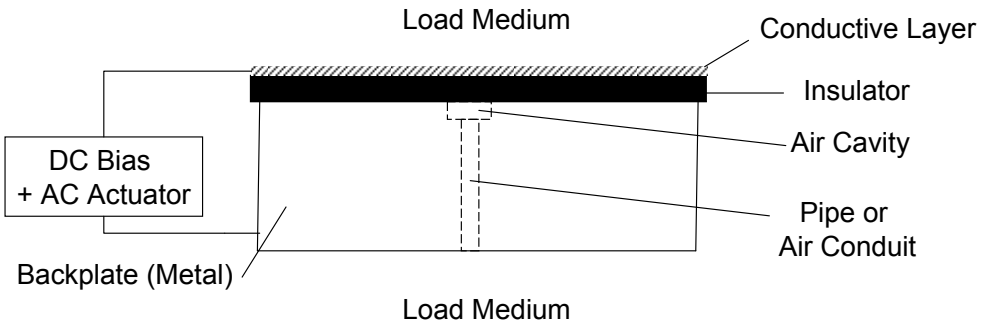

Figure 3.18: Schematic Diagram of FLAUT with Single Cavity and Pipe Designed Backplate

3.5.1 Analytical Analysis for Developing Single Cell Transducer

Based on the previous discussion, it could be identified that the proposed FLAUT transducer has the following main characteristics:

- Operating frequency range of between 20 kHz and 40 kHz.
- Single unit cell.
- Kapton film on top of the single cell cavity backplate

The analytical model has been previously described; Equation 3.4 has been used to calculate the thin plate resonant frequency as a function of thin plate diameter or cavity diameter for a range of thin plate thickness; as shown in Figure 3.19. From the plot in Figure 3.19, it could be observed that as the resonant frequency of the thin plate is increased, the required thin plate diameter required to match the resonant frequency reduces in an inverse square root power function. At the same time for a given thin plate resonant frequency, it could be observed that as the thin plate thickness reduces, the required thin plate diameter also reduces proportionally. A similar dataset for cavity resonant frequency can be calculated using Equation 3.6, these data are plotted in Figure 3.20. A similar trend could be observed, as the cavity

resonant frequency increases, the required cavity depth reduces in an inverse squared power function. However, in contrast to the diaphragm diameter, at a particular resonant frequency, as the diaphragm thickness increases, the required cavity depth reduces.

As a summary, from both Figure 3.19 and Figure 3.20, it could be determined that the smaller the cavity diameter and the cavity depth the higher the resonant frequencies. In addition, it is also observed that as the thin plate thickness increases, the cavity diameter needed for a matched thin plate and cavity resonance also increases, while the required cavity depth reduces to maintain the needed matched resonant frequency. This creates a challenge during the manufacturing process, since it is very difficult to fabricate a cylindrical geometry, which has a very low aspect ratio i.e. large cavity diameter but very shallow in depth; or very high aspect ratio i.e. a small cavity diameter but deep in depth. Thus, the 3D-resolution, capability and repeatability of the equipment proposed for manufacture of the FLAUT needs to be identified and considered during the design consideration stage. (A full discussion on different capability of the proposed equipment and the applicable aspect ratio will be given in the next Chapter).

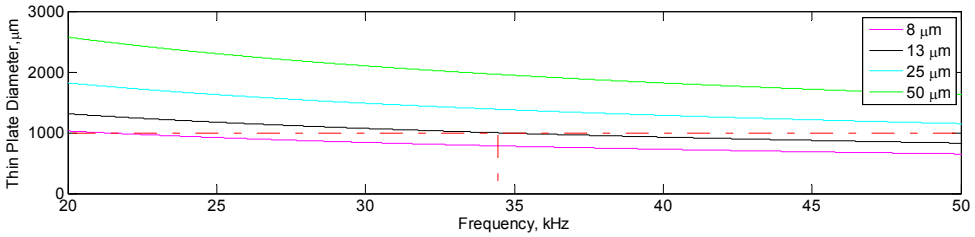

Figure 3.19: Plot of Thin Plate Diameter as a Function of Resonant Frequency for a Range of Thin Plate Thickness

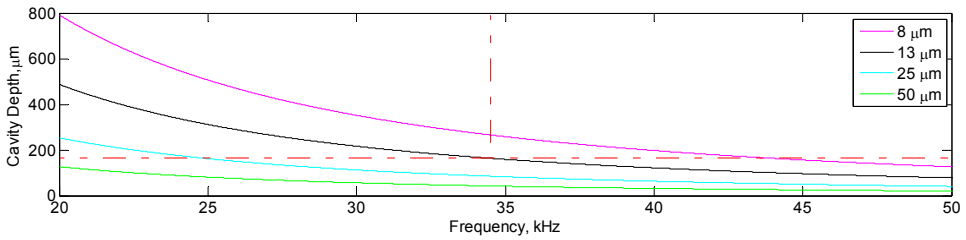

Figure 3.20: Plot of Cavity Depth as a Function of Frequency for a Range of Thin Plate Thickness

Some compromise will be inevitable and will be governed by the selected manufacturing method. Although there are various methods, that could be utilised to manufacture the FLAUT with variable sizes, as a proof of concept design, there is a need to be practical enough that the conventional drilling method could be utilised. However, if a more suitable method could be adapted, then it is possible as such to change the technique of manufacture to suit the current FLAUT design. A full review of different manufacturing techniques and processes will be discussed in the next Chapter. Thus, assuming in the first pass a conventional drilling technique is utilised, then using the commercially available standard slot drill sizes of 1 mm, 1.5 mm and 2 mm, it was found that the most suitable thin plate thickness for the current investigation is 13 μm; considering the cavity depth needed to match. Although 8 μm could be considered based on the current design, 13 μm seems to be a more suitable choice based on the thin plate diameter to thickness ratio and cavity diameter to depth ratio. Thus, from Figure 3.19, it is observed that the suitable cavity diameter is 500 μm at a resonant frequency of 34.5 kHz as denoted by the cross section of the red dash, while the matching cavity depth is 164 μm as shown in Figure 3.20 by the vertical and horizontal red dash.

The next step is to identify the suitable pipe diameter. However, since there are no extensive investigations that have been performed with regards to the effect of cavity diameter to pipe diameter aspect ratio; the choice was to use some of the standard available drill sizes: 300 μm, 600 μm and 900 μm. This corresponds to an aspect ratio of cavity diameter to pipe diameter of 3.33, 1.67 and 1.11 respectively. The relationship between the pipe length and the pipe radius could be observed in Figure 3.21. From the Figure 3.21, it could be observed that the pipe length reduces in approximately an inverse power function with respect to pipe resonant frequency. In addition, as illustrated by Figure 3.21, there is a small increase in pipe length of about 1% when the ratio of cavity diameter to pipe diameter is increased from 1.11 to 3.33. To ensure that the geometry of the pipe cross-section could be maintained as per design tolerance required during fabrication, it is the opinion of the author that a 600 μm pipe diameter is used to illustrate the FLAUT design and verification process.

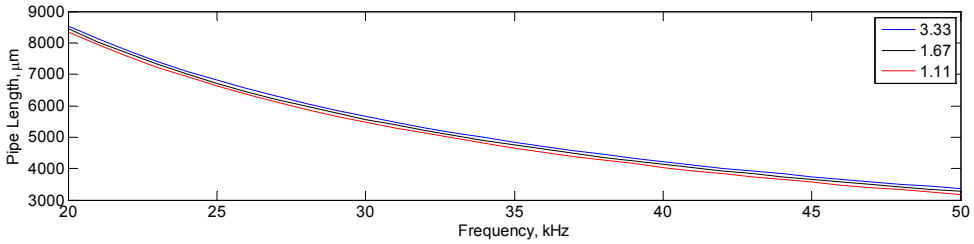

Figure 3.21: Plot of Pipe Length as a Function of Frequency for a Range of Cavity Diameter to Pipe Diameter Ratio

Based on the previous discussions, it could summarised that the following design would be used to develop the FLAUT transducers and is shown in Table 3.5.

Table 3.5: Table of FLAUT Design Dimensions and the Expected Resonance Frequency

Design Parameters	Plate Resonance, kHz	Cavity Resonance, kHz	Pipe Resonance, kHz
Thin Plate Thickness = 13 µm Thin Plate Diameter = 1000 µm Cavity Depth = 164 µm Pipe Diameter = 600 µm Pipe Length = 4827 µm	34.5	34.5	34.5

Once the matching geometry has been identified, it is important that the geometry goes through a rigorous simulation process before a prototype is produced. As described earlier, the analytical model provides a "first-cut" design, more detailed information, particularly analysis on the membrane surface deformation, can be gained from the FE models.

3.5.2 Finite Element Analysis Techniques for Geometric Analysis

Geometric analysis is performed to identify the individual resonant frequency of each component within the FLAUT as well as a single system. This analysis is performed mainly to verify the analytical model analysis in term of individual components as well as to identify any possible frequency shift that may occur once the three individual geometries are coupled.

Utilising the technique discussed in the previous Chapter, a simulation using FEA for each individual component the thin plate, the cavity, the pipe and the combined cavity and pipe have been performed. In order to complete a component analysis using FEA, the individual components that make up the FLAUT have been separated into three distinct geometries, which are the thin plate, the cavity and the pipe.

FEA simulation of the thin plate has been performed in 2D axi-symmetric with an input load of 1 Nm^{-2} in the negative z-direction. The thin plate boundary for z-direction for both surfaces is set to be free; while the edge of the thin plate at x-direction of 500 μm is set to be fixed. A predefined normal triangular mesh size has been utilised for the simulation. The material properties for the FE modelled in this thesis are as shown in Table 3.6.

Table 3.6: Material Properties for FEA Simulation

Material	Details	Values
Kapton [100]	Young's Modulus	2.5 x 10^9 Pa
	Poisson's Ratio	0.34
	Density	1420 kgm^{-3}
	Relative Permittivity	3.4
Air Temperature of 20^oC Atmospheric Pressure of 101.325 kPa [111]	Density	1.204 kgm^{-3}
	Relative Permittivity	1
	Speed of Sound	343

The z-direction vibrational velocity at the centre of the thin plate as a function of frequency has been simulated and is shown in Figure 3.22. From Figure 3.22, it could be observed that the resonant frequency of the thin plate is at 34.5 kHz. In order, visualise the mode shape of the thin plate at 34.5 kHz; a deformed domain plot at 34.5 kHz has been calculated during post processing. The deformed domain plots are usually utilised when a visualisation of the motion is required; as generally a static plot with different magnitude is displayed as standard. The result of the mode shape plot could be seen in Figure 3.23. As observed, the magnitude and phase of the thin plate shows that at 34.5 kHz the thin plate is vibrating at its fundamental mode (0,1); which corroborated with the analytical model. Furthermore, in Figure 3.23, the thin plate radius could be determined by the x-axis, while the thin plate thickness could be determined by the z-axis.

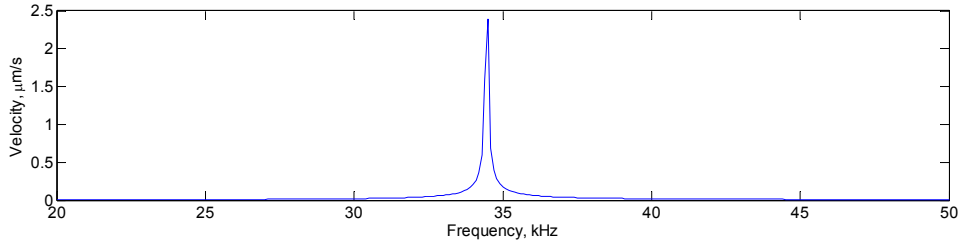

Figure 3.22: Plot of Thin Plate's Velocity at the Centre of the Thin Plate as a Function of Frequency

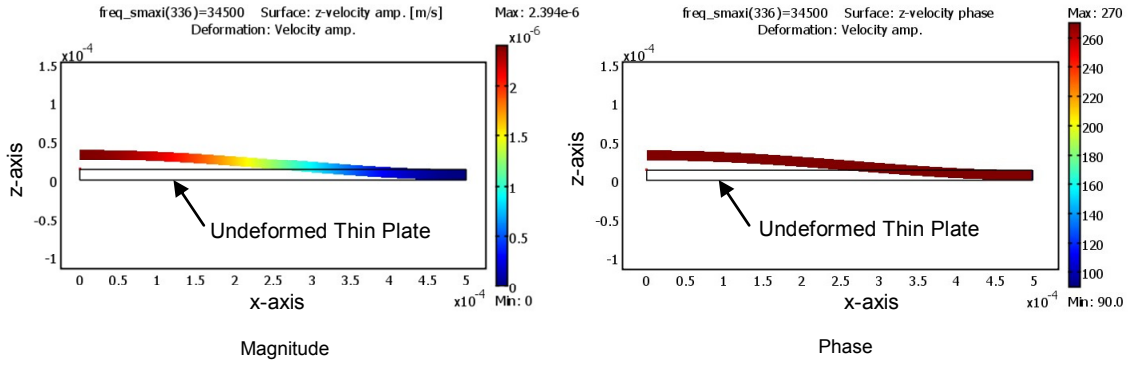

Figure 3.23: Plot of Mode Shape for Thin Plate at Resonant Frequency of 34.5 kHz

As before, the 2D axi-symmetry FEA model has been employed to identify the resonant frequency of the cavity. The Figure 3.24, shows the calculated cavity

frequency response at the centre of the cavity-thin plate interface when a cylindrical wave pressure input of 1 Pa is applied at the cavity-thin plate interface. The cylindrical wave is applied to the thin plate-cavity interface to simulate the pressure input afforded by the thin plate to the cavity. Except for the cavity-thin plate boundary input pressure and the axi-symmetrical axis boundary, the rest of the boundary condition is considered thick walled. A predefined normal triangular mesh size has been utilised. As illustrated by Figure 3.24, the fundamental resonance frequency of the cavity is around 32.5 kHz, which is about 4% difference to the analytical model. In addition to determine the vibrational mode for the resonant frequency of the cavity, a model that predicts the pressure variation inside the cavity is simulated and is shown in Figure 3.25. From the plot in Figure 3.25, it could be observed that the cavity behaves in a fundamental mode with the maximum pressure at the centre of the cavity. In Figure 3.25, the cavity radius could be determined by the x-axis, while the cavity depth could be determined by the length of the coloured spectrum in z-axis.

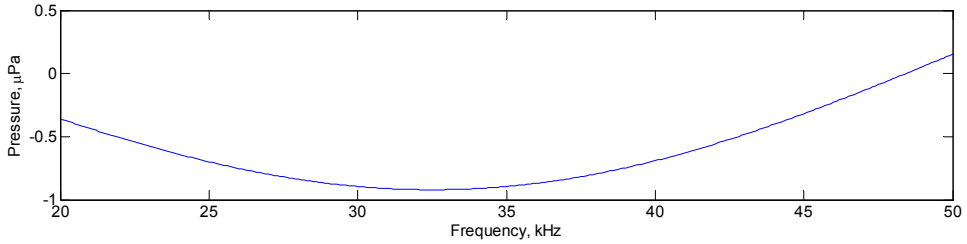

Figure 3.24: Plot of Pressure at Cavity-Thin Plate Interface as a Function of Frequency

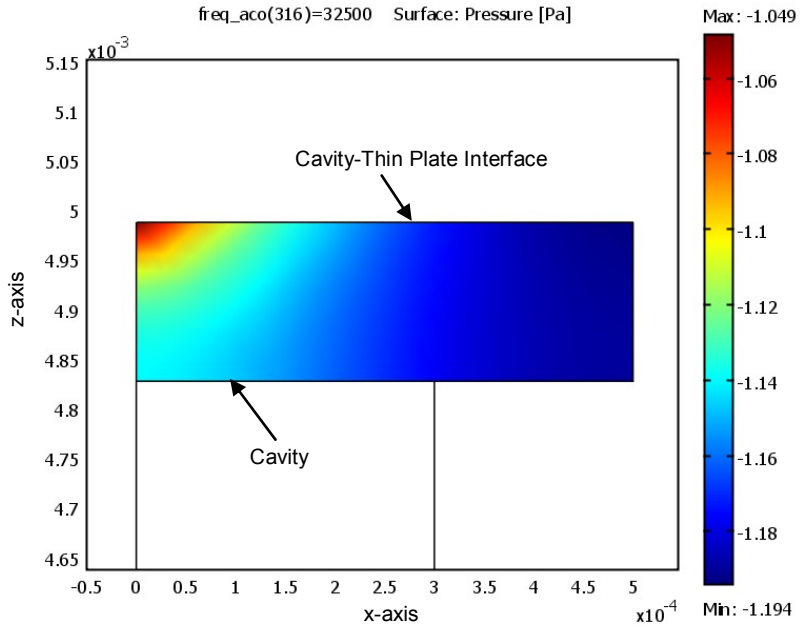

Figure 3.25: Plot of Pressure Trend in Cavity

The final component that needs to be identified is the pipe resonance. In this case, as before a 2D axi-symmetric simulation has been performed; with a 1 Pa input pressure at the pipe-cavity interface. Except for the pipe input pressure, the axi-symmetrical axis boundary and the internal built-in boundary condition by Comsol Multiphysics software, the rest of the boundary condition is considered thick walled. A predefined normal triangular mesh size has been utilised. The frequency response at centre of the pipe-air interface from the simulation is illustrated in Figure 3.26. From the simulation, it is observed that the frequency of the pipe is at around 34 kHz as in the analytical model. To identity the operating mode of the pipe, two simulations have been performed - to identify the variation of pressure within the pipe column (Figure 3.27) and the variation of pressure across the length of the pipe at its centre (Figure 3.28). In Figure 3.27, it could be observed that the pressure within the radial of the pipe is generally equal. In addition, the maximum pressure across the pipe axis is at the centre of the pipe at around 2.4 mm of the pipe length from pipe-air interface. The pipe radius could be determined from the x-axis, while the pipe length could be determined from the z-axis starting from the pipe-air interface. The pressure along the axial length of the pipe has been plotted as is shown Figure 3.28. From the Figure

3.28, it could be observed that the maximum pressure is around 13 Pa at axial length of 2.3 mm. Thus, the standing wave observed in Figure 3.28, correlates with the expected response for the fundamental mode of an open cylinder or pipe as detailed in the Figure 3.4. This indicates that the pipe is behaving in a fundamental mode.

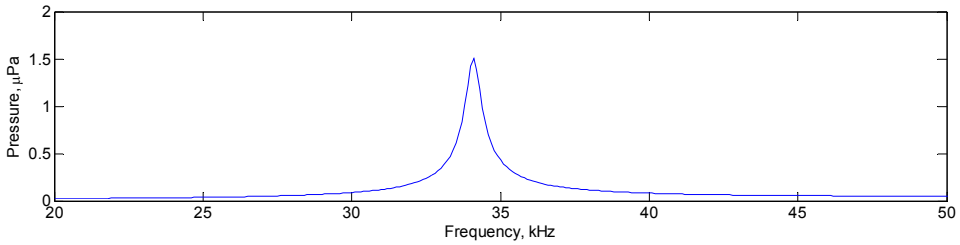

Figure 3.26: Plot of Pressure at Pipe-Air Interface as a Function of Frequency

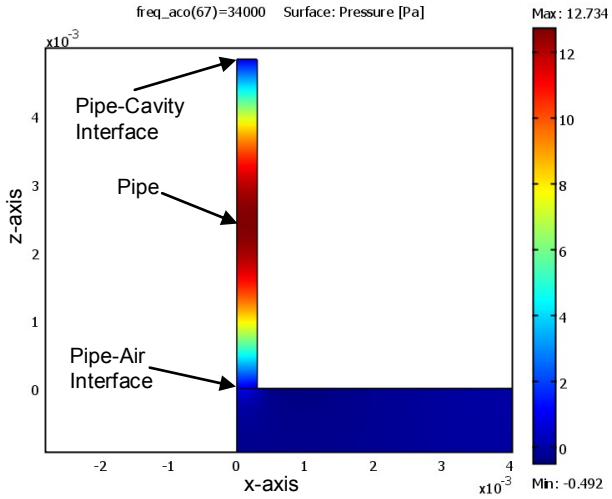

Figure 3.27: Plot of Pressure Output in Pipe at 34 kHz

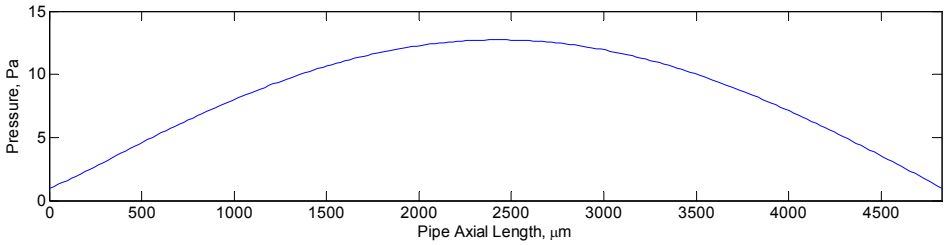

Figure 3.28: Plot of Pressure at the Centre of the Pipe Geometry as a Function of Pipe Axial Length at Resonant Frequency of 34 kHz

From the previous discussion, it could be deduced that the resonant frequency of the combined system should around 34 kHz based on the resonant frequencies of the individual components. This is suggested as the observed centre resonant frequency from the thin plate, cavity and pipe only is at 34.5 kHz, around 33 kHz and 34 kHz, respectively. Upon further simulation using FEA, it is found that the combined resonant frequency of the cavity and pipe geometry is at around 33 kHz, as shown in Figure 3.29. The data point is taken at the centre of the cavity-thin plate interface. An input pressure of 1 Pa has been utilised for the FEA boundary condition at the cavity-thin plate interface, with a predefined normal triangular mesh size utilised. With the exception of the input pressure, the axi-symmetrical boundary, and the internal built-in boundary condition at cavity-pipe and pipe-air interface, the rest of the boundary condition is considered thick walled. In order to confirm that the 33 kHz observed is the first harmonic, the cavity and pipe pressure output has been plotted in Figure 3.30, along with the plot of cavity and pipe standing wave as shown in Figure 3.31. The plots show a typical fundamental or 1st harmonic pipe resonance output pressure and standing wave with the pressure maximum approximately at the centre of the pipe length. All this suggests that the analytical model is able to identify the relevant geometry that corresponds to the required resonant frequency as simulated by FEA. As such, it could be concluded that there is good corroboration between the analytical model and FEA simulation as far as the individual resonant frequency and component geometry are concern. However, it is important to notice that once the cavity and pipe geometry were matched, a frequency shift might still occur to some degree once the device is excited.

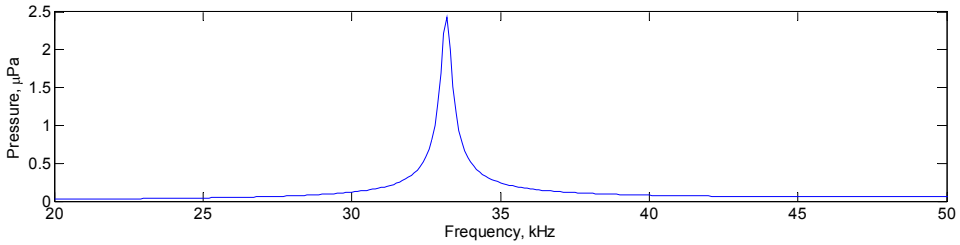

Figure 3.29: Plot of Pressure Output for a Matched Cavity and Pipe as a Function of Frequency

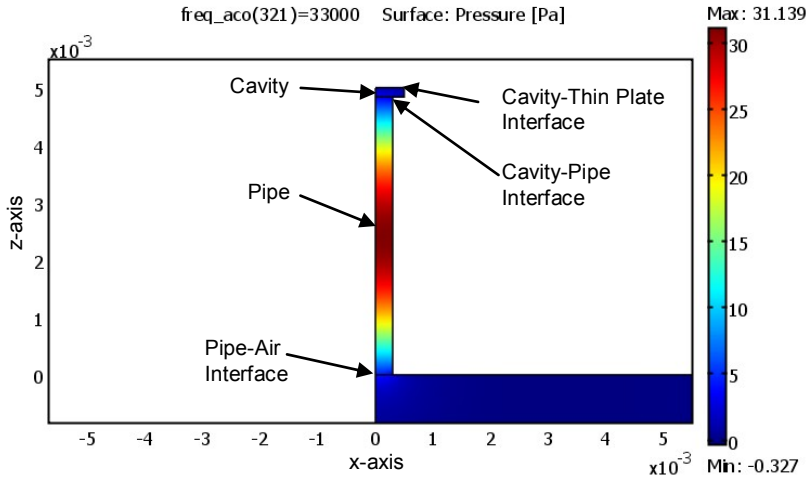

Figure 3.30: Plot of Pressure Output in Pipe and Cavity at 33 kHz

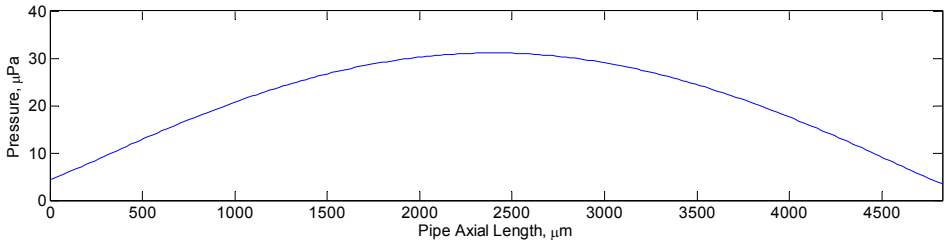

Figure 3.31: Plot of Pressure at the Centre of the Cavity/Pipe Geometry as a Function of Pipe Axial Length at Resonant Frequency of 33 kHz

3.5.3 Finite Element Analysis Techniques for Excited Model Analysis

Previously, analysis has been performed which indicates that the analytical model is able to identify the resonance frequency of an individual component within a FLAUT. In addition, it has been shown through FEA that there is a small frequency shift once the cavity and pipe geometry are fully matched. However, the previous analysis only considers the effect of the geometry alone. From this simulation, it could be suggested that if the consideration of the design is purely based on the structure of the cavity and pipe, then the analytical design does correlate to the finite element modelling. However, since the prototype will include the pre-stressed (DC biased) thin plate and the vibration of the thin plate, then further simulation needs to

be performed which includes the pre-stressed thin plate vibration and the acoustic coupling.

3.5.3.1 Modelling using Comsol

Comsol FEA modelling requires that the different physical domains i.e. electrical, structural, acoustic and fluid to be fully coupled. This interaction requires three different types of coupling which are: a unidirectional coupling from electrical to structural and a bidirectional coupling between structural and acoustics and between structural and fluid dynamics.

In addition to the interactive coupling of electrical/structural/acoustic and fluid dynamic domains within the FLAUT, another domain around the FLAUT transducer has been created to simulate the air load. The excited model analysis is performed using an axi-symmetrical boundary condition. Furthermore, the same boundary condition as before applies - for thin plate, the z-direction boundary condition is free, with x-direction at the 500 μm edge fixed; while for cavity and pipe micro-structure, the cavity-thin plate interface and the thin plate-air interface utilises the built-in internal boundary condition. The rest of the geometry is assumed to have a rigid boundary condition or termed hard walled in Comsol. However, as the excited model requires that the thin plate is pre-stressed, the use of a triangular meshing is not possible as the FE solvers are unable to converge due to the inverted mesh issues [112]. Thus, in excited model analysis, a predefined orthogonal mesh is utilised instead.

Using the previously described method, FEA simulations have been performed in order to confirm the microstructure and visualise the thin plate surface deformation. Figure 3.32 details the frequency response of the device calculated at the centre of the thin plate-air interface compared with a predicted resonant frequency of the FLAUT of 34.5 kHz - expected from the analytical model. The resonant mode shape

of the membrane is shown in Figure 3.33, this mode is confirmed as the fundamental mode (0,1) - as shown by the deformed thin plate magnitude and phase plot.

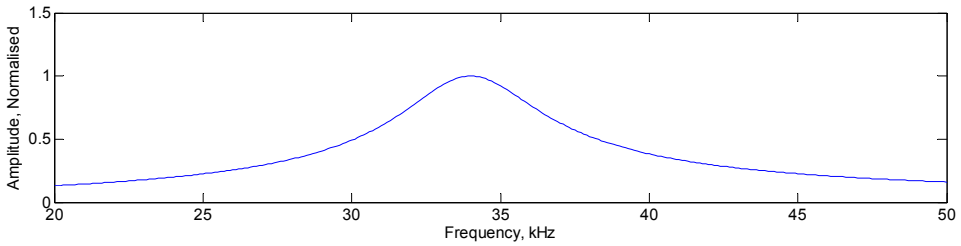

Figure 3.32: Plot of FLAUT Simulated Frequency Response with Designed Resonant Frequency of 34.5 kHz Utilising Comsol Multiphysics

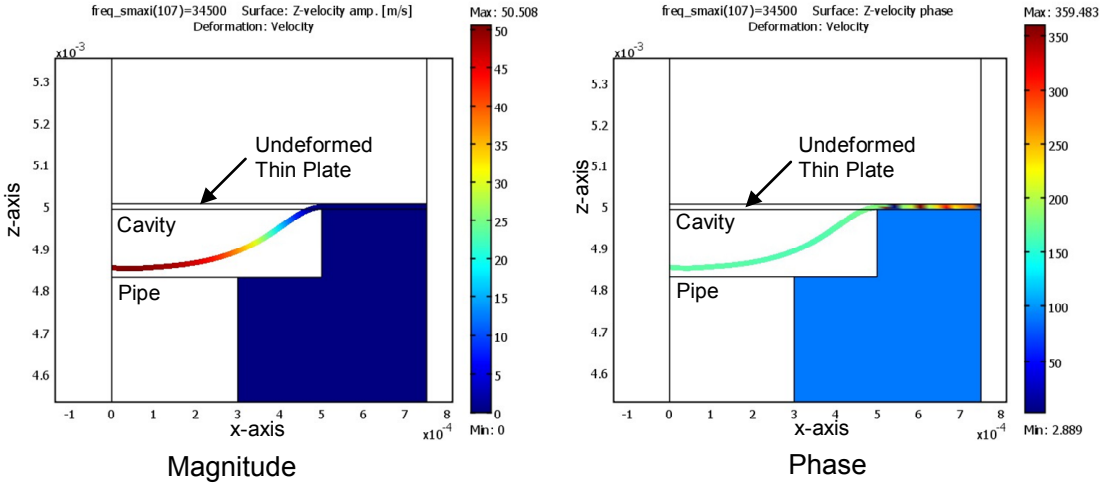

Figure 3.33: Plot of Mode Shape for FLAUT at Resonance Frequency of 34.5 kHz

3.5.3.2 Modelling using PZFlex

PZFlex was also used to identify the resonant frequency of the matched cavity/pipe design. The accuracy of this and the previous simulations is important as it determines the accuracy of the subsequent optimisation process. Although, 3D modelling is usually preferred for accurate modelling, this would constitute a longer simulation time, which may not be suitable for all design verification and preliminary

design suggestions. As such, as in simulation using Comsol, a 2D axi-symmetry has been performed to identify the resonant frequency of the device. A similar boundary condition as in Comsol is applied for the PZFlex.

PZFlex uses a time domain solver. As such, a time domain response from an impulse excitation and the frequency domain (FFT) results with damping applied is shown in Figure 3.34. From the Figure 3.34, it is observed that the resonant frequency of the cavity/pipe system simulated at the centre of the thin plate-air interface is at around 33 kHz. This constitutes about 4% difference from analytical model and Comsol model. Although the model shows that there is only a small difference between the three models, it is still important to identify the behaviour mode of the thin plate. The results of the mode shape shown in Figure 3.35 indicate that the behaviour represent a fundamental mode (0,1).

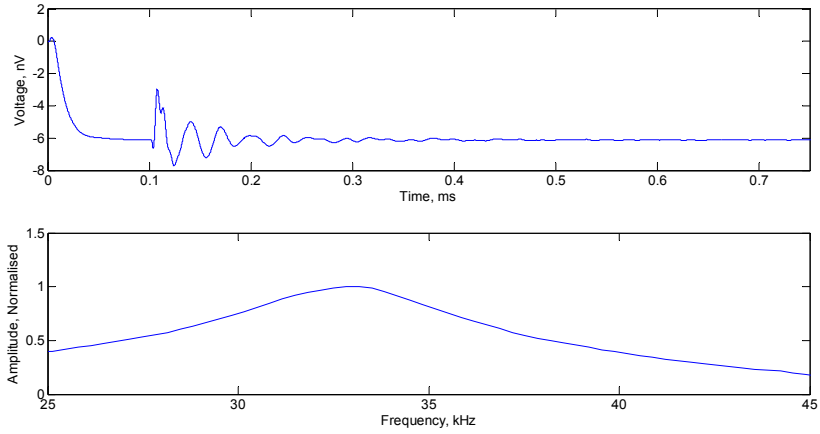

Figure 3.34: Plot of FLAUT Simulated Frequency Response with Designed Resonant Frequency of 34.5 kHz Utilising PZFlex

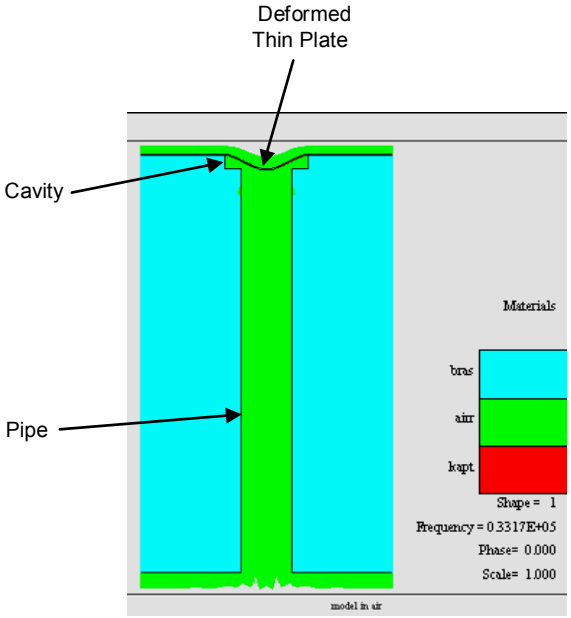

Figure 3.35: Plot of Mode Shape for FLAUT at 33.2 kHz

3.5.3.3 Comparison between Analytical Model, Comsol and PZFlex

From the previous discussion, it could be summarised that the two FEA models do corroborate with each other at around 4% between Comsol and PZFlex. Moreover, there is a match between the analytical model and Comsol and a difference of 4% between PZFlex and analytical model. This could be clearly seen by the overlay plot by the three different modelling techniques as shown in Figure 3.36. The comparison between the Comsol and PZFlex is necessary to identify the accuracy and differences of the model. Comsol being a frequency domain solver requires that enough frequency resolution is utilised to ensure that the output from the simulation is accurate, which is not inherent in PZFlex that utilises the time domain solver. From the comparison, it could be summarised that Comsol Multiphysics is able to give smaller error when compared to the analytical model compared to PZFlex. At the same time, being frequency domain solver, it is possible with Comsol that the frequency response is performed at around the desired operating frequency range only. This will effectively reduce the overall simulation time needed for the FEA.

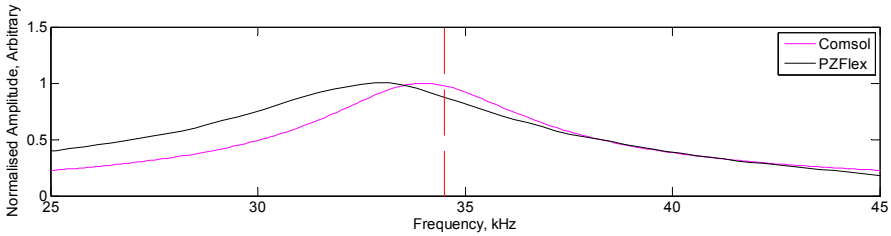

Figure 3.36: Plot of Simulated Excited Model Analysis Measured at the Centre of the Thin Plate-Air Interface as a Function of Frequency for Three Different Modelling Techniques (Comsol, PZFlex and Analytical (Red Dash Line).

However, although the corroboration between the 3 models indicates the error is less than 5%, there is still a need to ensure that the model does corroborate with the measured prototypes, which will be perform in the next Chapter.

3.6 Conclusion

This Chapter has described the different modelling and simulation tools that could be utilised to develop the FLAUT model. This Chapter have shown that FLAUT could be developed through a step-by-step approach of defining the geometry using the analytical model, and verifying the geometry configuration and the fully coupled configuration using the finite element modelling method. This Chapter has been the precursor to the following Chapter that deals with the different manufacturing and prototyping techniques, and the analysis and measurement of the FLAUT using surface displacement measurement to verify the FLAUT model.

4. Manufacturing Review, Prototyping and Analysis of Fluidic Amplified Electrostatic Transducer (FLAUT) using Surface Displacement

4.1 Introduction

In the previous Chapter, the specific process of design and development of a FLAUT and the influences of the design geometry changes, in term of simulation has been introduced, analysed and discussed in detail. The motivation of the previous Chapter was to analyse the behaviour of the FLAUT in order to enhance understanding of device operation and identify the critical aspects of the device implementation. Essentially, the components that comprise a device have been analysed with particular attention to a sensitivity analysis of each component for a design operating at a given frequency. In addition, the criticality of each component has been illustrated. This requires an appropriate selection and assessment of the different manufacturing techniques for device implementation, which will be discussed in this Chapter.

Moreover, during the course of this Thesis a number of different modelling tools have been employed in the analysis of the FLAUT device. Analytical models and FEA have both been employed to analyse the design variables. However, modelling of devices will typically result in some theoretical optimality and it is important to consider the ensuing manufacturing methodology in order that optimised designs are realistic in the context of the manufacturability.

4.2 Manufacturing Review for FLAUT Manufacture

In this section, different techniques in manufacturing the FLAUT prototypes are discussed, along with the advantages and disadvantages of each technique in terms of

cost, reliability, accuracy and feasibility of manufacture for the desired microstructure. This discussion is required to ensure that a suitable manufacturing technique is utilised. Moreover, as previously described and shown in Figure 3.19 and Figure 3.20, the requirement to reduce the size of cavity and pipe for high frequency devices makes the choice of backplate manufacture much more prominent.

4.2.1 Review on Different Manufacturing Techniques

One of the critical aspects in the manufacturing of a FLAUT is to ensure that the critical dimensions of the backplate are maintained. As expressed previously, there are two parts that constitute an assembled FLAUT - the thin vibrating plate and the structured backplate. Since, the thin plate is commercially sourced; the critical aspect of control will be on the backplate microstructure. In the previous Chapter, four dimensions critical to the resonant frequency of the device have been detailed - the cavity radius, the cavity depth, pipe radius and pipe length. These four dimensions need to be controlled during manufacturing to enable an effective coupling between thin plate, cavity and pipe resonant, thus maximising the fluidic amplification factor.

4.2.2 Challenges in Manufacturing FLAUT Backplate

There are a few techniques that have been considered for manufacture of a FLAUT backplate both in house and externally. Among the techniques considered were Conventional Drilling, Micro-Stereo Lithography (MSL), Electrical Discharge Machining (EDM), Computer Numerical Control (CNC) Drilling, Laser Cutting and Photolithography. The relative merits of each of these methods will now be reviewed in the context of FLAUT manufacture

4.2.2.1 MSL

MSL is part of a general manufacturing technique known as rapid prototyping. In rapid prototyping, the prototype is built upon successive additions of a single layer, which later forms the desired shape and object from the multiple layers. In MSL, each layer or voxel (volumetric pixel) is formed by the curing of a liquid photopolymer resin that solidifies when exposed to ultraviolet light (UV) as shown in Figure 4.1 [113]. Each voxel will have a dimension on the order of 10 μm to 100 μm [114]. Generally, a computer controlled X-Y translation stage is utilised to control the movement of the deposition head, which determines the UV light curing location. The computer controlled elevator, then moves down a voxel plane after each UV cure process. Once finished, the voxel planes will form a three-dimensional structure. The size of the voxel determines the smoothness of the final three dimensional structures [114]. Thus, in MSL manufacturing process, the critical structure dimensions are controlled by the X-Y-Z computer controlled translation resolution [113, 115] and the UV penetration depth [115]. In a MSL the build volume depends on the working table size, with a larger build volume corresponding to a lower resolution as shown by Bertsch *et al* [116]. The largest MSL build volume process developed as reviewed by Bertsch *et al* was 50 x 50 x 50 mm^3, with voxel size of 10 μm x 10 μm x 1 μm, while the smallest was a few 100 μm^3, with voxel size of sub-micrometer. In general, smaller voxel size would enable the object to have a much better resolution but limited total build volume, in comparison to a larger voxel size with larger build volume capability. In practice, this means that a trade off between voxel size or resolution and build volume is generally needed. Thus, there is a clear trade-off between build volume and voxel size using MSL for manufacture.

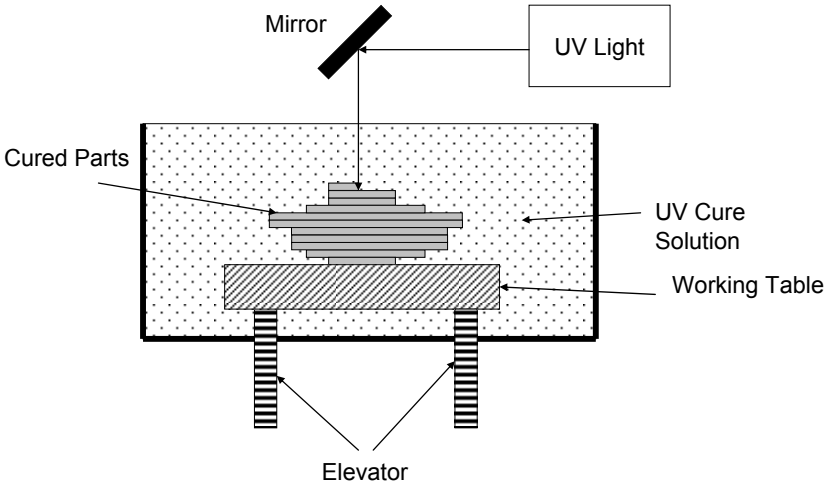

Figure 4.1: Schematic Diagram of Basic Principle MSL

In this thesis, the MSL process utilises a 3D printer Objet model Eden 350 [117], which has a net build volume size of 340 x 340 x 200 mm^3, with voxel size of 42 µm x 84 µm x 16 µm. The voxel size is governed by three main components within the MSL machine, which are the z-elevator, the quality of the UV beam and the X-Y stepper motor motion movement. Since MSL is an additive process, it is prone to error from the stepper motor (X-Y) and the elevator (Z) movement.

For a FLAUT device operating at 34.5 kHz, the required cavity depth is 164 µm, hence there is a ratio of ten to one between the single voxel planes and the required cavity depth. With this ratio, ten voxel planes are required to produce the prototype. The analysis presented in the previous Chapter indicated that the cavity depth is one of the critical dimensions - the cavity depth has an inverse power squared function with respect to frequency. Therefore, tight control of the cavity depth is required. For example, reducing the cavity depth by one voxel plane would result in a cavity resonant frequency of 36.3 kHz, a 1.8 kHz or 5.3% increase from the desired resonant frequency. Furthermore, if a higher frequency device were required, for example 85 kHz the required cavity depth reduces to 44 µm. This significantly reduced the ratio between the cavity depth and the voxel planes to two. (A full geometry size for a FLAUT operating at 85 kHz will be detailed in Chapter 6). As such, MSL process is not suitable for high frequency device manufacturing. In

addition, as concluded by Hutchins *et al* [118], MSL albeit being flexible requires a device to be designed with a thicker membrane and air gap; thus only suitable for a device operating in the low frequency regime. In this case, in order to manufacture high frequency electrostatic devices using MSL, a significant improvement in the resolution of the MSL technique is required.

4.2.2.2 EDM

EDM is a process where conductive metallic materials such as stainless steel, brass etc. can be machined using a series of electrical discharges passed between two electrodes [119]. The two electrodes consist of a tool electrode and a workpiece electrode. During operation, a tool electrode is guided along the desired trajectory very close to the workpiece to remove the workpiece material. There are three different type of EDM process which depends on the way the tool electrode was used which are: wire EDM [120], ram EDM [120] and small hole EDM [120].

In wire EDM, the electric discharges moves from the wire electrode to the workpiece and erode both the wire and the workpiece as shown in Figure 4.2. This process is primarily used in through-hole machining. However, the main disadvantages of this technique is the requirement to have the wire to pass through a ready-made hole, either through mechanical drilling or small hole EDM drilling.

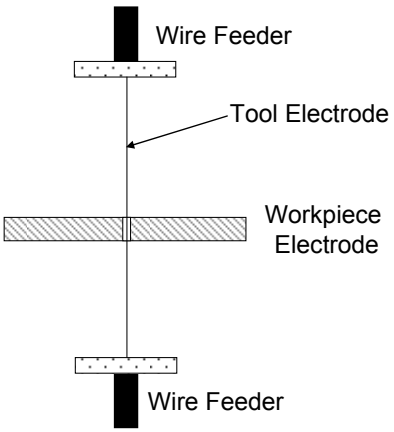

Figure 4.2: Schematic Diagram of Wire EDM

In contrast to wire EDM, the more conventional Ram EDM is generally used to produce blind cavities. As before, the electrical discharge moves from the electrode to the workplace causing the material to be removed as shown in Figure 4.3. However, in this case the tool electrode does not pass through the workpiece

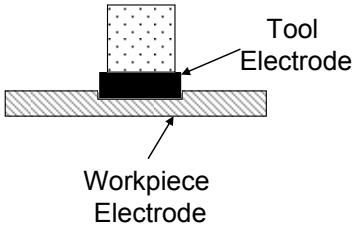

Figure 4.3: Schematic Diagram of Ram EDM

Lastly, a small hole EDM or known as start hole EDM uses a hollow electrode to drill a hole by eroding material from the workpiece through electrical discharges as shown in Figure 4.4.

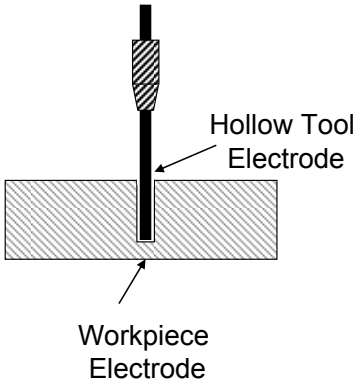

Figure 4.4: Schematic Diagram of Small Hole EDM

One of the main attractions in using EDM for device manufacture is its' ability to produce a deep straight hole. Based on the EDM handbook [120], using 1 mm diameter small hole EDM, it is possible to achieve a taper tolerance of +/- 0.013 mm at 25.4 mm depth. In addition, since there is no contact between the electrodes and the work item, EDM drilling is able to produce holes free from any burr.

Lastly, Liu *et al* [121] have shown that a micro-EDM process is able to mill to a depth of 0.5 μm, with a centre hole of 0.3 mm. However, to produce a small part, a much smaller tool electrode is required. This requires a more specialist tool to be utilised for manufacture, thus increasing the tooling electrode cost due to the increased tolerance required [120]. Moreover, FLAUT device typically comprises of a large number concentric cavities and pipes or an array on a backplate. This will significantly increase the cost of manufacture by around 200% compared to the single cell fabrication, due to the increasing time required to produce such a backplate.

4.2.2.3 Drilling and Milling

Conventional milling and drilling also presents itself as a candidate for device manufacture. It is possible to process a complex array of counter bore holes and through holes with high aspect ratio of five or more, using conventional drilling technique such as deep hole cycle and pecking cycle [122]; the need for a very shallow cavity requirement for high frequency makes controlling of the cavity depth tolerance to be difficult. For example, to design a 101 kHz FLAUT transducer with 8 μm thin plate thickness would require that the cavity to be counterbored at depth of 31 μm; and assuming that the pipe diameter required is at 400 μm, then the pipe need to be drilled through to 1648 μm.

In producing this part, two main manufacturing requirements needs to be considered; which are the blank plates needs to be aligned and parallel, and the centre of the cavity diameter needs to be coaxial with the centre of the pipe diameter. A perfectly aligned and parallel blank plate is required to ensure that the cavity depth tolerance is maintained. A high level of propagated error may occur if the blank plate were not parallel. (The manufacturing sensitivity analysis, which introduces the concept of propagation error, will be detailed later). A 10 μm error in the plate parallelism could results in the cavity depth tolerance to be in the range of 21 μm to 41 μm, a 20 μm error. In addition, to drill the pipe that has an aspect ratio of 4.2 requires a suitable

material to be utilised and optimum drill speed to maintain the tolerance of the pipe hole. Moreover, the centre of the cavity diameter needs to be coaxial with the centre of the pipe diameter to enable FLAUT to function optimally. In order to ensure that the coaxial requirement of the cavity and pipe is maintained, the repeatability of the drill head movement at both single location and multiple locations needs to be considered. Generally, the machine drill head movement tolerance repeatability needs to be less than the required cell-to-cell tolerance. This is to ensure that any error due to the machine is still within the acceptable limit of the design specification. (An example of how these tolerance influence the FLAUT manufacture will be detailed later in Chapter 6).

Furthermore, conventional drilling could be a manufacturing process of choice if the tolerance required could be further controlled using a specialised machine with suitable spindle speed. Identification and investigation towards identifying the suitable spindle speed will be expressed later in Chapter 6. In addition, commercially available twist drill and slot drill bits with variable sizes and tolerances have made the conventional drilling technique as a flexible choice of manufacture. Although, drill bits as small as 0.1 mm are commercially available [123], there is a need to identify suitable backplate material to suit such micro drill sizes, of which the micro drills tend to be fragile. However, the micro drill diameter to depth aspect ratio need to correspond to the required device geometry, since the diameter to depth ratio for the drill bit is generally standardised by the manufacturer.

4.2.2.4 Laser Cutting and Engraving

The next option would be laser drilling, cutting and engraving. Typically, a laser could be used to drill, cut and engrave through most surfaces and materials depending upon the available power and type of laser. Within the University, a Versa Model VLS3.50 [124] CO_2 Laser with 50 W power is typically used for standard design profiling on acrylic and architectural presentation on paper. Although it is possible for the laser to cut through metal surfaces, due to the required thickness of

more than 1.5 mm this process is not possible with the current laser power. As such, a laser cutting on an acrylic was originally proposed for a higher frequency design.

Upon further investigation, it was found that laser cutting at a depth is unable to produce a straight hole desired in FLAUT pipe geometry [125]. Due to the laser focusing profile, the spot size of the laser beam at the inlet of the material will generally be larger than the outlet at the opposite end of the material [126]. This in turn produces a tapered cross-section along the pipe length, which changes the resonant frequency of the pipe; thus causes a mismatch in the FLAUT design. From the preliminary investigation using the Versa Laser, it was found that the taper could be as high as 13%, which makes this approach unsuitable in the present context. However, as discussed by Dhar *et al* [126], there are various techniques that could be utilised to reduce the taper inherent in a laser drilling system such as Single Pulse, Percussion and Trepanning. These techniques have their relative merits in producing the desired pipe and cavity microstructure. Single pulse, although very fast will create a large tapered hole, which is not desirable. With the percussion approach, the taper angle is reduced, however due to multiple pulses; this process is slower and causes the materials to re-solidify at the wall of the hole, which is also not desirable. Lastly, although trepanning is able to produce the least amount of tapered in a laser drilling process; the process require that the inlet diameter to be large typically 500 μm or more due to the circular motion required when the laser drilling is performed.

On the other hand, for a very shallow cavity, a laser is able to produce satisfactory results. Since the laser power is sensitive to depth, there should not be any problem for the laser to engrave a very shallow counterbore in the surface of the backplate. Using the previous example, to design a 100 kHz FLAUT transducer with 8 μm thin plate thickness would require a cavity depth of 31 μm. In general it is possible to produce a zero tapered counter bore using a laser provided that the depth is small enough that the laser power is consistent throughout the depth. As such, it is possible to produce a cavity only device. However, as a FLAUT is a device which incorporates a concentric cavity and pipe, the use of laser as a manufacturing process

is not possible due to the tapered issues inherent when laser cutting is utilised at depth [125].

4.2.2.5 Photolithography

Photolithography is a subtractive process by which a material is selectively removed from a thin film or a substrate as shown in Figure 4.5. In photolithography, UV is utilised to transfer a pattern from a photo mask, into a light sensitive photo resist on the substrate [127]. Depending whether a negative or positive photo resist is utilised; the development process would either remove the exposed photo resist material in the case of positive photo resins, or remove the unexposed photo resins materials in the case of negative photo resins. A transfer process such as chemical etching is then utilised to remove the masking film made of material such as Si_3N_4, SiO_2 etc, before the remaining photo resist is finally removed.

One of the main weaknesses of this technique is that it requires a line of sight during the pattern transfer process, thus requires a flat surface to start with. This process is generally utilised because it can create a pattern over an entire surface effectively reducing the manufacturing total cost per unit, which is well suited for mass manufacture. In addition, this process is also able to create a small pattern and maintain the desired sizes through the use of photo mask or control of light.

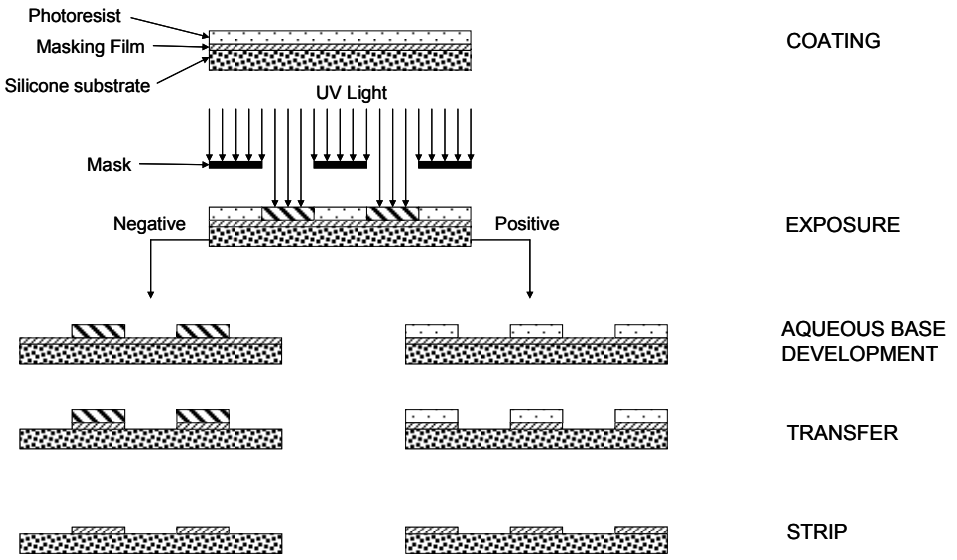

Figure 4.5: Flow Diagram of a Photolithography Process Utilising Positive and Negative Photo Resins.

4.2.3 Final Determination of Manufacturing Techniques Implemented

Based on the discussion above, it could be observed that there are advantages and disadvantages for each type of manufacturing process. Although MSL is the easiest among the five processes, it lack the resolution required for backplate microstructure, especially for higher frequency FLAUT devices. The EDM process although highly reliable and a highly accurate process; tends to be very expensive especially when high numbers of cells are involved. Conventional and CNC drilling processes, although this takes longer and are much more complicated to setup when compared to the standard MSL process of plug and play, are still better choices when final device operation is considered. In addition, a drilling process tends to be much faster and easier to manage when compared to EDM processes mainly due to the electrode setup requirements. However, maintaining the requirement level of accuracy during the drill process with a high pipe radius to pipe length ratio will be a challenge along with the shallow cavity depth especially for a high frequency device. Although, it is highly preferable and desirable to use a metal as a backplate to ensure that there are

no residual charges on the material that would disrupt the transducer operation, the use of photo-resist plastic such as those in MSL with evaporated electrodes has also shown that it is possible to use a non-metal backplate successfully.

Based on the discussion above, and considering the relative merits of the different technologies and considering the cost of prototyping involved, two different technologies will be utilised for the manufacture of prototypes in the remainder of this thesis. With the requirements to adapt a low cost solution, the conventional technology of drilling in this case drilling and micro drilling is considered, along with MSL for low frequency devices. These two technologies are considered because of cost as well as the expected accuracy from the two processes based on the desired frequency ranges. It is relatively difficult to micro drill on hard surfaces such as metal. Thus, the micro drilling process is considered here due to the possibility of drilling on softer surfaces such as a polymer substrate; which could then be rendered conductive via the deposition of electrodes on its surfaces. Lastly, MSL is only considered for the low frequency devices due to the inherent resolution issues within the MSL process as discussed earlier.

4.3 Manufacturing, Assembly and Prototyping of Transducers

Following on from the modelling and manufacturing review it is essential that verification of the constructed prototype is conducted. There are two parts to the FLAUT prototype assembly, which are:

- Thin Plate
- Backplate

In the manufacture of prototypes, the thin plate is a Kapton film of thickness 13 μm. The thin plate is bonded to a metallic ring 56 mm in diameter as shown in Figure 4.6 – the ring forms part of the transducer assembly. It was also observed that if the pre-tension is minimised, the device reliability is improved, which was also commented by Schindel *et al* [18].

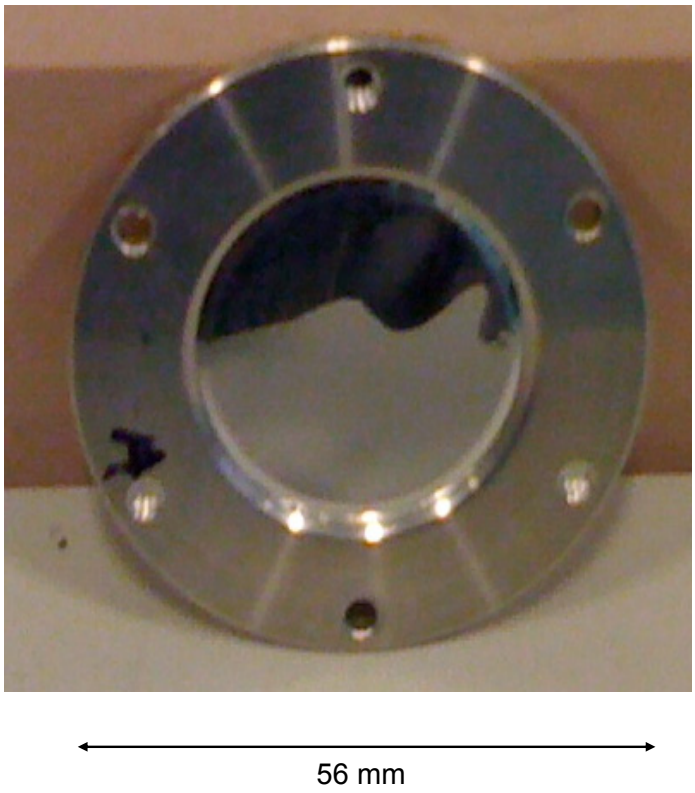

Figure 4.6: Picture of Kapton Film Bonded on a Metallic Ring

Next, a cylindrical backplate with a diameter of 30 mm is manufactured using the MSL process. The total thickness of the backplate is dependent upon the cavity depth and the pipe length. Finally, aluminium is coated as the electrode utilising the thermal evaporation process, Edward Coating System model E306A. Typically, the aluminium electrode will have a thickness of 150 nm. The process consists of three major steps, which are plasma cleaning, saturation of evaporation chamber with energetic vapour and spinning of sample for coating.

First of all, in order to ensure that the adhesion of the aluminium to the polymer plastic is good, a cleaning process using energetic plasma is performed in ionised low-pressure argon gas for 10 minutes. The cleaning will remove impurities and contaminants such as oil, water, dust etc to make the sample ready for coating. Next, the aluminium ball is attached to the tungsten filament. Then the sample or substrate is fully attached to the substrate spinner, which spins at 1 rev/min, while the aluminium ball is placed at the curvature of the tungsten filament as shown in Figure

4.7: Left. To change the state of the aluminium, the aluminium ball is heated up to 1000°C to melt and change the aluminium into energetic vapour - spreading outwards from the tungsten filament. Once the chamber is saturated with the aluminium vapour, the sample is turn at 1 rev/min to coat them as shown in Figure 4.7: Right. The thickness of the coating is measured using the crystal monitor. The coating process takes around 10 minutes. Once the sample is fully coated on one face, the sample would then be turned over and the previous process steps are then repeated.

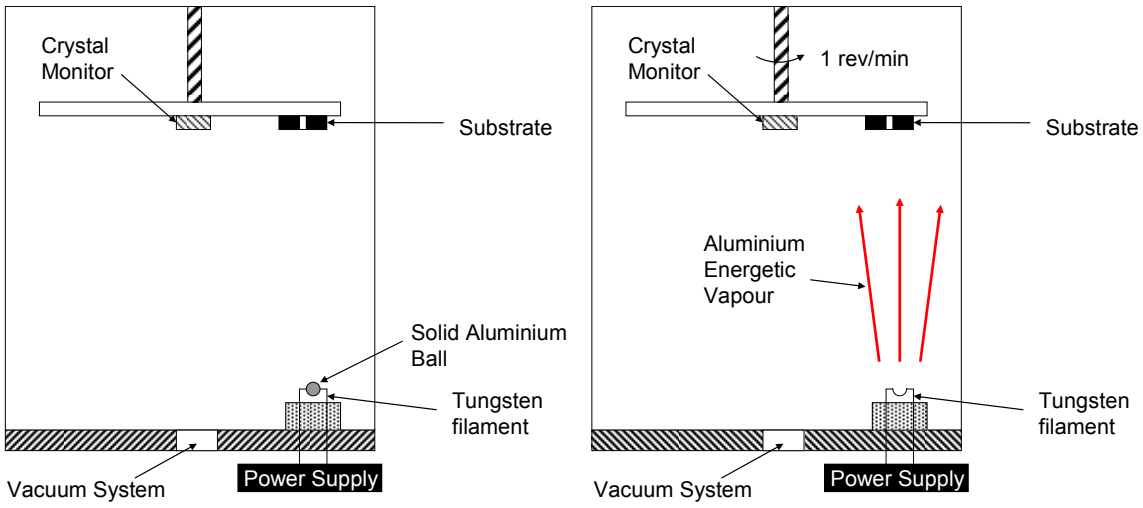

Figure 4.7: Schematic Diagram of Thermal Evaporation Process. Left: Preparation Stage Right: Evaporation Stage

Generally, it is straight forward to aluminium coat the backplate and the cavity microstructure using the thermal evaporation process. However, as previously discussed, FLAUT consists of a cavity and pipe microstructure. In addition to coating the cavity backplate, the pipe backplate needs to also be fully electroded. The thermal evaporation coating is typically a line of sight process. Thus, the location of the tungsten and the sample, needs to be aligned in such a way that it is in the centre of the aluminium ball and centre of the pipe hole for a single cell design or the centre of the array backplate for an array design as shown in Figure 4.7. (The concept of array design will be discussed later in Chapter 6). This would help to ensure that the aluminium vapour is able to coat the pipe as deep as possible. In addition, the

backplate is also turned 180^{o} so that the pipe hole could be evaporated from the opposite direction enabling the continuity needed for the FLAUT microstructure.

In addition to issues with resolution on low frequency, parts manufactured using MSL are also observed to suffer poor surface finish as shown in Figure 4.8. Due to the nature of the process, there is a corrugated peak and trough structure across the surface of the backplate. Although, only a single unit cell is considered here, the uneven surface roughness may effectively cause the single unit cell not to be properly clamped at its peripheral edges due to the uneven surfaces surrounding the unit cell.

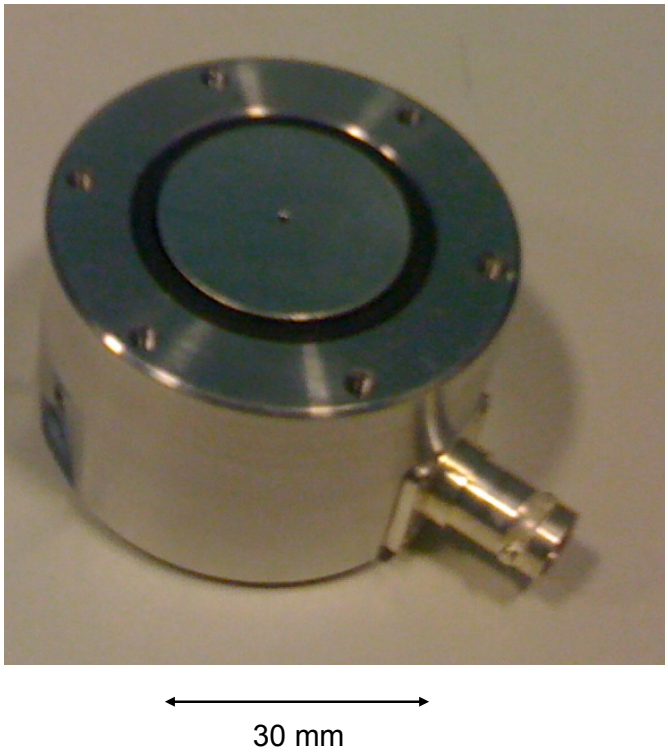

Figure 4.8: Picture of Backplate Produced using MSL Technique on a Final Assembly (Without Membrane on Top)

A full assembly of the device inclusive of the membrane could be seen in Figure 4.9. From Figure 4.9, it could be observed that the thin plate has been assembled on top of the slightly protruding MSL backplate with a minimal tension to ensure that no large air bubbles are trapped between the backplate and the membrane.

As mentioned earlier, in general a smaller size cavity will tend to produce a higher resonant frequency when compared to a larger size cavity. This characteristic is important since a suitable frequency and geometry consideration could be made during simulation process to enable prototypes to be produced effectively.

Figure 4.9: Picture of Full FLAUT Transducer Assembly

4.4 Review of Different Measuring Techniques

The behaviour of each manufactured prototype will be assessed using a number of different analysis tools. The key device metrics are FLAUT impulse response, beam directivity and uniformity of the surface deformation. The experimentally measured data will be used to assess device performance and to corroborate the modelling methods that have been employed in the design process.

Each of the measurement methods will now be discussed in turn.

4.4.1 Laser Interferometer

A laser interferometer relies on the interference between a reference laser beam and the reflected laser beam from the object being scanned. By measuring the phase differences between the two laser beams, the overall surface velocity of the object being scanned can be measured [128]. The typical setup for the laser interferometer based system measurement utilised in this thesis is shown in Figure 4.10. As illustrated, the system consists of three different sections: the PC for control, data acquisition and display; the laser head and its peripherals that consist of a 3-axis manipulator, motor controller and decoder; and lastly the transducer excitation circuit, which consist of a waveform function generator and a high voltage power supply. The laser interferometer utilised in this thesis is the Polytec PSV300 Scanning Laser Vibrometry System with the following specification as shown in Table 4.1.

Table 4.1: Polytec PSV300 Scanner Laser Vibrometry Specification

Item	Specification
Velocity Resolution	0.08 μm/s for measurement range of 25 $mm.s^{-1}$ /V
Typical Spot Size	15 μm for measurement distance of 450 mm
Angular Resolution	$< 0.002^{o}$
Pointing Stability	$< 0.01^{o}$ / hour

There are three different measurement types that could be performed using the laser interferometer based system which are displacement, velocity or acceleration. In addition to the different measurement types, different measurement locations or techniques could be performed using the laser interferometer based system such as a single point measurement, a cross section measurement, and an average surface displacement/velocity/acceleration measurement.

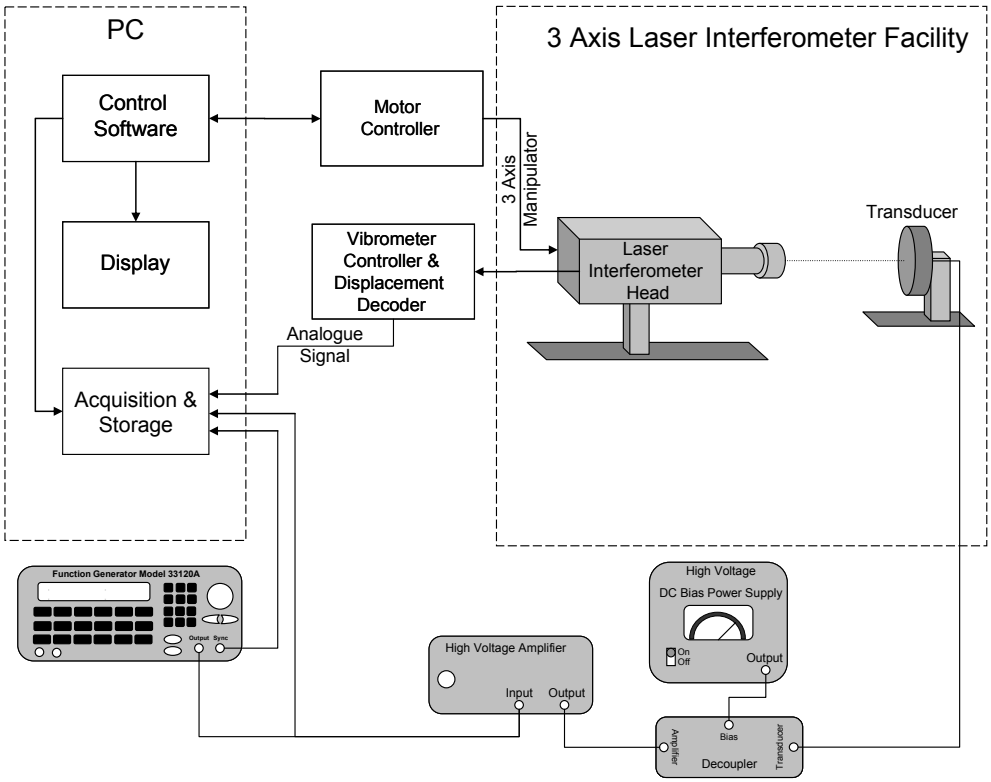

Figure 4.10: Schematic Diagram of Setup for Scanning Laser Interferometer Measurement [88]

Although it is possible to perform a single point measurement using the laser interferometer based system, it is not possible to accurately pin point the exact centre of the thin plate. Thus, it is more appropriate to perform a total surface displacement scan. The measured surface deformation data can then be corroborated with the mode shape obtained from the FEA simulation. The surface deformation data from a 25 kHz FLAUT device are shown in Figure 4.11, Figure 4.12 and Figure 4.13. The measurements were performed with the transducer front face having a distance of 250 mm from the laser interferometer mirror face. Five points, in a cross formation, distributed equally across the transducer surface have been utilised to align the laser. The user could choose to visualise the surface displacement in 3D view as shown in Figure 4.11, or a 2D plan view as shown in Figure 4.12 or in cross section view as in Figure 4.13. These three views have their own merits in term of two main aspects which are visualisation and corroboration. In term of visualisation, the different views i.e. 3D and 2D are suitable for video and print respectively. In terms of corroboration, these laser measurement data are able to indicate the mode shape

observed during measurements. For example, in all the previous figures the mode shape that the laser has visualised is the fundamental mode (0, 1). Utilising the 3 different views, it could be clearly observed that in 3D, the fundamental mode is represented by the semi hemisphere domed shape as shown in Figure 4.11. Next, in 2D plan view, with two different views - the magnitude and phase; the mode shape could be observed through visualisation with colour spectrum moving from green to red representing magnitude of the velocity from low to high. The phase on the other hand, indicates the level of phase uniformity within the surface displacement with relevant phase value utilising the same spectral concept. From the magnitude plot in Figure 4.12 (Left), it could be observed that the circular centre has a higher magnitude compared to the circumference which also indicate a mode (0,1) in plan view – with 3D equivalent of which the centre of the dome having a higher amplitude compared to its edges. The phase plot in Figure 4.12 (right) also indicates that almost all surfaces are in phase. Lastly, in the 2D cross section, a further quantisation of the level of deflection across the surface of the membrane could be made. As in the previous 2D plan visualisation, in 2D cross section visualisation, the magnitude across the section of the plan is made, with the magnitude of the cross section visualised as shown in Figure 4.12. From the measurement, it could be observed that the mode shape is mode (0, 1) fundamental with a dome shaped peak at the centre of the membrane. These three visualisation and corroboration techniques are important to enable the visualised measured mode shape to be corroborated with the simulated mode shape effectively.

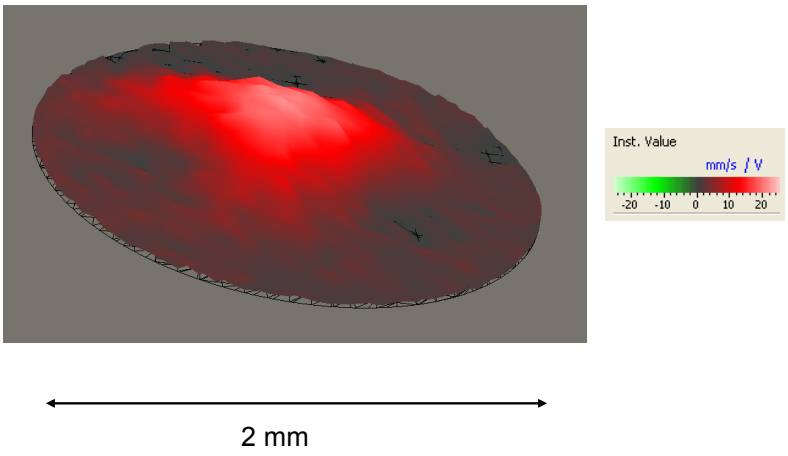

Figure 4.11: Plot of 3D View of Thin Plate Surface Deformation

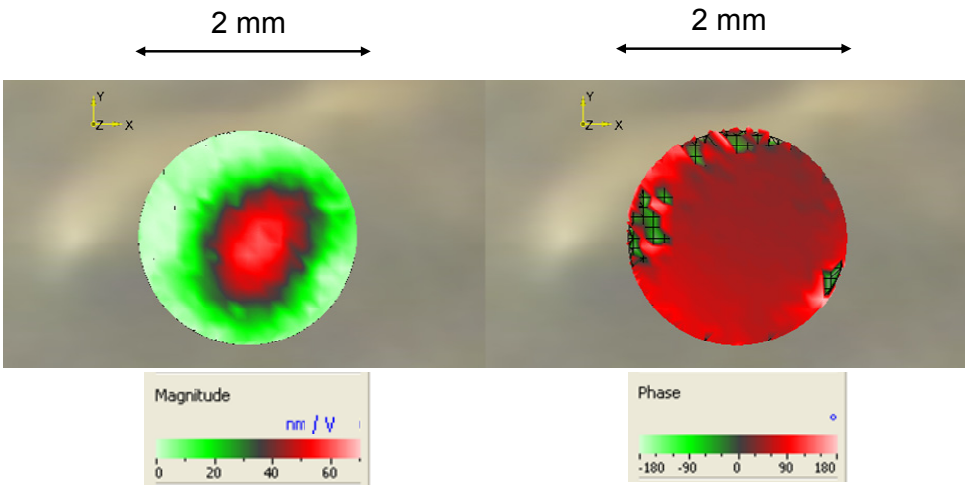

Figure 4.12: Plot of a 2D Plan View of Thin Plate Surface Displacement: Magnitude (Left) and Phase (Right)

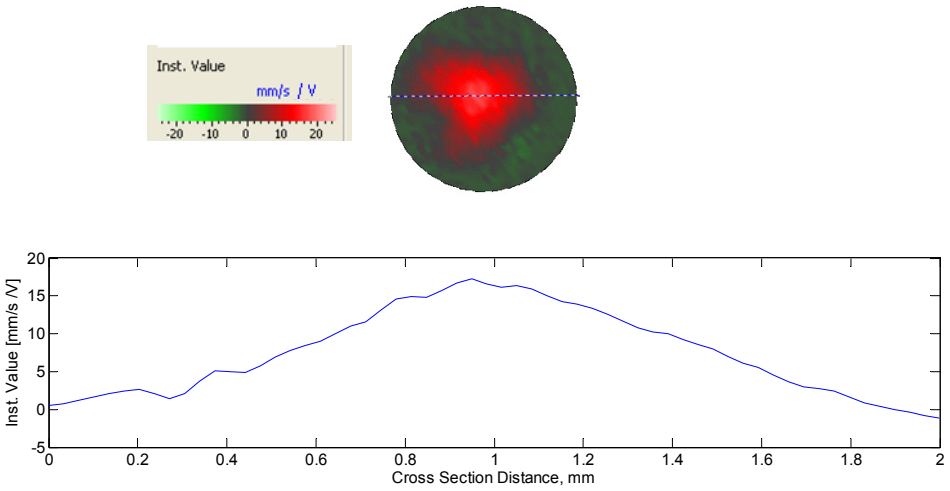

Figure 4.13: Plot of Cross Section View of Thin Plate Surface Velocity

However, the visualisations observed by the user through the laser interferometer based system still depend on the excitation frequency and voltage specified to the transducer. There are three types of excitation that could be applied to the transducer, a continuous sinusoidal wave at a desired frequency (narrow band), a single cycle sinusoidal frequency excitation or an impulse excitation (wide band) and a sinusoidal frequency sweep (periodic chirp). The choice of excitation will depend on the FLAUT prototype being measured. In most cases, the periodic chirp excitation signal

as shown in Figure 4.14 is utilised to identify the measured frequency response of a thin plate displacement for a FLAUT device due to its higher frequency content when compared to the single cycle excitation. A frequency domain response of thin plate displacement for a FLAUT transducer designed at 25 kHz is shown in Figure 4.15. From Figure 4.15, it could be observed that there are various peaks within the plot. However, as observed, the highest peak is at 25 kHz, which is the fundamental mode of the device.

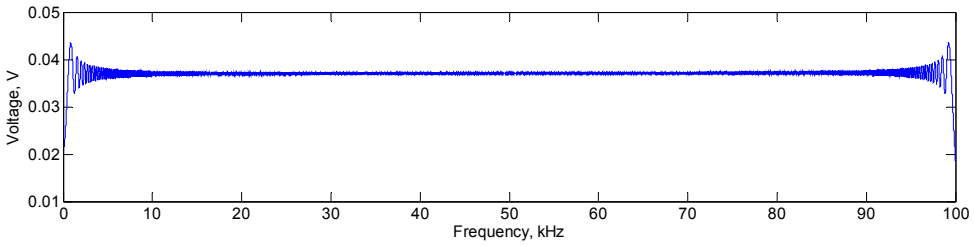

Figure 4.14: Plot of Periodic Chirp Excitation in Voltage as a Function of Frequency

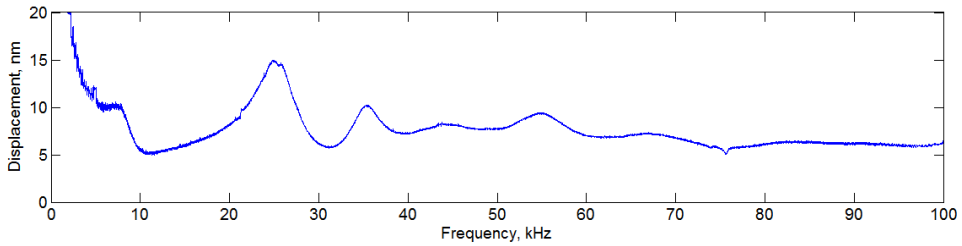

Figure 4.15: Plot of FLAUT Thin Plate Average Displacement as a Function of Frequency

Previously, in Figure 4.13, the cross section of membrane surface deformation across the cavity diameter has been plotted. However, the plot only illustrates that the FLAUT is behaving in the fundamental mode (0,1) with the maximum amplitude at the centre of the cavity. Although, the plot in Figure 4.13 shows that the velocity at the circumference of the cavity is low at around ±0.5 mms^{-1} /V and thus the circumference could be considered clamped by the bias voltage; there is still a possibility that the rest of the surface is vibrating at a higher velocity. As such, full surface deformation scans for the backplate with the diameter of 30 mm have been performed at 25 kHz and is shown in Figure 4.16. From the magnitude plot in Figure

4.16, it could be observed that there is a higher surface deformation across the surface of the cavity compared to the rest of the backplate. This does indicate that the bias voltage is clamping the surface sufficiently as expected. Investigation on the phase of Figure 4.16, reveals that there is a small random anti-phase area across the surface, suspected due to the air trapped underneath.

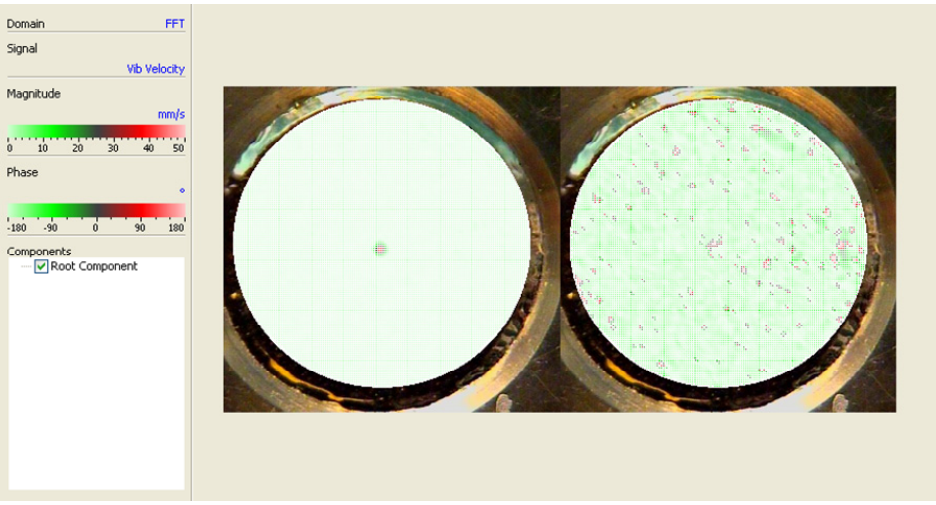

Figure 4.16: Plot of a 2D Plan View of Thin Plate Surface Velocity for the 30 mm Diameter Electrostatic Transducer Backplate: Magnitude (Left) and Phase (Right)

A further cross section plot is also performed, to identify the different level of deformation across the surface of the thin plate as shown in Figure 4.17. From the plot in Figure 4.17, it could observed that at the centre of the cavity, deformation velocity is at 41.4 mms^{-1} /V, while at the surface area away from the cavity have the deformation velocity of 1.3 mms^{-1} /V; a 30 dB difference. Thus, as the different is significant, it could be proposed that the clamping afforded by the bias voltage is sufficient. In addition, as observed in Figure 4.17, the measured distance between the peripheral edges of the cavity from the surface deformation measurement is almost the same as the cavity diameter. With this respect, the assumption that the thin plate is clamped at the circumference is corroborated.

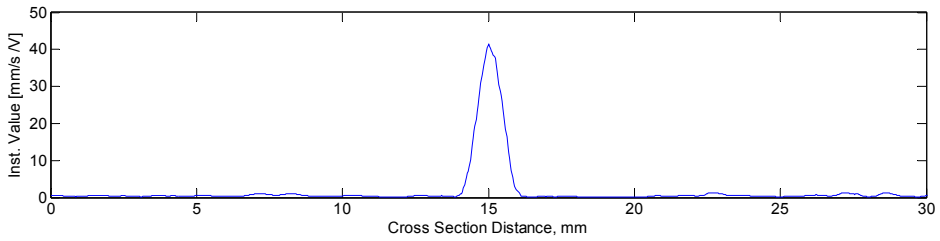

Figure 4.17: Plot of Cross Section View of Thin Plate Surface Velocity for 30 mm Diameter Electrostatic Transducer Backplate

Although, the plot in Figure 4.17 shows that the velocity outside the cavity is almost flat when compared to the velocity of the cavity centre. There is still a possibility of a surface wave propagating from the centre of the cavity due to the thin plate displacement to the edges of the 30 mm backplate and further to the 32 mm metallic ring. Thus, an extended view for the Thin Plate cross section outside the cavity for different phases has been plotted and is shown in Figure 4.18. From the plot of Figure 4.18 two possibilities could be considered – vibration due to air pockets and the surface wave propagating from the centre of the cavity.

From the different phase plot in Figure 4.18, it could be observed that the thin plate has a different velocity magnitude across the thin plate surface for different phases. Assuming that the vibrations are due to air pockets, the higher and smaller velocity magnitude across the thin plate surface may indicate that there is a different size of air pocket underneath the thin plate. While, if it is assumed that there is a surface wave, then what is observed is the surface wave propagating across the thin plate surface. Although, the wave may not seem to be in a typical surface wave vibration period, the issues with reflection of the surface wave at the edge of the 32 mm circular ring need to be considered. This reflection wave would cause the reflected wave to interfere with the propagating waves, creating a complex wave pattern as shown in Figure 4.18.

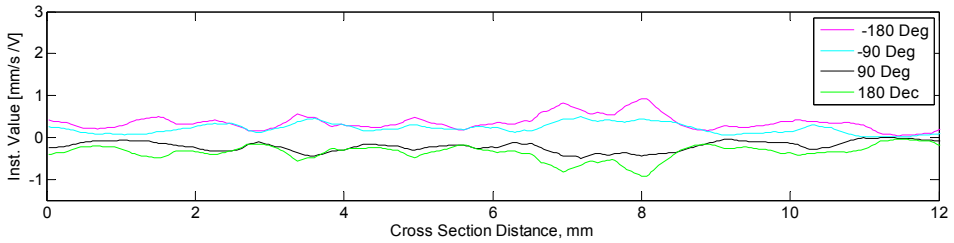

Figure 4.18: Plot of Thin Plate Surface Deformation Outside the Cavity Periphery for Different Phases

4.4.2 Impulse Response

In order to characterise the device impulse and frequency response, a typical setup for the measurement is shown in Figure 4.19. A Panametrics Model 6062PR pulser/receiver is utilised to generate a wideband excitation pulse. The excitation voltage will cause the electrostatic ultrasonic transducer membrane to vibrate thus producing sound waves in the load medium. The glass block reflects the sound waves to the transducer; this received sound wave will then be converted into an electrical signal. A digital storage oscilloscope is then employed to record the received signal prior to analysis or additional processing using the fast Fourier transform.

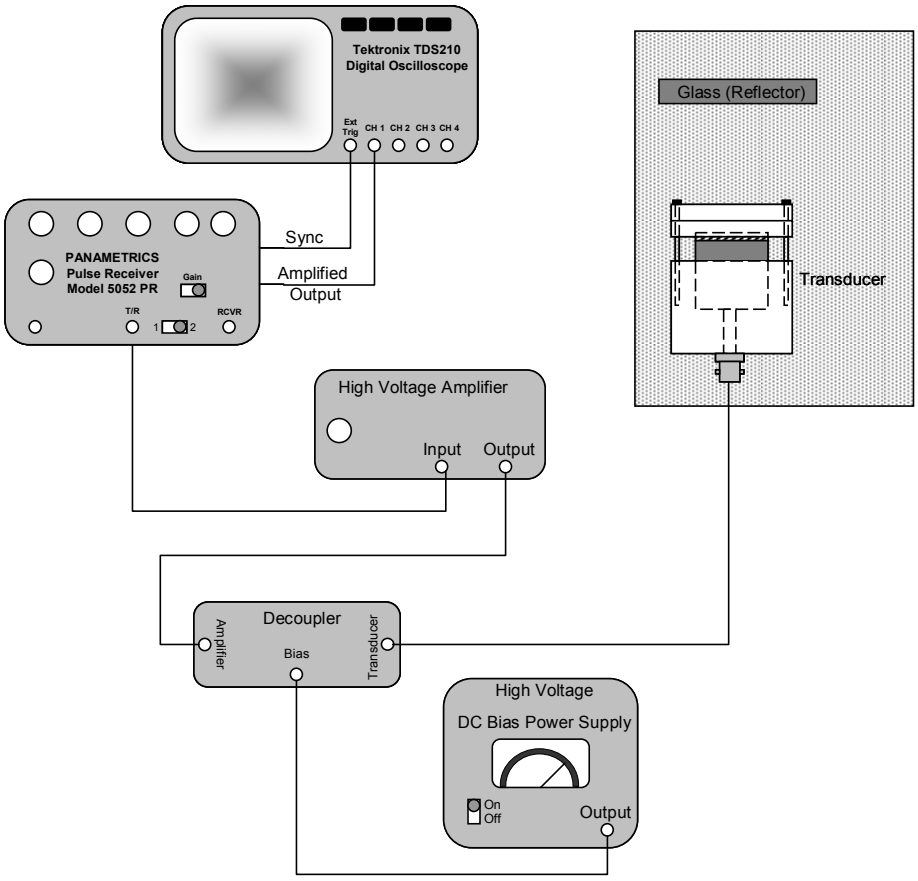

Figure 4.19: Schematic Diagram of Setup for Pulse-Echo Measurement [57]

The experimentally measured data are then compared to the FEA derived response in either the time or the frequency domain. The echo signal set at a distance of 200 mm received through the pulse-echo method could be observed in Figure 4.20. The corresponding frequency spectrum through the Fast Fourier Transform (FFT) is shown in Figure 4.21. From the FFT data, it could be deduced that the resonant frequency of the device is at around 220 kHz. Due to the single unit cell design, the output from the electrostatic transducer designed at 25 kHz is expected to be low as observed in Figure 4.21. With the cavity area of 0.04 mm^2 to the overall active transducer area of 0.71 mm^2, the expected output the transducer would mainly be from the roughened surface. As such, to investigate the matter further a surface deformation profile utilising the laser vibrometer have been performed at the frequency of 220 kHz. The surface deformation profile for the 220 kHz could be observed in Figure 4.22. From the Figure 4.22, it could be observed that the whole

surface is vibrating, thus causing the 220 kHz pressure output to overshadow the 25 kHz pressure output. In addition, as could be observed, approximately 70% of the surface area is vibrating in phase, causing the higher amplitude at 220 kHz observed in Figure 4.21.

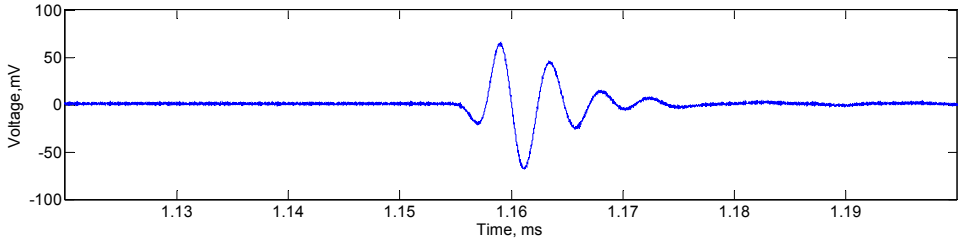

Figure 4.20: Plot of Time Domain for Signal Receive through the Pulse-Echo Method

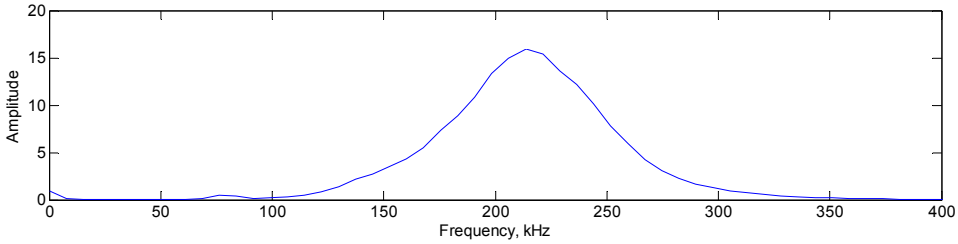

Figure 4.21: Plot of Frequency Spectrum through FFT Transformation

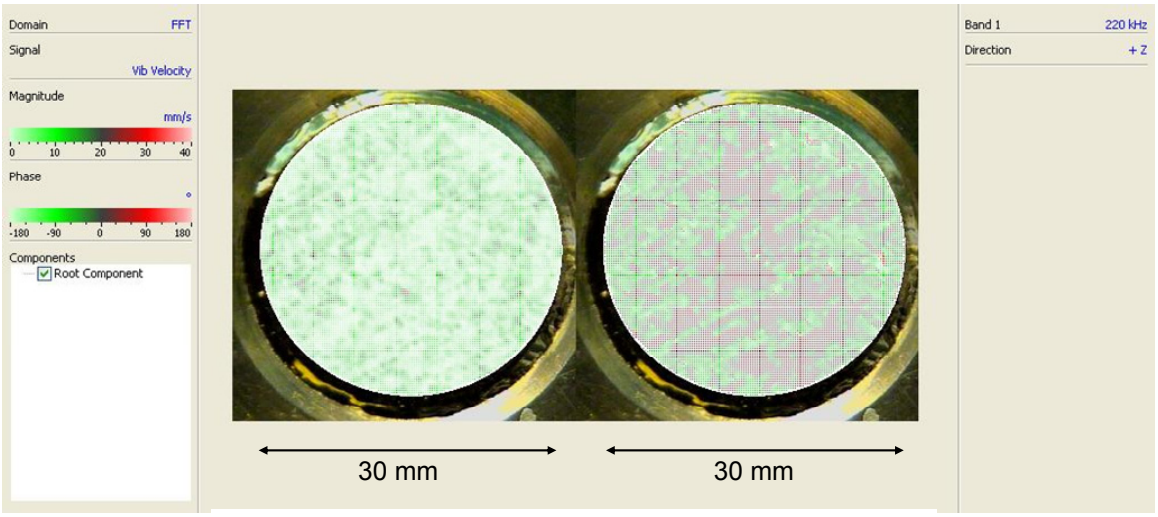

Figure 4.22: Plot of Surface Deformation Profile for FLAUT at Frequency of 220 kHz

From the plot in Figure 4.20, it could be observed that the output voltage measured is at around 75 mV. This measurement does include the effect of attenuation due to air. The lab conditions during the measurements are assumed to be at the standard temperature, relative humidity and pressure of 20^{o}C, 50% and 101.325 kPa respectively. Thus, since the measurement is performed at a distance of 200 mm and resonant frequency of around 200 kHz, then attenuation coefficient could be identified [129] to be at 3 dB/m – giving the loss due to attenuation in air for the 200 mm distance round trip to be at 1.2 dB. As previously described, in an imaging situation, in order for a defect to be detected - the wavelength needs to be smaller than the expected defect. In this case, the wavelength is calculated to be at 1.6 mm, giving rise to the same expected imaging resolution.

4.4.3 Directivity and Frequency response

In contrast to the wide band excitation in pulse-echo measurement technique, in a directivity and frequency response measurement, a calibrated microphone is placed at a predetermined distance in front of an active surface of the transducer under test. A Brüel and Kjær (B&K) 4138 eighth-inch microphone in conjunction with a B&K 2690 conditioning amplifier is employed to measure the resultant acoustical output. The microphone has a calibrated frequency response of between 6.5 Hz and 140 kHz, and a maximum sensitivity of 1 mV/Pa. A B&K 2670 preamplifier is incorporated into the body of the microphone, which has a flat frequency response over the range of 15 Hz to 200 kHz.

In a directivity response, the transducer is driven with a defined waveform at a single frequency. A two-stage manipulator (X-Y direction) is utilised to move the transducer laterally, while a one-stage manipulator (Z-direction) is utilised to move the microphone axially to produce the acoustic beam profile. An automated procedure using Labview^{TM} virtual instrument has been employed. The Labview software could be configured either to save the waveform or to save the peak voltage output over the desired spatial range and resolution for further analysis. The

excitation and receive waveforms were also displayed in a digital storage oscilloscope. A complete setup for the frequency response measurement is illustrated in Figure 4.23. The simulated and measured directivity responses in terms of beam profile response for a 25 kHz FLAUT design could be observed in Figure 4.24. (The detail of the simulation process will be explained in Chapter 6). From the comparison, it could be observed that the two plots have almost the same beam profile for the main lobe. It could be observed as well, that the simulated side lobe profile does corroborate generally with the measured, with some variations.

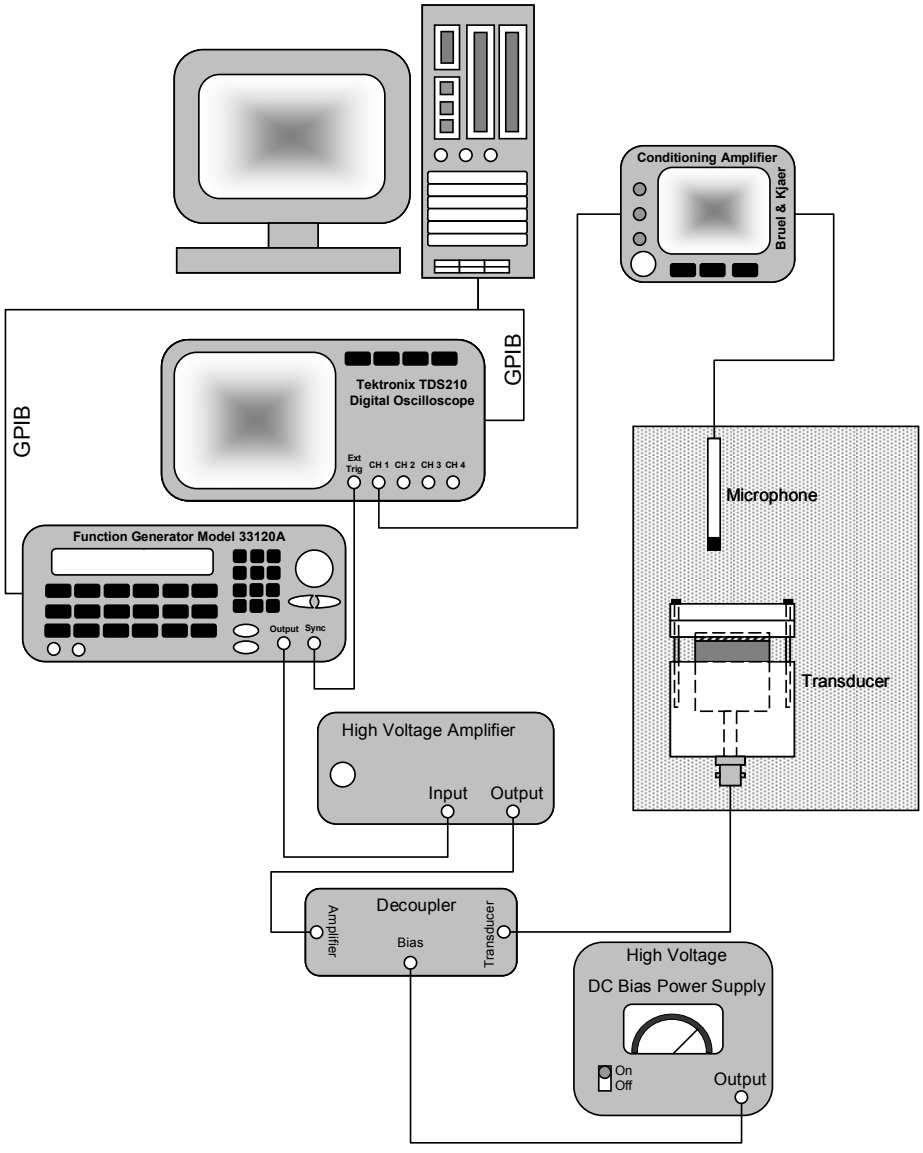

Figure 4.23: Schematic Diagram of Setup for Directivity and Frequency Response Measurement [55]

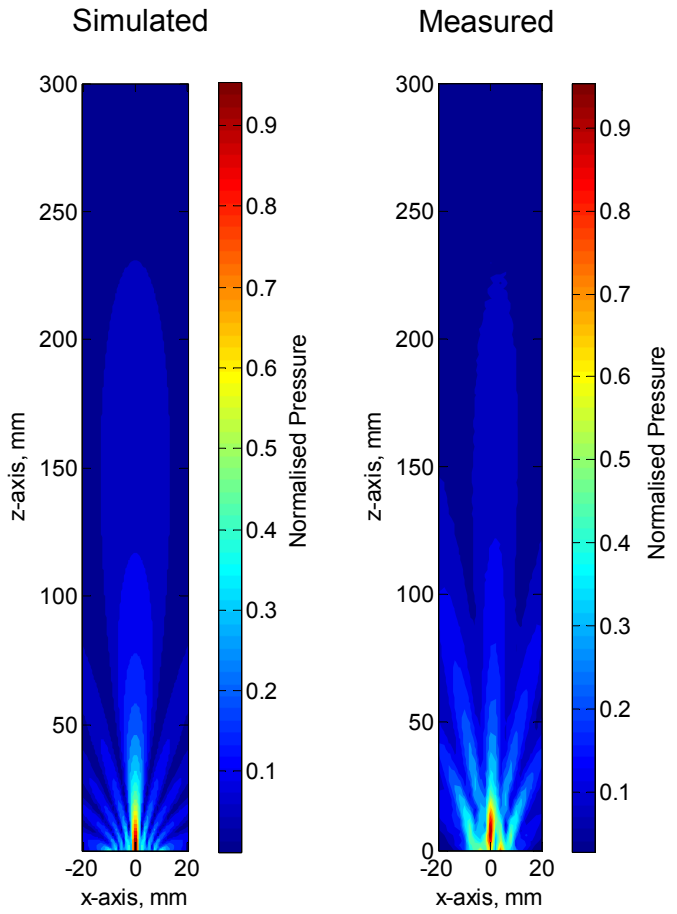

Figure 4.24: Plot of Simulated Beam Profile (Left) and Measured Directivity Profile Response (Right) and for 25 kHz Transducer Design as a Function of Normalised Pressure Amplitudes

In a frequency response, the transducer to be driven at a defined waveform over a range of frequency at a specified distance from the microphone. An automated procedure using Labview^{TM} virtual instrument, which has the same capability as in directivity response has been employed. The Labview software is configured to save the peak voltage output over the desired frequency range for further analysis.

4.5 Measuring and Verification of Prototypes

It has been mentioned that there are three types of verification that could be performed, which are the laser interferometer, the pulse-echo measurement and the

field characteristics as a function of frequency. However, since the initial prototypes are single cell devices, assessment of their behaviour will be limited to laser vibrometry in order to visualise the surface deformation – in particular the mode shape of the vibration. The scanning nature of the vibrometry measurement allows identification of the thin plate resonances and visualisation of the mode shapes. The pulse-echo and beam profile measurement would not provide further useful information for the assessment of the single cell designs. Due to the single cell design, testing has shown that the pressure outputs are too low to be detected through a pulse-echo method; and the pressure outputs are noisy for a microphone to detect at a distance. In essence, the Signal to Noise ratio of the single cell design is low due to the low pressure output and high noise level found during the test performed. From the analysis, it was found that the pressure output observed using the pulse-echo method with a single cell is mostly due to the rough surfaces surrounding the single cell cavity/pipe. Since the excitation is provided by a broadband chirp, this will excite all of the available modes within the device including the modes in the surrounding rough surfaces.

In order to compare simulated data as shown in Figure 3.32 and Figure 3.34, the frequency response of the FLAUT transducer designed at 34.5 kHz using the laser interferometer measurement has been performed and is shown in Figure 4.25. From the Figure 4.25, it could be observed that the peak frequency is at around 36.6 kHz. The full geometrical parameter of the device had been tabled previously in Table 3.5. The acquired surface deformation data for the 34.5 kHz transducer has been used to determine the mode shape of the resonance at the measured peak frequency – the mode shape is shown in Figure 4.26. From the plot, it could be identified that the vibrational mode at 36.6 kHz is at fundamental mode (0,1) with uniform phase across the vibrating membrane and a peak magnitude of around 100 mm/s /V.

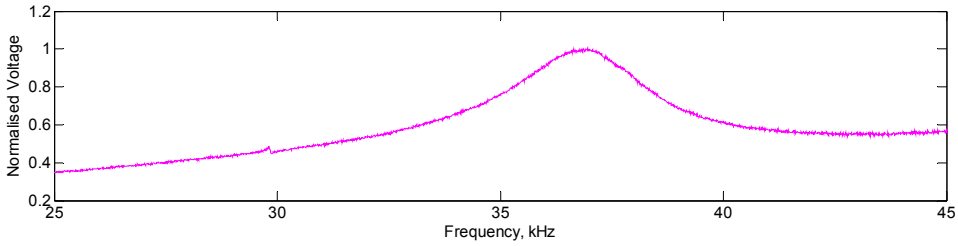

Figure 4.25: Plot of Frequency Response for Measured 34.5 kHz Cavity/Pipe Design

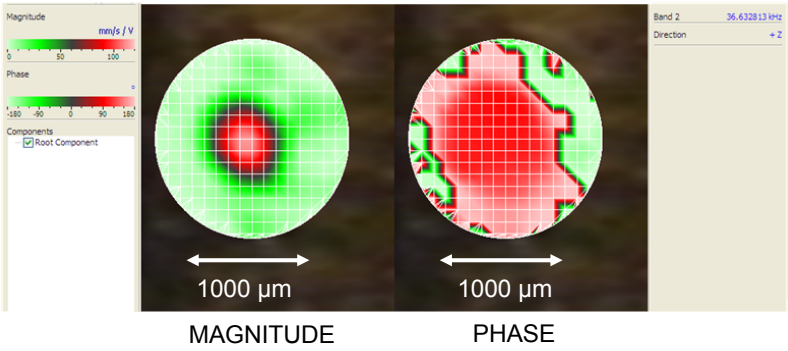

Figure 4.26: Plot of Vibrational Mode for 34.5 kHz Transducer Design, which Shows Left: Magnitude and Right: Phase of the Vibrational Mode

The laser interferometer measured average surface deformation across the entire membrane surface as a function of frequency for the 34.5 kHz transducer design is then compared to the simulated single point surface deformation at the centre of the membrane as a function of frequency. The laser measured resonant frequency and the simulated finite element modelling resonant frequency, identified by the peak normalised surface deformation amplitude across the frequency spectrum of 25 kHz to 45 kHz have been compared and is shown in Figure 4.27. From the measurement it was found that the difference between Comsol FEA and the measured results is about 6%. However, the Comsol FEA corroborated generally with relatively low differences to the analytical model at around 1.5%. On the other hand, comparing the PZFlex FEA and the measured results, the difference is at 10%. The PZFlex results also have a difference of 4% with the analytical model. This gives the impression that the simulation results are suitable to be utilised for future modelling within the

FLAUT scope for both technique of simulation analytical and FEA with an acceptable error of 10%.

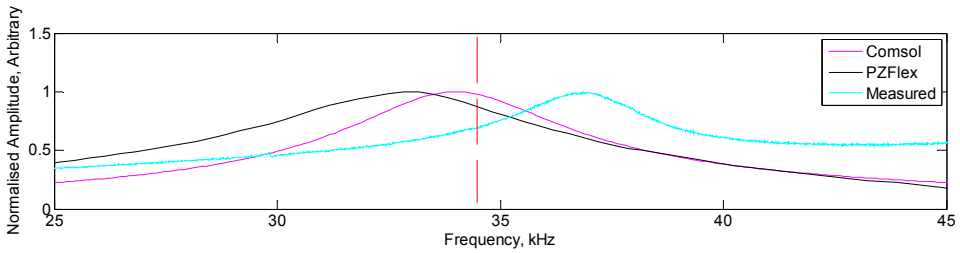

Figure 4.27: Plot of Comparison between Measured Using Laser Interferometer and Simulation Using Comsol and PZFlex as a Function of Frequency for 34.5 kHz FLAUT Device

There are two main possible corresponding contributions to this error, which are: due to the different data set points between measurement and simulation; and due to the fabrication of MSL. As stated previously, the finite element modelling resonant frequency is based on the surface deformation dataset taken at a single point in the centre of the membrane. While, the measured resonant frequency is based on the surface deformation measurements across the entire measured surface, and thus giving the possibility of causing the FLAUT resonant frequency to differ between the simulation and measurement. In addition, by taking an average measurement across the surface, the dataset would include different phases of surface deformation across the whole measured surface; which may also cause the resonant frequency to differ when compared to simulation.

Secondly, MSL being an additive process, tend to produce surfaces that are not perfectly smooth at the edges of the cavity. This causes air to flow from edges of the cavity as shown in Figure 4.26. This could be observed by the small phase difference between the centre of the cavity and the periphery. Since, the MSL UV curing process is typically performed in a straight-line vector, tiny grooves lines results due to the surface tensions during UV curing on the peripheral surfaces to the cavity. This is indicated by the elongated phase difference in Figure 4.26, which shows that the thin plate is not fully clamped at the edges, thus causing the active air cavity diameter to differ compared to model. This is due to the increased in the size of the air gap surrounding the cavity edges, subjected by the plate clamping edges change

from circumference of the cavity to a larger area as depicted by the phase plot. In order to comprehend the situation further, an analysis using the measured phase plot has been performed.

In addition, since FLAUT is an amplification system, whereby three different component – thin plate, cavity and pipe need to work synergistically; the mismatch in resonant frequency between the three different components would also cause FLAUT not to perform effectively. From the Figure 4.26, there is also a possibility of a mismatch between the cavity and the thin plate resonant frequency, whereby the thin plate is vibrating in a much larger surface area when compared to the cavity diameter – thus causing the overall frequency to shift.

As previously discussed, the thin plate is observed to be supported i.e. not fully clamped at the edges of the cavity, thus having a much larger surface area. In order for the observation to be analysed, a simplified model that considers three main criteria have been identified.

- Using the geometric size from the phase, the near common phase could be measured and approximated to be around 1050 μm wide (x-axis) by 1700 μm (y-axis) length, rectangular in shape. The edged of the rectangular thin plate are assumed to be moving freely, as shown by the phase plot in Figure 4.26.
- Next, as the cavity is not fully clamped at its circumference and it is also not fully free; a built-in internal boundary condition in Comsol FEA is utilised. This boundary condition would enable the plate to displace at the cavity circumference but still having the expected influence to the periphery.
- The pressure input is expected to be mainly from the active area - which is within the cavity diameter. A pressure input of 1 Pa, is added as a boundary condition at the thin plate-air interface (z-axis), to simulate such a situation.

However, due to the boundary condition, 3D modelling is required; in view of the fact that it is not possible to perform the above condition is 2D or 2D axial symmetry. Thus, based on the assumption above, a frequency response simulation has been performed using Comsol FEA and is shown as Figure 4.28.

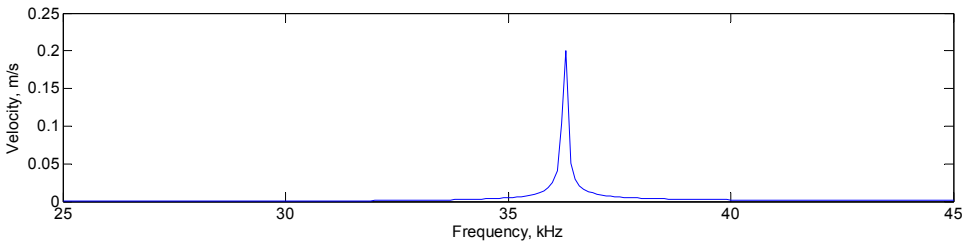

Figure 4.28: Plot of Simulated Frequency Domain Response for 34.5 kHz FLAUT Device Incorporating Supporting Cavity Periphery

As shown in Figure 4.28 the resonant frequency is at 36.3 kHz, which is 0.3 kHz or 0.8% error from the measured. This is expected since the error could be due to the approximation of the rectangular size identified previously from the phase plot in Figure 4.26. From the plot in Figure 4.29 (Top), it could be observed that the thin plate does not displace in a fully concentric circle, but in a slightly elongated manner due to the influence of the rectangular periphery. This is clearly noted with the results from the measurement in Figure 4.26 (Left), whereby the thin plate is also displaced in a similar condition. In addition, when the phase plots in Figure 4.29 and Figure 4.26 are compared, it could be noticed that the phase change is also similar within the surrounding area, i.e. there is a 180^{o} phase change between the centre and the periphery, denoted by red-green and red-blue respectively. In addition, as observed in Figure 4.29, the simulated phase is also elongated suggesting the same influence noted previously. However, the 90^{o} phase difference between the cavity diameter edges and the other edges, which is observable in the measurement, is not observable in the simulation. This may be due to approximation assumptions within the boundary condition such as the size or shape of the external influence periphery of the cavity and differential influence of the cavity to its periphery.

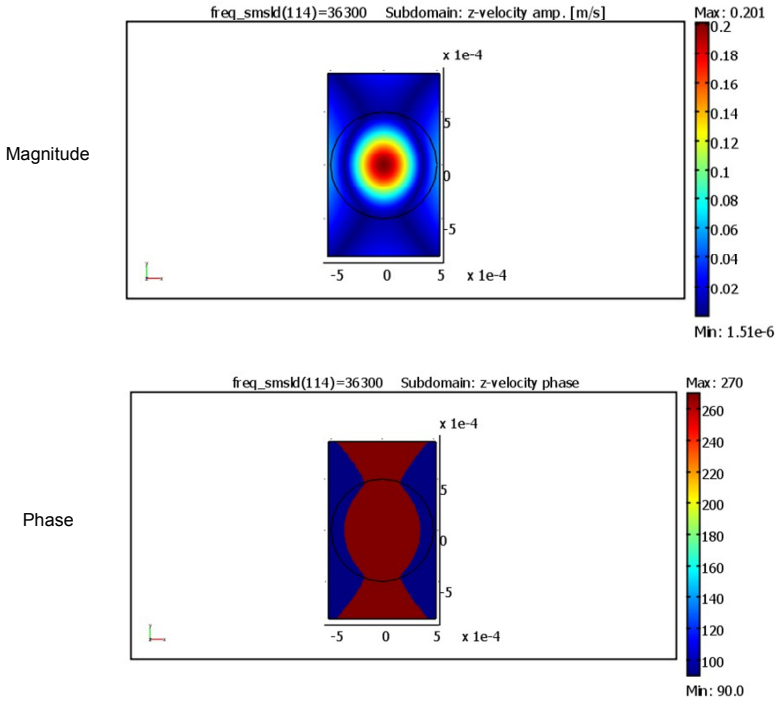

Figure 4.29: Plot of Simulation for Thin Plate Cavity and Supporting Influence; Magnitude (Top), Phase (Bottom)

Thus, from the simulation and measurement, it could be concluded that there is generally good correlation with a gross error of around less than 10% between the analytical/FEA predicted design of 34.5 kHz transducer and the measured results. As depicted earlier, this error is due to the differences in dataset between the FEA simulation and the laser measurement; and issues with the fabrication process.

4.6 Effect of Resonant Frequency Due to Pipe Radius

4.6.1 Introduction

Previously, a method to identify and match a design of a FLAUT have been fully described and developed. In addition to the previously mentioned processes, it is also important that the characterisation of FLAUT behaviour is performed to enable an

effective optimisation process. Utilising the same technique to identify the resonant frequency and its suitable geometry for a FLAUT as previously described, changes to the geometry that affect the resonant frequency have been identified.

Although, there are three main choices that need to be made when designing a FLAUT transducer which are thickness of the thin plate, the cavity radius and the pipe radius; in most cases, the designers actually only need to be concerned with only a single parameter which is cavity radius. This is mainly because in most instances the choice is to have as thin of a thin plate as practically possible to enable a high sensitivity of the device [56]. Unless it is a CMUT type of device where the diaphragm is designed co-dependently, the thin plate thickness within the context of this thesis is constrained by the commercially available thin plate thicknesses which are 8 μm, 13 μm, 25 μm, 50 μm and 75 μm for Kapton [100]. Next, with regards to cavity radius, the designer mostly does not need to be concerned with the geometric design, but instead on the operating frequency required. This is due to the fact that operating frequency of the device is directly coupled to the cavity radius or thin plate radius as illustrated in Figure 3.19. The term thin plate radius and cavity radius could be used interchangeably because the thin plate is assumed to be stationary at the cavity diameter circumference. In this case, since the thin plate is assumed to be stationary at its edges, then the cavity radius could be considered the thin plate radius since the size of the thin plate radius is the same as the cavity radius.

Since the pipe is fundamental to the desired amplification, it is important to analyse the pipe geometry in this regard. The selection of the pipe geometry must ensure that the resonant frequency of the pipe is matched to the cavity and the thin plate resonant frequency. Thus, it is also the intention of this thesis to identify the optimum pipe radius for the design.

4.6.2 Identification of Suitable Pipe Radius

Previously through experiment, Tan and Miao [82] has shown that in order to increase the pressure output of a condenser microphone, the exhaust hole needed to be made as large as possible. However, in order to verify that this conclusion is true even for a FLAUT, a simulation and subsequent validation has been performed using the following thin plate and cavity design.

To investigate the effect of pipe radius only; the FLAUT geometry (with the exception of pipe geometry) and the resonant frequency need to be made constant. As such, utilising the thin plate and cavity combination detailed in Table 4.2 - the required pipe length for a specified pipe radius as a function of frequency can be calculated using Equation 3.14.

Table 4.2: Table of Thin Plate and Cavity Combination with Resonant Frequency of 29.44 kHz

Design Parameters	Plate Resonance, kHz	Cavity Resonance, kHz
Thin Plate thickness = 25 μm Thin Plate radius = 750 μm Cavity depth = 112 μm	29.44	29.44

Given three different scenarios of cavity radius to pipe radius ratio of 1.07, 1.5 and 2.5, with pipe radius of 700 μm, 500 μm and 300 μm respectively; the equivalent pipe length for a given frequency of 29.44 kHz as noted by the dotted-hash red line could be identified from Figure 4.30 - with the detailed pipe radius and pipe length given in Table 4.3.

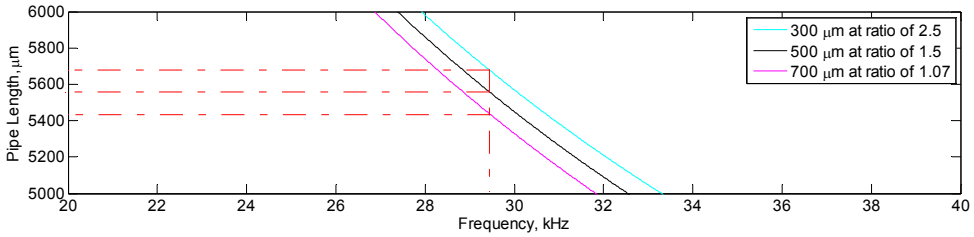

Figure 4.30: Plot of Pipe Length as a Function of Frequency for a Given Pipe Radius with Ratio of 2.5, 1.5 and 1.07

Table 4.3: Table of FLAUT Design Dimensions and the Expected Resonance Frequency for Pipe Radius Changes

Design Parameters		Plate Resonance, kHz	Cavity Resonance, kHz	Pipe Resonance, kHz
Thin Plate thickness = 25 μm Thin Plate radius = 750 μm Cavity depth = 112 μm		29.44	29.44	29.44
Pipe Change Parameters				
Pipe Radius	Pipe Length			
700 μm	5439 μm			
500 μm	5559 μm			
300 μm	5679 μm			

From Table 4.3, it could be observed that for a single thin plate and cavity combination, there are three different pipe diameter and pipe length combinations. These three different pipe diameter and pipe length combinations represent three different analytical models given the same operating and resonant frequency for all three models. It is important to note that the aspect ratio of the pipe length to radius has an inverse linear relationship with a slope of 0.6; of which the resonant frequency of the device determines the linear intersect of the plot. Therefore, a larger radius will result in a shorter pipe as shown in Table 4.3 and Figure 4.31. However, the previous analysis only indicates the pipe length and pipe diameter required for a

given resonant frequency. In order to analyse the expected pipe output given a specific pipe input, a FEA analysis for the three different pipe length and pipe diameter combinations has been performed using Comsol and is shown in Figure 4.32

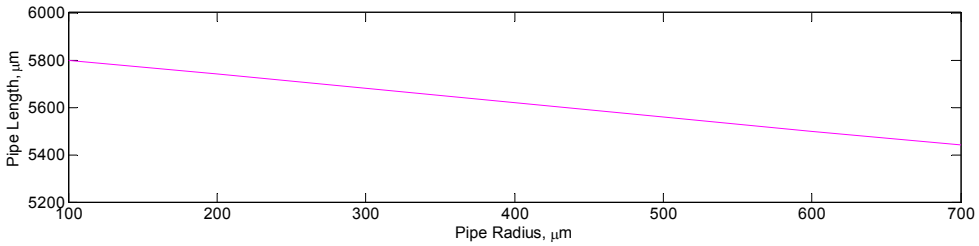

Figure 4.31: Plot of Pipe Length as a Function of Pipe Radius at Resonant Frequency of 29.44 kHz

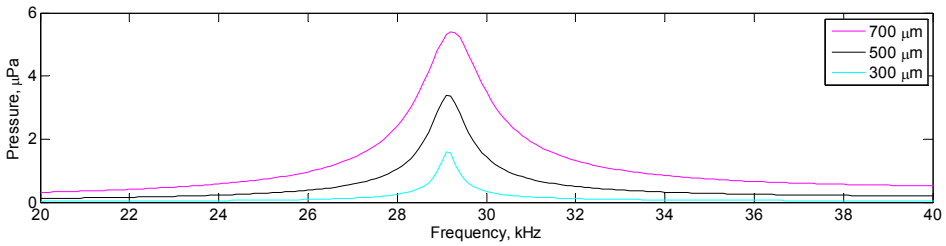

Figure 4.32: Plot of Simulation of Geometrical Pressure Output at Pipe-Air Interface Using Comsol as a Function of Frequency for Three Different Pipe Radii Identified in Table 4.3

From Figure 4.32, it has been shown that the resonant frequency of the pipe does match closely with the design resonant frequency with all different pipe length/pipe diameter combinations having the same centre frequency of around 29.1 kHz. This gives an error of 0.34 kHz or 1.2% between the analytical model and the FEA model. It is important to observe, based on the FEA simulated results shown in Figure 4.32 with all having the same input pressure of 1 Pa at one end of the pipe, the maximum absolute pressure output at the other end of the pipe is 5.4 μPa, 3.4 μPa and 1.6 μPa for 700 μm, 500 μm, and 300 μm respectively. This is expected due to the different pipe radii and thus consequently the different pipe length between each of them. According to Rossing and Fletcher [94] if the pipes are assumed to be rigid, perfectly

smooth and thermally insulating then the existence of the pipe has no effect in wave propagation. However, this may not always be the case as has been discussed earlier. Due to the nature of the MSL process that requires layer by layer UV curing; the wall of the pipe could not fabricated as a perfectly smooth wall.

While the data shown in Figure 4.32 indicate that the shorter pipe length will result in enhanced pressure output, it is the thin plate vibration that is key to the overall performance of the FLAUT. Moreover, in some pipe geometries the effect of viscosity within the fluid need to be considered [94]. The nature of the wall, the viscous boundary layer, the angular velocity and the pipe radius all contribute to the effect of viscous drag [94]. In order to assess this effect, the Comsol FEA, which incorporates fluid behaviour, is employed. Utilising the fluid module, the effect of the viscous boundary condition that relates to the pipe radius and length is incorporated as part of the study to accompany the different effect of pipe radii.

Figure 4.33 shows the FLAUT normalised amplitude as a function of frequency for three different pipe radii. It can be seen from Figure 4.33 that the largest diameter pipe results in the highest FLAUT normalised amplitude. This could be explained from two points of view: Tan and Miao [130] described how viscous damping affects the surface of the cavity due to the squeezing effect of fluid. In this case, the smaller the pipe radius, the larger the remaining cavity surface influenced by the damping effect. Rossing and Fletcher [94] on the other hand, expressed that the smaller the pipe radius the larger the influence of viscous boundary layer on the pipe wall. Thus, in a small pipe radius viscosity is an issue; since the ratio of the pipe surface area to the pipe volume is higher. These two influences - the viscous damping on the surface of the cavity and the viscous boundary layer on the pipe wall; contribute to the pressure output reduction for a small pipe radius as shown in Figure 4.33.

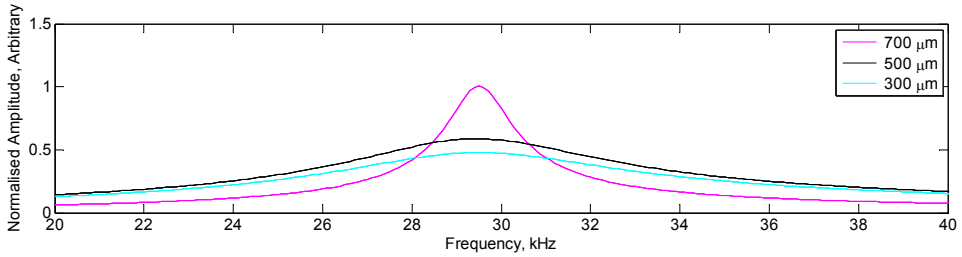

Figure 4.33: Plot of Simulation of FLAUT Normalised Amplitude as a Function of Resonant Frequency for Three Different Pipe Radii

In addition, from Figure 4.33 it could be observed that the normalised FLAUT amplitude reduces from around 1 to 0.45 for pipe radius of 700 µm to 300 µm. Thus, although the reduction is not perfectly linear, it could be considered that the output of the FLAUT is directly proportional to the size of the pipe radius as depicted in the measurement results shown in Figure 4.35.

From the simulation, it has been indicated that the output of the transducer is higher when the reduction of the cavity radius is smaller. This is to be expected, as the larger the pipe radius the larger the influence of the pipe to the cavity. In order to ensure that the assumption and modelling is true, prototypes corresponding to the previous design have been fabricated.

A laser interferometer measurement has been performed to validate the previous simulation. The results from the simulation at 700 µm cavity radius and the measured results could be observed in Figure 4.34. From the comparison it could be deduced that the measured results and the simulated results resonant frequency have an error of about 7%; 27.3 kHz versus 29.4 kHz respectively.

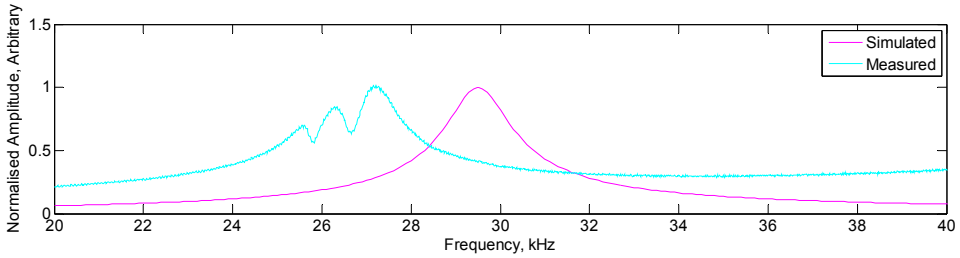

Figure 4.34: Plot of Comparison between Simulated and Measured Results for 700 µm pipe radius

In addition, results from the laser interferometer measurements for 500 µm and 300 µm are also incorporated into Figure 4.35 to illustrate the different output for the different pipe radius. From the measurement, it was observed that there are three distinct resonant frequency peaks. Although, in general it is expected that the resonant frequency to be a match with a single peak, due to the differential resonant frequency of thin plate, cavity and pipe and non-perfect matching due to geometry tolerances during fabrication, these peaks of around 25.5 kHz, 26.2 kHz and 27.2 kHz are observed. Further affects due to the different manufacturing equipment, which affects the machine resolution and thus the resonant frequency output, will be explained later in the Chapter.

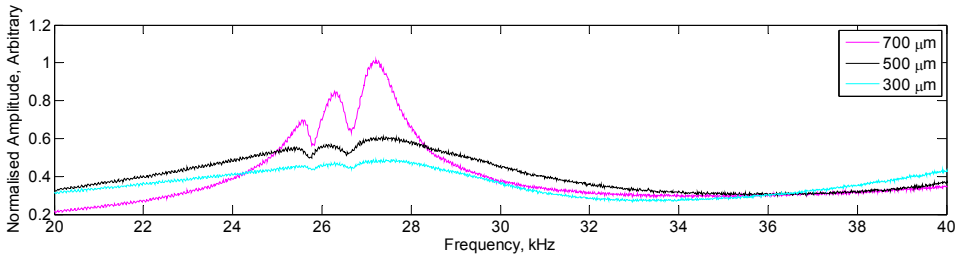

Figure 4.35: Plot of Frequency Response using Laser Interferometer Measurement for 700 µm, 500 µm and 300 µm Pipe Radius Dimensions

Moreover, there are also issues with the layer-by-layer fabrication that causes an increase in the pipe viscous effect. Theoretically, it is expected that the pipe is smooth and rigid to counteract the viscous effect due to the pipe surface roughness and the mechanical vibration. However, due to the nature of the MSL prototyping process, this may not be fully possible; as such the error considered within this thesis could be further reduced if smoother surface is fabricated and a much rigid material are used.

4.6.3 Summary

From the simulations and measurements of the different pipe radii it could be deduced that for FLAUT output sensitivity to be maximised the pipe radius needs to

be as large as practically possible. In this exercise, the ratio utilised was at 93% of the cavity radius. It is also determined from the output measurement that there is a law of compounding returns whereby at small pipe radius, the output sensitivity does not make a significant improvement as observed in Figure 4.35 - when the pipe radius is increased from 300 μm to 500 μm. However, when the pipe radius is increased from 500 μm to 700 μm, a significant improvement in output sensitivity is observed. Furthermore, it is also found that there is a need to incorporate the effect of the pipe wall especially when the geometric sizes are small because the smaller the size the larger the effect of the viscous boundary layer and viscous damping.

4.7 Effect to Resonant Frequency due to Machine Resolution

4.7.1 Introduction

Previously it has been shown that in order to maximise the pressure output of a FLAUT the active membrane should be as thin as possible, the resonant frequency of the thin plate, cavity and pipe should be matched and the pipe radius should be as large as possible. This technical concept seems to be the solution to enable a good FLAUT output.

However, one of the features that also needs to be considered on top of the design specification is the manufacturing capability. In this section, the need to identify suitable machine resolution and the effect of tolerances during fabrication of prototypes will be discussed with a view to understanding the influence of fabrication accuracy on device performance. At the end of this section, it will be concluded that a suitable manufacturing process with the tolerance required if the desired output from the FLAUT is to be realised.

4.7.2 Manufacturing Sensitivity Analysis

One of the most common challenges in any design and development process is to assure that the manufacturing and fabrication processes are able to produce a prototype that matches the design specification. In general, the choice of manufacturing route is chosen based either on experience or from recommendation. However, those recommendations may or may not suit the current design requirement.

As such, a method that is able to quantify the level of error expected by the recommended manufacturing processes needs to be developed. In most cases, the errors are due to the differences between the design requirement and the final prototype geometry. In the case of a FLAUT device, in order to increase the resonant frequency the FLAUT dimensions must be scaled down accordingly. For example, in order to increase the resonant frequency of the FLAUT device to 100 kHz; the cavity and pipe diameter need to be reduced to around 400 μm and 300 μm respectively, with the cavity depth being reduced to a mere 30 μm. Thus, to ensure that a good corroboration could be made between the design and the prototype geometry, manufacturing tolerances need to be identified and expected error due to the tolerance analysed.

In order to identify the required geometric tolerance to enable a good matching of thin plate, cavity and pipe, a manufacturing sensitivity analysis would need to be performed. The manufacturing sensitivity analysis would enable subsequent designs to be assessed based on the identified tolerances for a given manufacturing route.

The sensitivity analysis that will be performed analyses the propagated errors and propagated uncertainties, that arise from the machining tolerances during fabrication of prototypes; which is an error associated with the design when compared to the manufactured components. As such, this error will be propagated from the dimensional tolerances to the resultant resonant frequency. Since, there is a need to

ensure that the matching between the thin plate, cavity and pipe is consistent, the need to identify the error in fabrication is significantly important.

In order to derive a propagation error, there are two main attributes that needs to be known - the output or desired results in this case the FLAUT resonant frequency and the FLAUT dependent variables in this case cavity radius, r_m, cavity depth, d_a, pipe radius, r_p, and actual pipe length, l_a. This could be re-written as such that the resonant frequency, F_n is a function of the dependent variable as shown in Equation 4.1.

$$F_n = f(r_m, d_a, r_p, l_a) \qquad \textbf{Equation 4.1}$$

Using the statistical relationship as expressed by Kass [131], the propagation of error for the resonant frequency, F_n could be simplified by taking the sum of partial derivates of F_n with respect to each of the variables as shown in Equation 4.2.

$$\sigma_{F_n} = \sqrt{\left(\frac{\delta F_n}{\delta r_m}\right)^2 \sigma_{r_m}^2 + \left(\frac{\delta F_n}{\delta d_a}\right)^2 \sigma_{da}^2 + \left(\frac{\delta F_n}{\delta r_p}\right)^2 \sigma_{rp}^2 + \left(\frac{\delta F_n}{\delta l_a}\right)^2 \sigma_{la}^2} \qquad \textbf{Equation 4.2}$$

Equation 4.2 above is the generalised term for the error propagation within the context of FLAUT. However, it is important to note that there is a specific propagation of error for each resonant frequency of thin plate, cavity and pipe.

From the generalised propagation of error above, a specific resonant frequency based on the geometry will be identified. The propagation of error for the FLAUT resonant frequency could not be generalised in a single form due to the fact that different geometry is being influenced by the different constructional parameters. For example in the case of the thin plate, the only parameter that could be controlled during manufacture, which affects the resonant frequency of the thin plate, is the plate radius. The rest of the parameters could not be controlled due to the Kapton film being commercially sourced. As shown in technical data sheet given by DuPont [100], a typical residual shrinkage of 0.17% is expected when a 25 μm thick Kapton

film is exposed to an elevated temperature of 150^{o}C. Furthermore, based on the data sheet, the typical residual shrinkage reduces linearly as the thickness of the Kapton film reduces. In addition, DuPont also indicate that for temperature range of 30^{o}C to 100^{o}C, the thermal coefficient of expansion for Kapton is at 17 ppm/^{o}C.

To investigate error influenced by the MSL fabrication technique, the MSL machine resolution utilised in producing the previous prototypes has been utilised to demonstrate the importance of identifying the manufacturing sensitivity. Despite the X-Y direction having a different resolution, for the purpose of this study the maximal resolution of 84 μm has been chosen for both X-Y directions. This is mainly to simplify the study.

Although, based on the machine resolution it is expected that the dimensions produced by the MSL will be within the stipulated tolerances, based on the author's investigation, it was found that this is not always the case. Due to variability within the movement of the stepper motor as well as surface tension of the material during fabrication, the final backplate dimensions may have an error above the expected machine resolution tolerances.

4.7.2.1 Thin Plate

As mention previously, the main influence that could be controlled during fabrication of the FLAUT backplate is the thin plate radius or effectively the cavity radius. This is because the thin plate is theoretically considered fixed at the edge of the cavity radius. From the variable derived from Equation 3.4, it could be deduced that there are more than two variables that determine the resonant frequency of the thin plate. Since, all of the thin plates materials employed are commercially available Kapton films from the same manufacturer, to this end the elastic properties are considered constant and only the thin plate radius is considered in the analysis. However, it is important to note that the commercially available thin films such as Kapton film will still have a tolerance of around +/- 10% of the nominal thickness [100]

In this case, according to Equation 4.2, the propagation error for thin plate could be simplified to Equation 4.3.

$$\sigma_{F_{tnp}} = \sqrt{\left(\frac{\delta F_{tnp}}{\delta r_m}\right)^2 \sigma^2_{r_m}} \qquad \textbf{Equation 4.3}$$

Utilising Equation 3.4 and performing the partial derivative for the effective variable r_m, the propagation error with respect to resonant frequency of thin plate could be observed in Figure 4.36.

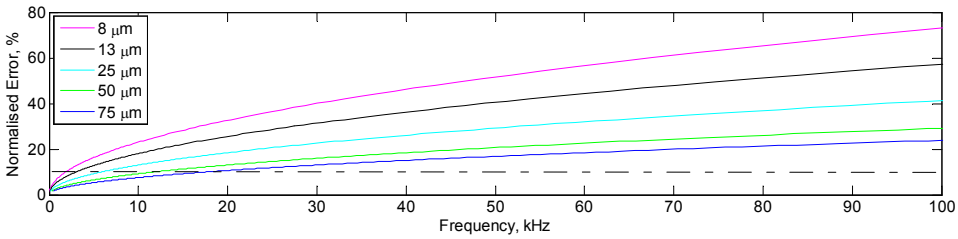

Figure 4.36: Plot of Propagation Error with respect to Resonant Frequency of Thin Plate

From Figure 4.36, it can be seen that if a 10% error is considered the maximum allowable tolerance, then the highest frequency that the MSL could produce to enable satisfactory matching thin plate resonant frequency is at around 20 kHz for a 75 μm thickness thin plate and 2 kHz for 8 μm thickness plate.

4.7.2.2 Cavity

Utilising the same technique as mentioned previously, there are five variables that could influence the resonant frequency of a cavity which are the adiabatic constant of air, the applied atmospheric pressure, the density of the thin plate, the thickness of the thin plate and the depth of the cavity.

Based on the same argument above, there is only one parameter that is influenced by the manufacturing process, which is the cavity depth. The rest of the parameters

could be considered as constant because they are beyond the control of the manufacturing processes.

Thus, according to Equation 4.2, the propagation error for the cavity could be simplified to Equation 4.4.

$$\sigma_{F_{nc}} = \sqrt{\left(\frac{\delta F_{nc}}{\delta d_a}\right)^2 \sigma^2_{d_a}} \qquad \textbf{Equation 4.4}$$

Utilising Equation 3.6 and performing the partial derivative for the effective variable d_a, the propagation error with respect to resonant frequency of plate could be observed in Figure 4.37.

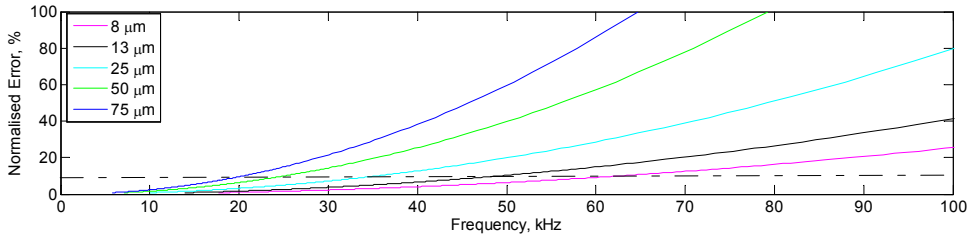

Figure 4.37: Plot of Propagation Error with respect to Resonant Frequency of Cavity

From Figure 4.37, it could be deduced that if a 10% error is considered the maximum allowable tolerance, then the highest frequency that the MSL could be utilised to fabricate a FLAUT device to enable a good matching cavity resonant frequency is at 20 kHz for a 75 μm thickness thin plate and at around 60 kHz for a 8 μm thickness thin plate.

This tolerance effect matches well if a 75 μm thickness is considered for both thin plate radius and cavity depth. However, the same is not true for 8 μm thickness. If a 10% maximum tolerance is considered during design, the membrane would have a maximum design frequency at around 2 kHz, while the cavity at around 60 kHz. This creates an impasse for FLAUT design since there is a need to match the thin plate,

cavity and pipe resonance. In addition, from the previous example, having two distinct frequencies at the different end of the frequency spectrum, i.e. 2 kHz for membrane and 60 kHz for cavity create a challenge to match both in term of operating resonant frequency during design and during manufacture.

4.7.2.3 Pipe

As previously discussed, the maximum frequency that a MSL could produce to enable a maximum allowable error of 10% is both at 20 kHz for thin plate and cavity, with a thin plate thickness of 75 μm. Utilising the same technique again, the three main variables which could influence the pipe resonant frequency are the speed of sound in air, the pipe length and the pipe radius.

Considering the same argument, it could be assumed that the speed of sound in air is constant if the test is performed at the same temperature and pressure. Thus, in this case the variable that could be controlled during fabrication would then be the pipe length and the pipe radius.

In this sense, according to Equation 4.2, the propagation error for the pipe could be simplified into Equation 4.5 assuming that the two variables are uncorrelated in terms of statistical distribution and machine resolution.

$$\sigma_{F_{np}} = \sqrt{\left(\frac{\delta F_{np}}{\delta r_p}\right)^2 \sigma_{r_p}^2 + \left(\frac{\delta F_{np}}{\delta l_a}\right)^2 \sigma_{l_a}^2} \qquad \textbf{Equation 4.5}$$

Utilising Equation 3.10 and performing the partial derivative for the effective variables r_p and l_a, the propagation error with respect to the resonant frequency of the pipe could be observed in Figure 4.38. Due to the different nature of the design geometry between the thin plate/cavity and the pipe, the error in the pipe design is shown to be lower with a maximum error of around 3% at 100 kHz. This comes from the fact that most of the dimension for the pipe comes from its length, which has a

better machine resolution of 16 µm compared to its radius that has an 84 µm resolution. From Figure 4.38, it could be deduced that if 10% error is considered the maximum allowable tolerance, then the highest frequency that the MSL could be utilised to produce a FLAUT device to enable a good matching pipe resonant frequency is beyond the author's target frequency of 100 kHz.

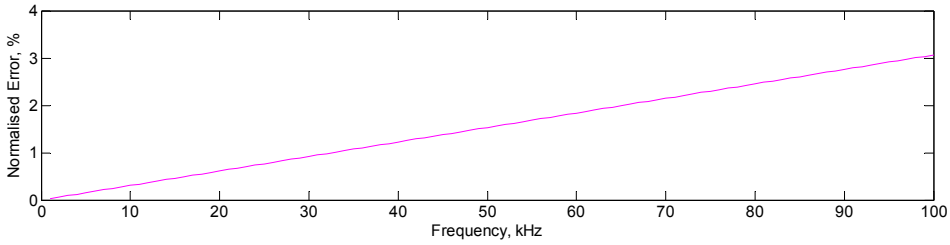

Figure 4.38: Plot of Propagation Error with respect to Resonant Frequency of Pipe

Although MSL are able to produce the pipe prototype within the 10% error limit, the need to match the resonant frequency of thin plate, cavity and pipe to within a 10% limit makes the process unsuitable for fabricating high frequency devices. In order to validate this theoretical argument, validations using the measurement have been performed.

From the measurements, it was found that the errors between the analytical model and the measurements were at 0.5 kHz, 2.5 kHz and 3 kHz for 7 kHz, 15 kHz and 30 kHz transducer designs respectively.

4.8 Conclusion

In this Chapter, a review of different manufacturing techniques that could be utilised for the manufacture of a FLAUT have been detailed. In addition, manufacturing techniques suited for the previously identify transducer design of 34.5 kHz have been identified and prototypes created and assessed experimentally. At the same time, to validate the prototypes made, a review of different measurement techniques that could be utilised to measure the prototype has been detailed. Validation and

corroboration between the simulated and measured data for the 34.5 kHz transducer has also been shown.

In addition, the effect of different pipe radius towards the device resonant frequency and output has also been discussed in detail. The suggested design towards which the device output can be maximised has also been illustrated. From the investigations, it was found that to maximise the FLAUT output, the pipe radius needs to be made as large as practically possible.

Finally, manufacturing sensitivity analysis has been performed. The effect of resonant frequency due to machine resolution has also been examined. From the examination and investigation, it was found that MSL is not suitable for high frequency device manufacture due to the expected high error during manufacture. As a conclusion, this Chapter has introduced the main key elements towards which a FLAUT is manufactured, verified and enhanced. By utilising as large a value as practically possible for the pipe radius geometry and the identification of a suitable manufacturing technique through manufacturing sensitivity analysis, the overall FLAUT output could be enhanced.

In the next Chapter, the effect of noise in an electrostatic transducer will be described. Techniques to measure sources of noise will be introduced and implemented. Subsequently in the final Chapter, high frequency devices will be modelled, manufactured and validated according to techniques developed in this and previous chapters; along with the effect of noise discussed in the next Chapter.

5. Modelling and Measuring FLAUT Noise

5.1 Introduction

In the previous three Chapters, issues with signal sensitivity analysis in terms of both modelling and measurements have been discussed. The issue of signal sensitivity is important as it determines the efficiency of a particular transducer or device. There are two types of signal sensitivity which are the transmit sensitivity and receive sensitivity. Generally, transmit sensitivity is the efficiency of an electrical input of a transducer being converted into pressure output measured at a specified distance from the transmitter and is often expressed in μPa/V; while receive sensitivity is the efficiency of a transducer to convert the input pressure into the electrical output measured at a specified distance from a calibrated transmitter and is often expressed as V/μPa. Thus, a sensitive transducer in transmit mode is a transducer which is able to convert the smallest input voltage into a large pressure output; while a sensitive transducer in receive mode is a transducer which is able to detect the smallest amount of pressure, and thus convert it into an electrical signal. For example, in a pulse-echo transmission technique, a transducer that has a good sensitivity in both transmit and receive would lead to a device that is able to transmit strong acoustic pressure to the test object and reciprocally is able to detect weak echo signal from the test object. This is why improving signal sensitivity is important.

In addition to improving signal sensitivity, it is also important that the inherent noise level is determined, controlled and ideally reduced. Having a high sensitivity alone is not sufficient. In general, a SNR improvement is required. This requires a focus on two main items; enhancing the signal sensitivity and at the same time maintaining or even reducing the baseline noise level.

In this Chapter, the development and implementation of a noise measuring system will be detailed. The development and implementation will be performed based on the following sequences:

- **Modelling of Noise Sources in FLAUT:** this includes the study of different types of noise sources and modelling of noise within a FLAUT device
- **Development of an Isolation Vessel:** this includes the study of different available designs, choosing a suitable design configuration; and modelling and validation to identify the suitability of the vessel to the test object.
- **Measurement and Validation of Noise for FLAUT:** this includes the implementation of noise measurement techniques using the isolation vessel; and the validation process for the FLAUT noise modelled previously.

5.2 Modelling of Noise in a FLAUT

According to Zuckerwar *et al* [132], there are three noise sources in an electrostatic transducer system which are:

- **Mechanical Thermal Noise**: this arises due to the molecular collision caused by Brownian motion of air molecules in the surrounding fluid impinging on the thin plate surface.
- **1/f Noise**: this arises due to the motion of the thin plate.
- **Electrical Thermal noise:** this arises due to random motion of charge carriers in the resistor.

In the next section, in order to evaluate the noise it is important that the effect of each noise source, along with the general relevant contributions is discussed. This would enable the analysis of the noise modelling to be developed in a holistic manner.

Before the mechanical thermal noise is described in detail, the general concept of fluctuation and dissipation theory needs to be introduced [133]. In general, a damped harmonic oscillator system with mass, m, spring constant, k, mechanical resistance, R and displacement, x could be written as:

$$m\frac{d^2x}{dt^2} + R\frac{dx}{dt} + kx = f_n(R,t) \qquad \textbf{Equation 5.1}$$

If only the left hand side of Equation 5.1 is considered, then inclusion of damping would suggest that the oscillation would continue to decay in amplitude forever. However, with the inclusion of the fluctuating force f_n on the right hand side, the system could still decay but only until it reaches equilibrium with its surroundings. Thus, with the fluctuating force, the system temperature would not drop below the system's surrounding.

In essence, the presence of the damping term in the equation requires that a fluctuating force is present as well. This is the essence of the Fluctuating-Dissipation theorem [133]. The damper enables the energy to leave the mass-spring system, but at the same time, the random movement from the environment also affect the oscillation of the mass-spring system. This theorem enables the mechanical-thermal noise to be analysed, however complex the system. Thus, according to Gabrielson [133], the mechanical thermal noise could be analysed by adding a force generator along with each damper, provided that the mechanical system is in thermal equilibrium.

Noise within an electrostatic transducer receives system could be divided into two main categories, which are due to the electrostatic transducer itself and due to the related preamplifier electronics. Although, typically the total noise is viewed as a system, it is also important that any individual noise component within the electrostatic transducer and preamplifier electronics is identified. This would enable a thorough understanding of the individual effect of electrostatic transducer noise and the preamplifier noise, on the overall system and the relationship between them. In addition to the noise due to the transducer and its supporting electronics, another key noise source is the environmental noise.

5.2.1 Transducer Noise

In general, the transducer noise is the intrinsic noise that is transferred into the system, by actuating the device itself. In addition, to the noise sources which have been described earlier, in the case of FLAUT, additional noise mechanisms due to the losses in the pipe need to be included. These noise sources are associated to the random movement of the molecules impinging both on the thin plate surface and across the pipes. The mean square voltage of this noise could be illustrated as a Nyquist equation as follows [133]:

$$E_s = \sqrt{4k_b TRF} \qquad \textbf{Equation 5.2}$$

where k_b = Boltzman's Constant (1.38 x 10^{-23} J/K), T = Transducer Temperature (K), R = Resistance of the Transducer (Ω) and F = Noise Bandwidth (Hz)

E_s is the Root Mean Square (RMS) thermal noise voltage of a given resistance R, and is normally expressed in $\mathrm{V}/\sqrt{\mathrm{Hz}}$ for unity noise bandwidth. As the noise spectrum is generally flat over a range of frequencies, the bandwidth is important, as the system with a wider operational bandwidth would contain a higher level of noise.

5.2.2 Modelling of Transducer SNR

There are various methods to model the noise for electrostatic transducers. However, the three common methods utilised are the free body diagram model, the equivalent circuit method and two port network diagram [133]. All these techniques could be performed either analytically or using electrical circuit simulation software such as PSpice. In this thesis, a free body diagram model is utilised, since this is a common modelling technique which has been developed by different authors [133-140], thus easily synthesised into a FLAUT model.

In order for a noise model to be developed, the electrostatic transducer signal model needs to also be developed. As in the previous Chapter, the electrostatic transducer

could be simplified into two parts, which are thin vibrating plate and the backplate. Depending whether it is in transmit or receive mode, either the thin plate is moved due to the change in electrostatic force when the voltage stimulus is applied; or the thin plate will be displaced according to the incident acoustic pressure wave. Each scenario will give rise to displacement of the thin plate. To simplify the noise modelling, an electrostatic transducer could be considered as a simple pressure sensor as shown in Figure 5.1. Assuming an arbitrary force, *F*, the displacement response, *Z* could be generalised as Equation 5.3 [133].

$$|Z| = \frac{F}{k} G(f) \qquad \textbf{Equation 5.3}$$

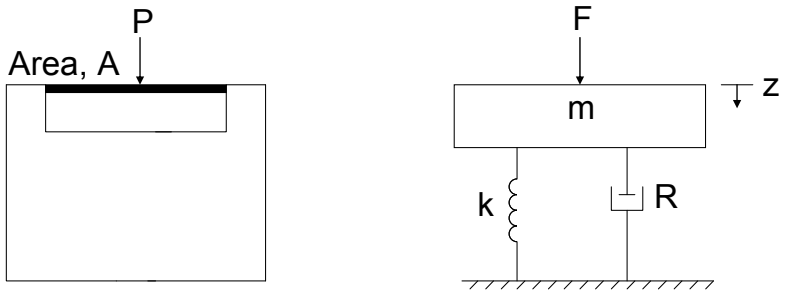

Figure 5.1: Schematic Diagram of Simple Pressure Sensor and the Mass/Spring/Damper System. Schematic Diagram (Right), Free Body Diagram (Left)

According to Gabrielson [134], for electrostatic signal, the force $F = p_s A$, where A is the area of the transducer face and p_s is the spectral density of the signal pressure. On the other hand, for noise calculation, the force, $F_{noise} = \sqrt{4k_b TR}$, thus the SNR for the system could be simplified as in Equation 5.4.

$$\left|\frac{Z_s}{Z_n}\right|^2 = \frac{(p_s A)^2}{4k_b TR} = \frac{Q(p_s A)^2}{4k_b T\omega_o m} \qquad \textbf{Equation 5.4}$$

where Q is the Quality Factor, m is the membrane mass and ω_o is the Fundamental Resonant Frequency of the Transducer = $\sqrt{k/m}$ in rad/sec.

Thus, according to Equation 5.4, the SNR can be improved through the following techniques:

1. Increasing the surface area of the thin plate.
2. Increasing the Quality Factor, Q of the transducer.
3. Reducing the resonant frequency of the device.
4. Reducing the mass of the thin plate, by reducing the thickness of the thin plate.

It could be argued that reducing the mass of the thin plate would effectively reduce the size of the transducer in general. However, due to the squared dependence of the area, the effect of reducing the size of the transducer will not be as great as increasing the surface area.

However, as a FLAUT is a device that is enhanced by the resonant frequency of the individual components within the device, the improvement suggested by the above analysis is limited. Increasing the surface area of the active thin plate would in effect reduce the resonant frequency of the thin plate, thus causing the resonant frequency component within the device to be mismatched. Although it is possible to reduce the resonant frequency of the device, the required operating frequency becomes key - typically, a higher frequency would result in better image resolution, which is generally a desirable device characteristic. On the other hand, although it could be suggested that improving the Q-factor would improve the SNR; FLAUT being a resonant device may not be able to exploit this fully as increasing the Q-Factor for a system which is already in resonance would effectively make the system unstable [133]. In this respect, within the four factors suggested, only one is feasible: reducing the thin plate mass by reducing the thin plate thickness.

5.2.2.1 Main Dissipation Mechanism

Part of the information needed to enable modelling of the transducer noise is the understanding of the sources of dissipation within the transducer system. As previously noted, any mechanism that allows the energy to escape from an ordered

system could be considered as dissipation. In the case of the electrostatic transducer for example, such mechanism may include mechanical damping, viscous drag, acoustic re-radiation, electrical leakage, thin film damping etc.

According to Gabrielson [133, 134], it is usually very difficult to differentiate the different damping mechanisms within a device or system, as such the system *Q* factor has been utilised to measure noise provided that the damping is independent of frequency. Fluctuating forces were generally calculated using the resistance, since the measurement of the system's vibration, *m* and *Q* factor are usually simple.

Since it is already established that the force can be calculated using resistance, it is now important that the relevant resistance value is identified. For an electrostatic transducer, there are two main dissipation mechanisms which are the squeeze film damping [130, 139, 141] or the mechanical resistance due to cavity [130, 139] and radiation resistance [47, 134].

In addition, for FLAUT, another mechanism needs to be added due to the addition of the pipe, which allows fluid to flow through it, rather than being squeezed at the edges of the cavity [137]. Although, there is another variety of mechanical thermal noise that is associated with a leaky dielectric, this is considered negligible and thus is not considered here. This is mainly due to the use of air as the dielectric where the loss tangent is negligible within the context of a FLAUT device [133]. In addition, the leaky dielectric of Kapton could also be considered negligible as the loss tangent is less than 0.004 [142].

In squeeze film damping, the loss is due to fluid being squeezed between, the thin plate and the backplate. Tan and Miao [130] and Starr [141] have described this loss, R_{film} using Equation 5.5 as shown below.

$$R_{film} = \frac{3\mu A^2}{2\pi d_a^{\,3}} \qquad \textbf{Equation 5.5}$$

where μ is the fluid viscosity which is 18 x 10^{-6} kg/m.s for air, d_a is the cavity depth and A is the surface area.

In addition to the squeeze film damping, another type of resistance considered is the radiation resistance. This mechanism is typically observed at frequencies above 5 kHz and for small cavity radii [134]. In those instances, the loading due to mass can sometimes exceed the mechanical mass. The radiation impedance, Z_{rad} could be approximated by Equation 5.6 [133].

$$Z_{rad} = \rho c \pi r_m^{\,2} [\frac{(kr_m)^2}{4} + (0.6kr_m)i] \qquad \textbf{Equation 5.6}$$

where k is the acoustic wave number (ω/c), ρ and c is the density and speed of sound in fluid respectively and r_m is the cavity radius.

In addition to the squeeze film damping and radiation resistance, the mechanical resistance due to the pipe needs to be considered. Skvor [137], has analysed the behaviour of backplate vented with holes. This is analogous to the pipe in the FLAUT design. The mechanical resistance due to a single vented hole or in the case of FLAUT a pipe could be approximated as given by Equation 5.7.

$$R_{1hole} = \frac{12\mu}{\pi d_a^3} G(A_{pm}) \qquad \textbf{Equation 5.7}$$

where $G(A_{pm})$ is given by Equation 5.8. This expression assumes that the fluid flows through the pipe only and not beyond the edges of the backplate.

$$G(A_{pm}) = \left[\frac{A_{pm}}{2} - \frac{A_{pm}^{\,2}}{8} - \frac{\ln A_{pm}}{4} - \frac{3}{8} \right] \qquad \textbf{Equation 5.8}$$

where A_{pm} is the ratio between area of each hole to the area of the cavity = $r_{pipe}^{\,2}/r_{membrane}^{\,2}$.

In this particular Chapter since there is only one hole and one cavity, Equation 5.8 could be utilised. However, for an array of holes and cavitities with a single

membrane on top as depicted earlier in Figure 2.20, a corresponding approximation by Bergquist *et al* [143] needs to be utilised as shown in Equation 5.9.

$$R_{perf} = \frac{R_{1hole} \times A}{N} \qquad \textbf{Equation 5.9}$$

where A is area of the membrane = $\pi r_{membrane}^2$ and N is the number of cavities and holes.

The effect of the total mechanical thermal noise could be expressed as a parallel combination of the individual noise resistance components [139]. Thus, the combined parallel resistance for FLAUT and cavity only design could be simplified and shown as in Equation 5.10 and Equation 5.11 respectively.

$$R_{FLAUT} = \frac{1}{R_{film}} + \frac{1}{R_{perf}} + \frac{1}{Z_{rad}} \qquad \textbf{Equation 5.10}$$

$$R_{Cav} = \frac{1}{R_{film}} + \frac{1}{Z_{rad}} \qquad \textbf{Equation 5.11}$$

5.2.2.2 Other Dissipation Mechanism

In addition to the main dissipation mechanism described above, it is also important that other dissipation mechanisms are discussed. These include acoustic re-radiation and temperature changes within the environment. However, these mechanisms are not considered as they are not significant mainly due to: [133]:

- **Acoustic Re-radiation**: This mechanism is not considered because the equivalent noise pressure does not contain any properties of the transducer. Thus, it is generally included in the environmental noise.
- **Temperature Changes**: This mechanism is not considered because the measurement temperature is considered constant throughout.

However, in this Thesis the noise considered here does not include any preamplifier noise during modelling. Although, the preamplifier is included during measurements as will be shown later, the use is mainly to identify the overall signal noise. As will be explored later, thermal noise of the transducer is then extracted from the total noise and preamplifier noise, through subtraction.

Thus, in this Thesis the effect due to shot noise, which is a non-equilibrium source of noise, and the 1/f noise whose spectral distribution is not flat but reduces with increasing frequency with power distribution of approximately 1/f is not considered. The shot noise is not considered because in this Thesis, the measurement of FLAUT is assumed to be performed in a system that is in equilibrium. Therefore, in this case thermal noise would provide a complete description of the internal transducer fluctuations [133]. On the other hand, the 1/f noise is not considered due to the frequency operating range of FLAUT. The 1/f noise is significant at low frequency with region of dominance between 0.6 kHz and 4.4 kHz for a 2.97 mm membrane radius [144]. However, the operating frequency of the FLAUT is above 34.5 kHz for both the proof of concept and the final confirmation run, which makes the 1/f noise insignificant for a FLAUT device operating within the expected frequency ranges.

5.2.3 Analytical Noise Model Evaluation

5.2.3.1 Transducer

Once a model has been formulated, the model then needs to be verified through means of measurement. However, before a comparison could be performed, it is imperative that the analytical model that has been developed is discussed and different effects of the model are evaluated.

As has been mentioned much earlier, in this Chapter, the noise model will be evaluated based on the same design that has proposed and verified in term of sensitivity in the earlier Chapters.

Using the same design parameters as in Table 3.5, the simulated transducer mechanical resistance for the 34.5 kHz transducer with a pipe radius of 300 μm is shown in Figure 5.2. From Figure 5.2, it could be observed that the combined mechanical resistance is almost independent of frequency as denoted previously by Tan and Miao [139], except at a very low frequency.

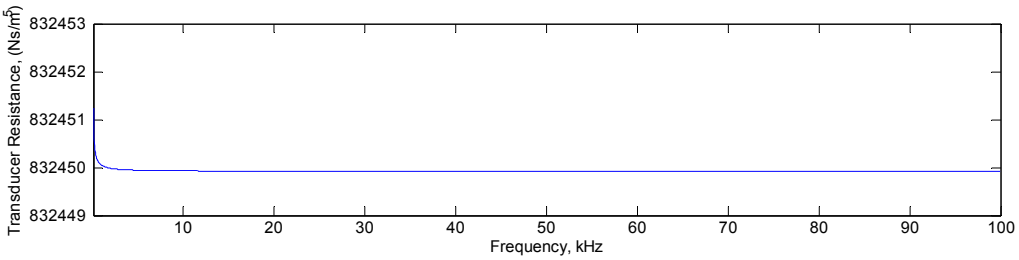

Figure 5.2: Plot of Transducer Resistance for 34.5 kHz FLAUT versus Different Frequency

Inserting Equation 5.10 into Equation 5.2, the FLAUT noise spectrum for the 34.5 kHz design has been calculated and is shown in Figure 5.3. From the equation, it could be seen that the noise for the FLAUT is weakly dependent on frequency at low frequency. The total spectrum in general is independent of frequency. From the component of Equation 5.10, it could be deduced that the main frequency dependent feature is from the influence of the radiation resistance since the operating frequency is above 5 kHz.

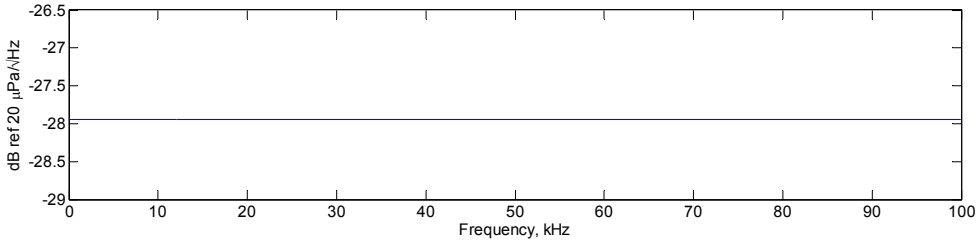

Figure 5.3: Plot of Noise Frequency Spectrum for the 34.5 kHz FLAUT Design with a Pipe Radius of 300 μm

In addition to the FLAUT designed at 34.5 kHz with a pipe radius of 300 μm, a comparison is also made with a larger pipe radius of 450 μm. The simulated frequency spectrum could be observed in Figure 5.4. This comparison is performed to identify the influence the different pipe diameter has. The comparison between the two pipe diameters will be discussed in detail in the later section.

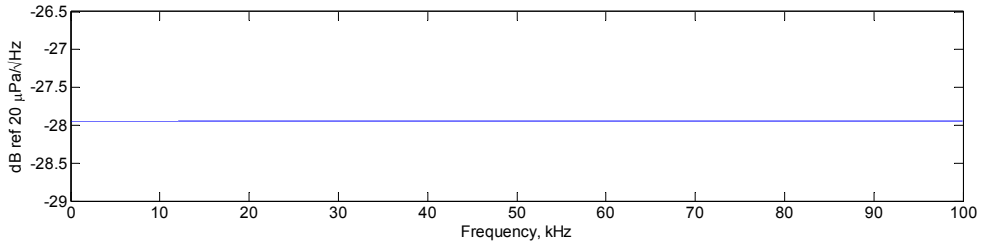

Figure 5.4: Noise Frequency Spectrum for the 34.5 kHz FLAUT design with a pipe radius of 450 μm

5.2.3.2 Environmental Considerations

In addition to modelling the transducer noise on its own, the level of environmental noise or background noise needs to also be considered. The environmental noise is any noise that is not directly generated by the transducer and its electronics, such as the ambient noise within the transducer system, the noise due to the electrical power system connected to the transducer system and all the noise that does not concern the transducer and its system. The environmental noise is represented by a random Gaussian distribution with a zero mean, and the RMS value specified by the end user. The distribution could be described mathematically as in Equation 5.12. The probability density function *f(x)* in Equation 5.12 is not a frequency dependent function. However, if the noise is frequency dependent, then the distribution can be weighted accordingly. This could be performed by increasing the magnitude of the noise at the desired frequency level.

$$f(x) = \frac{1}{\sigma\sqrt{2\pi}} \exp\left[\frac{(x-\mu)^2}{2\sigma^2}\right] \qquad \textbf{Equation 5.12}$$

where μ is mean or average, and σ is standard deviation or RMS value of the variable, x

Since the modelling technique has now been developed, the next stage is to validate the model. This needs to be performed in an isolation vessel, which will be discussed next.

5.3 Development of Noise Isolation Vessel

Once the noise modelling has been performed, it is important that the noise model is validated through measurements. Few measurement techniques have been proposed along with their advantages and disadvantages. However, it is important to note that most of the measurement techniques were originally designed for audio ranges or microphones, thus the ranges depicted are mainly from low frequency to 20 kHz.

In this chapter however, the main focus of the modelling and measurement will be in the ultrasonic range. Thus, the frequency focus would be from 20 kHz to 100 kHz. For microphones, the minimum detectable signal in term of minimum detectable frequency is important, since bandwidth is generally about 20 kHz. In this Thesis, the focus is on the noise at around the resonant frequency of the FLAUT device, mainly due to the resonant nature of the FLAUT device. However, to investigate and characterise the noise behaviour, a full noise frequency spectrum until 100 kHz will be discussed and investigated in this Chapter. Although, it is expected that there is also noise above 100 kHz, this is not considered within the Chapter due to the operational requirement of the FLAUT transducer.

In measuring noise, it is not usually practical to measure it at its source due to the possibility of very low amplitude. Moreover, noise measured at source may not be the sole contributor of noise, rather than being diffused across the whole system, i.e.

noise measured at the end of the transducer may include noise mechanisms such as the transducer itself, the environment and in the receive system the preamplifier and its electronics.

5.3.1 Review on Different Measuring Techniques

In order to measure noise for an electrostatic transducer, three main approaches by four different authors Zuckerwar [132, 144], Ngo [145, 146], Olson [147] and Tarnow [138, 148] have been adopted. Although, other authors have proposed different techniques such as an anechoic chamber, thick-wall isolation vessel and a dummy microphone, these techniques have some gross limitations. Whilst the anechoic chamber, which is typically designed for echo suppression, is effective, it has a limited isolation from exterior sound sources. Although, a thick-walled isolation vessel shows good promise in measuring background noise [138], Ngo and Zuckerwar [146] noted that thick-wall isolation is impractical at low frequencies due to the thickness required to sustain the isolation. At a frequency of 200 Hz, with required 80 dB attenuation using brass as the wall material; would require the wall to be 0.78 meter thick. Finally, the dummy microphone method, although insensitive to ambient noise, has a major drawback due to its inability to indicate the Brownian motion of air molecules. This is due to the fixed plate of the microphone. Furthermore, the dummy microphone method does not reveal the dielectric losses as in an actual electrostatic transducer.

Following the approach by Ngo [145] and Olson [147], the measuring equipment as shown in Figure 5.5 has been utilised. As illustrated, Ngo proposed a two layered vessel system, with the vacuum pump external to the vessel, while Olson proposed a glass bell jar enclosed in a wood cover with the vacuum pump attached to the base of glass jar. This has proved to be a good concept since there is no better acoustic isolator other than a vacuum. Tarnow [138] on the other hand proposed measuring noise using an air tight Dewar Vessel filled with liquid nitrogen to identify the noise level with respect to changes in temperature.

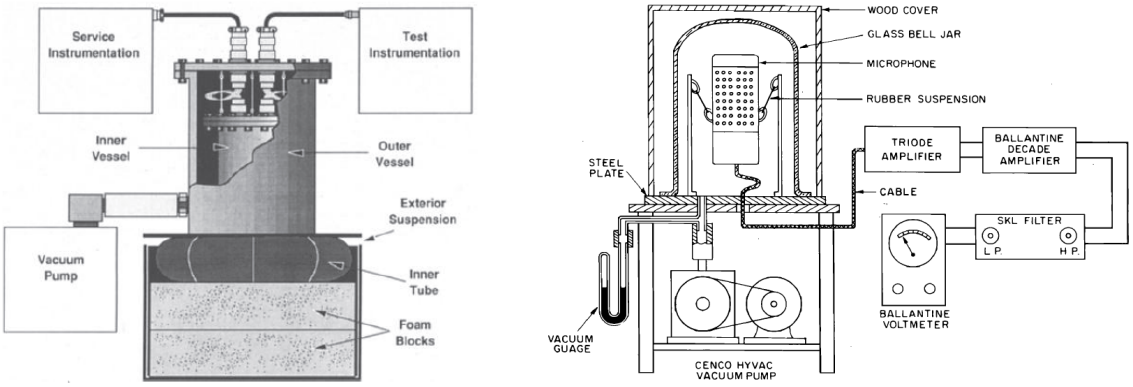

Figure 5.5: Picture of Noise Measuring Equipment by Ngo [145] (Left) and Olson [147] (Right)

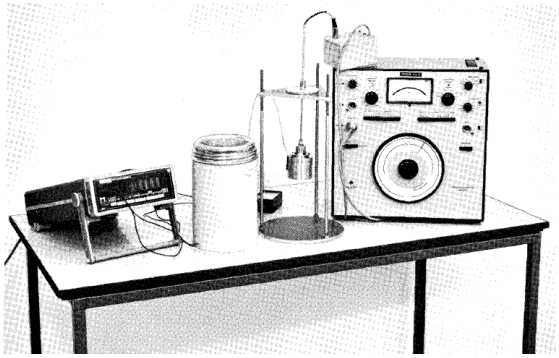

Figure 5.6: Picture of Experimental Arrangement by Tarnow [138]

However, it is vital to note that these three approaches were different because they served different purposes. Ngo's acoustic isolation vessel was designed with the ability to measure the 1/f or low frequency noise, while Olson's acoustic isolation glass bell jar was designed to measure the thermal electric noise and thermal acoustic noise in a ribbon type velocity microphone. On the other hand, Tarnow's purpose was to identify changes in noise as a function of temperature.

These three techniques serve as a good base in ensuring that the majority of the noise sources are covered. Before detailed discussions are detailed in the next section, it is essential that the basic definitions were introduced. According to Zuckerwar [132], background noise of a measurement in this case electrostatic transducer noise could

be defined as the RMS output of an electrostatic transducer in the absence of acoustical and electrical (AC) excitation.

5.3.2 Proposal for Hybrid Acoustic Isolation Vessel (HAIV)

From the three concepts that have been discussed earlier, a HAIV has been developed as shown in Figure 5.7. However, due to safety concerns, Tarnow's method of using liquid nitrogen to identify the noise variation due to changes in temperature needs to be modified. An alternative solution has been proposed. Using a heater pad located within the confines of the inner vessel, the air temperature within the vessel could be controlled to a temperature between 20^{o}C to 30^{o}C.

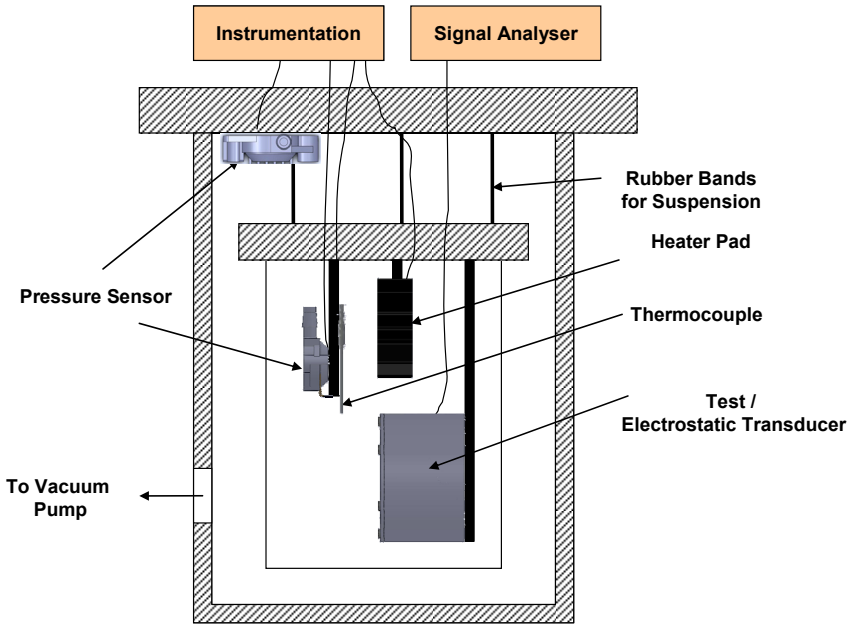

Figure 5.7: Schematic Diagram of Hybrid-Acoustic Isolation Vessel

In this design proposal, there are 8 major components in the vessel design which are:

- **Inner Vessel:** this vessel is where all the major measurement took place.
- **Outer Vessel:** this vessel is where the acoustic isolation took place, as it will be in vacuum.

- **Pressure Sensors:** there are two pressure sensors installed in the design. One, at the inner chamber to measure the ambient pressure inside the inner chamber. The other at the outer chamber, to measure the vacuum pressure of the outer chamber.
- **Temperature Sensor:** to measure the change in temperature with respect to time during the measuring sequences.
- **Heater Pad:** to maintain the temperature at the required test level. This works along with a temperature regulator and a temperature sensor.
- **Suspension:** rubber bands as suspension to reduce the vibration from the outer chamber to the inner chamber.
- **Instrumentation:** all the connections for the temperature sensor, pressure sensor and heater pad goes through this.
- **Signal Analyser:** the test connection goes through this. The purpose of this separation between the signal analyser and instrumentation is ideally to reduce interefence between the two.

5.3.2.1 Development of Isolation Vessel

In order to isolate the electrical thermal noise from the mechanical thermal noise, a two-vessel system utilising a vacuum to reduce the mean free path of air has been fabricated. The Mean Free Path, λ_f can be calculated using the following equation [149]:

$$\lambda_f = \frac{RT}{\sqrt{2}\pi d^2 N_a P} \qquad \textbf{Equation 5.13}$$

where R is Ideal Gas Constant = 8.3144621 $JK^{-1}mol^{-1}$, T is temperature in Kelvin, d is the nominal molecular diameter of air = 3.6 $x10^{-10}$ m [150], N_a is the Avogadro's Number = 6.02214 x 10^{23} mol^{-1} [150] and P is the pressure required. The mean free path of air has been calculated for a range of pressures and is shown in Figure 5.8.

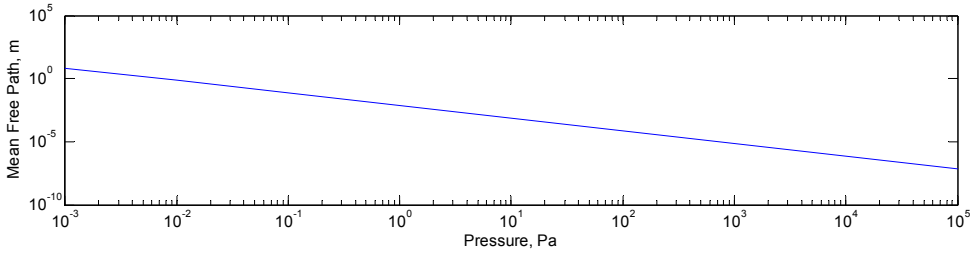

Figure 5.8: Plot of Mean Free Path of Air as a Function of Pressure at 20^{o}C

One of the main constraints in using such a vacuum vessel system is to ensure that the vessels are designed in such a way that the mean free paths of air molecules are smaller than the gap between the inner and outer vessel. This is to ensure that the collisions between the air molecules are relatively insignificant thus making the air molecules to be considered as a non-interacting particles. Assuming that the gap between the inner vessel and the outer vessel has an average distance of 100 mm; then the air pressure within the vessel needs to be reduced to a level of around 8-10 times the equivalent mean free path of a single air molecule. In this case, the minimum pressure required is around 0.8 - 1 Pa, with a mean free path of 8.7 mm - 7.0 mm respectively. At this minimum vacuum level, any sound propagation from the environment into the inner vessel should be suppressed. Thus, a design for the vessel isolation has been suggested as shown in Table 5.1.

Table 5.1: Table for Properties of the Inner and Outer Vessel

Properties		Dimensions
Outer Vessel	Outer Diameter, 2_{a_1}	0.314 m
	Inner Diameter, 2_{a_2}	0.250 m
	Inside Height	0.435 m
	Wall Thickness	0.032 m
Inner Vessel	Outer Diameter, 2_{a_3}	0.150 m
	Inner Diameter, 2_{a4}	0.140 m
	Inside Height	0.190 m
	Wall Thickness	0.005 m
Acoustic Impedance	Air: $\rho_1 c_1$, $\rho_5 c_5$*	413 Rayls
	Outer Vessel: $\rho_2 c_2$	1.79 MRayls
	Inner Vessel: $\rho_4 c_4$	17.33 MRayls
Intervening Distance		0.1 m

* The acoustic impedance at 20°C and atmospheric pressure of 101.325 kPa.

The isolation vessel above could be considered as a five-media model as shown in Figure 5.9. In this case, the model shown could be expressed as having transmission of the acoustic wave which takes place from the first medium (air) into the second medium (vessel wall – outer) into the third medium (vacuum) into the fourth medium (vessel wall – inner) and finally into the fifth medium (air). All the transmissions are assumed to be at normal incidence and the transmission is considered lossless.

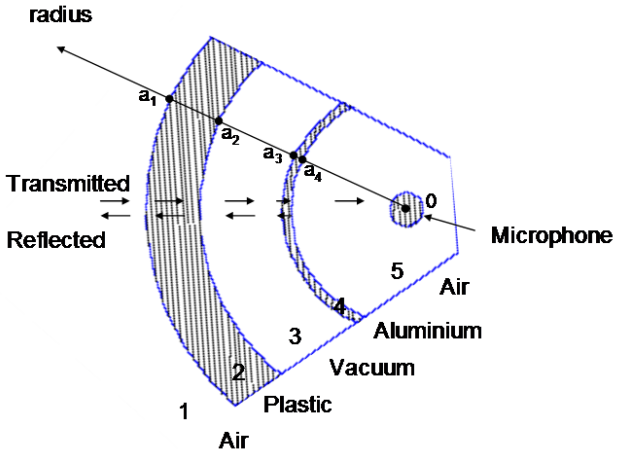

Figure 5.9: Visual Representation of the Isolation Vessel Assembled in a Five-Media Model

However, Ngo and Zuckerwar [146], have shown that the five-media model problem above could be approximated by separating it into two discrete three-media model problem. This could be performed by considering that the transmission from medium 3 (vacuum) to medium 4 (vessel wall – inner) to be extremely small. Utilising the method that has been derived by Ngo and Zuckerwar [146], the theoretical transmission coefficient for a selected isolation pressure has been calculated and is plotted in Figure 5.10. From the plot in Figure 5.10, it could be observed that the transmission coefficient attenuates rapidly from around -150 dB at atmospheric pressure to around -300 dB in vacuum.

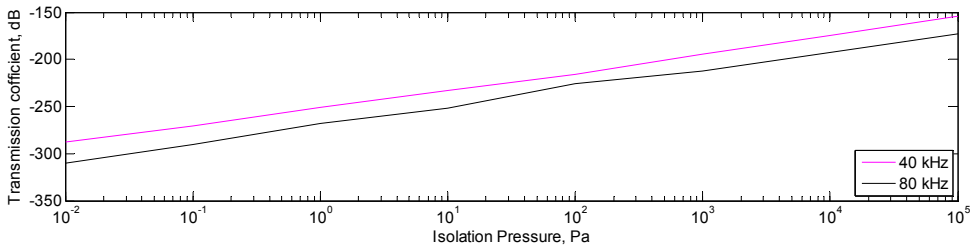

Figure 5.10: Plot of Theoretical Transmission Coefficient as a Function of Isolation Pressure at 40 kHz and 80 kHz Resonant Frequencies

There are two significant parts within the HAIV, which are the Thermal Noise-Hybrid-Acoustic Isolation Vessel (THAIV) and the mechanical damping system. These two parts play an important role in the measurement system. THAIV is where all the measurement is performed; while mechanical damping system guarantees that the vibration and movement within the measurement are isolated so that no further resonance within the THAIV is experienced. This is performed using a vibration isolation table and 7 x 1¼" Sorbothane Hemispheres attached at the bottom of the external vessel. Sorbothane hemispheres on their own are able to absorb vibration until 94.7% [151], while the vibration isolation table which utilises the NRC pneumatic isolation mount type KL-A should further isolate external vibration. The overall view of the Hybrid Acoustic Isolation Vessel System is shown in Figure 5.11.

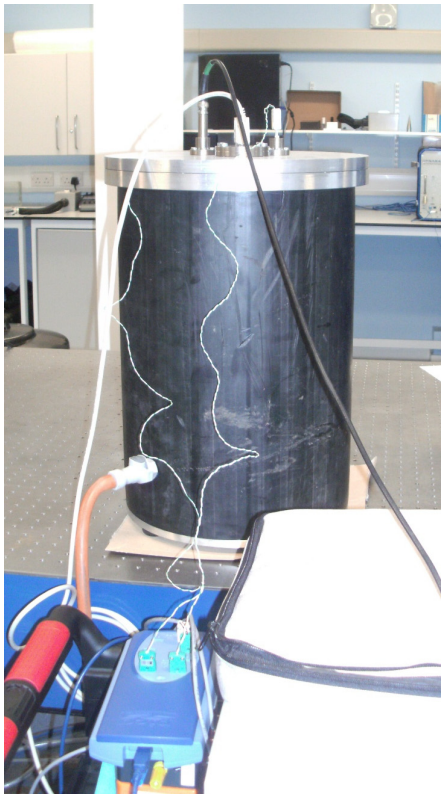

Figure 5.11: Picture of Overall View of Hybrid Acoustic Isolation Vessel System

In addition to using vibration isolation table and the Sorbothane hemispheres to isolate the external vibrations, the inner vessel vibration is isolated through a means of suspension by six equally spaced rubber bands and hooks from the interior of the

outer vessel cover and the exterior of the inner vessel cover, as shown in Figure 5.12. This system constitutes a mechanical filter of the inner vessel mass-spring system.

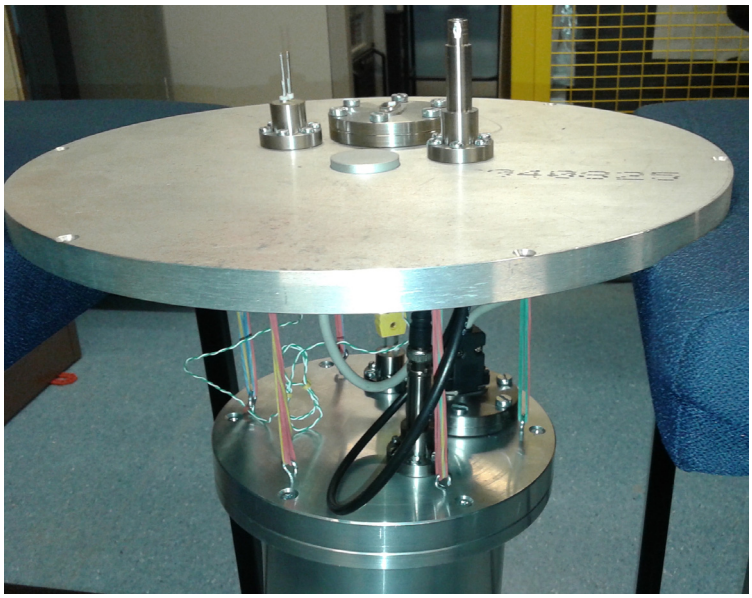

Figure 5.12: Picture of the Connection between the Inner Vessel and the Outer Vessel

To maintain the vacuum level or atmospheric pressure level depending on the measurement to be taken, sealing is performed using a cover and an o-ring with several screws between the cover and the vessel. This seal is performed for both the inner and the outer vessel. A vacuum pump would then be attached to the external vessel to evacuate the air within the intervening vessel.

As described earlier, to maintain the temperature, a system that consists of a temperature sensor within the confines of the inner, a heater pad and a temperature controller is utilised. During the noise measurement, the temperature within the inner vessel is controlled at $20^{o}C \pm 0.2^{o}C$. The layout of the inner vessel could be observed in Figure 5.13.

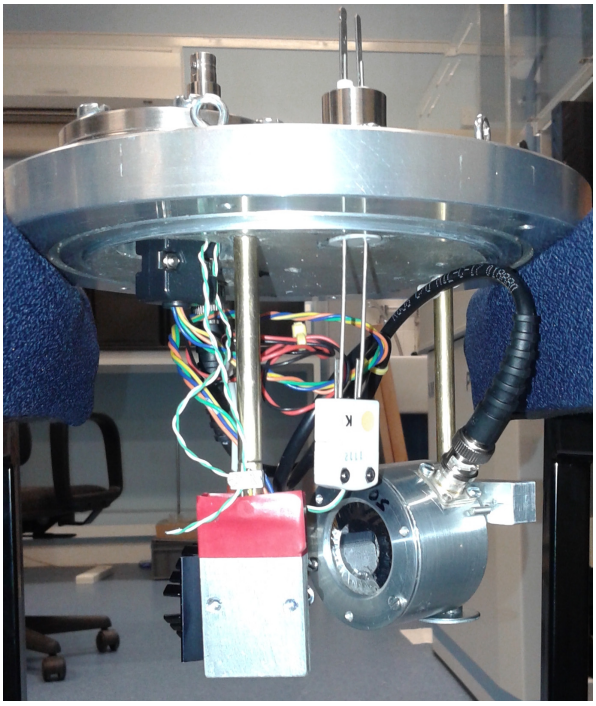

Figure 5.13: Picture of Inner Vessel

Within the system, there are two types of wire feed through as shown in Figure 5.12. First, is for the thermal noise system which is being measured by a signal analyser / oscilloscope and second, is the instrumentation system which consist of two pressure sensors, a thermocouple and heater pad embedded within the inner vessel. To enable the signal analyser / oscilloscope to able to accept and read with the bias (polarisation) voltage, an isolation circuit is introduced to the measuring system. In addition, to maintain the temperature within the inner vessel to a specified temperature, a thermocouple, a heater pad, and a digital temperature controller is utilised as previously described. In addition, pressure sensors are utilised to monitor the condition of the vacuum isolation during the measurement.

5.3.2.2 Transducer Calibration

Before any measurements could be carried out using the HAIV system, it is important that transducer calibration is performed. The pressure output of the transducer was calibrated using the Brüel & Kjær (B&K) 1/8" calibrated microphone type 4138 in free field condition. The transducer was then installed to the inner chamber to enable the required measurements to be performed.

From the calibration, the sensitivity of the transducer, which is usually expressed in V/Pa is determined. This step is mainly to ensure that the thermal noise voltage could be expressed in the equivalent pressure unit, which is in $\mathrm{Pa}/\sqrt{\mathrm{Hz}}$.

Since the calibration technique has now been described, there are two more verifications that are required before the vessels could be fully utilised. The two verifications required are the leak test and the through-transmission test. This will be discussed next.

5.3.2.3 Leak Test for Isolation Vessel

The leak test is performed to ensure that the vessel is working as per expectation. Although a certain level of pressure increase (in the case of outer vessel) and pressure decrease (in the case of inner vessel) is expected, the level should be low enough that it does not interfere with the measurement results. As such, tests were performed to identify that the measurement is within the needed requirement and specification. Results for the inner and the outer vessel pressure measurements for duration of 60 minutes could be observed in Figure 5.14 and Figure 5.15 respectively. From Figure 5.14 and Figure 5.15, it could be observed that the overall pressure for both inner and outer is almost constant except for the outer vessel, which reduced in pressure as a function of time until stabilisation is achieved.

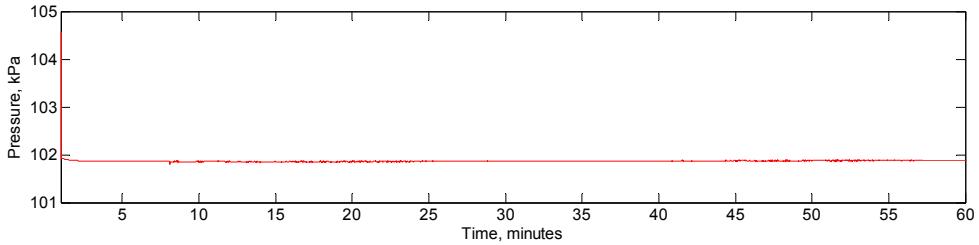

Figure 5.14: Plot of Measured Inner Vessel Pressure Level as a Function of Time for the Duration of 60 minutes

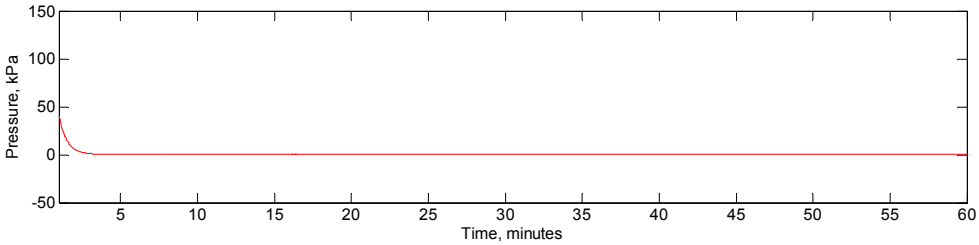

Figure 5.15: Plot of Measured Outer Vessel Pressure Level as a Function of Time for the Duration of 60 minutes

Generally, the noise measurements will be performed once the desired vacuum level of 1 Pa or less is obtained; which typically takes around 15 minutes. Once the desired pressure is achieved, the pump connected to the outer vessel will be disengaged to eliminate the vibration from the vacuum pump. The extended view for the inner vessel and the outer vessel after 15 minutes duration with the vacuum pump removed could be observed in Figure 5.16 and Figure 5.17. From the pressure trend, it could be observed that there is a fluctuation in outer vessel pressure within the range of 101.84 kPa to 101.87 kPa; which could be considered low. At the same time, from the inner vessel trend, it could be observed that the inner vessel pressure increases after the pump is removed at a rate of around 0.01 Pa/s. However, since the measurements will only take around one minute or less, these increases in pressure could be considered negligible. Thus, the measurement condition could be assumed to be constant throughout as indicated by the fluctuation level within the inner vessel as shown previously in Figure 5.16

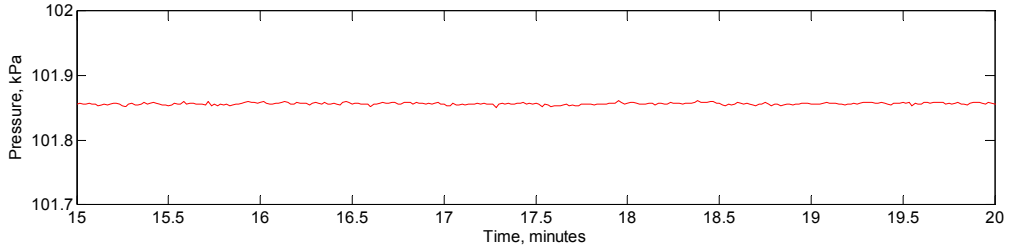

Figure 5.16: Plot of Measured Inner Vessel Pressure Level as a Function of Time after the Vacuum Pump removed for the Duration of 5 minutes

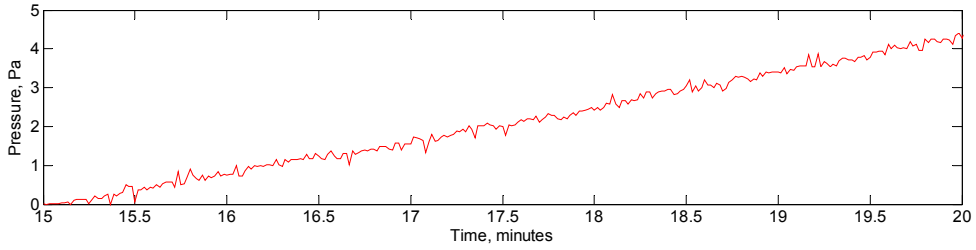

Figure 5.17: Plot of Measured Outer Vessel Pressure Level as a Function of Time after the Vacuum Pump Removed for the Duration of 5 Minutes

5.3.2.4 Through-Transmission for Isolation Vessel

Before the noise measurement could be performed using the configuration above, a through-transmission experiment needs to be performed to verify the effectiveness of the HAIV. This is performed using the assembly as shown in Figure 5.18. To perform the measurement, a loudspeaker is attached close to the external wall of the external vessel. Two calibrated microphones are fitted to measure the pressure output. One near the loudspeaker, while the other within the confines of the inner vessel. A drop in acoustic pressure between the two microphones will indicate the transmission level between the outer vessel and the inner vessel. Noise measurement is performed from an atmospheric pressure down to a vacuum of 0.01 Pa to display the trend of transducer noise as the pressure changes.

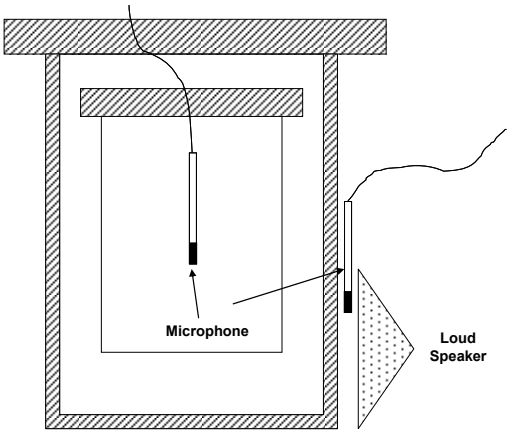

Figure 5.18: Schematic Diagram of Through-Transmission Assembly for HVAIC

The measured transmission coefficient based on the above setup is shown in Figure 5.19. As was found through the simulation and measurement performed by Ngo and Zuckerwar [146]; there are also the same discrepancies observed between theory and measured data in this Thesis. As concluded by Ngo and Zuckerwar [146], this could be due to the unaccounted theoretical formulation, internal modal vibration of the vessel and alternative propagation of acoustic waves via the connective cables or suspension connectors. However, the transmission coefficient of around -100 dB or less should be a sufficient enough isolation to measure the background noise of the desired transducers at current 34.5 kHz and especially later at 80 kHz onwards.

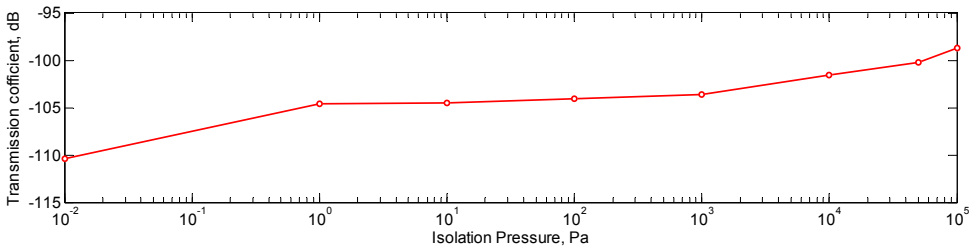

Figure 5.19: Plot of Measured Transmission Coefficient as a Function of Isolation Pressure at 40 kHz Frequency

5.4 Measurement and Validation of Noise for FLAUT

As has been mentioned earlier, it is important that the vacuum level is maintained at a certain level for a specific duration during measurement. From Figure 5.19 the minimum vacuum level should be at around 1 Pa. To ensure that any vibration from the vacuum pump was eliminated, the outer vessel was pumped down to the required vacuum and the pump was switched off before any measurement was taken.

There are two noise sources within the system, which are the preamplifier and electronic noise for a receive system and the electrostatic transducer noise itself. Earlier, it has been mentioned that there are other techniques to differentiate the noise sources, among them dummy microphones. Although, this technique was also considered by Ngo [145] with the thermal noise isolation vessel, this technique is unsuitable for the current design of FLAUT mainly because the cavity/pipe were not mechanically clamped to the backplate. This makes the FLAUT work as a fully supported system rather than a clamped system if no bias (polarisation) voltage were applied.

Utilising both Ngo [146] and Olson [147] noise measuring methods, a hybrid noise measuring technique has been proposed. In this technique, three measurement configurations would be performed to identify the bias circuitry, the total noise and the noise of the transducer under the influence of electrostatic bias. The three measurement configurations that need to be performed along with the expected output from each measurement configuration could be seen in Table 5.2.

Table 5.2: Table of Noise Measurement and Expected Output

No.	Circuitry Condition			Expected Output
	Transducer	Pre Amplifier	Bias	
1	Connect	On	On	Total Noise
2	Disconnect	On	Disconnect	Preamplifier Noise
3	Disconnect	On	On	Preamp & Bias Noise

For measurement number 1, a total noise measurement could be identified since in this configuration, the bias and its electronic is active, while the transducer is subjected to a thermal agitation on the thin plate surface due to the Brownian motion.

For measurement number 2, the preamplifier electrical noise could be identified since in this configuration, the preamplifier is switched on; while the bias and its electronics is switched off and disconnected.

Finally, for measurement number 3, the noise in the preamplifier and the bias could be identified, since both of the circuit are switched on, while the transducer is disconnected from the circuit. Thus, the noise is mainly from the preamplifier and bias circuitry.

From the three configurations, individual noise sources could be deduced and are shown as in Table 5.3.

Table 5.3: Table of Noise Measurement Configuration

Noise	Configuration
Transducer	1 – 3
Bias	3 – 2
Preamplifier	2

5.4.1 Comparison of Noise Modelling and Measurements

Previously, the simulation of FLAUT noise has been conducted and the measurement method identified. In this section, the comparison between the previously found FLAUT simulated noise and the experimental measurement will now be performed. The setup for the FLAUT noise measurement is shown in Figure 5.20. Since there is a bias requirement for a FLAUT device, there is a need for a de-coupler to connect to the signal analyser / oscilloscope. With this introduction, the electrical noise inherent within the de-coupler circuit will also be diffused as noise within the transducer system. Utilising the different setup arrangement as in Table 5.2, the specific noise due to the transducer could then be extracted. Once the transducer noise within the system is classified, the transducer noise itself is then compared with the model.

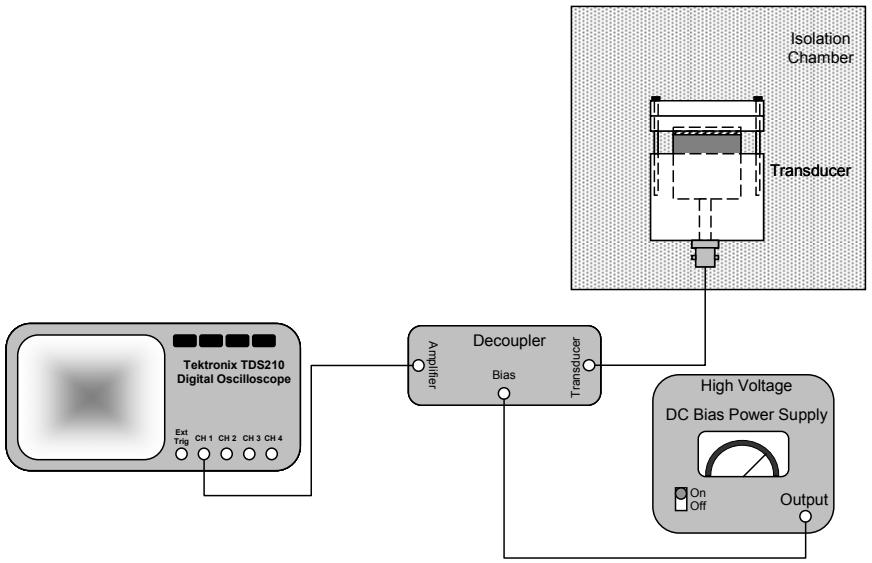

Figure 5.20: Schematic Diagram of Setup Arrangement for Measurement of FLAUT

The noise was measured with 10 averages at different configurations for the operating frequency of 34.5 kHz. The averaged measurement results are shown in Figure 5.21. From Figure 5.21, it could be observed that the total noise (transducer, bias and preamplifier noise) has a power of about 20 W for a bandwidth of 100 kHz, while the preamplifier and bias combination have a power of about 13 W, and the preamplifier only has a power of about 11 W. In addition, a segmented view of

Figure 5.21, between 30 kHz and 40 kHz is also performed to identify any resonances that may be occurring within the measured noise spectrum. The segment view between 30 kHz and 40 kHz could be observed in Figure 5.22. Although, it may not be very obvious, there is a subtle different in the trend between 33 kHz and 34 kHz, indicating the possible resonant occurrence within the frequency range.

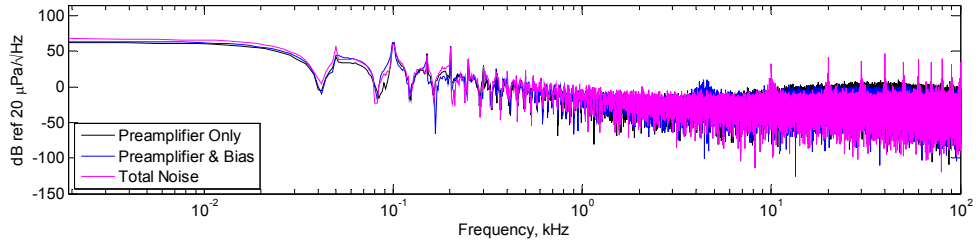

Figure 5.21: Plot of Noise Measured at Different Configuration for Operating Frequency of 34.5 kHz for 300 μm Pipe Radius

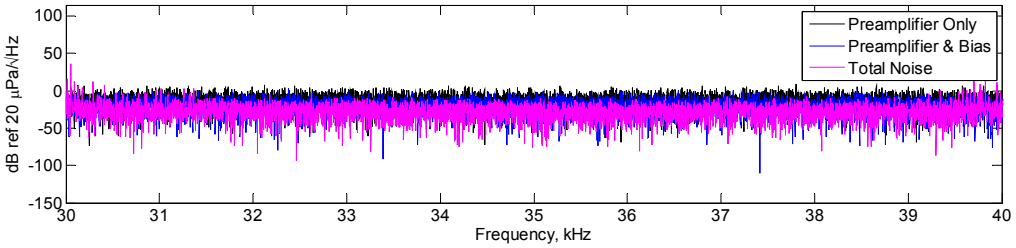

Figure 5.22: Plot of Segmented View between 30 kHz and 40 kHz for Noise Measured at Different Configuration for Operating Frequency of 34.5 kHz for 300 μm Pipe Radius

Once the measurement has been performed, the noise due to the transducer is then decomposed and compared with the simulation and is show in Figure 5.23. From Figure 5.23, it could be observed that there is correlation between the simulation and measurement, with the average spectrum of the measured noise to be around the simulated noise level. When the simulation and the measurement are compared, it could be observed that there is an increase in noise at the low frequency spectrum. This similar trend is also observed in Figure 5.2 for the simulated transducer resistance. Thus, this would suggest that there is a significant influence of the transducer resistance to the overall transducer noise, compared to the rest of the noise being simulated.

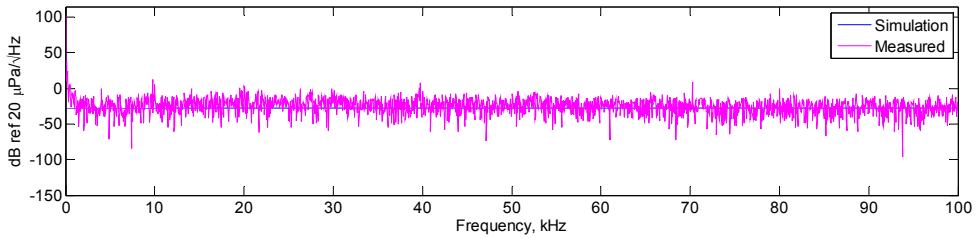

Figure 5.23: Plot of Comparison between Simulation and Measured for Transducer Noise at Operating Frequency of 34.5 kHz for 300 μm Pipe Radius

In addition to comparing the simulated and measured results, the noise measurement results for the same operating frequency of 34.5 kHz but with a larger pipe radius of 450 μm is also analysed as a comparison. The measurement results for a FLAUT with a 450 μm pipe radius operating at a resonant frequency of 34.5 kHz are shown in Figure 5.24 and Figure 5.26. A similar segmented view of Figure 5.24, between 30 kHz and 40 kHz is also performed to identify for any resonance that may be occurring within the noise spectrum measured. The segment view between 30 kHz and 40 kHz could be observed in Figure 5.25 – with subtle peaks observed at around 34.2 kHz – 34.3 kHz, indicating a resonance in the area.

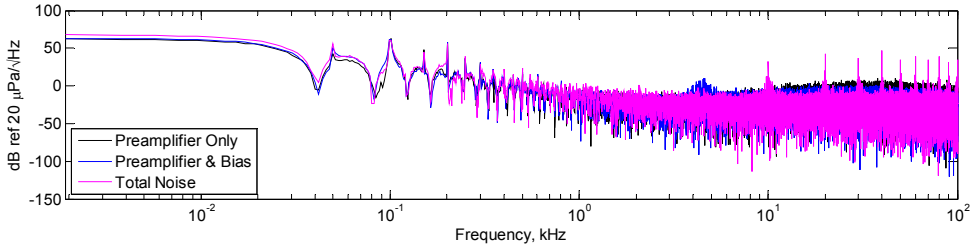

Figure 5.24: Plot of Noise Measured at Different Configuration for Operating Frequency of 34.5 kHz for 450 μm pipe radius

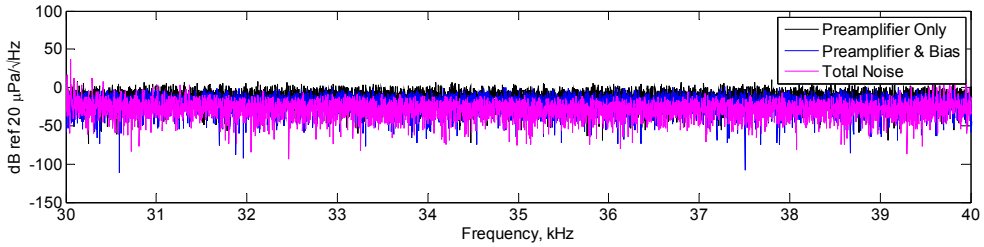

Figure 5.25: Plot of Segmented View between 30 kHz and 40 kHz for Noise Measured at Different Configuration for Operating Frequency of 34.5 kHz for 450 µm Pipe Radius

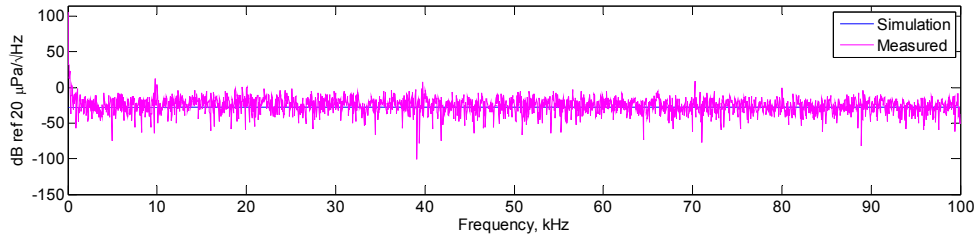

Figure 5.26: Plot of Comparison between Simulation and Measurement for 34.5 kHz FLAUT transducer with pipe radius of 450 µm

From the measurements it could be observed that there is reasonably good agreement between simulation and measurement for the 34.5 kHz transducer for both small and large pipes. Similar trends at the low frequency end of the spectrum suggest the same significant influence of the transducer resistance even for the large pipe diameter.

The results above indicate that the noise power level for the larger FLAUT pipe diameter operating at 34.5 kHz FLAUT is smaller when compared to a smaller pipe by about -0.08 dB. Although, the difference is small, from Figure 5.27 it could be observed that there is a difference in trend between the 300 µm pipe and the 450 µm pipe radius; the 300 µm pipe radius shows a slightly higher noise transducer noise floor across the 100 kHz bandwidth. This is expected; since albeit the air within the inner vessel could be assumed to be stationary, due to the bias voltage being used during the measurement, the capacitance between the larger pipe and the smaller pipe is different since the electrode area is different. However, considering the difference in electrode area and the pipe opening area for the small pipe and large pipe

transducer having a difference of 10.6 dB and 7 dB respectively, the improvement due either of these could not be clearly characterised.

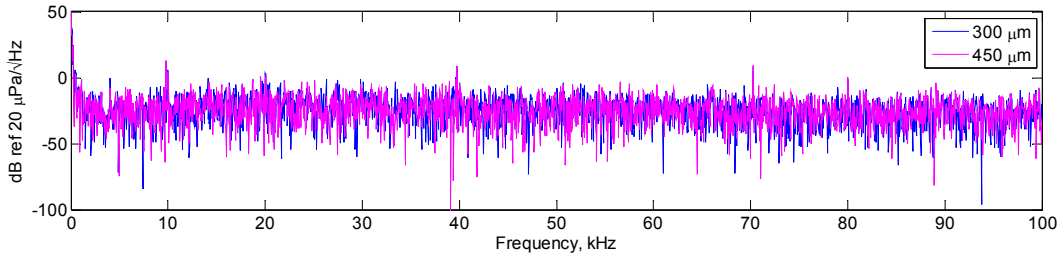

Figure 5.27: Comparison of Measured Transducer Noise for Different Pipe Size the 300 μm and the 450 μm Pipe Diameter

Finally, in order to capture the improvement afforded by the isolation table, a measurement with and without the isolation table has been performed. One of the main features of the isolation table is to remove the low frequency vibration that may influence the measurement. However, since the main noise of the transducer is on the higher end of the spectrum the use of an isolation table may or may not be warranted. From the measurement performed, it was found that the isolation table does reduce the noise level by around 7 dB for a bandwidth of 100 kHz. Thus, the use of the isolation table is fully warranted to reduce the effect of noise and vibration further.

5.5 Conclusion

In this Chapter, modelling and measurement of noise for electrostatic transducers have been performed. Various techniques to model and measure the noise have been identified and discussed. From the discussions, the approach from Ngo and Olson have been utilised to develop the noise measuring equipment and technique. From this Chapter, it is found that there is a need to ensure that the pipe radius is designed to be as large as practically possible to reduce the FLAUT noise level. In addition, as depicted in this Chapter, the use of a vacuum isolated vessel is important to enable a good measurement of an acoustic device be it at low frequency or at higher frequency. In the next Chapter, a higher frequency device will be proposed, along

with further discussion on several manufacturing techniques and their related requirements.

6. Development of High Frequency FLAUT

6.1 Introduction

In the preceding Chapters, a methodology for the design and analysis of the FLAUT device was presented. The design focuses on identifying a suitable geometry for each of the FLAUT components. The overall design goal is that the resultant geometry needs to be able to match the resonant frequency of the three components – thin plate, cavity and pipe. Analytical and FEA modelling have been utilised to enable the FLAUT geometries to be assessed theoretically.

In addition, further experimental verification through the use of laser interferometer/vibrometer measurements to identify the resonant frequency of the device has also been performed. From the findings, it was found that there is a good collaboration between the FLAUT measured frequency response and both the analytical model and finite element analysis. Noise measurement and simulation have also been performed and corroborated.

To further exemplify the method, a higher frequency design of the FLAUT will now be assessed. In addition to the previously performed analysis, in this Chapter the concept of array design will be introduced. In this Chapter, the discussion will be covered as follows:

- **Modelling and Simulation of FLAUT at High Frequency:** this includes modelling of a single unit cell, identifying suitable array configurations and beam profile simulation; and modelling of FLAUT noise.
- **Manufacturing and Assembly:** this includes the use of propagation of error to determine suitable and acceptable manufacturing processes, identifying suitable equipment to manufacture FLAUT prototypes and identifying suitable material for the FLAUT backplate.

- **Characterisation of FLAUT Prototype and Modelling Validation:** this includes the comparison between modelling and simulation for a single cell and array design of a FLAUT device, validation of beam profile measurement and comparison between simulation and measurement for FLAUT noise. Finally, the comparison between the FLAUT design and a conventional electrostatic transducer is shown.

6.2 Modelling and Simulation of FLAUT in High Frequency

6.2.1 Modelling a FLAUT with a Single Cell Backplate Design

Before a full array is considered during the design, it is important that the main geometry of a single unit or cell is defined. Utilising the same method as in Chapter 3 the proposed main characteristics of the High Frequency FLAUT are as follows:

- Operating frequency range of between 60 kHz and 120 kHz.
- Single unit cell. (The array design will be incorporated in the subsequent section).
- Kapton film on top of the backplate. However, since the single unit cell geometry is expected to be very small, the use of the thinnest commercially available Kapton film is therefore warranted. In this case, 8 μm Kapton will be utilised as part of the process.

6.2.1.1 Analytical Model to Determine Geometry

Using Equation 3.4 and Equation 3.6, for thin plate resonant frequency and cavity resonant frequency respectively, the resonant frequency of the required geometry as a function of cavity diameter and cavity depth could be observed as shown in Figure 6.1 and Figure 6.2 respectively. Since the thin plate is assumed to be fixed at the

cavity circumference, the air across the surface of the cavity-thin plate interface effectively supports the thin plate and hence determines the resonant frequency.

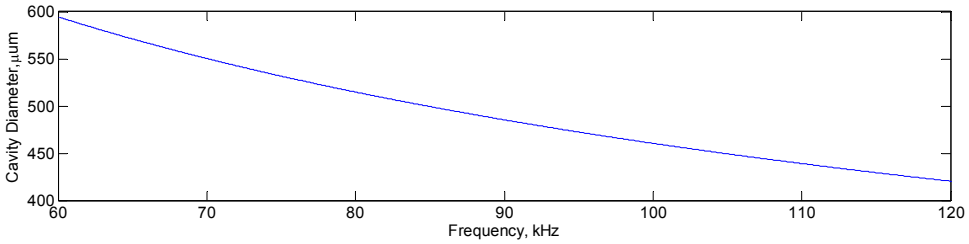

Figure 6.1: Plot of Cavity Diameter as a Function of Resonant Frequency for an 8 µm Thin Plate Thickness

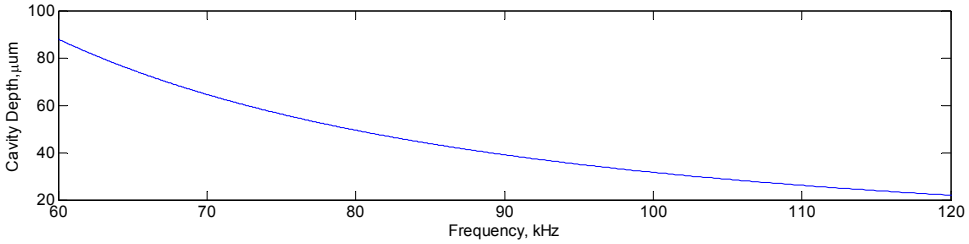

Figure 6.2: Plot of Cavity Depth as a Function of Frequency for an 8 µm Thin Plate Thickness

As expected, based on previous discussions; where a higher resonant frequency is desired, there is a concomitant reduction in both cavity diameter and depth. In this case, as previously noted, compromise in the design is required. Now the choice of design becomes critical, as it is not only dependent on the required resonant frequency but also aspects of manufacturability. Although, it may be possible to realise a design comprising a very shallow and very small cavity diameter to match the required resonant frequency, the constraints of manufacture must be considered.

Thus, in the context of this Thesis, to enable a suitable design of FLAUT to be identified, a commercially available standard drill size is considered during the design process. This is a reasonable assumption for the model due to the fact that the remainder of the manufacturing processes are much more customised. For example, if MSL, EDM, laser drilling or photolithography is being utilised, then the sizes of the design are not critical; since the machine and process could be adjusted to suit the design. However, due to cost constraint, a solution that exhibits the foundation of

cost minimisation; whilst still maximising the operating resonant frequency is proposed.

The standard slot drill sizes that are within the expected range of operating frequency are 0.4 mm, 0.5 mm and 0.6 mm in diameter. However, when considering that a through hole would need to be drilled on top of the slot drill and the matching cavity depth required; a more suitable slot drill to be considered would be 0.5 mm. This corresponds to a resonant frequency of 84.8 kHz. Even at this reasonably large cavity diameter, the equivalent required cavity depth is at 0.044 mm. Thus, the suggested cavity geometry is shown in Table 6.1.

Table 6.1: Table of Suggested Design for Cavity Geometry

Frequency	Cavity Diameter	Cavity Depth
84.8 kHz	500 µm	44 µm

Next, a suitable pipe size needs to be considered. Although, there are various pipe diameter sizes that could be considered from 0.3 mm, 0.35 mm, 0.4 mm and 0.45 mm based on the available drill sizes. Previously, it has been found that to enhance the pressure output signal the pipe diameter needs to be maximised. However, practically there is still a need to ensure that the size chosen for the pipe diameter matches the available machine tolerances, while still giving the expected enhancement to output pressure signal. In this case, assuming that a 0.01 mm tolerance is utilised, then the most suitable pipe diameter for the design is at 0.40 mm. In addition to the dimensions for the pipe diameter, the pipe length needs to also be identified. The pipe length for a range of cavity diameter to pipe diameter ratio as a function of frequency could be seen in Figure 6.3.

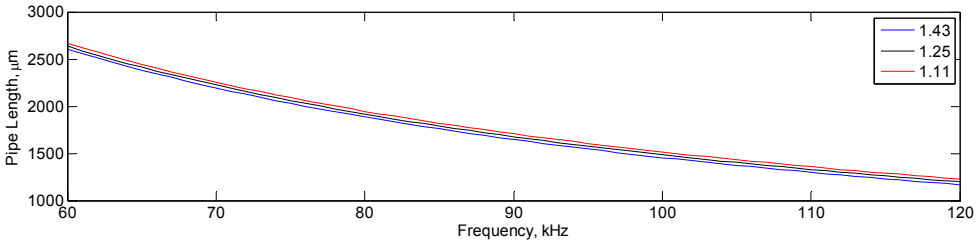

Figure 6.3: Plot of Pipe Length as a Function of Frequency for a Range of Cavity Diameter to Pipe Diameter Ratio

From Figure 6.3, it could be shown that the most suitable design for the pipe to match the resonant frequency of the cavity and the thin plate for the 84.8 kHz design is as shown in Table 6.2. The thin plate diameter and cavity depth is also included within Table 6.2 as a completion to the design geometry. From the above, it could be observed that there is a slight frequency shift for a given pipe length when the ratios are changed from 1.43 to 1.11.

Table 6.2: Table of Geometric Design Configuration for a FLAUT Device Operating at 84.8 kHz

Frequency	Thin Plate / Cavity Diameter	Cavity Depth	Pipe Diameter	Pipe Length
84.8 kHz	500 µm	44 µm	400 µm	1914 µm

6.2.1.2 Simulation and Geometric Analysis using FEA for 84.8 kHz Device

As before, FEA has been utilised to validate the resonant frequency of the individual geometry. In addition, FEA has also been utilised to identify the frequency shift, the expected pressure output and the effect of damping in a fully coupled device. Using the same technique as in Chapter 4, the geometric analysis for the 84.8 kHz FLAUT transducer has been performed. FEA simulation of the thin plate has been performed in 2D axi-symmetric with an input of load of 1 Nm^{-2} in the negative z-direction. The

thin plate boundary for z-direction for both surfaces is set to be free; while the edge of the thin plate at x-direction of 250 μm is set to be fixed. A predefined normal triangular mesh size has been utilised for the simulation. The material properties utilised are the same as previously noted in Table 3.6.

A frequency response analysis simulated at the centre of the plate has been performed for the thin plate, and the result is shown in Figure 6.4. From Figure 6.4, it could be observed that the resonant frequency of the thin plate is at 84.8 kHz, which is as expected from the design resonant frequency at 84.8 kHz. To further visualise the thin plate movement, magnitude and phase plots have been simulated using the FEA and are shown in Figure 6.5. From the plot in Figure 6.5, it could be identified that the thin plate is moving in a piston like motion or a fundamental mode of (0,1). This is the expected mode of vibration for the design.

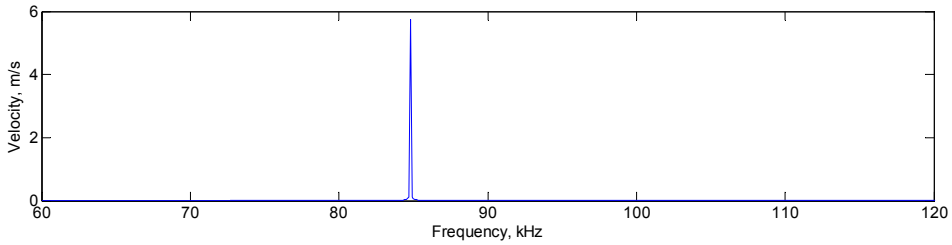

Figure 6.4: Plot of Velocity on the Surface of the Thin Plate at the Centre as a Function of Frequency

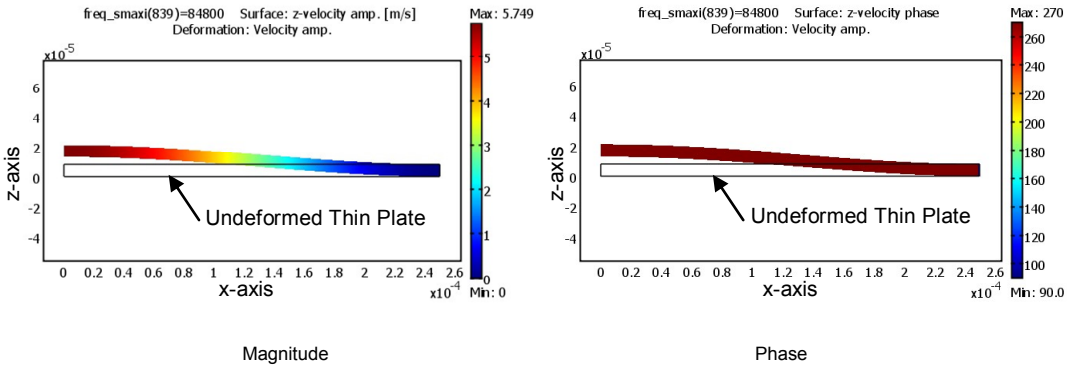

Figure 6.5: Plot of Mode Shape for Thin Plate at Resonant Frequency of 84.8 kHz

Now that the thin plate have been validated using the FEA, it is also important that the cavity and pipe is verified through the same technique. Figure 6.6 shows the simulated cavity frequency response at the centre of the cavity-thin plate interface when a cylindrical wave pressure input of 1 Pa is applied at the cavity-thin plate interface. The cylindrical wave is applied to the thin plate-cavity interface to simulate the pressure input afforded by the thin plate to the cavity. Except for the cavity-thin plate boundary input pressure and the axi-symmetrical axis boundary, the rest of the boundary condition is considered thick walled. A predefined normal triangular mesh size has been utilised. The resonant frequency of the cavity is found to be at 82.6 kHz, as shown in Figure 6.6. This contributes to an error of about 2.6%, which generally could be contributed from the depth requirement of the cavity. In addition, to determine the vibrational mode for the resonant frequency of the cavity, a model that predicts the pressure variation inside the cavity is simulated and is shown in Figure 6.7. From the plot in Figure 6.7, it could be observed that the cavity behaves in a fundamental mode with the maximum pressure at the centre of the cavity.

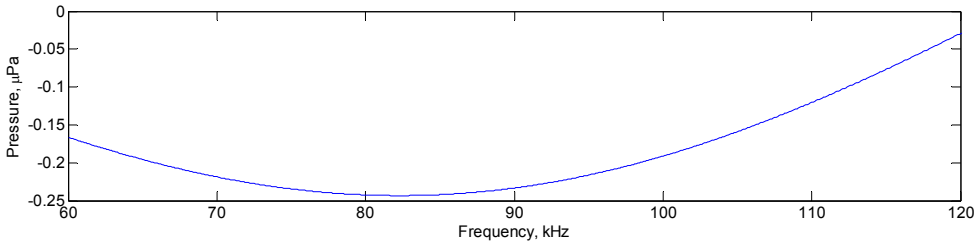

Figure 6.6: Plot of Pressure at Cavity-Thin Plate Interface as a Function of Frequency

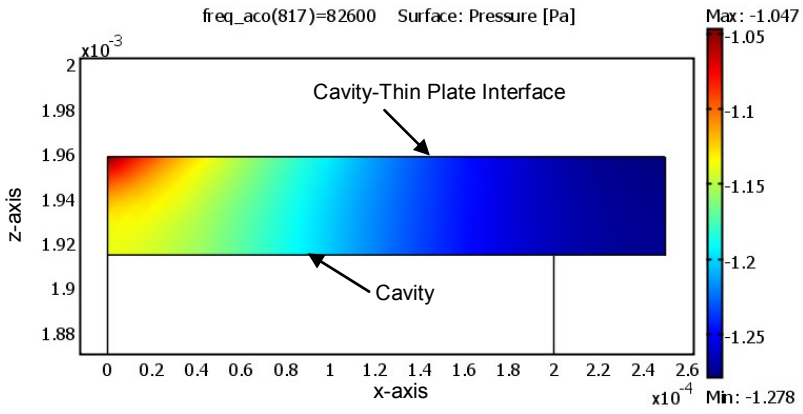

Figure 6.7: Plot of Pressure Trend in Cavity

The final component that needs to be identified is the pipe resonance. In this case, as previously, a 2D axi-symmetric simulation has been performed; with a 1 Pa input pressure at the pipe-cavity interface. Except for the pipe input pressure and the axi-symmetrical axis boundary, and the internal built-in boundary condition by Comsol, the rest of the boundary condition is considered thick walled. A predefined normal triangular mesh size has been utilised.

The frequency response from the simulation is illustrated in Figure 6.8. From the simulation, it is observed that the frequency of the pipe is at around 83.5 kHz with a 1.5% error compared to the analytical geometric modelling. To identity the operating mode of the pipe, two simulations have been performed - to identify the variation of pressure within the pipe column (Figure 6.9) and the variation of pressure across the length of the pipe at its centre (Figure 6.10). In Figure 6.9, it could be observed that the pressure within the radial of the pipe is generally equal. In addition, the maximum pressure across the pipe axis is at the centre of the pipe at around 850 µm of the pipe length. To illustrate this, the pressure along the axial length of the pipe has been plotted as is shown Figure 6.10. From the Figure 6.10, it could be observed that the maximum pressure is around 4.5 Pa at axial length of around 1000 µm. Thus, the standing wave observed in Figure 6.10, corresponds with the expected response for the fundamental mode of an open cylinder or pipe as detailed in the Figure 3.4. This indicates that the pipe is behaving in a fundamental mode.

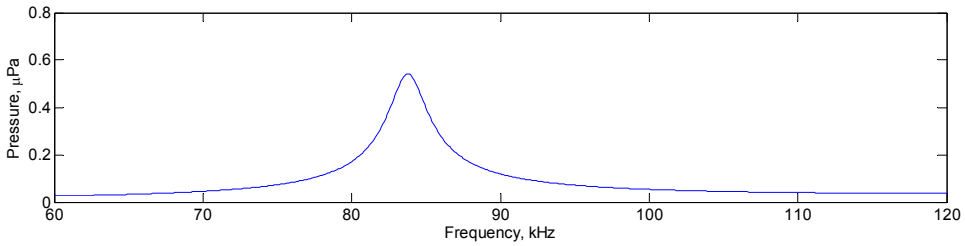

Figure 6.8: Plot of Pressure at Pipe-Air Interface as a Function of Frequency

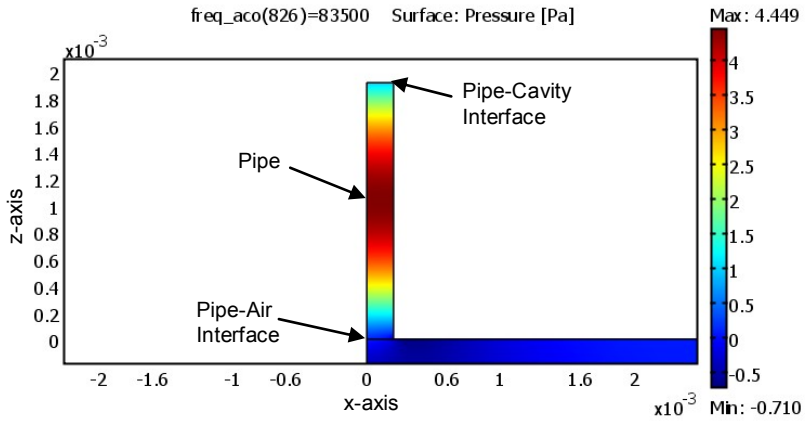

Figure 6.9: Plot of Pressure Output in Pipe Geometry for Design Frequency of 84.8 kHz

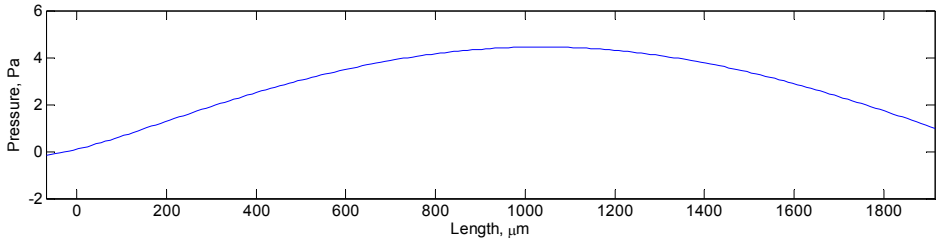

Figure 6.10: Plot of Pressure at the Centre of the Pipe Geometry as a Function of Pipe Axial Length at Design Resonant Frequency of 84.8 kHz

Although, it is expected that the resonant frequency of the combined system to be around 82 kHz - 85 kHz from the FEA and analytical modelling, it is still important to model the effect of cavity and pipe as a geometric coupled pair.

As such, the frequency response for the 84.8 kHz designed transducer has been simulated and the plot is shown in Figure 6.11. The data point is taken at the centre of the pipe-air interface. The same input pressure of 1 Pa has been utilised for the FEA boundary condition at the cavity-thin plate interface, with a predefined normal triangular mesh size utilised. Except for the input pressure, the axi-symmetrical axis boundary, and the internal built-in boundary condition at pipe-cavity interface and pipe-air interface, the rest of the boundary condition is considered thick walled.

In addition, from Figure 6.11, it could be observed that there is a slight frequency shift of about 3.5 kHz, which corresponds to 4.1 % error when compared to the

analytical model. In addition, to confirm that the 84.8 kHz observed is the first harmonic, a standing wave of the frequency has been plotted as shown in Figure 6.13. The plot shows a typical fundamental or first harmonic pipe resonance standing wave with the maximum pressure at the centre of the pipe. The pressure plot within the cavity and pipe geometry is also plotted in Figure 6.12. From the pressure plot, it could be observed that the maximum pressure is at slightly off centre of the pipe length towards the pipe-air interface; with an internal pressure of around 11.5 Pa. Once the geometric resonant frequency has been verified, then a simulation of a fully electrical and dynamic coupling for the device as a single unit cell will need to be performed - to identify any frequency shift due to the electrical excitation and dynamic vibrations within the thin plate, cavity and pipe microstructure.

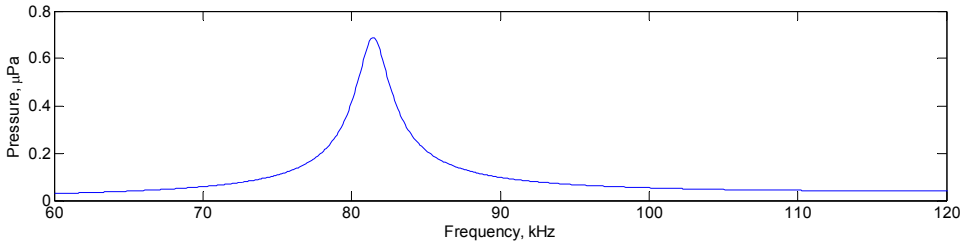

Figure 6.11: Plot of Pressure Output for a Matched Cavity and Pipe as a Function of Frequency

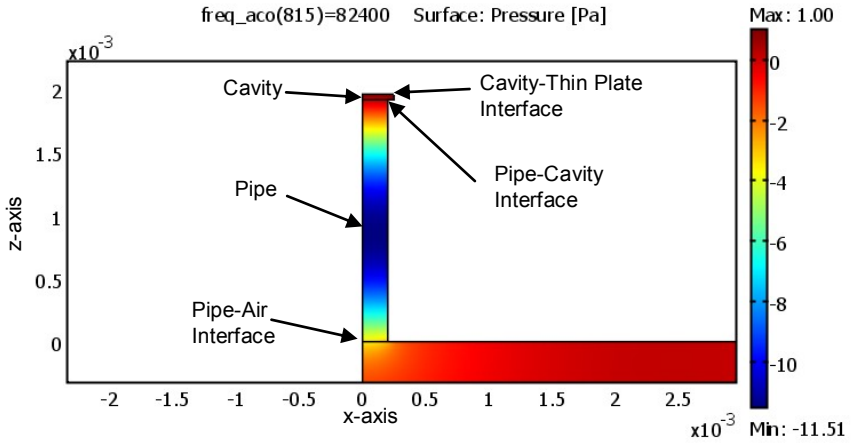

Figure 6.12: Plot of Pressure Output in Cavity and Pipe Geometry at 82.4 kHz

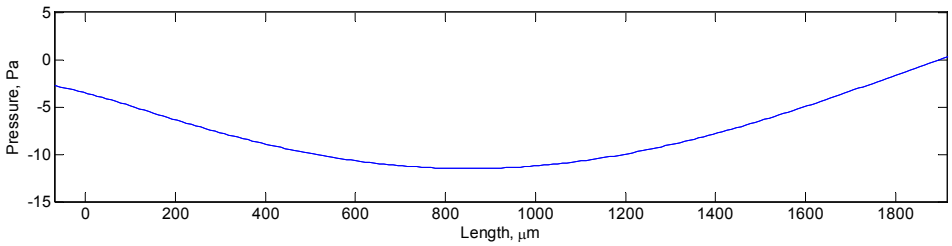

Figure 6.13: Plot of Pressure at the Centre of the Cavity/Pipe Geometry as a Function of Pipe Axial Length at Resonant Frequency of 84.8 kHz

As mentioned previously, there are two software packages being utilised to simulate the full electromechanical behaviour of the device, which are Comsol and PZFlex. As such using the same method, the 84.8 kHz transducer device is simulated using the equivalent software to identify the expected resonant frequency under pre-stressed (bias) with the electrical and mechanical dynamics of the system.

In addition to the above interactive coupling between the electrical and mechanical dynamics of the system, as before a further model of the FLAUT transducer has been created including the air load. The excited model analysis is performed utilising an axi-symmetrical boundary condition. Furthermore, the same boundary condition is applied - for thin plate, the z-direction boundary condition is free, with x-direction at the 250 um edge fixed; while for cavity and pipe micro-structure, the cavity-thin plate interface, pipe-air interface and the thin plate-air interface utilises the built-in internal boundary condition. The rest of the geometries assumed to have a boundary condition of hard walled. However, as the excited model requires that the thin plate is pre-stressed, the use of triangular meshing is not possible as the FE solvers are unable to converge due to the inverted mesh issues. Thus, in excited model analysis, a predefined orthogonal mesh and a mapped mesh are utilised instead.

The simulated frequency response at the centre of the thin plate-air interface as derived using Comsol and PZFlex is shown in Figure 6.14 and Figure 6.16. From Figure 6.14 and Figure 6.16, it could be observed that the resonant frequency of the FLAUT is at 83.5 kHz and 82.5 kHz for Comsol and PZFlex respectively. This

constitutes a 1.5% different between the analytical model and Comsol and 2.7% between the PZFlex and the analytical model. This level could be considered good since the level of tolerance error expected from manufacturing is more than the model. As before, a mode shape analysis has been performed to identify whether the resonant frequency is behaving as a fundamental mode (0,1) or other higher order modes. From Figure 6.15, it could be observed the magnitude plot of the FLAUT performed using Comsol, indicates that the thin plate is behaving in the fundamental mode. From the phase plot, it could also be observed that the thin plate is vibrating at the same phase throughout the free section of the thin plate indicating fundamental mode behaviour. Alternatively, from Figure 6.17, using PZFlex it could also be observed that the thin plate is behaving in fundamental mode, thus indicating that the design of the FLAUT is resonating at a fundamental mode. It is interesting to note however, that both Comsol and PZFlex indicate that the maximum pressure is when the thin plate is moving outwards from the thin plate-air interface. This would suggest that there is a pressure build-up within the cavity and pipe, which forces the thin plate to bulge at the resonant frequency. In addition, it is also possible to suggest that the electrostatic force may not be sufficient to pull in the thin plate fully during excitation.

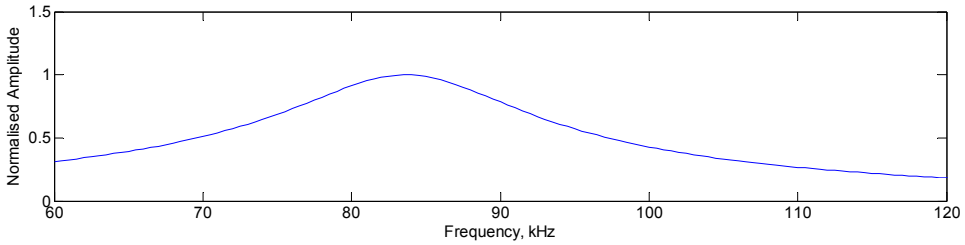

Figure 6.14: Plot of Simulated Frequency Response for Coupled FLAUT at Designed at 84.8 kHz Utilising Comsol Multiphysics

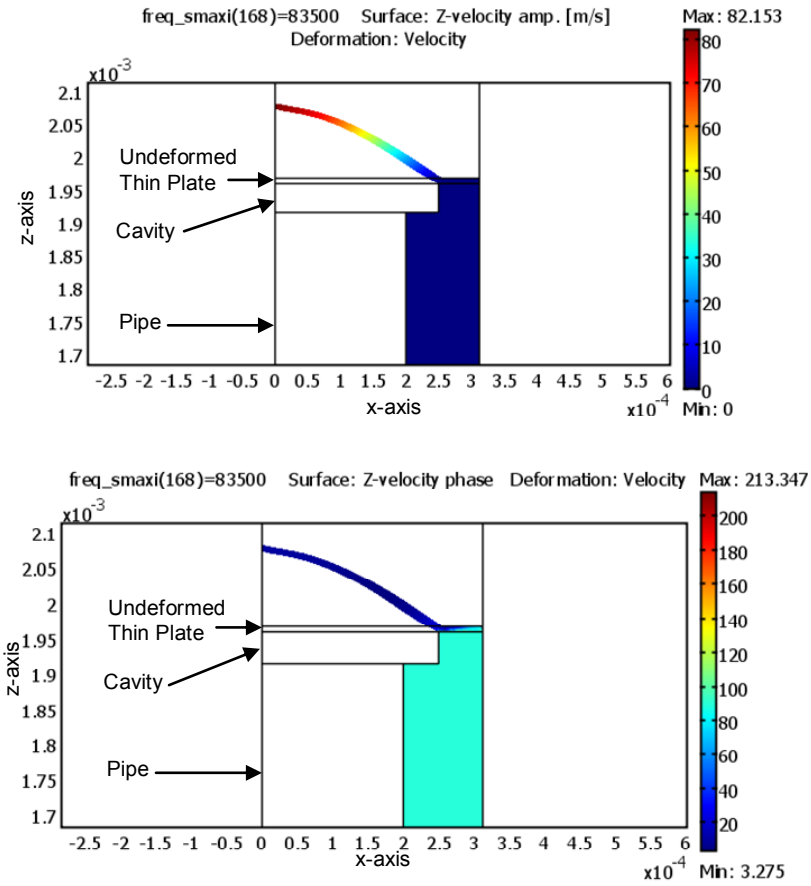

Figure 6.15: Plot of Mode Shape for FLAUT: Magnitude (Top) Phase (Bottom) at Resonant Frequency of 83.5 kHz (Comsol)

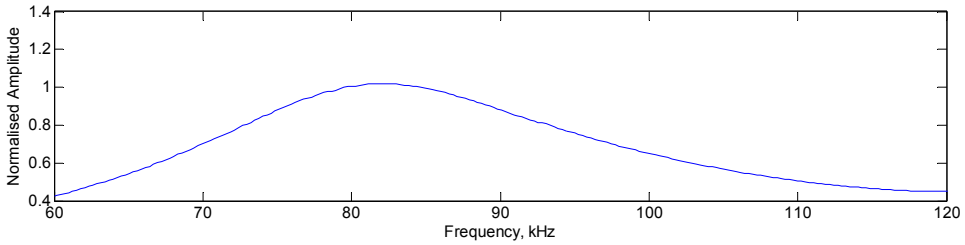

Figure 6.16: Plot of Simulated Frequency Response for Coupled FLAUT at Designed at 84.8 kHz Utilising PZFlex

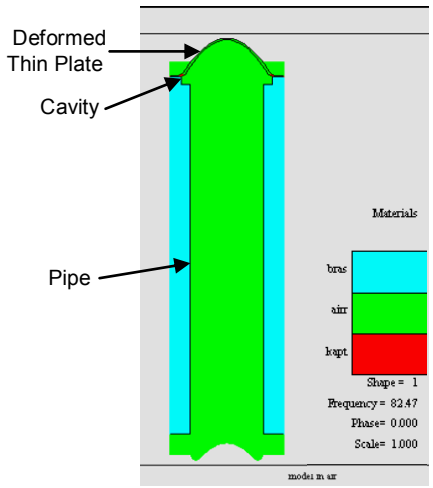

Figure 6.17: Plot of Mode Shape for FLAUT at 83.5 kHz (PZFlex)

From both of the simulations in Figure 6.15 and Figure 6.17, it was found that the thin plate is deformed outwards. To investigate the item further, simulation for different pipe radii was performed to identify the thin plate mode shape. From the investigation, it was found that the thin plate mode shape is similar i.e. deformed outwards towards the thin plate-air interface as the different pipe radii is increased to 450 µm or reduced to 300 µm; which suggests the different pipe radii do not influence the mode shape of the thin plate. From the investigation, no specific ratio could be identified which corresponds to whether the thin plate will be deformed towards the thin plate-air interface or towards the pipe-cavity interface. Thus, in this case, no specific optimum designs of the cavity diameter to pipe diameter ratio exist, other than to ensure that the pipe diameter is as large as practically possible as previously proposed in Section 4.6.3 and 5.4.1.

6.2.2 Backplate Array Design

Previously, the geometry for the single unit cell has been identified. Simulation to verify the geometry of the single cell FLAUT, and the coupled simulation using PZFlex and Comsol have also been performed. However, a Micromachined Ultrasonic Transducer (MUT) device is typically comprised of a large number of

active cells on a backplate. The resonant frequency of the array is dependent on the device microstructure. The microstructure is expected to be in phase and in similar amplitude to enhance the overall output of the transducer. In reality, this is not the case. There are always some non-uniform and out of phase cells within the array. This increases the parasitic capacitance, which in turn can reduce the dynamic range, bandwidth and sensitivity [152, 153]. The parasitic capacitance affects the electromechanical coupling of the device thus causing the device performance to be reduced due to the uncontrolled displacement of the membrane [154]. This is because the quantity of the phase and anti-phase cells determines the final beam profile. Due to the fact that cells with the same phase generate a constructive interference which amplifies the overall output of the transducer; while cells which have phase and anti-phase generate a destructive interference reducing the overall output of the transducer. A suitable array separation and configuration is thus required. This will be discussed in detail in the next section.

6.2.2.1 Optimising Array Separation

There are always some trade offs that need to be made in any design. In order to design a high frequency electrostatic transducer, a small cavity radius and a shallow depth is needed, which generally reduces the overall device sensitivity [25, 155]. In order to compensate for this reduction, an optimised fill factor is needed. Fill factor is defined as the ratio of active area (diaphragm over cavity) versus the total area of the diaphragm. The higher the fill factor, the higher the average cell displacement of the device. But, this comes at a price, as increasing the fill factor increases the number of non uniform cells operating within the array as well as increasing the presence of higher order modes in the device as highlighted by Wong *et al* [90]. In terms of geometry, hexagonal packing has the highest fill factor followed by orthogonal/rectangular packing and circular packing as shown in Figure 6.18. This makes hexagonal to be the packing of choice. In addition, according to Lee *et al* [156, 157] and Pritchard [158], the acoustic loading for the hexagonal packing is expected to be more uniformly distributed due to the mutual acoustic impedance

influences. Thus, in this case, to ensure that the cell-to-cell separation is optimised and the device output is enhanced, a hexagonal packing is chosen.

a)

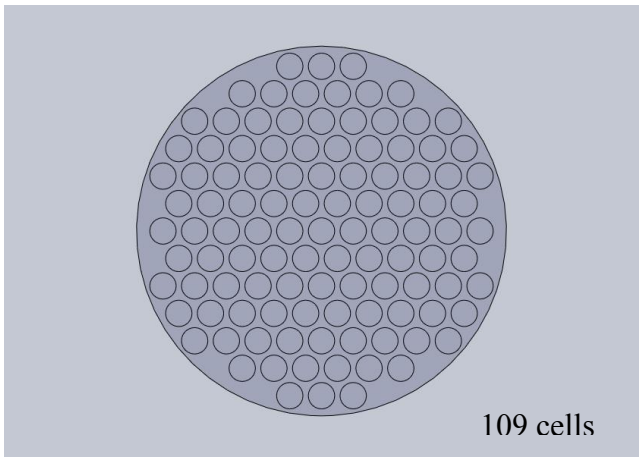

Hexagonal

b)

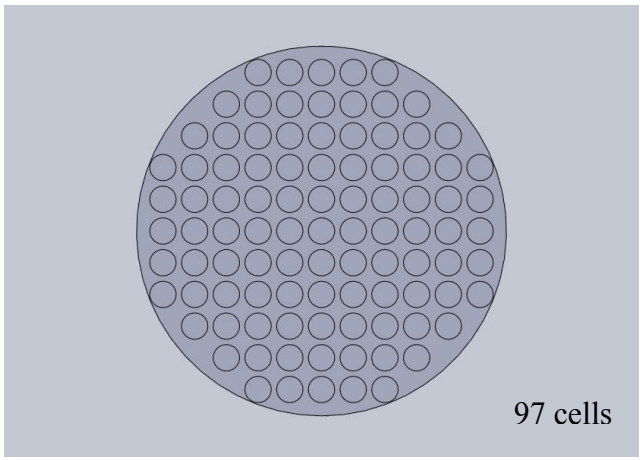

Orthogonal/
Rectangular

c)

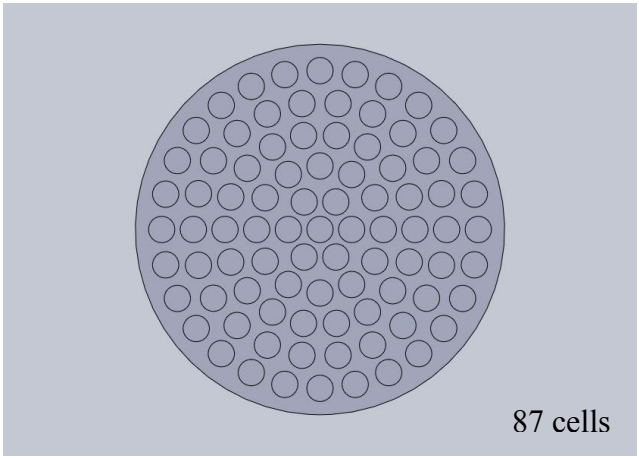

Circular

Figure 6.18: Schematic Diagram of Circular Cell with Different Fill Factor a) Hexagonal b) Orthogonal/Rectangular c) Circular

Wong *et al* [90] cited that other than improving the fill factor, having a mechanical cell-to-cell isolation within the array is paramount. The non-active contact area of the diaphragm to the surface needs to be as small as possible to maximise the fill factor, but large enough to maintain the stiffness of the diaphragm to prevent non-uniformity within the array.

Another key important characteristic that need to be considered for an array is the separation between the individual cells. In this case, Senlik *et al* [83, 159] and Lee *et al* [156] have suggested that pressure sensitivity could be improved by increasing the radiation resistance. This could be performed by having the array to be separated at 1.25λ [83, 159] or 1.17λ [156] . However, this primarily works when *ka* is larger than 1, where *k* is the wave number and *a* is radius of the cavity as expressed by Senlik *et al* [83, 159] and Lee *et al* [156].

In the current context, at 84.8 kHz, the *ka* is less than 1. Thus, according to Lee *et al* [156] and Pritchard [158], the most optimised separation, *d* which allows best possible radiation efficiency is at *d* equal to *2a*. However, in the case of FLAUT in order for the parts to be running at its operating frequency, there is a need to ensure that all the key geometric components are coupled to each other. In this case, in order for the FLAUT to operate effectively, physical geometry of the FLAUT needs to be controlled and maintained.

Effectively, being a coupled resonant device and thus operating in a narrow bandwidth; although it is theoretically recommended to have a separation to be at double the cavity radius, a good geometric control still needs to be achieved through means of sound manufacturing processes and design. As such, the separation needs to be arranged in such a way that the separation gives a good cell to cell isolation and geometric resonant frequency first, then the actual array optimisation. This would enable a good individual cell performance being enhanced by the good array design.

If a machine X-Y placement tolerance of 0.01 mm is assumed, it was found that when *d* is less than *2.25a*, the corresponding geometric features do not allow a good cell-to-cell separation. This is due to the possibility of an inter-cell surface damage primarily caused by the X-Y placement tolerance that the machine could handle. In the schematic diagram shown in Figure 6.19, it could be observed that the distance between the circumferential edges of one cell to the circumferential edge of the other cell is at 0.125 mm, giving the tolerance of ±0.0625 mm for each cell. This matches well with the machine tolerance repeatability of ±0.05 mm, giving the final individual cell tolerance at ±0.0125 mm.

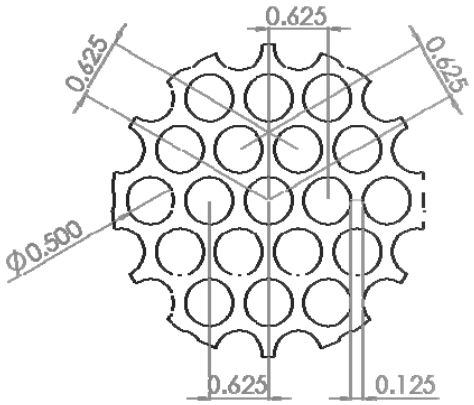

Figure 6.19: Schematic Diagram of Hexagonal Packing Tolerances (All Dimensions are in mm)

From the consideration above, the FLAUT array has been designed to incorporate the hexagonal packing and the inter cell separation of 0.63 mm. The final schematic diagram for the FLAUT array, which consists of 447 cells, is shown Figure 6.20.

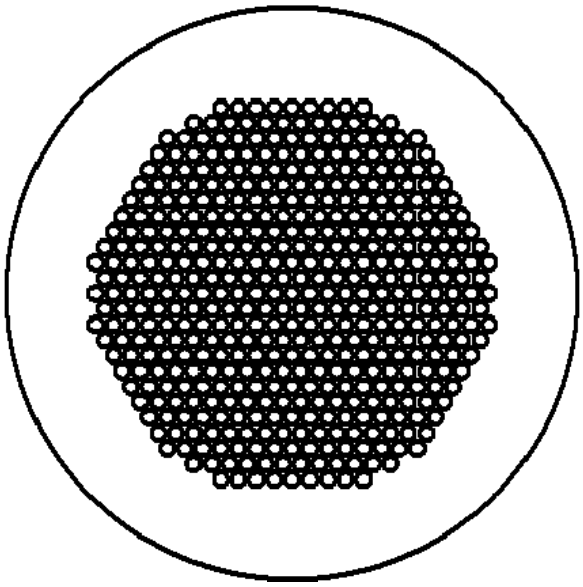

Figure 6.20: Schematic Diagram of a FLAUT Array Incorporating Hexagonal Packing and Separation of $d = 2.25a$ or 0.63 mm.

6.2.3 Beam Profile Simulation

In addition to the frequency response in terms of velocity and pressure output, another key characterisation that needs to be investigated is the resultant acoustic field or the beam profile for the FLAUT array design. This beam profile effectively describes the amplitude and the directivity of the sound propagating from the transducer into the load medium.

The beam profile of the FLAUT array was simulated using a Matlab code developed by Benny and Hayward [88] based on Huygen-Fresnel Principle [160] which assumes a continuous wave signal at a specific frequency is utilised. The FLAUT array surface is approximated as a ground of radiating point sources. From there, the contributions of these point sources are summed at points in the field. A beam profile simulation of the FLAUT array based on the cell size of 0.50 mm in diameter and cell-to-cell separation of 0.63 mm has been performed and is shown in Figure 6.40 (Left). The effects of attenuation have been considered within the Matlab codes developed by Benny and Hayward.

6.2.4 Simulation of a FLAUT Noise

Now that the signal sensitivity have been identified. It is also important that the noise within the FLAUT is simulated to ensure that a full characterisation of the FLAUT performance in terms of both sensitivity and noise are identified. As such, utilising the same technique that has been described in the previous Chapter, the noise simulation for the 84.8 kHz transducer has been calculated at temperature of 20^{o}C and atmospheric pressure of 101.325 kPa.

From the array design, the number of cells has been identified to be 447. Thus, the total mechanical resistance due to the holes, R_{perf} could now be calculated. In this case since there is more than one hole, then the Equation 5.9 needs to be utilised. The array transducer resistance could then be determined and is shown in Figure 6.21.

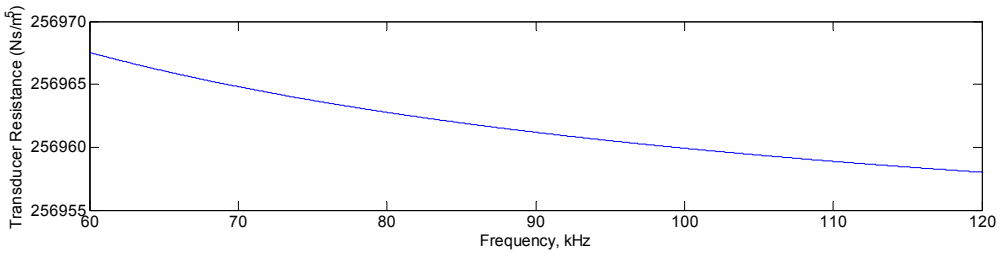

Figure 6.21: Plot of Transducer Resistance as a Function of Frequency for a FLAUT Designed to Operate at 84.8 kHz for Frequency Range of 60 kHz to 120 kHz

From Figure 6.21, it could be observed that the transducer resistance is reduced as the frequency is increased within the frequency range of interest of 60 kHz to 120 kHz. However, within the total frequency spectrum, the mechanical resistance is almost independent of frequency, as discussed earlier as shown in Figure 6.22.

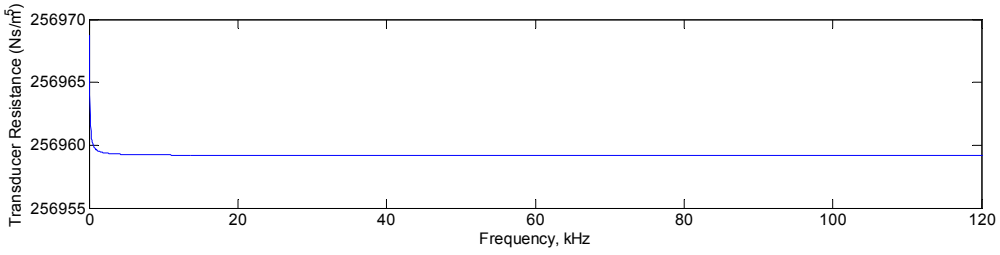

Figure 6.22: Plot of Transducer Resistance as a Function of Frequency for a FLAUT Designed to Operate at 84.8 kHz for Full Frequency Range Until 120 kHz

Utilising the same simulation techniques that have been utilised in the previous Chapter, the simulated noise frequency spectrum within the desired range could be calculated and is shown in Figure 6.23.

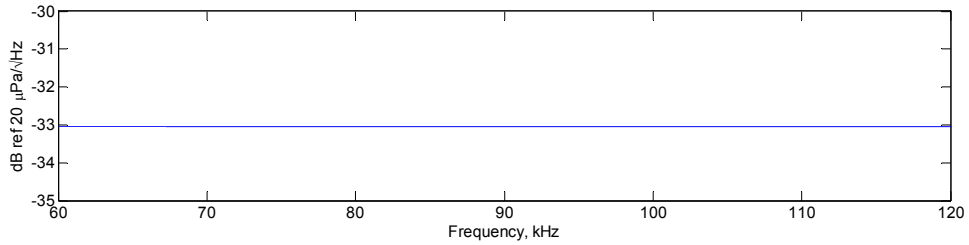

Figure 6.23: Plot of Simulated Noise as a Function of Frequency Spectrum for FLAUT Designed at 84.8 kHz

Finally, in order to assess the overall performance of the FLAUT design, a comparison to a conventional electrostatic transducer with cavities only was undertaken. The same noise simulation technique has been utilised to simulate the conventional electrostatic transducer. However, with the removal of the pipe microstructure within the conventional electrostatic transducer, there is a need to remove the effect of pipe noise within the conventional electrostatic transducer noise simulation. Thus, in the case of the conventional electrostatic transducer with cavities only, Equation 5.11 is utilised. As such, the simulation for the noise frequency spectrum for cavities only is also plotted and is shown in
Figure 6.24. From the simulations, it could be observed that there are no major differences in the noise level between the FLAUT and the conventional electrostatic transducer. In addition, from the simulations, it could be observed that the noise level is independent of frequency for the range of 60 kHz to 120 kHz for both the FLAUT and the conventional electrostatic transducer.

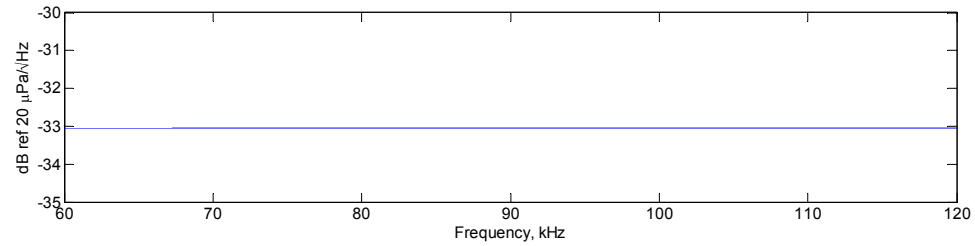

Figure 6.24: Plot of Simulated Noise as a Function of Frequency Spectrum for Conventional Electrostatic Transducer Designed at 84.8 kHz

6.3 Manufacturing and Assembly

Now that the modelling of the FLAUT both in term of sensitivity and noise has been performed, the next step is to produce a prototype, which could verify the modelled FLAUT. However, before a prototype could be manufactured, the necessary minimum manufacturing tolerances and a suitable manufacturing process to match - needs to be identified which will be discuss next.

6.3.1 Manufacturing Tolerance Review

One of the key components in the manufacture of a FLAUT is to ensure that the geometry of the individual FLAUT component is being controlled and maintained at its desired tolerance. As previously described, a FLAUT operates on a basis of resonant geometries being coupled to each other to amplify the final pressure output at the FLAUT front face. As such, for this amplification to be optimised, the individual resonant frequency of each thin plate, cavity and pipe needs to be matched. In order, to understand the effect of manufacturing tolerance towards the final resonant frequency tolerance, the manufacturing sensitivity analysis performed in Section 4.7 will be utilised.

To investigate the effect, the proposed manufacturing tolerance of 1 μm, 5 μm, 10 μm and 20 μm have been considered for a 84.8 kHz FLAUT transducer. With that consideration, and utilising the method of manufacturing sensitivity analysis previously performed in Section 4.7.2, the tolerance of the individual resonant frequencies of the FLAUT geometry could be calculated and plotted in Figure 6.25, Figure 6.26 and Figure 6.27.

From Figure 6.25, it could be observed that as the manufacturing tolerance increased from 1 μm to 20 μm for the manufacture of the cavity radius geometry, the resonant frequency error for the thin plate increased from 84.8 kHz ± 0.8% to 84.8 kHz ± 16.0%.

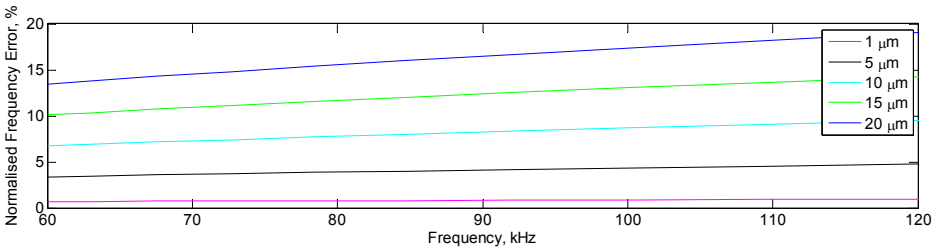

Figure 6.25: Plot of Thin Plate Resonant Frequency Error as a Function of Frequency for Different Manufacturing Tolerance of 1 μm, 5 μm, 10 μm and 20 μm

In addition, from Figure 6.26, it could be observed that as the manufacturing tolerance increased from 1 μm to 20 μm for the manufacture of the cavity depth geometry, the resonant frequency error for the cavity increased from 84.8 kHz ± 1.1% to 84.8 kHz ± 22.9%.

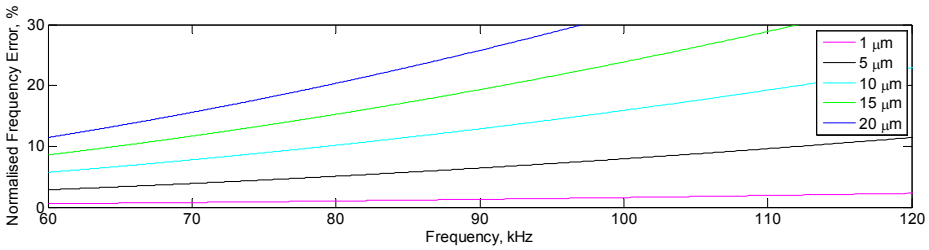

Figure 6.26: Plot of Cavity Geometry Resonant Frequency Error as a Function of Frequency for Different Manufacturing Tolerance of 1 μm, 5 μm, 10 μm and 20 μm

Lastly, from Figure 6.27, it could be observed that as the manufacturing tolerance increased from 1 μm to 20 μm for the manufacture of the pipe geometry, the resonant frequency error for the pipe increased from 84.8 kHz ± 0.06% to 84.8 kHz ± 1.15%.

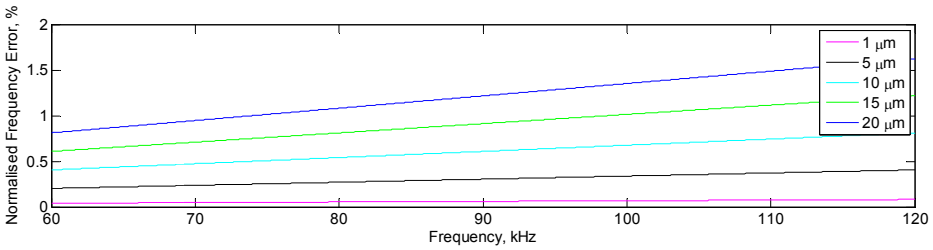

Figure 6.27: Plot of Pipe Geometry Resonant Frequency Error as a Function of Frequency for Different Manufacturing Tolerance of 1 μm, 5 μm, 10 μm and 20 μm

From Figure 6.25, Figure 6.26 and Figure 6.27, it can be observed that, as the desired transducer operating frequency increases, the manufacturing tolerance needed to maintain the same level of resonant frequency error must be reduced. As such, to manufacture a FLAUT at high frequency, the manufacturing tolerance needs to be high In the case of a 84.8 kHz design transducer, a maximum manufacturing tolerance of 15 μm for the choice of manufacture is suggested giving the resonant frequency error for the thin plate, cavity and pipe to be at ±12.0%, ±17.1% and ±0.9% respectively. From the discussion above, it could be seen that the manufacture of the cavity depth is critical in determining the manufacturing process for a FLAUT. Given the same tolerance for manufacture at 15 μm, the error on resonant frequency for 84.8 kHz transducer design due to cavity depth is 5% higher compared to the cavity radius.

Thus, what these signify is as the tolerance of manufacture increases, the error of variation within the resonant frequency of the individual thin plate, cavity and pipe changes. With this respect, the ability to manufacture devices to the specification needed is important. The choice of manufacture and the tolerance afforded by such a manufacturing process is directly affecting the resonant frequency of the FLAUT. The lower the tolerance or error during manufacture, the smaller the variation of frequency between the individual FLAUT components, which is desirable.

Next, the choice of manufacture will be discussed and the repercussions based on individual component will be viewed.

6.3.2 Choice of Manufacture

In Chapter 4, different manufacturing processes have been discussed. Based on the discussion, MSL was found to be the easiest technique to manufacture but lacks the resolution and tolerance required to produce such a device at high frequency. On the other hand EDM, although showing good promise of manufacturing micro-sized devices is expensive and time consuming. Lastly, laser manufacture, although it is

possible to control the laser beam to manufacture the cavity geometry; it still has the issue of tapering. This tapering issue causes the pipe inlet to be larger than the pipe outlet, thus causing the resonant frequency of the FLAUT to behave differently. Therefore, in this case the conventional manufacturing processes of drilling and milling are being suggested to manufacture the FLAUT, provided that the required tolerances are met and within acceptable limits.

6.3.3 Manufacturing Sensitivity Analysis

Once that manufacturing process has been identified, as discussed earlier the expected propagation of error or machine sensitivity analysis needs to be calculated. The purpose of this exercise is to ensure that the process to manufacture devices itself is capable of producing such a prototype, since one of the key characteristics of an efficient FLAUT is to have the design to be within tolerance. This is to ensure that the FLAUT amplification is optimised. As such, with this technique, it is possible to identify with reasonable confidence that the design could be produced per the expected design tolerance; and/or the expected error that is associated with such an out of tolerance manufacture.

In producing the 84.8 kHz FLAUT, the suggested manufacturing process for the backplate is to utilise the two processes which are: the drilling technique utilising Roland Engraver Model EGX-600 [161] and a standard lathe machine. The Roland Engraver is suggested because the spindle is able to produce speeds of up to 15,000 revolution per minute (RPM) critical to manufacture such a microstructure required in the FLAUT. In addition, from the tooling and machine specification, it is found that the tolerance for the drilling of a single hole and counterbore is at 0.01 mm while the tolerance for the lathe machine, which concerns the thickness of the plate, is at 0.01 mm. Several preliminary studies have been performed to identify the suitable spindle speed for manufacture. Upon, investigation it was found that the maximum spindle speed of 15,000 rpm gives the best results both in term of cavity/pipe dimensions and consistency.

From these two specifications, a machine sensitivity analysis could be performed to identify whether the manufacturing process is able to accommodate the 84.8 kHz design. From the Sensitivity Analysis Techniques introduced in Section 4.7.2, the propagation of error in terms of resonant frequency tolerance for the different geometry (thin plate, cavity and pipe) with a design resonant frequency of 84.8 kHz is shown in Figure 6.28. From Figure 6.28, it is clear that the resonant frequency tolerance for the plate and pipe are both less than 10% or at 8% and 0.6%, respectively. While at the same time, the resonant frequency tolerance for the cavity is marginally above the desired 10% with a calculated error at 11.4%. This is expected due to the fact that a small change in the cavity depth would in fact give a significant change in resonant frequency of the cavity. For example, in order to have a cavity resonating at 84.8 kHz, a 0.044 mm cavity is primarily required. However, due to manufacturing tolerance, in this case a ±0.005 mm tolerance or 0.01 mm tolerance; then the resonant frequency could be from 80.3 kHz to 90.1 kHz giving a 9.8 kHz error range. Utilising this technique, the designer not only could identify what is the critical aspect of the FLAUT design that needs to be considered, the designer could also identify what is the critical control that the designer needs to be aware of to ensure that the final prototype could be produced according to the specification. In essence, with the Sensitivity Analysis (SA) consideration being made before the final prototype is produced, the suitable method of manufacturing could be analysed thus reducing prototyping cost and implementation cycle.

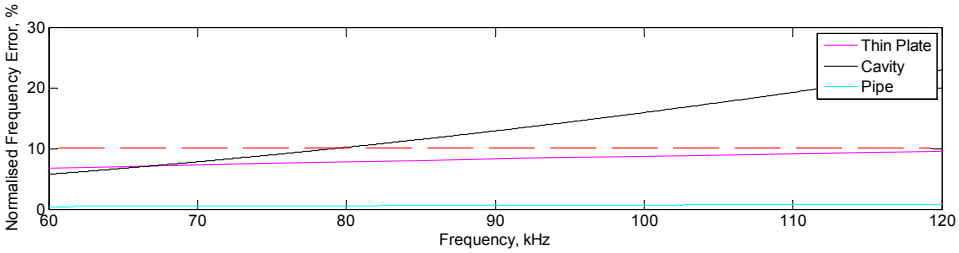

Figure 6.28: Resonant Frequency Error as a Function of Frequency for Three Different FLAUT Geometry Configuration

Lastly, from Figure 6.28, it could be shown that in the process to manufacture the parts, tight control for the cavity depth is crucial. This is clearly indicated by the

different slope in the plot between the thin plate, cavity and pipe. It could be observed that the thin plate and pipe have much lower slopes when compared to the cavity, thus indicating how crucial the cavity tolerance needs to be controlled.

6.3.4 Prototyping and Assembly

Before the manufacture of the prototype could be performed, an appropriate backplate material needs to be selected. There are four different backplate materials that have been tested:

- **Aluminium**: this material is not suitable due to damage that it cause to the micro drill bit.
- **Acrylonitrile butadiene styrene (ABS)** [162]: this material is easy to drill and is appropriate for a single cell design. However, the excess heat generated when machining a cell caused problems of dimensional stability of the material.
- **Acrylic** [163]: this material is not suitable due to its brittleness and damaged that it caused to the drill bit.
- **Ebalta Ebaboard PW920** [164]: this material is also easy to drill as in the ABS. However, this material is more dimensionally stable under prolonged machining cycles required for the manufacture of the backplate

From the selection above, the Ebalta Ebaboard PW920 is chosen as the backplate material due to its suitability to the current process.

In order to manufacture the FLAUT a blank of the appropriate thickness and diameter was prepared using the lathe machine. The cavity and pipe pattern was machined into the blank using the Roland Engraver. Devices comprising a single unit cell and an array of 447 cells were prepared using this process. Once the backplates have been drilled, the backplates were then coated with aluminium using the thermal evaporation process discussed previously in Section 4.3 to make them conductive. Typically, the thickness of the aluminium layer is at around 150 nm. The final

FLAUT backplate for both a single cell and the array of cells is shown in Figure 6.29.

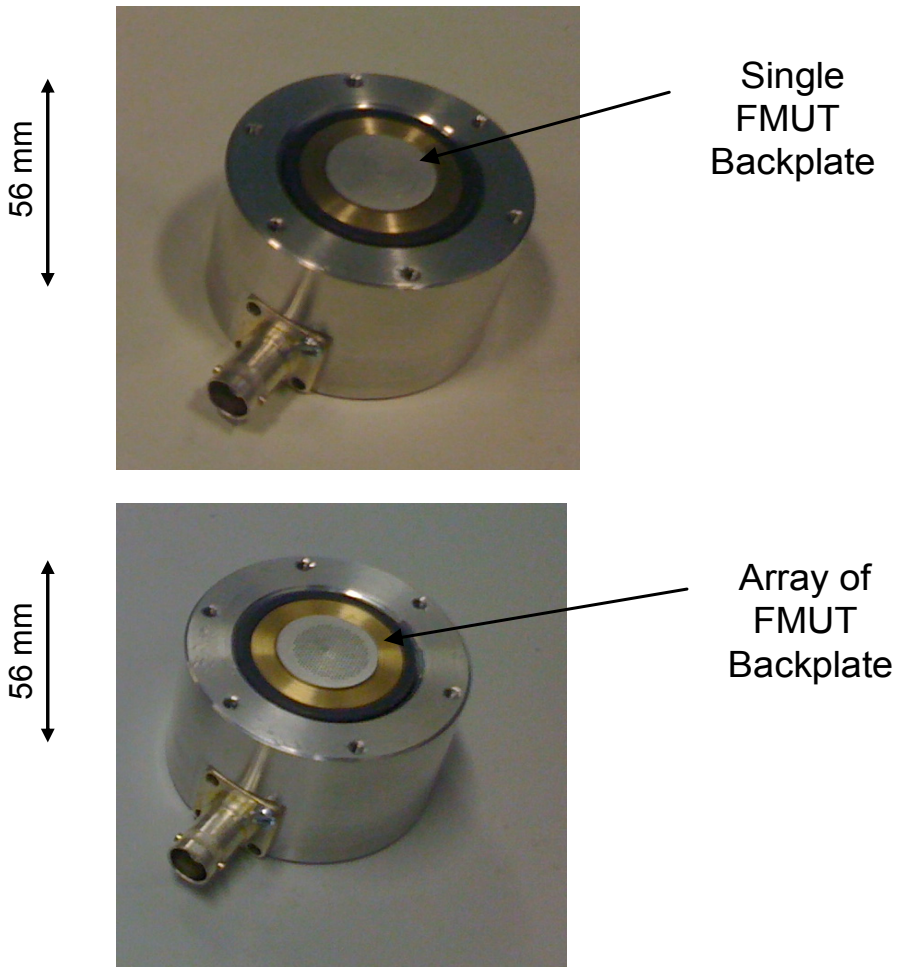

Figure 6.29: Picture of Single Cell FLAUT on an Ebalta Backplate (Top) and Array of FLAUT Cells on an Ebalta Backplate (Bottom)

Lastly, the backplate above was covered using the 8 μm Kapton film which had been bonded to a metallic ring. The fully assembled FLAUT is shown in Figure 6.30. From the previous review, it was found theoretically that the thin plate tension does not play a great role in the FLAUT resonant frequency. However, it is still a good practise to ensure that the tension of the thin plate is made to be uniform. Utilising a torque screwdriver, the tension of the thin plate is made to be uniform by ensuring that each of the screw is tighten to a torque of 0.45 Nm. The torque value was chosen

based on experimentation that had been performed previously. From the experiment, it was found that the chosen torque of 0.45 Nm was able to ensure that the thin plate was uniformly tensioned across the surface of the membrane; whilst maintaining a good mechanical bond between the metallic ring and the main assembly.

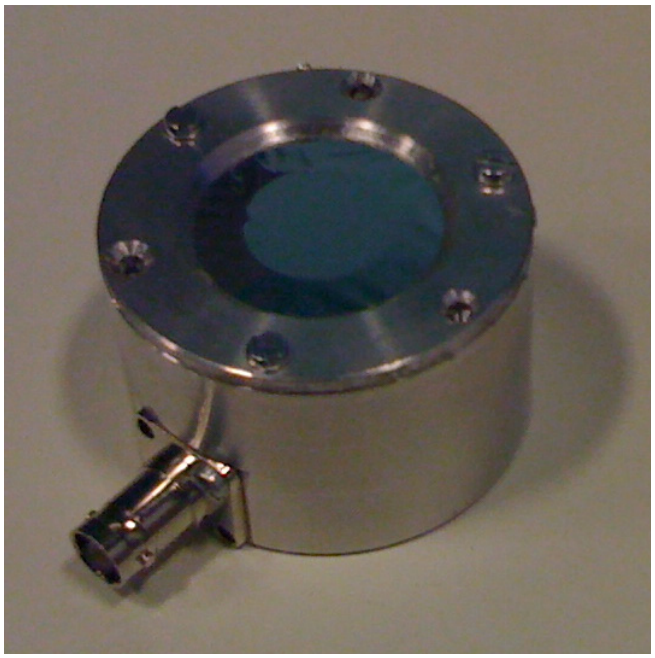

Figure 6.30: Picture of a Fully Assembled FLAUT

6.4 Characterisation of FLAUT Prototype and Modelling Validation

6.4.1 Measurement of a FLAUT Sensitivity

In order to characterise the FLAUT output sensitivity fully, the measurements for the FLAUT have been performed in three different stages: the single cell measurement, the array measurement and the beam profile measurement.

6.4.1.1 Measurement of Single Unit Cell

The performance of the prototypes was assessed in the same manner as before: laser vibrometry of the thin plate vibration and acoustic measurements using a B&K microphone. The results for the laser interferometer measurement were then compared to the FEA simulations for a single cell and are shown in Figure 6.31.

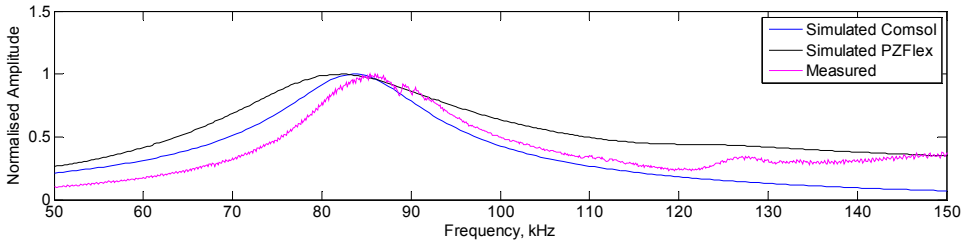

Figure 6.31: Plot of Comparison between Simulation and Measured Results for a Single Cell FLAUT Designed at 84.8 kHz

From Figure 6.31, it could be identified that the resonant frequency for the 84.8 kHz design transducer is at 86 kHz, measured using the laser interferometer. That constitutes to a 1.4% error between the measured and the analytical design. Although, this corroboration could be considered reasonably good, this measurement only constitutes a design with a single cell FLAUT structure of which it is still possible to control both in term of the axial alignment of cavity and pipe and other geometric tolerance requirements during the manufacture. However, as the number of cell increases, so does the complexity of control both in term of concentricity and overall tolerance. In addition to the resonant frequency of the device which has been identified to be at around 86 kHz, the mode shape is also plotted and is found to be a fundamental or mode (0,1) as shown in Figure 6.32.

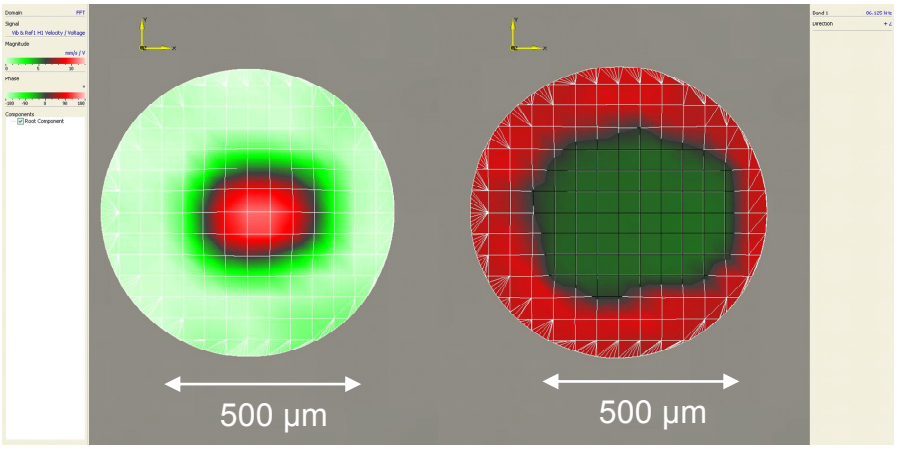

Figure 6.32: Plot of Measured Mode Shape 84.8 kHz transducer design. Left: Magnitude Right: Phase

6.4.1.2 Measurement of Array

In addition to the single cell measurement, an average surface velocity measurement and output pressure measurement for a FLAUT array is also performed. This is mainly because a single cell is suitable as an indicator that the device is operating at its required resonant frequency range. However, it could not indicate the final operational behaviour of the FLAUT device. From the laser interferometer measurement, it was found the FLAUT array is operating at a frequency of around 80 kHz as depicted in Figure 6.33.

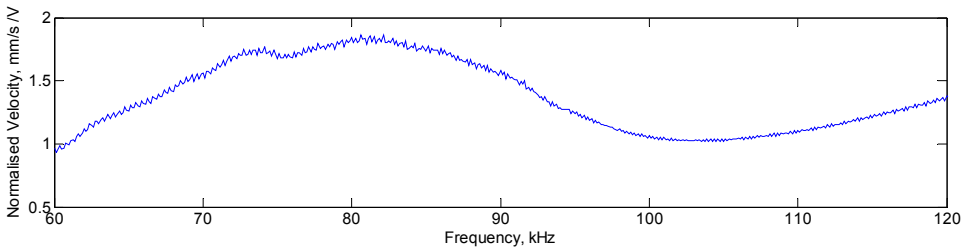

Figure 6.33: Plot of Normalised Average Surface Velocity in the Active Area of the FLAUT as a Function of Frequency Measured Using Laser Interferometer

From the measurement, it was found that that the average normalised velocity for the array is around 1.9 mm/s /V. In comparing the single cell and the array cell surface displacement resonant frequency profile; it has been found that although the output resonant frequency of a single cell corroborates very nearly to the design resonant frequency, the array differs considerably more although within the expected manufacturing tolerance of 80 kHz to 90 kHz. This is due to the fact that the overall output of every individual transducer is not fully in phase with each other as shown Figure 6.34 (Phase). This may be due to the manufacturing defects such as cavity and pipe not matching at the centre of each other and the general mismatch in term of cavity and pipe frequency resonances due to the individual geometric tolerances. Improvement in manufacture through the use of a different manufacturing technique is needed to enable a good output.

In addition, due to the nature of FLAUT which requires the three components to be matched for it to operate optimally, the mismatch will cause a degradation of pressure output as individual cells will start to resonate at slightly different frequencies and amplitude. The magnitude and phase plot for the FLAUT array is shown in Figure 6.34.

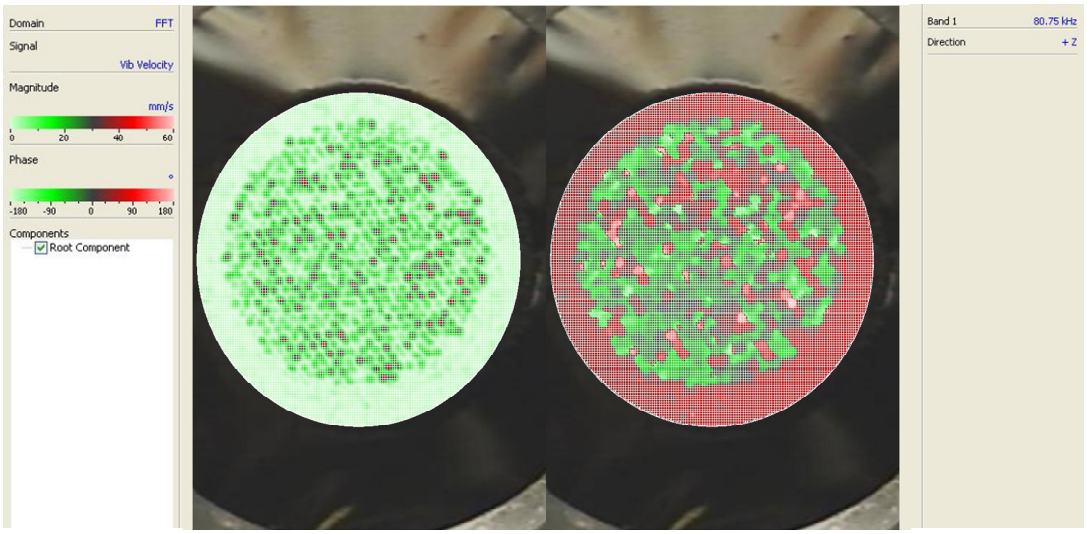

Figure 6.34: Plot of Surface Deformation Profile for FLAUT with Cavity Pipe Design. Left: Magnitude Right: Phase

Furthermore, during the modelling of the FLAUT, each individual cavity is assumed to be clamped at the periphery of the cavity radius. This assumption is considered valid, for a single cell design as previously discussed in Chapter 4. However, there is still a need to investigate further, whether the clamp afforded by the bias voltage is sufficient in the hexagonal array packing design. Although hexagonal packing is able to produce a uniform acoustic loading and the highest fill factor compared to orthogonal or circular packing as previously illustrated in Figure 6.18, the hexagonal packing tend to suffer from lower potential contact area between the active cells - effectively reducing the amount of potential clamping afforded by the bias voltage. In order to investigate this claim, a focus area has been identified and is shown in Figure 6.35.

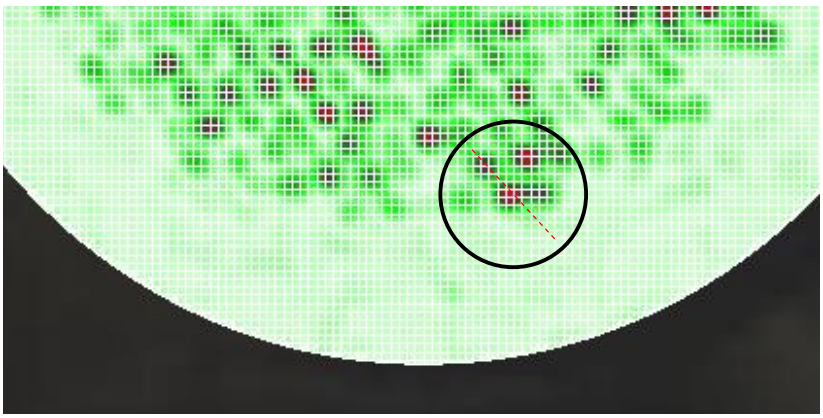

Figure 6.35: Plot of Focused Surface Deformation Profile for FLAUT with Cavity Pipe Design from Figure 6.34

In order to assess the extent of the clamping, a surface deformation of the membrane at resonant frequency of 80 kHz was measured using the laser vibrometer. Figure 6.36 details a membrane surface deformation, taking a cross-section through two adjacent elements/cells from the periphery of the device on the left. As shown in Figure 6.36, the region of around 100 µm – 400 µm represents the periphery of the device and the region between 950 µm and 1000 µm represent the area between the two adjacent cells. From Figure 6.36, there is a surface deformation in the periphery indicating that the membrane is appropriately is biased as previously expected from Figure 4.17. However, it is also clearly shown from Figure 6.36 that there is a surface

deformation in the inter-cavity region indicating that the membrane is not appropriately biased within the region. In order to understand the situation, visual analysis utilising the X-Y-Z Meiji optical microscope has been performed on the device. From the investigation, it was found that the surface roughness and the electrode surface continuity between the periphery region and the inter-cavity region are similar. Further investigation also shows that the bias clamping across several areas within the surface is also comparable - the surface roughness and electrode surface continuity shows visually similar profile to before. Thus, from the plot it could be proposed that the designed inter-cavity cell area is not sufficient for the cell-to-cell vibration to be independent and sufficiently clamped at its periphery by the bias voltage. Since there is no specific modelling that has been performed to identify the most suitable area, a model needs to be developed to identify the suitable array separation, which considers sufficient bias voltage to clamp the thin plate periphery. However, a trade off is still required to ensure that the improvement in device output sensitivity through an optimised fill factor arrangement is considered along the array separation requirements. This will be proposed in future work.

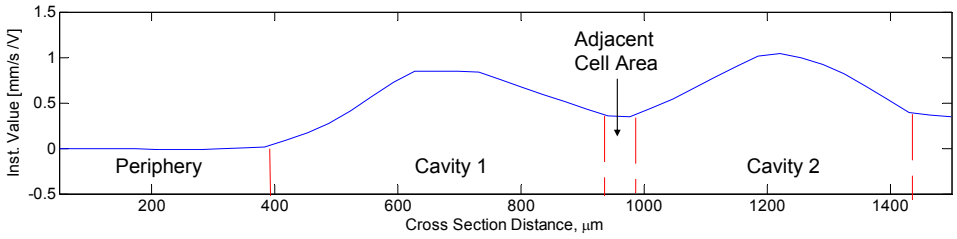

Figure 6.36: Plot of Cross Section View of Thin Plate Surface Velocity for Two Cavity at the Edge of the Backplate

Furthermore, from Figure 6.33, it could be observed that the normalised velocity increases as the frequency increases to above 100 kHz for a FLAUT. To understand this situation, an extended plot for Figure 6.33, has been performed and is shown in Figure 6.37. However, as previously discussed, it is generally expected that the frequency above the resonance will be of higher order complex modes. As such, to verify these assumptions, a surface velocity profile for the peak frequency of 150

kHz has been performed and is shown in Figure 6.38. When plots in Figure 6.38 and Figure 6.35 are compared, it could be observed that the magnitude plot of the thin plate in Figure 6.38 is generally at around 0.2 – 0.6 mm/s across the surface, while the thin plate magnitude for Figure 6.35 is generally at around 20 – 40 mm/s. The large difference of around 100 fold between the velocity magnitude across the surface of the thin plate shown in Figure 6.35 and Figure 6.38 suggests that the transducer at 150 kHz is operating at higher order modes. This also is supported when the two magnitude plots are visually compared. In Figure 6.35, it could be observed that there is a distinct cell-to-cell difference in magnitude, compared to Figure 6.38, where the distinction is not that pronounced – suggesting higher order modes of operation involved.

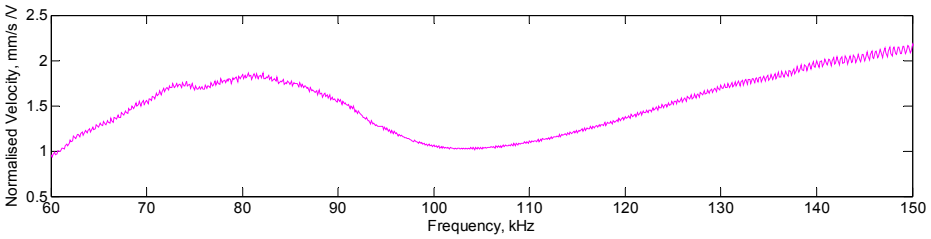

Figure 6.37: Plot of a FLAUT Surface Velocity Profile for Frequency until 150 kHz

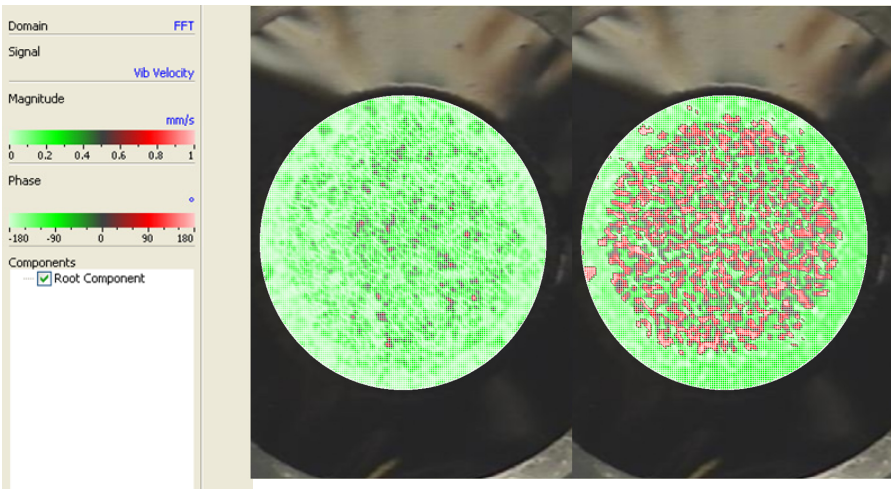

Figure 6.38: Plot of Surface Velocity Profile for FLAUT at 150 kHz

On top of measuring the FLAUT surface velocity profiles, it is also important that the output pressure for the FLAUT is characterised to ensure that the final usable output from the transducer i.e. pressure output is also as per the expected design frequency. As such, the setup for the pressure frequency response as discussed earlier in Chapter 4 has been utilised and the results for the frequency response measurement at 1 kHz resolution are shown in Figure 6.39.

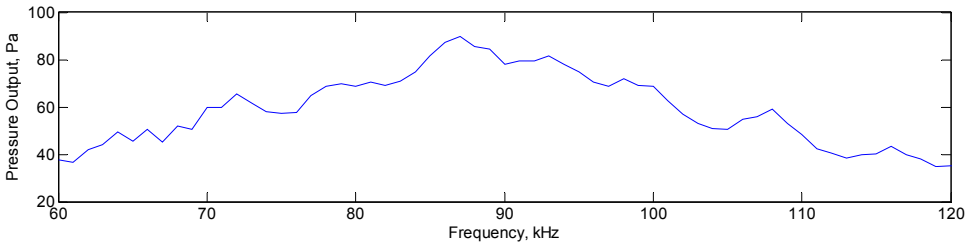

Figure 6.39: Plot of Pressure Output Frequency Response for FLAUT transducer

From the measurements performed, it has been found that the resonant frequency for the FLAUT is at around 80 kHz to 90 kHz, which is as expected by the design consideration and manufacturing constraint. Furthermore, from the measurement it could be calculated from Figure 6.39 that the -3 dB fractional bandwidth is at 27%. In this case, it could be concluded from the measurements performed that the FLAUT does operate within the expected design and manufacturing constraint and tolerances. The fractional bandwidth of 27% is expected in FLAUT design since a FLAUT is considered a resonant device and thus is expected to be a narrowband device.

6.4.1.3 Beam Profile Measurement

In order to measure the beam pattern, a 3-axis manipulator with 1 mm resolution has been utilised. The beam profile for the FLAUT at 84.8 kHz has been measured and compared with the simulated piston mode as shown in Figure 6.40. From the beam profile measurement plotted in Figure 6.40, it could observe that the FLAUT beam

profile does correspond to the piston mode. In addition, it has also been observed that there is one large major lobe present. This is expected since theoretically, when *ka* is less than 1 as in the case of 84.8 kHz design, a major lobe should be present [47].

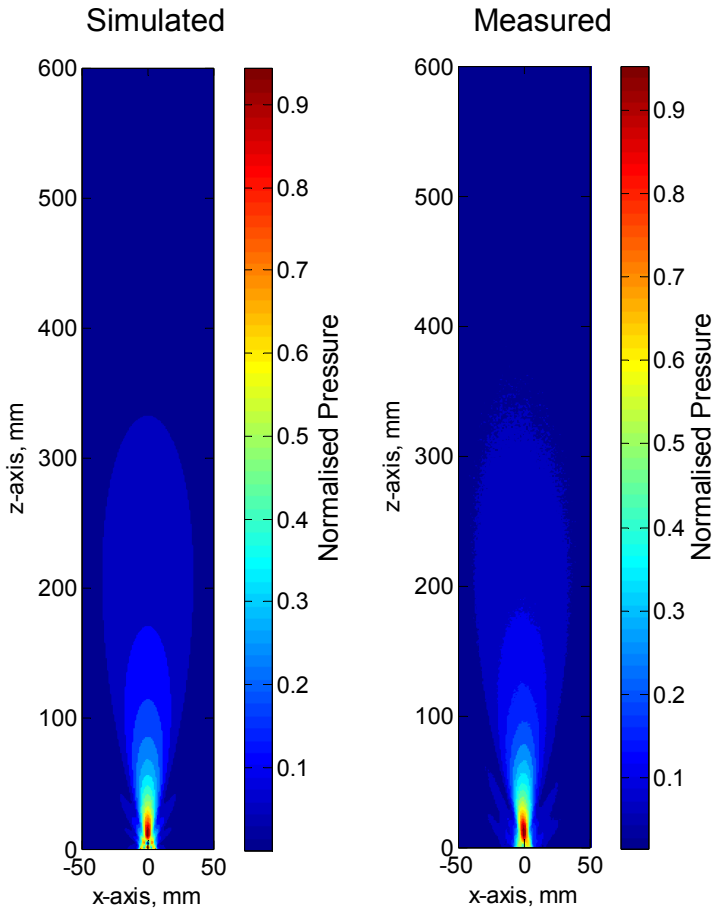

Figure 6.40: Plot of Simulated Beam Profile (Left) and Measured (Right) for FLAUT Operating at 84.8 kHz as a Function of Normalised Pressure Amplitude

6.4.2 Measurement of a FLAUT Noise

Finally, in order to corroborate the noise simulation results, the measured FLAUT transducer noise designed to operate at 84.8 kHz has been compared with the previously simulation data as shown in Figure 6.41. From Figure 6.41, it has been

found that there is a good corroboration between the simulation and measured results.

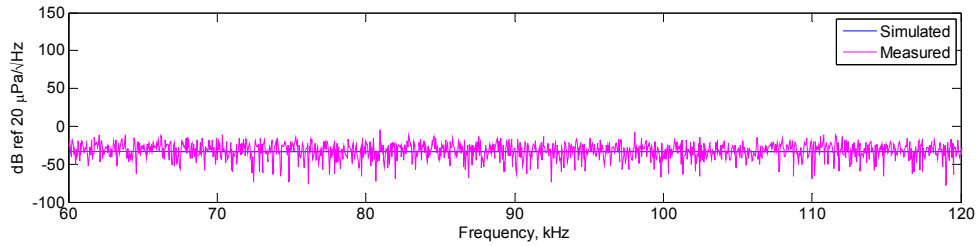

Figure 6.41: Plot of Comparison between Simulation and Measurement for FLAUT Noise at Operating Frequency of 84.8 kHz

6.4.3 Comparison between Measured FLAUT and Measured Conventional Electrostatic Transducer with Cavity Only Design

As discussed in the earlier Chapter the FLAUT is expected to improve the overall output of the transducer to some extent. As such within the context of this thesis, an experimental measurement comparing the FLAUT (Cavity/pipe) and Conventional Electrostatic Transducer (Cavity Only) has been performed. This could be shown with the comparison between the cavity only design designed at 84.5 kHz and the FLAUT cavity and pipe design designed at 84.5 kHz for the measured surface velocity profile in the single cell and array design; as well as the measured pressure frequency response trend as depicted in Figure 6.42, Figure 6.43 and Figure 6.44 respectively.

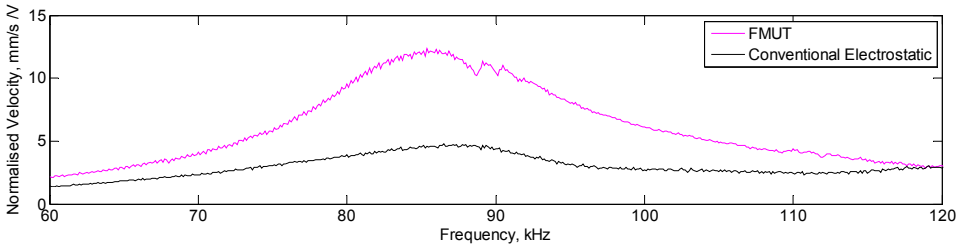

Figure 6.42: Plot of Comparison between FLAUT (Cavity/Pipe) and Conventional Electrostatic (Cavity Only) for Surface Velocity Profile of a Single Cell Design

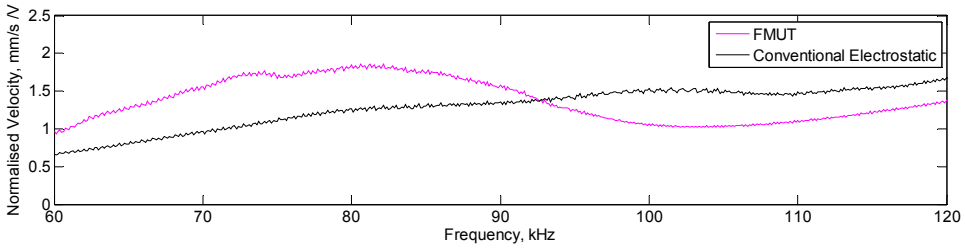

Figure 6.43: Plot of Comparison between FLAUT (Cavity/Pipe) and Conventional Electrostatic (Cavity Only) for Surface Velocity Profile of an Array Design

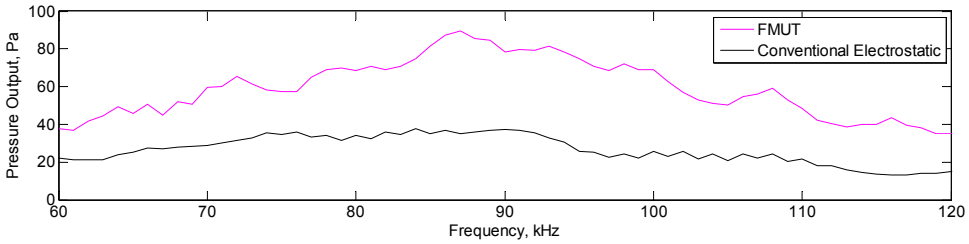

Figure 6.44: Plot of Comparison between FLAUT (Cavity/Pipe) and Conventional Electrostatic (Cavity Only) for Pressure Output of an Array Design Measured Using Frequency Response Technique

From the measurement it could deduced that the improvement noted when compared between the cavity only and cavity/pipe for the three different measurements is about -8.6 dB, -3.2 dB and –8.1 dB for surface velocity profile of a single cell, surface velocity profile of an array and pressure output respectively. Comparing the single cell output, it could be observed, although the improvement in output for the single cell is not as per expectation, the difference could be accounted for due to the fact that the single cell cavity has a higher order mode on top of the single fundamental mode (0,1) which causes the overall thin plate displacement to increase. This is mainly due to the need for the trapped air to escape from the thin plate in the cavity only design. This has created an air pocket around the single cell thus producing further resonance, which is not within the context of the design. This could be observed in Figure 6.45, whereby a distinct mode (0,1) could not be observed at the resonant frequency of the cavity only system, but instead a mode (0,1) with 'leaked' pattern is observed. This is due to air exiting from inside the cavity to the edges of

thin film, and the air pocket surrounding the cavity and thus produces an active area much larger than the FLAUT cavity, which may increase the device output.

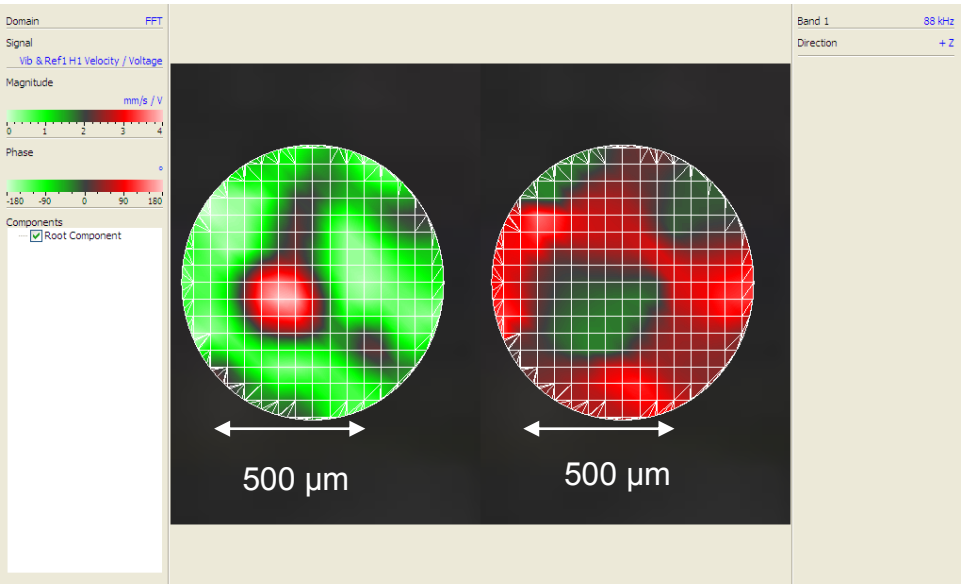

Figure 6.45: Plot of Mode Shape for Cavity Only Design Single Cell

As explained earlier, in order for a good output of the FLAUT to be obtained, the thin plate, cavity and the pipe need to be perfectly matched to each other to enable optimum constructive amplification between the three different geometries. However, in actual fact this is not always possible. Based on the current manufacturing process, it has been observed and found that the cavity and pipe do not perfectly match in the centre, but may be slightly offset due to the machine X-Y repeatability tolerance of 0.05 mm in the two-step drilling process as shown in Figure 6.46. This may create a partial constructive amplification of the individual cell, thus causing the output to be sub-optimal. In addition, due to the component tolerances i.e. disc tolerance at 0.01 mm and drilling counterbore tolerance at 0.01 mm has caused the counterbore depth possibility to be within the range of 0.034 mm to 0.054 mm, thus changing the resonant frequency of the cavity and in essence changing the overall matching of the FLAUT and the cavity only design.

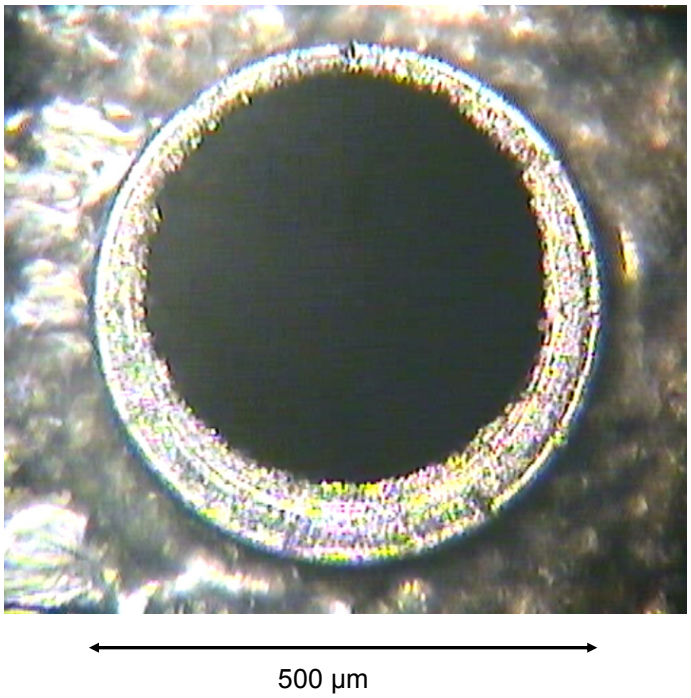

Figure 6.46: Picture of an Offset Concentric Cavity and Pipe

In order to confirm the different possible variation of cavity depth expected from the manufacturing tolerance, 15 random measurements have been performed across the FLAUT backplate utilising a X-Y-Z Meiji optical microscope capable of measuring depth at resolution of 0.0025 mm/div and measuring spatial at resolution of 4.97 µm/div. From the measurement, it was found that the minimum depth of the cavity is at 0.0325 mm, while the maximum depth is at 0.0625 mm. Based on the random sample it was found that the average cavity depth across the surface is at 0.0425 mm. Next, it is also important to investigate the cavity diameter and the pipe diameter. Based on the random sample performed, the cavity diameter and the pipe diameter both indicate that the variance is less than 0.01 mm with means of 500 µm and 400 µm respectively. With this in mind and assuming the cavity and pipe are made concentric, the resonant frequency of the FLAUT could be analytically calculated from the mean value and was found to be at around 87 kHz. This corresponds well with the pressure output measurement previously shown in Figure 6.44.

When comparing the results for the FLAUT incorporating the cavity/pipe design and conventional electrostatic with a cavity only design as in Figure 6.34 and Figure 6.47 respectively, it could be noticed that the mode shape for the cavity/pipe is much more pronounced when compared to the cavity only design. This phenomenon could be explained as in the issues observed with the single cell cavity only design. Primarily, the cavity/pipe design enables not only the amplification of the output signal due to mutual resonances, but also reduces the collective air pocket and thin film damping within the system observed in cavity only design.

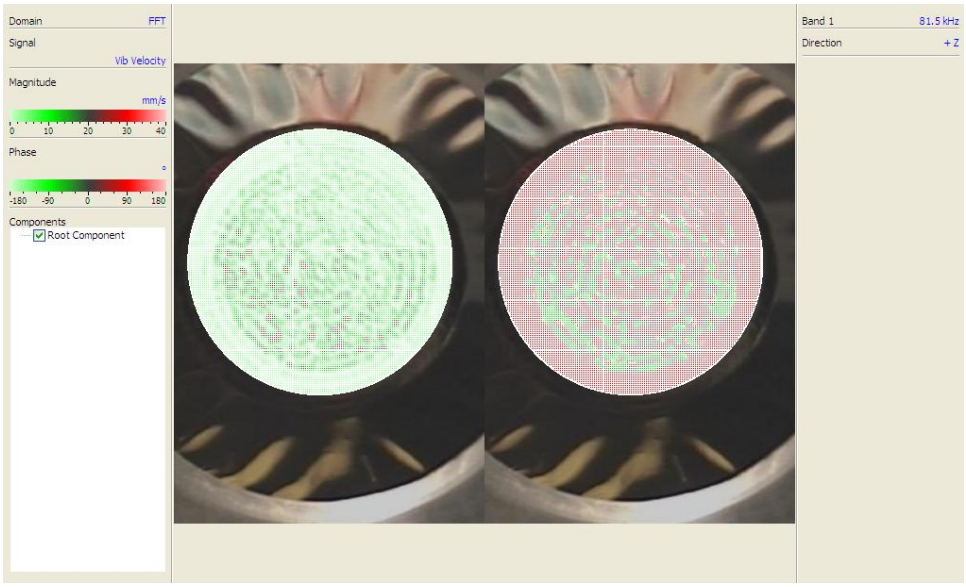

Figure 6.47: Plot of Surface Deformation Profile for Conventional Electrostatic Transducer with Cavity Only Design

The only difference in term of design between FLAUT and Conventional Electrostatic Transducer is the inclusion of pipe microstructure for FLAUT. However, when the two transducer responses were measured at a distance of 100 mm, their performances are different. From the measurements it were found that the transmit voltage response for FLAUT and conventional electrostatic transducers are at 130.2 dB (ref: 1 µPa/V) and 127.5 dB (ref: 1 µPa/V) respectively; while open circuit voltage response for the FLAUT and conventional electrostatic transducers are at -160.7 dB (ref: 1V/µPa) and -163.9 dB (ref: 1V/µPa) respectively. Thus, from

the measurements it could be noted that FLAUT offers a 3 dB improvement in transmission and reception performance of the electrostatic transducers.

In order to illustrate the improvement in FLAUT, the beam profile for the FLAUT and conventional electrostatic transducer with cavity only is plotted and is shown in Figure 6.48. From the plot, it could be observed that the FLAUT has a higher pressure output in the field when compared with the conventional electrostatic transducer. In addition, it is also observed that the FLAUT has a comparable major lobe as the conventional electrostatic transducer.

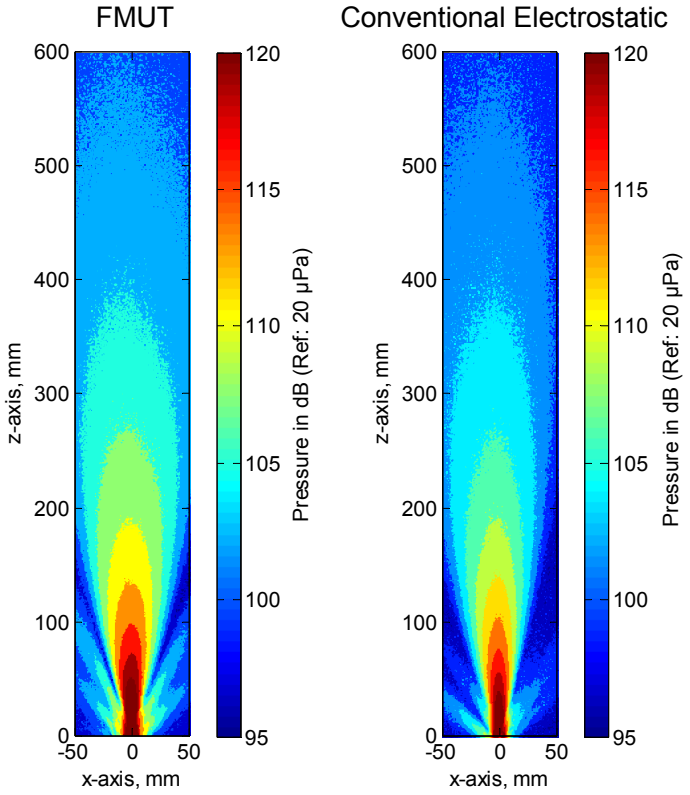

Figure 6.48: Plot of Comparison of Pressure Output Beam Profile in dB (ref: 20µPa) Between FLAUT and Conventional Electrostatic Transducer.

At the same time, in order to understand the differences between FLAUT and the conventional electrostatic transducer noise, the noise for the conventional electrostatic transducer incorporating cavities only has also been measured and is illustrated in Figure 6.49.

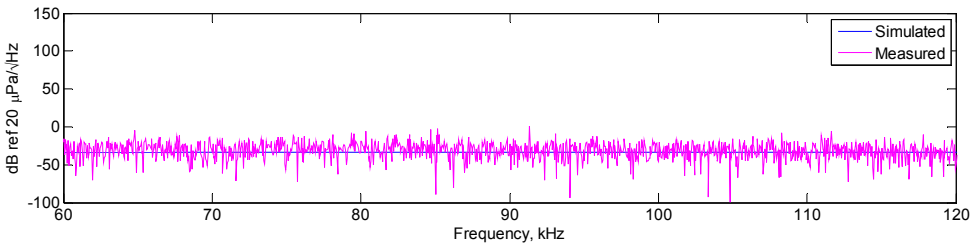

Figure 6.49: Plot of Comparison between Simulation and Measured for Conventional Electrostatic Transducer Noise at Operating Frequency of 84.8 kHz

Although from the plot of Figure 6.41 and Figure 6.49, the two levels of transducer noise look similar, the noise power extracted from the area under the curve in the plot indicate that they are different. Upon further investigation and calculation, it was found that the thermal noise power for the cavity only transducer for a bandwidth of 120 kHz is larger than the cavity/pipe system. From the measurement it was found that the cavity only transducer has a thermal noise power of about 7.9 W while the cavity/pipe system has the thermal noise power of about 5.8 W for the same bandwidth measured. This does indicate that the pipe structure helps to reduce the overall thermal noise power by about -2.7 dB. Thus, it could be concluded that adding a pipe structure to the cavity only system, not only improves the overall device sensitivity but also reduces the overall noise floor within the device as shown through the measurement performed in this Thesis.

Although, the performance benefit in terms of transmit and receive response as well as noise improvement may not illustrate a significant improvement individually. As a SNR combination, it does help. With FLAUT utilised as a transducer, the noise floor for the transducer has been illustrated to be lower than the conventional electrostatic transducer, while at the same time the signal sensitivity has been shown to improve – giving a much larger SNR improvement overall. Through further manipulation and with the use of signal processing, this SNR improvement could be exploited further to enhance the overall efficiency and effectiveness of the system, which utilises FLAUT as the transduction mechanism.

Finally, as a completion, two-way insertion loss measurements have also been performed for both the FLAUT and conventional electrostatic transducer. The measurements were performed using a 4 MHz Ultrasonic Pulser in a pulse-echo arrangement with 40 dB gain. The broadband pulser has an impulse input voltage at 1.2 V. The echo input voltage detected by the FLAUT and the Conventional Electrostatic Transducer at a distance of 100 mm is shown in Figure 6.50. From the Figure 6.50, it could be clearly seen that the FLAUT has a higher input voltage amplitude of around 9 dB when compared with the conventional electrostatic transducer. The two-way insertion loss for both devices has also been calculated and is found to be at 61.3 dB and 70.4 dB for FLAUT and conventional electrostatic transducer respectively. This clearly indicates that FLAUT have a lower insertion loss of 9.1 dB when compared to the conventional electrostatic transducers.

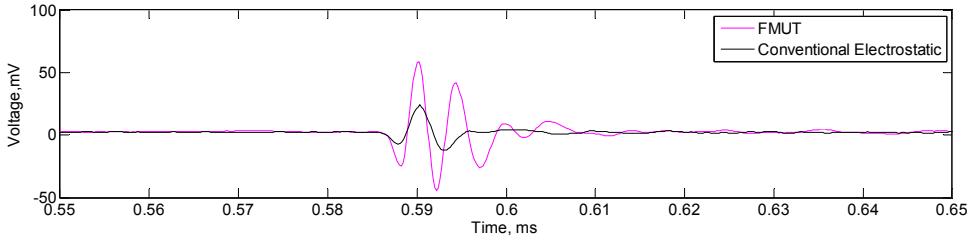

Figure 6.50: Plot of Comparison of Detected Pressure Input Voltage in mV for FLAUT and Conventional Electrostatic Transducer Front Face

In all the cases above, it could be noted that FLAUT are able to improve the signal and reduce the noise within an electrostatic transducer. Since the only difference between the two is the relief function of the pipe and the reduction in electrode area in the cavity/pipe microstructure, then the possibility of improvement would depend generally on these two cases.

In the first case, the inclusion of a relief function as in the pipe, have shown through previous study [24, 25, 82] to reduce the thin film damping, radiation resistance and thus reduce the noise and improve sensitivity due to reduction in transducer resistance. On the second case however, with the reduction of electrode area in the cavity/pipe microstructure, it is expected that the electric field between the two

surfaces to be reduced by around 8.9 dB as the conductive surfaces between the two thin plates reduces. With the electric field across the thin plate and the cavity backplate at the circumference reduced, the thin plate is left to vibrate without a strong electrostatic influence and effect. Effectively, the parallel plate capacitance for the two could be calculated using the Equation 6.1 as shown:

$$C = \varepsilon \frac{A}{d} \qquad \textbf{Equation 6.1}$$

where $\varepsilon = \varepsilon_r \varepsilon_0$, $\varepsilon_0 = 8.8541878176 \times 10^{-12}$ Fm^{-1}, A is the area for the parallel plate capacitor and d is the separation between the parallel plate capacitor. Substituting Equation 6.1, with the corresponding parallel plate area, A for cavity only (conventional) design and cavity/pipe (FLAUT) design, with d separation as cavity depth, d_a, gives the theoretical capacitance for the conventional transducer, $C_{conventional}$ and FLAUT, C_{FLAUT} as 1.3×10^{-13} F and 4.8×10^{-14} F respectively.

In addition, there is a different dielectric constant, k_ε, thus reflective index, n ($n = k_\varepsilon^2$) [165] between air and the FLAUT/conventional backplate. Thus, according to Donohue [166] there will be transmitted, reflected and incident electromagnetic waves just as in the acoustic waves previously discussed in Chapter 4. With the same analogy, the conventional electrostatic transducer could be assumed to have almost 100% reflection at the backplate due to the large refractive index between the air and the conductive aluminium [167]. On the other hand, FLAUT will have a 36% reflected electromagnetic wave to the front face load at the cavity-thin plate interface and about 64% transmitted electromagnetic wave to pipe face load at the cavity-pipe interface.

Thus, another possibility of the improvement could be from the reduction of the reflected electromagnetic wave afforded by the electric field between the two parallel plates. This could be illustrated by the observed correlation, between the reflected waves calculated at 8.9 dB to the insertion loss measured at 9.1 dB – giving an error of 0.2 dB; and between the transmitted waves calculated at 3.9 dB and to the sensitivity and noise improvement of around 3 dB – giving and error of 0.9 dB.

6.5 Conclusion

In this Chapter, the implementation of the High Frequency FLAUT Transducers has been discussed utilising the concept previously noted in Chapter 4 and Chapter 5. However, as the frequency requirement increases, the FLAUT size required to accommodate the required frequency would also need to be reduced accordingly. Thus, in this Chapter, the need for an array design to enable an improvement in FLAUT pressure output has been shown. From the investigation, it has been found that by having a separation of $d = 2.25a$, the pressure output of the FLAUT array could be optimised. Although it is suggested that $d = 2a$, is the best packing to improve overall output, issues regarding the higher order modes which are seen even at separation, $d = 2.25a$, coupled with the issue of X-Y linear motor tolerance for the Roland Engraver - made this a challenge to manage and control.

This Chapter has proven that FLAUT transducer could be designed and fabricated to work at frequency range of above 60 kHz, provided that the rules pertaining to the design is considered. In spite of manufacturing an 84.8 kHz transducer using the conventional drilling technique could be considered stretching the limit, the output of the transducer proved that it was still possible. In this Chapter, the noise measurement has also been performed, thus giving a full characterisation of the device.

Lastly, from the measurement it was found that the insertion loss for the FLAUT is at -61.3 dB, while for the conventional electrostatic is at -70.4 dB. This is a -9.1 dB improvement when the two are compared. In addition, FLAUT have also demonstrated that there is a -2.7 dB thermal noise reduction for a 120 kHz bandwidth, compared to a conventional electrostatic transducer. Thus, FLAUT has significant potential in improving the pressure output to be utilised in an air-coupled application.

However, this work could still be considered in its infancy stage. Further research is needed in modelling and simulation of the FLAUT array, improving the current

manufacturing process and identification on how to enable FLAUT to operate at a higher frequency region of 100 kHz and beyond - suitable for industrial applications. As such within the next Chapter, a full conclusion of the Thesis and suggested future work with a view to enabling commercially viable FLAUT solution, in addition to improving current research structure and methodology is proposed.

7. Conclusion and Recommendation for Further Work

7.1 Conclusion

This Thesis has presented a theoretical and experimental analysis of a FLAUT. A range of modelling tools has been employed to analyse the design variables of the components that comprise the FLAUT. The modelling tools have been corroborated using a number of prototypes. In addition, the noise mechanisms within the FLAUT devices have been analysed theoretically and experimentally.

7.1.1 General Overview

From the investigation, it has been found that in order for the development of a FLAUT to be a success, there are four main considerations that need to be made. The first is to identify the required design parameters, the second is to identify the relevant geometry that relates to the required design parameters, the third is to simulate the design using FEA and the last is to identify a suitable manufacturing technique and its suitability using the manufacturing sensitivity analysis/propagation of error analysis. Once this design cycle is completed, and the transducer has been manufactured and assembled, a verification process has to be performed. With the device verified as per design, the whole production cycle could be considered complete.

7.1.2 Main Finding of this Thesis

From this thesis, in conclusion from the theoretical and experimental analysis, the following guidelines have been determined for the development of a FLAUT device operating in air.

- Using commercially available membranes such as Kapton, increasing the thin plate resonant frequency would require that the thin plate diameter be reduced in an inverse square root power function.
- In matching the FLAUT, it is important to realise that a FLAUT is a resonant device thus, there is always a need to ensure that all the components of the FLAUT i.e. thin plate, cavity and pipe are matched to the same frequency in order to optimise the amplification.
- Matching of the thin plate and cavity resonant frequency is interchangeable in terms of sequence based on the necessity of the manufacturing requirement, i.e. if the requirement to achieve the cavity resonant frequency by controlling cavity depth is more onerous then the matching could be performed by matching the thin plate resonant to the cavity resonant.
- As a resonant device, it is important to notice during FEA of the FLAUT that a single resonant frequency is observed within the scope of our work. If another frequency is observed, then there is a possibility that a mismatch occurs thus a re-evaluation of the analytical model may be warranted.
- In order to have the full effect of the pipe amplification in FLAUT, it is required both in term of sensitivity improvement and noise reduction to have the pipe diameter to be as large as possible. However, the constraint of manufacturing still needs to be considered since amplification warranted in FLAUT still requires that the resonant frequency of thin plate, cavity and pipe to be matched. So, the term as large as practically possible for the FLAUT pipe diameter should be considered, to enable optimum output to be realised from the device.

From the measurement performed, the FLAUT performance compared to the conventional electrostatic transducer could be characterised and summarised as follows:

- From the laser interferometer and frequency response measurements, it has been found that the improvement of between around 3 dB and 9 dB in term sensitivity output is observed when compared to the conventional electrostatic transducer devices.

- From the sensitivity measurements, it was also found that the FLAUT has a transmit voltage response and an open circuit voltage response of 130.2 dB (ref: 1 μPa/V) and -160.7 dB (ref: 1V/μPa) at a distance of 100 mm respectively. In addition, improvements of around 3 dB for both transmit voltage response and open circuit voltage response in FLAUT are observed when compared to conventional electrostatic transducers.
- From the noise measurements, it was found that the FLAUT is able to reduce the thermal noise by 2.7 dB for a bandwidth of 120 kHz when compared to the conventional electrostatic transducers.
- In a two-way insertion loss measurement, measured at a distance of 100 mm; the FLAUT insertion loss was found to be at 61.3 dB, a 9.1 dB reduction when compared to the conventional electrostatic transducer.

7.2 Suggestions for Further Work

From the thesis, there are specific areas that could be improved further. This could be divided into 4 areas, which are:

- Analytical Modelling
- Finite Element Modelling
- Backplate Manufacturing Processes
- Assembly Process

7.2.1 Analytical Modelling

The current analytical modelling suggests the use of resonant frequency for individual thin plate, cavity and pipe. In this thesis, the techniques suggest that FLAUT geometry is identified and finite element modelling is utilised to identify the frequency response and the mode shape for the design.

An improvement could be made which could identify the frequency response directly from the analytical model, which considers the thin plate, cavity and pipe as a total system. Although, the geometry could be still identified using the individual component analysis, the system based analysis such as those proposed by Walker *et al* [101] needs to be extended to include such a geometric identification feature. In addition, a system-based approach could also be proposed - with thin plate, cavity and pipe being considered as one system; and thus analysed as such. However, a suitable geometry analysis still needs to be identified. In FLAUT geometrical analysis, there are five main variables, which are the thin plate thickness, the cavity radius, cavity depth, pipe radius and pipe depth. These variables contribute to the geometrical design of the FLAUT. Although in this thesis the use of a component by component approach is utilised, a ratio based approach as proposed by Campbell *et al* [99] could also be investigated for the system based approach.

7.2.2 Finite Element Modelling

In this thesis, two software packages have been utilised for the finite element modelling which are Comsol Multiphysics Ver. 3.5a and PZFlex. In addition, there are two types of finite element modelling performed - the single component and the excited modal analysis.

In this thesis, only a single unit cell is modelled using axi-symmetrical boundary. For further improvement, an array of FLAUT cells could be modelled using finite elements. However, the 2D axi-symmetrical boundary is not suited for modelling of such arrays. Thus, in this case 3D modelling needs to be performed for the array. To reduce the size of the model and assuming that the same fundamental mode is considered in the modelling, a quarter symmetrical boundary of the cylindrical backplate could be utilised in the 3D. Furthermore, the effect of array spacing within the design could also be modelled in the 3D modelling which has not been performed in this Thesis.

In addition, to evaluate the corroboration between modelling and measurement, a white light interferometer laser scanning of the cavity and pipe surface both to identify the surface roughness and the level of concentricity between the pipe and cavity for an array design could be performed. This surface measurement could then be imported into Comsol Multiphysics Ver. 4.1, and the frequency response evaluated based on the actual backplate fabricated. This would help to further investigate the effect of cavity/pipe mismatch, as well as the effect of array spacing tolerance within the fabricated backplate.

7.2.3 Backplate Manufacturing Process Improvement (Analysis and Fabrication)

One of the research areas that required development that is more comprehensive is the manufacturing of the FLAUT backplate. Within the context of this Thesis, a non-correlated sensitivity analysis for manufacture has been considered due to the complexity in adding several correlated parameters together. As a further work, correlated geometrical tolerances between different processes and geometries could be made. This would enable a more accurate analysis of the proposed manufacturing techniques and processes when a new design of a FLAUT is proposed.

In this Thesis, the highest frequency pursued from the available in-house manufacturing processes is the 85 kHz transducer device. It is possible to increase the FLAUT transducer frequency range further to beyond 100 kHz. However, the need to control and reduce the cavity thickness further has made this a challenge with the current manufacturing and assembly process incorporating a thin plate and rigid backplate. Furthermore, as the frequency increases the needed FLAUT geometry will need to be reduced accordingly. Thus, as previously discussed this increases the influence of viscous boundary layer on the pipe wall and the viscous damping on the surface of the cavity, which needs to be considered.

Some of the reviews on the manufacturing method, especially which relate to effectiveness of manufacture, improving cost efficiencies and utilisation of micro and

nano manufacturing technologies employ processes such as Deep Reactive Ion Etching (DRIE), Ultra Violet (UV) based-LIGA, Soft Imprint Lithography and Nano Imprint Lithography will be discussed. From the current design, there are few actions that could be considered to improve the pressure output of the transducer further.

7.2.3.1 Utilising Higher Repeatability Tolerance for Manufacture of the FLAUT

In this matter, although the current 0.08 mm and 0.01 mm tolerances are minimally sufficient for the 35 kHz and 85 kHz transducer respectively; improvement could still be made. By considering a higher repeatability tolerance, around 0.005 mm or even at 0.001 mm for the manufacturability of the single unit cell, the concentricity of the cavity and pipe could be improved, thus improving the overall amplification of the device.

7.2.3.2 Utilising Deep Reactive Ion Etching (DRIE) as a Manufacturing Process

One of the difficulties in producing a FLAUT is the high aspect ratio and the vertical wall required during the manufacturing process. In this respect, DRIE is a suitable candidate as it is able to produce a very high aspect ratio of above 15 [168] and with almost vertical walls, $88^{o} – 90^{o}$ being typical [169, 170]. The DRIE process [170] involves the use of high density plasma and an alternating steps of silicon etching and polymer deposition. The polymer deposition protects the already carved feature from further lateral etching. As the process etched through the silicon in the order of 0.5 – 5.0 μm deep, ripple effect occurs at the vertical sidewalls. This is similar to the MSL vertical walls edges. However, Fu *et al* [170] noted that the ripple effect could be minimised, by properly optimising certain critical parameters. Thus, it is possible using DRIE process to manufacture the 85 kHz transducer FLAUT that have cavity of 44 μm and a vertical pipe with high aspect ratio of around 5 with a better accuracy

since the DRIE process are able to etch at 0.5 μm deep and vertically at 90^{o} as noted in the review.

7.2.3.3 Utilising Ultra Violet (UV) based-LIGA as a Manufacturing Process

In addition to DRIE, a Micro Electro-mechanical System (MEMS) manufacturing technique is also proposed. A typical sequence of the MEMS production process is shown in Figure 7.1 [171].

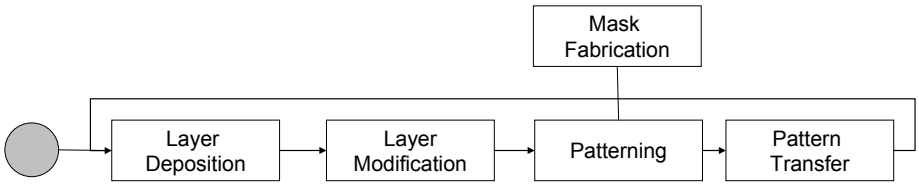

Figure 7.1: Process Flow of a Typical MEMS Production Process

To produce the micro sized cavity and pipe geometry for the FLAUT, an Ultra Violet (UV) based-LIGA process is proposed. LIGA is a German acronym for lithography (LIthographie), electroforming (Galvanoformung), and molding (Abformung). Using a UV-LIGA process it is possible to build a 3D structure with a very high aspect ratio with a wide variety of materials such as plastics, metals, alloys and ceramics, or a combination of these materials. Generally, in a UV-LIGA process, a thick SU-8 resist and an ultraviolet light source are used. To produce a FLAUT, SU-8, which is a negative epoxy-type photo resist that works near UV will be utilised. The SU-8 photo resist can be spin-coated to meet the thickness of the desired FLAUT [172]. However, since there is a need to have two different hole thicknesses and diameters, the SU-8 photo resist needs to be spin-coated twice, once for the pipe and the next for the cavity.

A similar process to produce such geometry has been developed by Zou *et al* [173], but with three layers of concentric holes. The same process could be utilised and adapted to suit the FLAUT. The proposed flow for the fabrication of FLAUT

utilising a SU-8 photo resist material is shown in Figure 7.2. The flow proposes a single cell FLAUT; however, the same concept could be applied for an array. In this process, precise alignment is necessary to ensure the concentricity of the two holes is maintained; as such, an alignment mark is added to the silicon substrate. A thin omnicoat layer is spin-coated on to the silicon substrate to reduce the SU-8 adhesion and acts as a sacrificial layer to release the SU-8 after it is developed. The first layer of the SU-8 is spin-coated on top of the omnicoat layer and then exposed to the UV light. Next, similar to the first layer, the second layer is then deposited and exposed. Lastly, the SU-8 structure is developed and released from the substrate. The FLAUT backplate is then sputtered with aluminium.

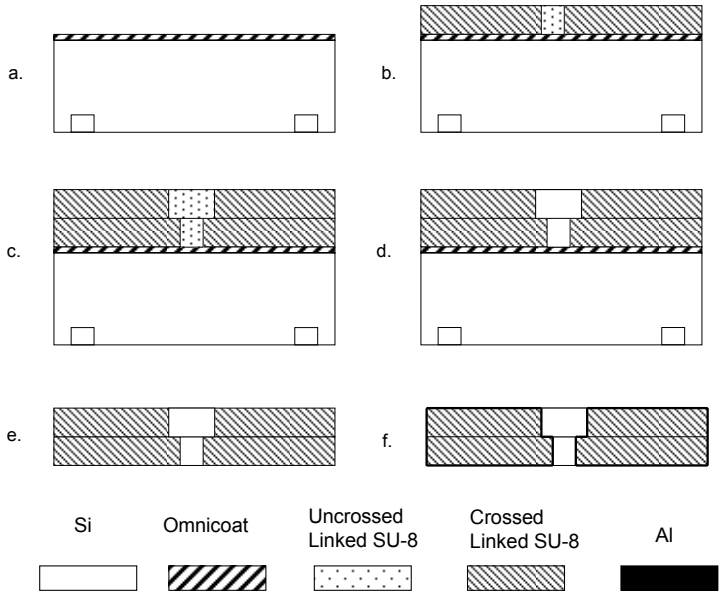

Figure 7.2: Schematic Diagram of a Two-Layer SU-8 Structure Fabrication Process to Fabricate a FLAUT: (a) Spin-Coating of Omnicoat™, (b) First Lithography, (c) Second Lithography, (d) Development (e) Released SU-8 Structure and (f) Metallisation

7.2.3.4 Utilising Generalised Application Technique in MEMS/NEMS (Nano Electro-mechanical System) Area which utilises Small Cavities and Pipes as a Manufacturing Process Consideration

Increasing the operating frequency of the FLAUT to the MHz range would ultimately require that the individual FLAUT cell geometry to be reduced proportionally to nanometer sizes. These MEMS/NEMS areas include such application as Lab-on-a-Chip (LOC), Lab-on-a-Print (LOP), microfluidic, Micro Total Analysis System (μTAS) etc, which requires the internal working mechanism to have a size from a few nanometers to micrometers size. In identifying any suitable future relevance to the FLAUT fabrication, it is noticed that MEMS/NEMS fabrication technique for small cavities and pipes are very diverse from photolithography, LIGA and all the processes that have been previously discussed; to other form of manufacturing processes such as soft lithography [174] and nanoimprint lithography [175]. These are some of the technologies to be considered both in term of cost and manufacturing effectiveness. As such, within the context of the FLAUT being an array device, a method that utilises lithography as a base is still a method of choice due to the controlled patterned requirement. However, with the diverse range of lithography methods, a method that could cover both the requirement of a concentric cavity/pipe and high aspect ratio whilst still able to be cost effective would be an ideal solution.

A lithography which promises a cost effective solution while still maintaining the possible accuracy is soft lithography [174]. This is a process which uses elastomers as stamps, molds or masks to generate patterns and structures without the use of light or other high energy particles [174, 176]. Some of the examples of soft lithography are microcontact (mCP), the replica molding, the micromolding in capillaries (MIMIC). In a review, Zhou *et al* [174] have shown that a feature size of 100 nm was accomplished by carrying out mCP under water.

Chou *et al* [175] and Torres *et al* [177] have reviewed a manufacturing process of nanoimprint lithography, which promised to be cost effective yet are able to cater for

nanometer sized resolution. In this process, three basic components are required: i) a mold or stamp with suitable features, ii) the material to be printed and lastly iii) equipment for printing. The process starts by a mold pressing on the materials to be printed to create a thickness contrast. An etching process is then performed to remove the non-desired feature in the compressed area. In the review by Chou *et al* [175], nanoimprint lithography is able to produce a hole of 25 nm in diameter with period of 120 nm, and strips of 70 nm wide and 200 nm tall with near perfect 90^{o} corners.

7.2.4 Assembly Process

In this thesis, as described in Chapter 6, the thin plate is not fully clamped to the backplate. As such, based on the previous discussion a more optimised separation between the cavities is suggested. This increase in separation is expected to improve the clamping afforded by the bias voltage at the expense of pressure output due to the sparsing of the individual cell in the active area. Another option that could be performed is to mechanically fixed the thin plate to the backplate as have been performed in 1-3 composite for piezoelectric polymers [49]. However, few considerations need to be made when the Kapton film is permanently attached to the backplate. During the assembly, the cavities and pipes edges and depth need to be maintained to ensure no resonant changes due to clamping size difference between the individual cells, when the Kapton film is bonded to the backplate. Furthermore, since Kapton film is easily damaged, careful consideration during the bonding and assembly process is required. Typically, a new backplate is needed once the Kapton film is damaged, as it is generally not possible to repair the backplate once the Kapton film is mechanically removed. Lastly, as previously discussed, as the cavity resonant frequency increases, the required cavity depth reduces in an inverse squared power function. Thus, to ensure that the device is operating at its desired operating frequency, the bonding thickness needs to be included as part of the FLAUT design process.

By utilising the manufacturing sensitivity analysis discussed in Section 4.7, the change of resonant frequency due to the inclusion of bonding material on the backplate could be calculated. For example, in the 85 kHz transducer design, it was found that if the thickness of the bonding film is at 10% of the cavity depth then the resonant frequency is expected to be at about 87 kHz, a 2 kHz error from the intended design. However, this does not include the tolerance due to the manufacture of the cavity and pipe. In this case, if both the cavity/pipe morphology and the bonding film thickness are considered, then the resonant frequency is expected to be at around 92 kHz. In addition, the geometrical control will become much more important when the device is operating at higher frequencies, since the level of manufacturing tolerance afforded by such a design will be narrower. For that reason, to mitigate the error due to bond thickness, the cavity depth needs to systematically include the expected bond thickness during the cavity resonant frequency identification. This could be performed by modifying Equation 3.6, to include the expected bond thickness as shown in Equation 7.1.

$$f_n = \frac{1}{2\pi}\sqrt{\frac{\gamma P}{\rho_m d_m (d_a + d_b)}} \qquad \textbf{Equation 7.1}$$

where d_b is the bonding thickness, while the rest of the variables are as defined previously.

Based on the discussion above, it could be noted that there are four main areas of improvement for future work – analytical modelling, FEA modelling, backplate manufacturing and assembly. In the analytical model, a ratio based analytical design approach utilising the proposal by Campbell *et al* has been put forward. In the FEA area, it has been suggested that an array of FLAUT cells is to be modelled and compared with the results obtained from the actual surface roughness and cavity/pipe morphology of the FLAUT. In the backplate manufacturing process, two main suggestions have been made – increasing the repeatability and tolerance of manufacture and utilising DRIE, UV Liga and MEMS/NEMS processes for manufacture. Lastly, the proposal for the membrane to be mechanically attached to the backplate is detailed.

Conclusively, this thesis has shown the improvement afforded by FLAUT utilising the one component at a time design approach. In addition, the thesis has shown through simulations and measurements that the pipe diameter needs to be made as large as practically possible to improve the overall output. Lastly, the importance of array separation is also noted, which gives rise to the future work suggestion of having the array to be modelled in FEA to identify the most optimised array separation, as well as to model the actual FLAUT and its backplate array morphology to enable improved modelling accuracy.

8. References

[1] U. Schnars and R. Henrich., "Application of NDT Methods on Composite Structures in Aerospace Industry," in *Conference on Damage in Composite Materials*, Stuttgart, Germany 2006, pp. 1-8.

[2] A. P. Cracknell, *Ultrasonics*. London: Wykeham Publications, 1980.

[3] D. Williams, *Guide to Cleaner Technologies: Cleaning and Degreasing Process Changes*. Washington DC, USA: United States Environmental Protection Agency, 1994.

[4] P. Wahl, "Put Sound Waves to Work in Your Shop," in *Popular Science*. vol. March, 1970.

[5] A. Weber, "Welding Still Ensures High-Strength Joints," in *Assembly Magazine* Troy, MI 48084, USA: BNP Media, 2007.

[6] S. Flowers, "Welding Beads: Welding Plastic," in *Assembly Magazine* Troy, MI 48084, USA: BNP Media, 2008.

[7] A. Bertolini, N. Beverini, G. D. Lago, R. DeSalvo, F. Fidecaro, F. Francesconi, M. Francesconi, and G. Omiccioli, "5-Axis CNC Ultrasonic Cutting Machine: Design and Preliminary Test," in *LIGO Document*: The Laser Interferometer Gravitational-Wave Observatory (LIGO) Laboratory, 2002.

[8] T. B. Thoea, D. K. Aspinwalla, and M. L. H. Wiseb, "Review on ultrasonic machining," *International Journal of Machine Tools and Manufacture,* vol. 38, pp. 239-255, 1998.

[9] T. Nelligan and D. Kass, "Intro to Ultrasonic Phased Array," in *Introduction to Olympus Technologies*, Olympus Corporation, Ed., 2013.

[10] C. Mathas, "The Five Senses of Sensors - Sound," in *Article Library* Thief River Falls, MN, USA: Digi-Key Corporation, 2013.

[11] Olympus Corporation, "Thickness Measurement of Aerospace Composites," in *Application Notes*: Olympus Corporation,, 2013.

[12] T. Nelligan, "Ultrasonic Flaw Detection," in *Introduction to Olympus Technologies*: Olympus Corporation,, 2012.

[13] J. Blitz, *Fundamental of Ultrasonics*. London: Butterworths, 1963.

[14] B. Jaffe, W. R. Cook, and G. Jaffe, *Piezoelectric Ceramics*. London: Academic Press, 1971.

[15] M. Logan, "Electrostatic Loudspeaker History." vol. 2010, 2010.

[16] Ö. Oralkan, "Brief History of CMUTs." vol. 2010, 2010.

[17] M. I. Haller and B. T. Khuri-Yakub, "A Surface Micromachined Electrostatic Ultrasonic Air Transducer," *IEEE Transactions on Ultrasonics, Ferroelectrics, and Frequency Control,* vol. 43, pp. 1-6, 1996.

[18] D. W. Schindel, D. A. Hutchins, L. Zou, and M. Sayer, "The Design and Characterization of Micromachined Air-Coupled Capacitance Transducer," *IEEE Transactions on Ultrasonics, Ferroelectrics, and Frequency Control,* vol. 42, pp. 42-50, 1995.

[19] X. C. Jin, F. L. Degertekin, S. Calmes, X. J. Zhang, I. Ladabaum, and B. T. Khuri-Yakub, "Micromachines Capacitive Transducer Array for Medical Ultrasound Imaging," in *IEEE International Ultrasonics Symposium*, 1998, pp. 1877-1880.

[20] Ö. Oralkan, X. C. Jin, K. Kaviani, A. S. Ergun, F. L. Degertekin, M. Karaman, B. T. Khuri-Yakub, and E. L. Ginzton, "Initial Pulse-Echo Imaging Results With One-Dimensional Capacitive Micromachined Ultrasonic Transducers Array," in *IEEE International Ultrasonics Symposium*, 2000, pp. 959-962.

[21] R. L. O'Leary, "An Investigation Into the Passive Materials Utilised within the Construction of Piezoelectric Composite Transducers " in *Department of Electronic and Electrical Engineering*. vol. Doctor of Philosophy Glasgow, United Kingdom: University of Strathclyde, 2003, p. 251.

[22] L. Pizarro, D. Certon, M. Lethiecq, and B. Hosten, "Airborne Ultrasonic Electrostatic Transducers With Conductive Grooved Backplates: Tailoring Their Centre Frequency, Sensitivity And Bandwidth," *Ultrasonics,* vol. 37, pp. 493-503, 1999.

[23] P. R. Scheeper, A. G. H. van der Donk, W. Olthuis, and P. Bergveld, "A Review of Silicone Microphones," *Sensors and Actuators,* vol. 44, pp. 1-11, 1994.

[24] A. S. Ergun, B. Temelkuran, E. Ozbay, and A. Atalar, "A New Detection Method for Capacitive Micromachine Ultrasonic Transducers," *IEEE Transactions on Ultrasonics, Ferroelectrics, and Frequency Control,* vol. 48, pp. 932-942, 2001.

[25] S. T. Hansen, A. S. Ergun, W. Liou, B. A. Auld, and B. T. Khuri-Yakub, "Wideband Micromachines Capacitive Microphone with Radio Frequency Detection," *Acoustical Society of America,* vol. 116, pp. 828-842, 2004.

[26] NDT Education Resource Centre, "Wave Propagation." vol. 2012: NDT Education Resource Centre, 2012.

[27] NDT Education Resource Centre, "Mode Conversion." vol. 2014: NDT Education Resource Centre, 2013.

[28] R. A. Banks, "A Frequency Agile Approach to Air-Coupled Lamp Wave Inspection," in *Department of Electronic and Electrical Engineering*. vol. Doctor of Philosophy Glasgow: University of Strathclyde, 1999, p. 233.

[29] W. Roye and S. Schieke, "Ultrasonic Probes for Special Applictions.," in *The European Conference on Non-Destructive Testing*, 2006, pp. 1-10.

[30] Olympus Corporation, "Ultrasonic Couplants," in *Application Notes*: Olympus Corporation,, 2010.

[31] M. Castaings and B. Hosten, "The Use of Electrostatic, Ultrasonic, Air-Coupled Transducer to Generate and Receive Lamb Waves in Anisotropic, Viscoelastic Plates," *Ultrasonics,* vol. 36, pp. 361-365, 1998.

[32] J. Buckley, "Air-coupled Ultrasound - A Millennial Review," in *The 15th World Conference on Non-Destructive Testing* Rome: NDT, 2000.

[33] M. Larson, "Ten Criteria for Accurate Ultrasonic Couplant Selection," in *Inspection Trend*, 2009.

[34] S. Bourne, M. Newborough, and D. Highgate, "Novel Solid Contact Ultrasonic Couplant Based on Hydrophilic Polymers," in *The 15th World Conference on Non-Destructive Testing* Rome: NDT, 2000.

[35] J. Buckley, "Principle and Applications of Air-Coupled Ultrasonics," Sonatest PLC.

[36] U. Demirci, A. S. Ergun, O. Oralkan, M. Karaman, and B. T. Khuri-Yakub, "Forward-Viewing CMUT Array for Medical Imaging," *IEEE Transactions*

on Ultrasonics, Ferroelectrics, and Frequency Control, vol. 51, pp. 886-894, 2004.

[37] W. A. Grandia and C. M. Fortunko, "NDE Applications of Air-Coupled Ultrasonic Transducers," in *IEEE International Ultrasonics Symposium*. vol. 1 Seattle, WA , USA 1995, pp. 697-709.

[38] J. O. Strycek and H. Loertscher, "Ultrasonic Air-Coupled Inspection of Advance Material," in *The Society for the Advancement of Material and Process Engineering*, California, USA, 1999.

[39] General Electric Company, "Ultrasonic Transducers: For Flaw Detection and Sizing," in *GE Sensing & Inspection Technologies*. vol. -: GE Measurement and Control, 2013, pp. 1-47.

[40] S. P. Kelly, "An Air-coupled Ultrasonic Array Scanning System for Rapid through Transmission NDT," in *Department of Electronic and Electrical Engineering*. vol. Doctor of Philosophy Glasgow: University of Strathclyde, 2000.

[41] I. J. O'Sullivan and W. M. D. Wright, "Ultrasonic Measurement of Gas Flow Using Electrostatic Transducers," *Ultrasonics,* vol. 40, pp. 407-411, 2002.

[42] J. Hietanen, "Closed-form Formulation for Sensitivity of Capacitive Ultrasonic Transducers using V-gooved Backplates," *Sensors and Actuators,* vol. 69, pp. 139-142, 1998.

[43] C. M. Fortunko, W. P. Dube, and J. D. McColskey, "Gas-Coupled Acoustic Microscopy in The Pulse Echo Mode," in *IEEE International Ultrasonics Symposium*, Baltimore, MD , USA 1993, pp. 667-671.

[44] P. Shuttleworth, J. Maupin, and A. Teitsma, "Gas Coupled Ultrasonic Measurement of Pipeline Wall Thickness," *Journal of Pressure Vessel Technology,* vol. 127, pp. 290-293, 2005.

[45] Airstar Inc, "Air Coupled Ultrasound." vol. 2010, 2010.

[46] E. Blomme, D. Bulcaen, and F. Declercq, "Air-coupled Ultrasonic NDE: Experiments in the Frequency Range 750 kHz - 2 MHz," *NDT&E International,* vol. 35, pp. 417-426, 2002.

[47] L. E. Kinsler, A. R. Frey, A. B. Coppens, and J. V. Sanders, *Fundamental of Acoustics* vol. 1: John Wiley & Sons Inc, 1982.

[48] J. Krautkrämer and H. Krautkrämer, *Ultrasonic Testing of Materials*. Berlin: Springer-Verlag, 1990.

[49] M. I. Haller and B. T. Khuri-Yakub, "1-3 Composites for Ultrasonic Air Transducer," in *IEEE International Ultrasonic Symposium*, Tucson, AZ, USA, 1992, pp. 937-940.

[50] "Piezoelectric and Acoustic Materials for Transducer Applications," A. Safari and E. K. Akdogan, Eds. New York, NY: Springer Science Business Media, LLC, 2008.

[51] R. Steinhausen, C. Pientschke, and H. Beige, "Modelling and Characterisation of Piezoelectric 1-3 Fibre Composite," in *Sensor and Test Conferences*, Nürnberg, Germany, 2011, pp. 199-204.

[52] G. W. C. Kaye and T. H. Laby, "The speed and attenuation of sound," in *Kaye and Laby Tables of Physical and Chemical Constant*, National Physical Laboratory, Ed., 2013.

[53] L. Jakevičius and A. Demčenko, "Ultrasound attenuation dependence on air temperature in closed chambers," *Ultragarsas Journal,* vol. 62, 2008.

[54] C. R. Nave, "Diffraction of Sound," in *HyperPhysics*. vol. 2014, George State University, Ed. Atlanta, Georgia, USA: George State University, 2012.

[55] A. P. Medley, D. R. Billson, D. A. Hutchins, and L. A. J. Davis, "Properties of an Electrostatic Transducer," *Acoustical Society of America,* vol. 120, pp. 2658-2666, 2006.

[56] M. Rafiq and C. Wykes, "The Performance of Capacitive Ultrasonic Tranducer Using V-Grooved Backplate," *Measurement Science and Technology,* vol. 2, pp. 168-174, 1991.

[57] T. H. Gan, D. A. Hutchins, D. R. Billson, and D. W. Schindel, "The Use of Broadband Acoustic Transducers and Pulse-Compression Techniques for Air-Coupled Ultrasonic Imaging," *Ultrasonics,* vol. 39, pp. 181-194, 2001.

[58] Ö. Oralkan, A. S. Ergun, J. A. Johnson, M. Karaman, U. Demirchi, K. Kaviani, T. H. Lee, and B. T. Khuri-Yakub, "Capacitve Micromachine Ultrasonic Transducer: Next-Generation Arrays for Acoustic Imaging?," *IEEE Transactions on Ultrasonics, Ferroelectrics, and Frequency Control,* vol. 49, pp. 1596-1610, 2002.

[59] W. M. D. Wright and D. A. Hutchins, "Air-Couple Ultrasonic Testing Of Metals Using Broadband Pulses In Through-Transmission," *Ultrasonics,* vol. 32, pp. 19-22, 1999.

[60] J. Salazar, A. Turó, J. A. Cháves, J. A. Ortega, and M. J. Garcia, "High-Power High-Resolution Pulser for Air-Coupled Ultrasonic NDE Applications," *IEEE Transactions on Ultrasonics, Ferroelectrics, and Frequency Control,* vol. 52, pp. 1792-1798, 2003.

[61] J. Hietanen, P. Mattila, J. Stor-Pellinen, F. Tsuzuki, H. Väätäjä, K. Sasaki, and M. Luukkala, "Factors Affecting the Sensitivity of Electrostatic Ultrasonic Transducers," *Measurement Science and Technology,* vol. 4, pp. 1138-1142, 1993.

[62] J. Hietanen, J. Stor-Pellinen, M. Luukkala, P. Mattila, F. Tsuzuki, and K. Sasaki, "A Helmholtz Resonator Model for an Electrostatic Ultrasonic Air Transducer with a V-grooved Backplate," *Sensors and Actuators,* vol. 39, pp. 129-132, 1993.

[63] A. Gachagan, G. Hayward, S. P. Kelly, and W. Galbraith, "Characterisation of Air-Coupled Transducers," *IEEE Transactions on Ultrasonics, Ferroelectrics, and Frequency Control,* vol. 43, pp. 678-688, 1996.

[64] J. Hietanen, J. Stor-Pellinen, and M. Luukkala, "A Model for an Electrostatic Ultrasonic Transducer With a Grooved Backplate," *Measurement Science and Technology,* vol. 3, pp. 1095-1097, 1992.

[65] J. Hietanen, J. Ignatius, and J. Stor-Pellinen, "Electrostatic Solutions for a Capacitive Ultrasonic Air Transducer with a Uniformly V-Grooved Backplate," *Sensors and Actuators,* vol. 45, pp. 95-98, 1994.

[66] P. Mattila, F. Tsuzuki, H. Väätäjä, and K. Sasaki, "Electroacoustic Model for Electrostatic Ultrasonic Tranducer with V-Grooved Backplates," *IEEE Transactions on Ultrasonics, Ferroelectrics, and Frequency Control,* vol. 42, pp. 1-7, 1995.

[67] S. G. McSweeney and W. M. D. Wright, "HfO2 High-k dielectric Layers in Air-coupled Capacitive Ultrasonic Transducers " in *IEEE International Ultrasonics Symposium*, 2011, pp. 864-867.

[68] Ö. Oralkan, B. Bayram, G. G. Yaralioglu, A. S. Ergun, M. Kupnik, D. T. Yeh, I. O. Wygant, and B. T. Khuri-Yakub, "Experimental Characterization of Collapse-Mode CMUT Operation," *IEEE Transactions on Ultrasonics, Ferroelectrics, and Frequency Control,* vol. 53, pp. 1513-1523, 2006.

[69] B. Bayram, E. Hæggström, G. G. Yaralioglu, and B. T. Khuri-Yakub, "A New Regime for Operating Capacitive Micromachined Ultrasonic Transducers," *IEEE Transactions on Ultrasonics, Ferroelectrics, and Frequency Control,* vol. 50, pp. 1184-1190, 2003.

[70] M.-C. Ho, M. Kupnik, K. K. Park, and B. T. Khuri-Yakub, "Long Term Measurement Results of Pre-charged CMUTs with Zero External Bias Operation," in *IEEE International Ultrasonics Symposium*, Dresden, Germany, 2012.

[71] M.-C. Ho, M. Kupnik, K. K. Park, K. Eckhoff, and B. T. Khuri-Yakub, "Wide Pressure Range Operation of Air-coupled CMUTs," in *IEEE International Ultrasonics Symposium*, Dresden, Germany, 2012.

[72] K. Suzuki, K. Higuchi, and H. Tanigawa, "A Silicone Electrostatic Ultrasonic Transducer," *IEEE Transactions on Ultrasonics, Ferroelectrics, and Frequency Control,* vol. 36, pp. 620-627, 1989.

[73] I. O. Wygant, M. Kupnik, B. T. Khuri-Yakub, M. S. Wochner, Wayne M. Wright, and M. F. Hamilton, "The Design and Characterization of Capacitive Micromachined Ultrasonic Transducers (CMUTs) for Generating High-Intensity Ultrasound for Transmission of Directional Audio," in *IEEE International Ultrasonics Symposium*, Beijing, China, 2008, pp. 2100-2102.

[74] E. Campbell, L. A. J. Davis, G. Hayward, D. Hutchins, and R. Noble, "Cross-coupling in Sealed cMUT Arrays for Immersion Applications," in *Unspecified*, 2007.

[75] D. A. Hutchins, J. S. McIntosh, A. Neild, and D. R. Billson, "Radiated Fields Of Capacitive Micromachines Ultrasonic Transducers In Air," *Acoustical Society of America,* vol. 114, pp. 1435-1449, 2003.

[76] S. T. Hansen, A. S. Ergun, W. Liou, B. A. Auld, and B. T. Khuri-Yakub, "Wideband Micromachines Capacitive Microphone With Radio Frequency Detection," *Acoustic Society of America,* vol. 116, pp. 828-842, 2004.

[77] G. Caliano, V. Foglietti, E. Cianci, and M. Pappalardo, "A Silicone Microfabrication Electrostatic Transducer: 1MHz Transmission In Air And Water," *Microelectronics Engineering,* vol. 53, pp. 573-576, 2000.

[78] E. Campbell, W. Galbraith, and G. Hayward, "A New Electrostatic Transducer Incorporating Fluidic Amplification," *IEEE Ultrasonic Symposium,* pp. 1445-1448, 2006.

[79] K. K. Park, O. Oralkan, and B. T. Khuri-Yakub, "Comparison of conventional and collapse-mode CMUT in 1-D array configuration " in *IEEE International Ultrasonics Symposium*, Orlando, FL 2011, pp. 1000-1003.

[80] M. Füldner, A. Dehé, and R. Lerch, "Analytical Analysis and Finite Element Simulation of Advanced Membranes for Silicon Microphones," *IEEE Sensors Journal,* vol. 5, pp. 857-863, 2005.

[81] P. C. Hsu, C. H. Mastrangelo, and K. D. Wise, "A High Sensitivity Polysilicon Diaphragm Condenser Microphone," in *IEEE Eleventh Annual International Workshop on Micro Electro Mechanical Systems*, Heidelberg, Germany, 1998, pp. 580-585.

[82] C. W. Tan and J. Miao, "Design Optimization of Condenser Microphone: A Design of Experiment Perspective," *Journal Acoustic Society of America,* vol. 125, pp. 3641-3646, 2009.

[83] M. N. Senlik, S. Olcum, H. Köymen, and A. Atalar, "Bandwidth, Power and Noise Considerations in Airborne CMUTs," in *IEEE International Ultrasonics Symposium*, Rome, Italy, 2009, pp. 438 - 441

[84] L. Pizarro, D. Certon, M. Lethiecq, O. Boumatar, and B. Hosten, "Experimental Investigation of Electrostatic Ultrasonic Transducers with Grooved Backplate," in *IEEE International Ultrasonics Symposium*, Toronto, Canada 1997, pp. 1003 - 1006.

[85] T. Lavergne, S. Durand, M. Bruneau, and N. Joly, "Displacement Field of the Membrane of Condenser Microphones at High Frequencies: Improvement of Analytical Solution," in *Acoustics*, Nantes, France, 2001.

[86] I. O. Wygant, X. Zhuang, D. T. Yeh, Ö. Oralkan, A. S. Ergun, M. Karaman, and B. T. Khuri-Yakub, "Integration of 2D CMUT Arrays with Front-End Electronics for Volumetric Ultrasonic Imaging," *IEEE Transactions on*

Ultrasonics, Ferroelectrics, and Frequency Control, vol. 55, pp. 327-342, 2008.

[87] R. Hickling and S. P. Marin, "The Use of Ultrasonics for Gauging and Proximity Sensing in Air," *Acoustical Society of America,* vol. 79, pp. 115-1160, 1986.

[88] G. Benny, G. Hayward, and R. Chapman, "Beam Profile Measurements and Simulations for Ultrasonic Transducers Operating in Air," *Acoustical Society of America,* vol. 107, pp. 2089-2100, 2000.

[89] Ö. Oralkan, X. Jin, F. L. Degertekin, and B. T. Khuri-Yakub, "Simulation and Experimental Characterization of a 2-D Capacitive Micromachined Ultrasonic Transducer Array Elelement," *IEEE Transactions on Ultrasonics, Ferroelectrics, and Frequency Control,* vol. 46, pp. 1337-1340, 1999.

[90] S. H. Wong, M. Kupnik, X. Zhuang, D.-S. Lin, K. Butts-Pauly, and B. T. Khuri-Yakub, "Evaluation Of Wafer Bonded CMUTS With Rectangular Membrane Featuring High Fill Factor," *IEEE Transactions on Ultrasonics, Ferroelectrics, and Frequency Control,* vol. 55, pp. 2053-2065, 2008.

[91] A. Caronti, A. Savoia, G. Caliano, and M. Pappalardo, "Acoustic Coupling in Microfabricated Ultrasonic Transducers: Modelling and Experiments," *IEEE Transactions on Ultrasonics, Ferroelectrics, and Frequency Control,* vol. 52, pp. 2220-2234, 2005.

[92] E. Ventsel and T. Krauthammer, *Thin Plates and Shells: Theory, Analysis, and Applications.* New York: Marcel Dekker Inc, 2001.

[93] W. C. Young and R. G. Budynas, *Roark's Formula for Stress and Strain*, 7 ed. New York: McGraw-Hill, 2002.

[94] T. D. Rossing and N. H. Fletcher, *Principles of Vibration and Sound*. New York, 1994.

[95] A. Wood and J. M. Bowsher, *Alexander's Wood's The Physics of Music*, 7th ed. London: John Wiley & Sons Ltd, 1975.

[96] The Open University, "Vibrating Air Column: Standing Waves in a Cylindrical Tube Open at Both Ends." vol. 2011 Milton Keynes: The Open University, 2011.

[97] The Open University, "Vibrating Air Column: Standing Waves in a Cylindrical Tube Closed at One End." vol. 2011 Milton Keynes: The Open University, 2011.

[98] S. H. Anderson and F. C. Ostensen, "Effect of Frequency on The End Correction of Pipes," *Physical Review,* vol. 31, pp. 267-274, 1928.

[99] E. Campbell, W. Galbraith, and G. Hayward, "A New Electrostatic Transducer Incorporating Fluidic Amplification," *IEEE International Ultrasonics Symposium,* pp. 1445-1448, 2006.

[100] DuPont de Nemours (Luxembourg) s.a.r.l., "DuPont™ Kapton® HN Polyimide Film Technical Data Sheet." vol. 2012 Luxembourg: DuPont de Nemours (Luxembourg) s.a.r.l., 2012.

[101] A. J. Walker, A. J. Mulholland, E. Campbell, and G. Hayward, "A theoretical model of a new electrostatic transducer incorporating fluidic amplification," in *IEEE International Ultrasonics Symposium*, 2008, pp. 1409-1412.

[102] A. Caronti, G. Caliano, A. Iula, and M. Pappalardo, "An Accurate Model for Capacitive Micromachined Ultrasonic Transducers," *IEEE Transactions On Ultrasonics, Ferroelectrics, And Frequency Control,* vol. 49, pp. 159-168, 2002.

[103] G. G. Yaralioglu, A. S. Ergun, and B. T. Khuri-Yakub, "Finite-Element Analysis of Capacitive Micromachined Ultrasonic Transducers," *IEEE Transactions On Ultrasonics Ferroelectrics And Frequency Control,* vol. 52, pp. 2185-2198, 2005.

[104] M. Kupnik, I. O. Wygant, B. T. Khuri-Yakub, and E. L. Ginzton, "Finite Element Analysis of Stress Stiffening Effects in CMUTs," in *IEEE International Ultrasonic Symposium Proceedings*, 2008.

[105] B. Bayram, M. Kupnik, G. G. Yaralioglu, O. Oralkan, A. S. Ergun, L. Der-Song, S. H. Wong, and B. T. Khuri-Yakub, "Finite Element Modelling and Experimental Characterization of Crosstalk in 1-D CMUT Array," *IEEE Transactions On Ultrasonics Ferroelectrics And Frequency Control,* vol. 54, pp. 418-430, 2007.

[106] H. Najar, "Combined FEA-Matlab Optimisation of Capactive Micromachined Ultrasound Transducer Cell," in *Proceeding of the ASME International*

Mechanical Engineering Congress & Exposition, Vancouver, British Columbia, Canada, 2010.

[107] P. Fesenko, "Capacitive Micromachined Ultrasonic Transducer (CMUT) for Biometric Applications," in *Department of Microtechnology and Nanoscience*. vol. Master of Nanoscience and Nanotechnology Goteborg, Sweeden: Chalmers University of Technology, 2012, p. 40.

[108] Weidlinger Associates Inc, "PZFlex Virtual Prototyping." vol. 2012 Mountain View, California: Weidlinger Associates, Inc, 2012.

[109] S. P. Timoshenko, *Vibration Problems in Engineering*, 1955.

[110] Institute of Mathematics and its Applications, "What Makes an Object Into a Musical Instrument?: Tuned Drums." vol. 2011, I. o. M. a. i. Applications, Ed. Southend-on-sea: Institute of Mathematics and its Applications, 2012.

[111] The Engineering ToolBox, "Dry Air Properties," in *Material Properties - Density, Heat Capacity, Viscosity and More - for Gases, Fluids and Solids*, Editor.engineeringtoolbox, Ed., 2013.

[112] Comsol AB, "Comsol Multiphysics: Modelling Guide Version 3.5a," Comsol AB, Ed.: Comsol AB, 2008.

[113] X. Zhang, X. N. Jiang, and C. Sun, "Micro-stereolithography of Polymeric and Ceramic Microstructures," *Sensors and Actuators,* vol. 77, pp. 149-156, 1999.

[114] Dutch Society for Precision Engineering, "Additive Manufacturing of Miniature Parts," in *Mikroniek*, 2010.

[115] A. Bertsch, S. Jiguet, P. Bernhard, and P. Renaud, "Microstereolithography: a Review," in *Materials Research Society Symposium Proceedings*, Boston, Massachusetts, 2002, pp. 3-15.

[116] A. Bertsch, S. Jiguet, and P. Renaud, "Microfabrication of Ceramic Components by Microstereolithography," *Journal of Micromechanics and Microengineering,* vol. 14, pp. 197-203, 2004.

[117] Stratasys Ltd, "Objet Eden 350/350V." vol. 2013 Eden Prairie: Stratasys Ltd, 2013.

[118] D. A. Hutchins, D. R. Billson, R. J. Bradley, and K. S. Ho, "Structural Health Monitoring using Polymer-based Capacitive Micromachined Ultrasonic Transducers (CMUTs)," *Ultrasonics,* vol. 51, pp. 870-877, 2011.

[119] E. C. Jameson, *Electrical Discharge Machining*. Dearborn, USA: Society of Manufacturing Engineers, 2001.

[120] C. Sommer and S. Sommer, "Complete EDM Handbook," R. EDM, Ed. Houston, Texas.

[121] K. Liu, B. Lauwers, and D. Reynaerts, "Process Capabilities of Micro-EDM and Its Applications," *The International Journal of Advanced Manufacturing Technology,* vol. 47, pp. 11–19, 2010.

[122] D. d. Caussin, "Drilling Deep Holes On A VMC." vol. 2012: Modern Machine Shop,, 2012.

[123] Mikron Corp. Monroe, "Mikron Machining Products." vol. 2013 Monroe, USA: Mikron Corp. Monroe 2011.

[124] Hobart Lasers Ltd, "VersaLaser - VLS series." vol. 2013 Kent: Hobart Lasers Ltd,, 2013.

[125] R. D. Schaeffer, "Understanding and Controlling Taper when Laser Machining," Northbrook, IL, USA: Micro Manufacturing, 2010.

[126] S. Dhar, N. Saini, and R. Purohit, "A Review on Laser Drilling and Its Techniques," in *International Conference on Advances in Mechanical Engineering*, Punjab, India, 2006.

[127] SPIE The International Society for Optics and Photonics, "Definition: Semiconductor Lithography." vol. 2013, SPIE The International Society for Optics and Photonics, Ed. Bellingham, WA, USA: SPIE The International Society for Optics and Photonics,, 2013.

[128] P. Reynolds, "Analysis and Design of Piezocomposite Ultrasonic Transducers Using Finite Element Technique and Surface Displacement Profiles," in *Department of Electronic and Electrical Engineering*. vol. Doctor pf Philosophy Glasgow: University of Strathclyde, 1998, p. 281.

[129] A. Vladišauskas and L. Jakevičus, "Absorption of Ultrasonic Waves in Air " *Ultragarsas Journal,* vol. 1, pp. 46-49, 2004.

[130] C. W. Tan and J. Miao, "Analytical Modelling for Bulk-Micromachined Condenser Microphones," *Acoustical Society of America,* vol. 120, pp. 750-761, 2006.

[131] R. D. Kass, "Propagation of Errors." vol. 2012 Columbus, Ohio: Department of Physics, Ohio State University, 2010.

[132] A. J. Zuckerwar, T. R. Kuhn, and R. M. Serbyn, "Background Noise In Piezoresistive, Electret Condenser, and Ceramic Microphones," *Journal Acoustic Society of America,* vol. 113, pp. 3179-3187, 2003.

[133] T. B. Gabrielson, "Fundamental Noise Limits In Miniature Acoustic and Vibration Sensors," Naval Air Development Centre, Warminster, PA 18974-5000 1991.

[134] T. B. Gabrielson, "Mechanical-Thermal Noise in Micromachine Acoustics and Vibration Sensor," *IEEE Transactions on Electron Devices,* vol. 40 pp. 903-909, 1993.

[135] R. W. Harris, "Electromechanical Analogies in Acoustics," *Applied Acoustics,* vol. 3, pp. 265-281, 1970.

[136] P. Mattila, J. Stor-Pellinen, J. Ignatius, J. Hietanen, and M. Luukkala, "Capacitive Ultrasonic Transducer with Net Backplate," *Measurement Science and Technology,* vol. 11, pp. 1119-1125, 2000.

[137] Z. Škvor, "On the Acoustical Resistance Due to Viscous Losses in the Air Gap of Ellectrostatic Transducers," *Acustica,* vol. 19, pp. 295-299, 1967.

[138] V. Tarnow, "Thermal Noise in Microphones and Preamplifiers," *Technical Review: To Advance Techniques in Acoustical, Electrical and Mechanical Measurement,* vol. 3, pp. 3-14, 1972.

[139] C. W. Tan and J. Miao, "Modified Skvor/Starr Approach in The Mechanical-Thermal Noise Analysis of Condenser Microphone," *Journal Acoustic Society of America,* vol. 125, pp. 2301-2305, 2009.

[140] F. A. Levinzon, "Fundamental Noise Limit of Piezoelectric Accelerometer," *IEEE Sensors Journal,* vol. 4, pp. 108-111, 2004.

[141] J. B. Starr, "Squeeze-Film Damping in Solid-State Accelerometers," in *IEEE Solid-State Sensor and Actuator Workshop*. vol. 90, 1990, pp. 44-47.

[142] Suzhou Dexlu Material & Tech Co. Ltd, "Polyimide Film (similar to Kapton® HN)," in *Product* Suzhou, China: Suzhou Dexlu Material & Tech Co. Ltd,, 2014.

[143] J. Bergqvist, "Finite-element Modelling and Characterization of a Silicon Condenser Microphone with A Highly Perforated Backplate," *Sensors and Actuators,* vol. 39, pp. 191-200, 1993.

[144] A. Zuckerwar and K. C. T. Ngo, "Measured 1/f Noise in the Membrane Motion of Condenser Microphone," *Journal Acoustic Society of America,* vol. 95, pp. 1419-1425, 1994.

[145] K. C. T. Ngo and A. J. Zuckewar, "Measurement of Thermal Noise In Condenser Microphones and Associated Preamplifier in a Vacuum-Isolation Vessel," in *IEEE Proceedings of Southeast Conference*, 1991, pp. 520-524.

[146] K. C. T. Ngo and A. J. Zuckerwar, "Acoustic Isolation Vessel for Measurement of The Background Noise In Microphone," *Acoustical Society of America,* vol. 93, pp. 2974-2980, 1993.

[147] H. F. Olson, "Microphone Thermal Agitation Noise," *Acoustical Society of America,* vol. 51, pp. 425-432, 1972.

[148] V. Tarnow, "The Lower Limit of Detectable Sound Pressures," *Acoustical Society of America,* vol. 82, pp. 379-381, 1987.

[149] G. S. U. Department of Physics and Astronomy, "Mean Free Path ". vol. 2012 Atlanta, Georgia: Department of Physics and Astronomy, Georgia State University, 2010.

[150] B. Z. Shakhashiri, *Chemical Demonstrations: A Handbook for Teachers of Chemistry, Volume 2*. Wisconsin: The University of Wisconsin Press, 1985.

[151] Sorbothane Inc, "About Sorbothane Materials Properties," 2012.

[152] C. H. Cheng, A. S. Ergun, and B. T. Khuri-Yakub, "Electrical Through-Wafer Interconnects with Sub-PicoFarad Paracitic Capacitance," in *Microelectromechanical Systems Conference*, IEEE, Ed. Berkeley, CA, USA, 2001, pp. 18-21.

[153] B. T. Khuri-Yakub, C.-H. Cheng, F.-L. Degertekin, S. Ergün, S. Hansen, X.-C. Jin, and Ö. Oralkan, "Silicon Micromachined Ultrasonic Transducers," *Japanese Journal of Applied Physics,* vol. 39, pp. 2883-2887, 2000.

[154] K. K. Park, E. L. Ginzton, H. Lee, K. M, and B. T. Khuri-Yakub, "Fabrication of Capacitive Micromachined Ultrasonic Transducers via Local Oxidation and Direct Wafer Bonding " *Microelectromechanical Systems,* vol. 20, pp. 95 - 103 2011.

[155] P. Mattila, J. Siirtola, and R. Suoranta, "Two-Dimensional Object Detection in Air using Ultrasonic Transducer Array and Non-Linear Digital L-Filter," *Sensors and Actuators,* vol. 55, pp. 107-113, 1996.

[156] H. Lee, J. Tak, W. Moon, and G. Lim, "Effects of mutual impedance on the radiation characteristics of transducer arrays," *Journal Acoustic Society of America,* vol. 115, pp. 666-679, 2004.

[157] H. Lee, D. Kang, and W. Moon, "A Micro-machined Source Tranducer for a Parametric Array in Air," *Journal Acoustic Society of America,* vol. 125, pp. 1879-1893, 2009.

[158] R. L. Pritchard, "Mutual Acoustic Impedance between Radiators in an Infinite Rigid Plane," *Journal Acoustic Society of America,* vol. 32, pp. 730-737, 1960.

[159] M. N. Senlik, S. Olcum, H. Koymen, and A. Atalar, "Radiation Impedance of an Array of Circular Capacitive Micromachine Ultrasonic Transducers," *IEEE Transactions on Ultrasonics, Ferroelectrics, and Frequency Control,* vol. 57, pp. 969-976, 2010.

[160] G. Benny and G. Hayward, "Beam Profile Measurements and Simulation for Ultrasonic Transducers Operating in Air," *Acoustic Society of America,* vol. 104, pp. 2089-2100, 1999.

[161] Roland DG, "Benchtop Engravers EGX-600/400 Specifications." vol. 2012 Cardiff: Roland DG, 2012.

[162] T. Whelan and J. Goff, *Injection Molding of Thermoplastics Materials*: Springer US, 1990.

[163] K. Deutsch, E. A. W. Hoff, and W. Reddish, "Relation between the Structure of Polymers and their Dynamic Mechanical and Electrical Properties," *Journal of Polymer Science,* vol. Volume 13, pp. 565–582, 1954.

[164] Ebalta Distribution Limited, "Block and Board Materials." vol. 2013 Retford, Nottinghamshire: Ebalta Distribution Limited, 2013.

[165] S. J. Orfanidis, "Electromagnetic Waves and Antennas," 2013 ed, Rutgers University, Ed. Piscataway, NJ: Rutgers University,, 2013.

[166] J. P. Donohoe, "Plane Wave Reflection Transmission," in *ECE3313*, J. P. Donohoe, Ed. Mississippi: Mississippi State University, 2014.

[167] M. Polyanskiy, "Refractive Index Database," in *Refractive Index Database*, M. Polyanskiy, Ed., 2013.

[168] J. Yeom, Y. Wu, J. C. Selby, and M. A. Shannon, "Maximum Achievable Aspect Ratio in Deep Reactive Ion Etching of Silion due to Aspect Rato Dependent Transport and the Microloading Effect," *Journal of Vacuum Science Technnology,* vol. 26, pp. 2319-2329, 2005.

[169] X. Li, T. Abe, and M. Esashi, "Deep Reactive Ion Etching of Pyrex Glass using SF6 Plasma," *Sensor and Actuators,* vol. 87, pp. 139-145, 2001.

[170] Y. Q. Fu, A. Colli, A. Fasoli, J. K. Luo, A. J. Flewitt, A. C. Ferrari, and W. I. Milne, "Deep Reactive Ion Etching as a Tool for Nanostructure Fabrication," *Journal of Vacuum Science Technnology,* vol. 27, pp. 1520-1526, 2009.

[171] F. Chollet and H. Liu, "A (Not So) Short Introduction to Micro Electromechanical Systems," 5.0 ed. vol. 2013, 2012.

[172] S. J. Jeong, "UV-LIGA Micro-Fabrication of Inertia Type Electrostatic Transducers and Their Applications," in *The Department of Mechanical Engineering*. vol. Doctor of Philosophy: Sungkyunkwan University, 2006.

[173] H. Zou, J. Li, Petr Jurčíček, and G. Wang, "Microfabrication of a Multilayer Nano-ESI Focusing Electrode Based on SU-8 Material," *Microelectronic Engineering,* vol. 103, pp. 150-155, March 2013 2013.

[174] X.-M. Zhao, Y. Xia, and G. M. Whitesides, "Soft Lithographic Method for Nano-Fabrication," *Journal of Materials Chemistry,* vol. 7, pp. 1069-1074, 1997.

[175] S. Y. Chou, P. R. Krauss, and P. J. Renstrom, "Imprint Lithography with 25-Nanometer Resolution," *Science,* vol. 272, pp. 85-87, 1996.

[176] A. T. Giannitsis, "Microfabrication of Biomedical Lab-on-a-Chip Devices. A Review.," *Estonian Journal of Engineering,* vol. 2, pp. 109-139, 2011.

[177] C. M. S. Torres, S. Zankovych, J. Seekamp, A. P. Kam, C. C. Cedeno, T. Hoffmann, J. Ahopelto, F. Reuther, K. Pfeiffer, G. Bleidiessel, G. Gruetzner,

M. V. Maximov, and B. Heidari, "Nanoimprint Lithography: An Alternative Nanofabrication Approach," *Journal of Materials Science and Engineering* vol. 23, pp. 23-31, 2003.

9. Appendixes

9.1 U.S. Navy Workshop on Acoustic Transduction Materials and Devices 2011

Improving the Sensitivity of Air-Coupled Ultrasound Transducers through Fluidic Amplification

R. L. O'Leary[1], S. B. Abdul Hamid[1], A. J. Walker[2], A. J. Mulholland[3]
[1]Centre for Ultrasonic Engineering, University of Strathclyde
[2]Department of Computing and Mathematics, University of Glamorgan
[3]Department of Mathematics and Statistics, University of Strathclyde

University of Strathclyde Engineering

Introduction

Electrostatic transducers are inherently wideband and posses a good acoustic matching to fluid media [1], although in many cases the sensitivity is still limited.

Recently, a new electrostatic transducer where the cavity is coupled to a resonant pipe has been proposed; with the amplification being provided by the resonant of the pipe [2]. In order for a matched resonant frequency to be evaluated, an iterative process to match the resonant frequencies has been developed; which encompasses a series of frequency and geometric matching in three individual components: the plate/membrane thickness and the cavity and pipe dimensions.

Utilizing the following equations, the three different individual resonances were matched.

$$f_r = \frac{K_r}{2\pi}\sqrt{\frac{Ed^3}{12(1-\nu^2)\rho_m a^4}}$$ Plate Resonance [3]

$$f_r = \frac{1}{2\pi}\sqrt{\frac{\gamma P}{\rho_a d_c d_p}}$$ Cavity Resonance

$$f_r = \frac{nc}{4(L_p + 0.6r)}$$ Pipe Resonance [4]

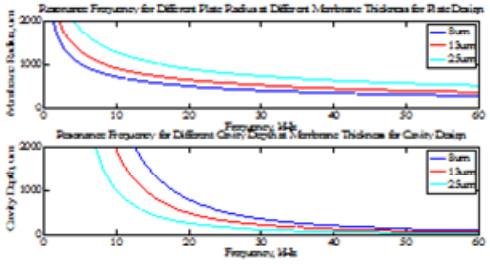

Potential Design Configurations

Due to the resonance frequency matching process that needs to be applied for a coupled cavity/pipe transducer, there are only 3 potential design configuration available:

- Change in plate/membrane thickness.
- Change in plate/membrane cavity radius.
- Change in aspect ratio between the plate/membrane cavity radius and pipe radius

Although, it is possible to change other geometries such as cavity depth and pipe length for the design, the need to match the three resonances renders this option not viable.

Analytical And Measurement Validation

In order to validate the model, prototypes incorporating the different backplate geometries have been fabricated and assembled.

Final Assembly

Assembly with brass backplate exposed

To validate, analytical model and FEA model is corroborated with the acoustic field measurement. An output of an almost two order of magnitude is observed between cavity only and cavity pipe pressure output measured using a calibrated Brüel and Kjær microphone.

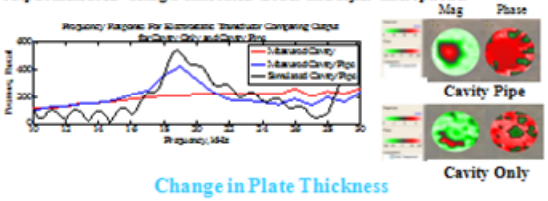

Change in Plate Thickness

Originally, three different thickness were proposed; due to design requirements for cavity depth of less 0.05mm, only two plate/membrane thickness are compared. A higher displacement is observed with a thicker plate.

Change in Pipe Radius

Another potential design is to change the size of pipe radius. In order to evaluate the effect of this changes, a single resonant frequency and plate thickness have been chosen for the different pipe radii. At resonance frequency, it is observed that the larger the pipe diameter the higher the output magnitude.

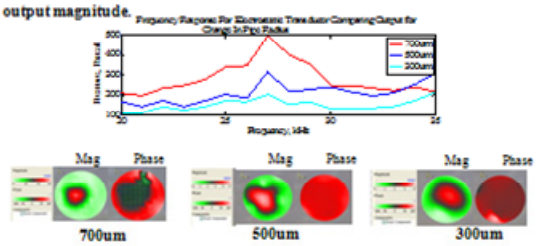

Summary of Results

The output for simulation and measurement for FMUT have been presented; with the effect of different membrane thickness and pipe dimensions analysed. It is found that a thicker membrane and larger pipe dimensions produce a higher output sensitivity for the FMUT. In addition, it is observed that control of the backplate tolerance is important to enable a good matching of FMUT.

Concluding Remarks

The process for matching an FMUT have been presented. The higher sensitivity output using FMUT have been portrayed and the different output for different FMUT configuration have been discussed and analyzed.

References
1. S. Ergun, B. Temelkuran, E. Ozbay et al., "A New Detection Method for Capacitive Micromachined Ultrasonic Transducers," *IEEE Transaction on IEEE Transactions on Ultrasonics Ferroelectrics and Frequency Control*, vol. 48, no. 4, pp. 1070-1076, 2001. Imaging Applications" *IEEE Transactions on Ultrasonics Ferroelectrics and Frequency Control*, Vol. 50, No. 11, pp. 1548-1557, 2003
2. E. Campbell, W. Galbraith, and G. Hayward, "A New Electrostatic Transducer Incorporating Fluidic Amplification" *IEEE Transaction on IEEE Ultrasonic Symposium*, pp. 1445-1448, 2006
3. Young, W.C. and R.G. Budynas, *Roark's Formula for Stress and Strain*. 7 ed. 2002, New York: McGraw-Hill.
4. Bowsher, J.M., *Alexander Wood's The Physics of Music*. 7th ed. 1975. London: John Wiley & Sons Ltd.